



3D Pyrolytic Carbon for Monitoring Type I Allergic Reactions

Esmail Tehrani, Sheida

Publication date:
2022

Document Version
Publisher's PDF, also known as Version of record

[Link back to DTU Orbit](#)

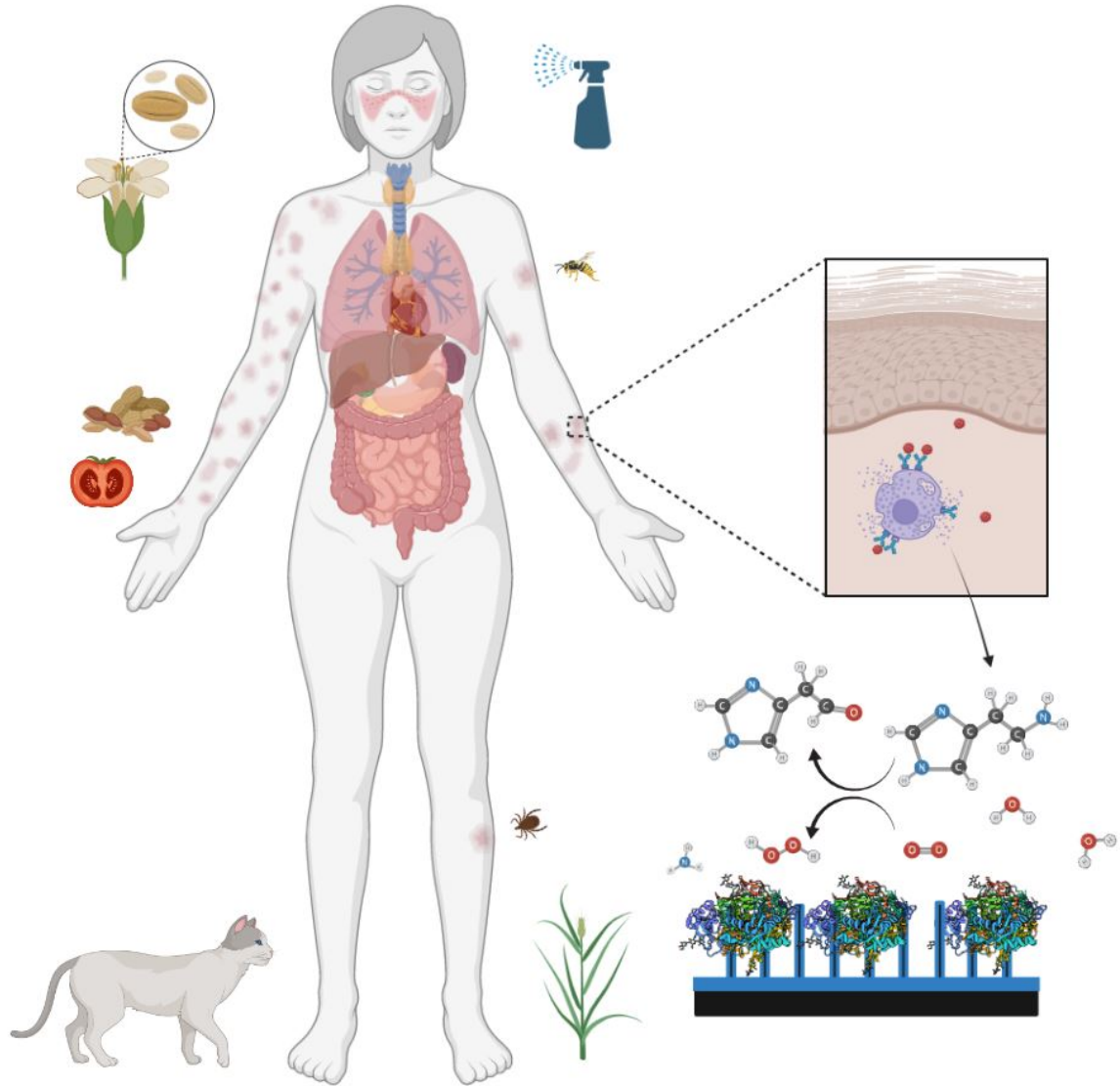
Citation (APA):
Esmail Tehrani, S. (2022). *3D Pyrolytic Carbon for Monitoring Type I Allergic Reactions*. DTU Nanolab.

General rights

Copyright and moral rights for the publications made accessible in the public portal are retained by the authors and/or other copyright owners and it is a condition of accessing publications that users recognise and abide by the legal requirements associated with these rights.

- Users may download and print one copy of any publication from the public portal for the purpose of private study or research.
- You may not further distribute the material or use it for any profit-making activity or commercial gain
- You may freely distribute the URL identifying the publication in the public portal

If you believe that this document breaches copyright please contact us providing details, and we will remove access to the work immediately and investigate your claim.



3D Pyrolytic Carbon for Monitoring Type I Allergic Reactions

Ph.D. Dissertation

Sheida Esmail Tehrani

August 2022

Main advisor: Professor Stephan Sylvest Keller
Co-supervised by: Professor Jenny Emnéus &
Associate Professor Bettina Margrethe Jensen

Pyrolytic Carbon for Monitoring Type I Allergy Reactions

Ph.D. Dissertation

DTU Nanolab

August 2022

By

Sheida Esmail Tehrani

Copyright: Reproduction of this publication in whole or in part must include the customary bibliographic citation, including author attribution, report title, etc.

Cover photo: Created with Biorender.com

Published by: DTU, National Centre for Nano Fabrication and Characterization, Oersteds Place,
Building 347, 2800 Kongens Lyngby
www.nanolab.dtu.dk

ISSN: [0000-0000] (electronic version)

ISBN: [000-00-0000-000-0] (electronic version)

ISSN: [0000-0000] (printed version)

ISBN: [000-00-0000-000-0] (printed version)

Preface

This dissertation is the documentation of the research which was carried out during my doctoral study at the Technical University of Denmark (DTU) from April 2018 to June 2021. My Ph.D. program was the first defined study within the framework of InstaPatch research project, which aimed to develop a new test for type I allergy and to address some of the current limitations experienced in the clinical practice of allergy diagnosis, thereby. My Ph.D. program was co-financed by the National Centre for Nano Fabrication and Characterization (DTU Nanolab), LEO Foundation and the Copenhagen Center for Health Technology (CACHET) whose financial support made this at all possible. Professor Stephan Sylvest Keller, who has the expertise in creation of carbon based micro-electro-mechanical systems (C-MEMS) for variety of applications, owned the InstaPatch research project, and therefore my Ph.D. work was conducted in his group, Biomaterial Microsystems (BIOMIC), at DTU Nanolab located in Kongens Lyngby, Denmark. I have known Stephan since I was a M.Sc. student. He was the lecturer for one of my favourite courses. His fairness, modesty and intelligence were outstanding and inspiring. During my Ph.D. study, there was no single moment when I have regretted joining his group. For me, Stephan has all the scientific and personal qualities that an excellent leader must have. With his open-office-door policy and the willingness to listen, he created a friendly working environment where I could talk about my frustrations and discuss my daily challenges when things did not go well in the lab. His positive mindset and constructive feedbacks even when he faced my failures, encouraged me to try again and again, and to improve my work constantly. I am deeply indebted to Stephan for his priceless support throughout all these years, for trusting me and for giving me the opportunity to do a Ph.D. project in his group. My work would have also been incomplete without the support of our collaborators. Professor Jenny Emnéus, who co-advised me throughout the project, and her research group at the Department of Biotechnology and Biomedicine (DTU Bioengineering) generously provided me with equipment, lab space, knowledge-sharing, hands-on support in the lab, constructive feedbacks, and valuable discussions during the group meetings. I am truly honored and grateful to have had the chance to present my work to Jenny and receive her opinion about it. As a supervisor, Jenny is a volcano of brilliant ideas, and as a person she is friendly and fun to be with. I enjoyed her company and her liveliness during our conference trip to Ireland in 2019. Her valuable advice specially when I was writing my two papers, truly lifted my work to a higher level. I am also thankful to senior researcher Arto Heiskanen for his kindness and generosity in devoting time and energy to answering my fundamental questions in the field of electrochemistry, giving me ideas and instructions for the design and fabrication of the electrochemical setup explained in chapter 4.1, and helping me in the lab with micromilling. In addition, my work was also co-supervised by Associate Professor Bettina Margrethe Jensen at the Allergy Clinic at Copenhagen University Hospital in Gentofte, Denmark. Enzyme characterization experiments in chapter 6 and mast cell titration and activation described in paper II in Appendix B were all planned and prepared by Bettina and performed in her lab. Although we did not meet often, Bettina always engaged herself so eagerly in the project, followed my progress and took interest in other aspects of the research than her own field, that she left me in grief for not having had the time and the chance to work more in her lab. I would like to express my sincere gratitude to Bettina for helping me to gain a fundamental knowledge of allergy that you can read about in chapter 1, for bringing new visions to my project and for giving me the opportunity to present my research to the medical students, biochemists, doctors, and the specialists at the Allergy Clinic. Bettina's

openness and warmth made me feel at home as a physicist among her many medical students and colleagues at the lectures, and when attending their meetings and seminars. During my external stay, Professor Tautgirdas Ruzgas from the Malmö University kindly hosted me in his electrochemistry lab at the Department of Biomedical Science for about 3 months. He owns the idea of exploiting the capacitive properties of the Prussian Blue (PB) for hydrogen peroxide and histamine detection presented in paper II. It was in his lab and under his supervision that I learned for the first time how to develop an electrochemical enzymatic biosensor for histamine detection. The primary experiments with PB and hydrogen peroxide were also conducted in Malmö. When I look back at the period which I spent at Taut's lab, I can say that I learned a lot during my external stay. I moved from 'not knowing anything' about PB and its electrochemical properties to 'being able' to transfer the knowledge to my own group at DTU, to equip our own electrochemistry lab and to establish the procedure for the modification of the pyrolytic carbon with PB for the first time ever. Paper I in Appendix A, which was published in 2021, is the proof for this claim. I hereby would like to thank Taut sincerely for taking his time, despite his busy schedule, to reflect on my arguments and challenges and to have long scientific discussions at times when I was struggling to find the answers to many questions that came to my mind.

I would also like to extend my gratitude to the current and the former BIOMIC group members for all the fun and cooperations. At the beginning of my project, Yasmin who was formerly a Ph.D. student trained me in the cleanroom to fabricate my own batches of 2D and 3D pyrolytic carbon electrodes as explained in chapter 3. However, Long (former postdoc working on InstaPatch project) and Jesper (fellow Ph.D. student) took over the electrode fabrication after a few months allowing me to focus on the sensor development and the electrochemistry. I know that they both spent many hours in the cleanroom to provide me with good electrodes, and for long time they struggled to overcome the troubles that a defected and mal-functioning pyrolysis furnace had caused. I want them to know that how much I value their efforts and appreciate their commitment. Jesper was always so humble and kind, which made me reach out to him when I needed help in the workshop with wafer dicing and 3D printing. He was always ready to give me a hand in the lab with a short notice, and I cannot thank him enough for all those times. I am also thankful to Galina and Babak, our postdoc researchers, for giving me ideas to improve my work. Galina humbly shared her experience and profound knowledge of electrochemistry with me and inspired me by her decisiveness and highly systematic work. Stephanie, the Ph.D. student who joined me and Long in the InstaPatch project, brought much joy to the group. She was the one with whom I could think of having a relaxing coffee break after intensive lab work. As a partial fulfilment for obtaining the Ph.D. degree, I co-supervised the final projects of three students who worked with me on parts of my Ph.D. project. Rikke (B.Sc. student) carried out some of the PB optimization studies and did a thorough and systematic literature review on the content of the dermal interstitial fluid included in chapter 1. Giulia, M.Sc. student, 3D designed the first-generation multi-electrode cell presented in 4.2.2 and established the 3D printing. Irem (M.Sc. student) optimized the enzyme immobilization protocol. I acknowledge their hard work.

The last year of my Ph.D. study coincided with the early phase of COVID-19 pandemic and the restrictions that followed it. I highly appreciate the DTU Nanolab leaders, administration team and the technicians for their efficient work and high degree of coordination, despite the distances and the restrictions, with which they created a safe environment where I could still go to the lab and perform some experiments.

Like millions of people who survived the pandemic but lost their jobs, their beloved ones, their health, their livelihoods and perhaps their hope in future, I was deeply impacted by all that rolled out in front of my eyes and in my absence, and that was the reason for handing in my Ph.D. thesis a year later than the initially planned date. Today, when I am writing these last words of my thesis, I am proud of myself for being able to stand up and try again to finish this chapter of my life. But, my thesis would be incomplete without acknowledging the most understanding, most patient and most supportive people who helped me to go safely through the dark, who helped me to see the light, to keep the hope, to cope with the difficulties and to get over the hard emotions and the feeling of being a failure; my parents, my supervisor Stephan, my fiancé and my precious daughter Elin.

Kongens Lyngby, 19th August 2022

Sheida Esmail Tehrani
Ph.D.Candidate

Abstract

The growing prevalence of type I allergies worldwide is an increasing concern. Allergy is caused by immunoreaction of the body towards in principle harmless allergens that are found, for example, in food. The conventional method for type I allergy screening in a clinical setting is the skin prick test (SPT). Different allergens are introduced into the skin of the forearms of the patient by 1-mm lancets. After 15-20 minutes, the local inflammations that appear on the skin because of the immunoreaction, are inspected visually by an experienced health care professional. SPT is a non-quantitative indirect method of monitoring allergic reactions, which may lead to false results. The number of SPTs that can be performed at a time is limited, and the skin irritation and itchiness might be unpleasant for patients.

This Ph.D. project was part of a bigger research project (InstaPatch) which aimed at addressing the limitations of the SPT by developing a miniaturized microneedle sensor patch, made of pyrolytic carbon, for both allergen delivery and instantaneous monitoring of allergic reactions as they occur in a small area ($1 \times 1 \text{ cm}^2$) of the skin. The overall aim was to develop a quantitative test for direct monitoring of allergic reactions, which is less uncomfortable and more accurate than the conventional test.

The research carried out in this Ph.D. dissertation contributes to the InstaPatch research project by enabling electrochemical detection of histamine, which is the primary allergy biomarker, secreted from activated skin immune cells (mast cells). The thesis presents distinct but interrelated aspects of the Ph.D. project including (1) the fabrication and the electrochemical characterization of three-dimensional (3D) pyrolytic carbon microelectrodes with high-aspect-ratio micropillar structures on a flat carbon base resembling out-of-plane microneedles configuration, (2) the design and manufacturing of a multi-electrode setup by stereolithography for electrochemical characterization of the microelectrodes, the batch preparation of sensors and histamine detection from activated mast cells, (3) sensor construction and optimization on the 3D pyrolytic carbon for obtaining reproducible results, (4) the development of a novel electrochemical technique for improving the sensitivity and the limit of detection (LOD) of the sensor, (5) the detection of histamine released from activated LAD2 human mast cells by the developed technique.

Dansk resumé

Den voksende forekomst af type I-allergier på verdensplan er en stigende bekymring. Allergi skyldes kroppens immunreaktion mod i princippet harmløse allergener, som findes for eksempel i fødevarer. Den konventionelle screeningsmetode til type I-allergi i kliniske omgivelser er priktesten (SPT). Udtræk af forskellige allergifremkaldende stoffer prikkes ind i huden på patientens underarme med 1 mm lancetter. Efter 15-20 minutter undersøges de lokale hævelser, der opstår på huden på grund af immunreaktionen, visuelt af erfarent sundhedspersonale. SPT er en kvalitativ og indirekte metode til overvågning af allergiske reaktioner, som kan føre til falske resultater. Antallet af priktester, der kan udføres ad gangen, er begrænset, og hudirritation og kløe kan være ubehageligt for patienterne.

Dette ph.d.-projekt var en del af et større forskningsprojekt (InstaPatch), som havde til formål at adressere SPT'ens begrænsninger ved at udvikle et miniaturiseret sensorplaster med mikronåle, lavet af pyrolytisk kulstof, til både påføring af allergener og øjeblikkelig undersøgelse af allergiske reaktioner, når de opstår i et lille område ($1 \times 1 \text{ cm}^2$) af huden. Det overordnede mål var at udvikle en kvantitativ test til direkte overvågning af allergiske reaktioner, som er mindre ubehagelig og mere præcis end standardpriktesten.

Forskningen som er udført i denne ph.d.-afhandling bidrager til InstaPatch forskningsprojektet ved at muliggøre elektrokemisk påvisning af histamin, som er den primære biomarkør for allergi, der frigives af aktiverede hudimmunceller (mastceller). Afhandlingen præsenterer distinkte, men indbyrdes forbundne aspekter af ph.d.-projektet, der omfatter (1) fabrikation og elektrokemisk karakterisering af tredimensionelle (3D) pyrolytiske kulstofelektroder med mikrosøjler med høje aspektforhold på et fladt grundlag af kulstof, der ligner mikronåle, (2) design og fabrikation af en elektrokemisk celle med stereolitografi til elektrokemisk karakterisering af flere mikroelektroder på det samme tid, batchpræparation af sensorer samt måling af histamin fra aktiverede mastceller, (3) sensor konstruktion og optimering på de 3D pyrolytiske kulstofelektroder for at opnå reproducerbare resultater, (4) udvikling af en ny elektrokemisk teknik til forbedring af sensorens følsomhed og detektionsgrænse (LOD), (5) påvisning af histamin frigivet fra aktiverede LAD2 humane mastceller med den udviklede teknik.

Contents

CHAPTER 1. INTRODUCTION	4
1.1 ALLERGY	5
1.2 ALLERGENS	5
1.3 ALLERGY BURDEN	5
1.4 TYPE I HYPERSENSITIVITY REACTIONS	7
1.5 CLINICAL TYPE I ALLERGY SCREENING AND DIAGNOSIS	8
<i>In vivo skin prick test</i>	8
<i>In vitro tests</i>	10
1.6 SKIN STRUCTURE AND PHYSIOLOGY	12
<i>Mast cells and allergic inflammation biomarkers</i>	12
<i>Interstitial fluid as a carrier of allergic inflammation biomarkers</i>	13
1.7 DERMAL MICRONEEDLE SENSORS AS A NEW GENERATION OF DIAGNOSTIC TOOLS FOR TYPE I ALLERGY SCREENING	16
<i>Microneedles for dermal drug delivery and sensing</i>	16
<i>Pyrolytic carbon microelectrodes</i>	17
<i>InstaPatch - Instantaneous monitoring of allergic reactions in the skin</i>	17
1.8 PH.D. PROJECT SCOPE, OBJECTIVES AND DELIVERABLES	18
1.9 STRUCTURE OF THE THESIS	20
CHAPTER 2. ELECTROCHEMISTRY AND ELECTROCHEMICAL METHODS.....	21
2.1 ELECTROCHEMISTRY	22
2.2 ELECTROCHEMICAL CELL	22
<i>Redox reactions</i>	23
<i>Faradaic and non-faradaic electrode processes</i>	24
<i>Nernst equation</i>	27
2.3 ELECTROCHEMICAL METHODS	28
<i>Cyclic voltammetry</i>	28
<i>Chronoamperometry</i>	31
<i>Open circuit potentiometry</i>	33
CHAPTER 3. MICROELECTRODE FABRICATION.....	35
3.1 CARBON MICROELECTROMECHANICAL SYSTEMS	36
3.2 PYROLYTIC CARBON MICROELECTRODE DESIGN	37
<i>2D pyrolytic carbon in three-electrode-chip configuration</i>	37
<i>3D pyrolytic carbon in three-electrode-chip configuration</i>	37
3.3 PYROLYTIC CARBON MICROELECTRODE FABRICATION	38
<i>2D microelectrode fabrication</i>	38
<i>3D microelectrode fabrication</i>	39
3.4 ELECTROCHEMICAL CHARACTERIZATION OF 2D AND 3D PYROLYTIC CARBON	41
3.5 MICROELECTRODE DESIGN MODIFICATION	42
CHAPTER 4. FABRICATION OF ELECTROCHEMICAL CELL	43
4.1 POLYMERIC SETUP WITH MAGNETIC CLAMPS FOR AN INDIVIDUAL THREE-ELECTRODE-CHIP	44
4.2 GLASS BEAKER WITH A DESIGNED CAP FOR ELECTRODE INSERTION	47
4.3 3D PRINTED MULTI-ELECTRODE CELL	48
<i>Additive manufacturing by stereolithography</i>	48
<i>First-generation 3D printed multi-electrode cell with magnetic clamp</i>	49
<i>Second-generation 3D printed multi-electrode cell with magnetic stirring</i>	52
<i>Third-generation 3D printed multi-electrode cell for static cell-based measurements</i>	54

CHAPTER 5. ELECTROCHEMICAL HISTAMINE SENSING	56
5.1 HISTAMINE	57
5.2 HISTORICAL EVOLUTION OF ELECTROCHEMICAL HISTAMINE SENSORS	58
5.3 STATE-OF-THE-ART OF ELECTROCHEMICAL HISTAMINE SENSING FOR BIOMEDICAL APPLICATIONS	63
<i>Chemical Sensors</i>	65
<i>Enzymatic Biosensors</i>	66
5.4 ELECTROCATALYSTS FOR ELECTROCHEMICAL DETECTION OF H ₂ O ₂	66
5.5 PRUSSIAN BLUE CRYSTAL STRUCTURE AND ELECTROCHEMICAL PROPERTIES	70
CHAPTER 6. ENZYMATIC HISTAMINE BIOSENSING WITH PRUSSIAN BLUE-MODIFIED PYROLYTIC CARBON MICROELECTRODES	72
6.1 BIOSENSOR DESIGN	73
6.2 BIOSENSOR OPTIMIZATION STRATEGY	73
6.3 PRUSSIAN BLUE FILM ELECTRODEPOSITION	75
6.4 ENZYME LAYER CONSTRUCTION	80
<i>Diamine Oxidase selection</i>	80
<i>Spectrophotometric determination of protein concentration</i>	81
<i>DAO activity and histamine degradation at different pH levels</i>	83
<i>Evaluation of DAO purity by gel electrophoresis</i>	85
<i>DAO immobilization</i>	87
CHAPTER 7. CONCLUSION AND OUTLOOK	89
BIBLIOGRAPHY	
APPENDIX A: PAPER I	
APPENDIX B: PAPER II	

Chapter 1. Introduction

This chapter provides the reader with a brief history of allergy, an overview of its status and socio-economic burden worldwide, and a short description of type I hypersensitivity (allergic) reactions. The chapter also includes a mini review of the standard tests and their pros and cons for type I allergy screening and diagnosis in the clinical practice. A section about the skin structure and physiology and its importance for type I allergy diagnosis is provided. Furthermore, the motivation behind this research is explained, and the main objectives are stated. Finally, the milestones and the main activities, which were defined to achieve the project objectives are listed, and the structure of the thesis is described at the end of the chapter.

1.1 Allergy

In 1906, a young pediatrician from Vienna named Clemens Freiherr von Pirquet used the term 'allergy' (meaning altered reactivity) to explain the abnormal immune response of some individuals to certain substances¹. Today, we identify many substances in the environment as allergens, such as harmless food ingredients, that can cause the symptoms of hypersensitivity reactions in some individuals and which in fewer cases even can be life-threatening.

1.2 Allergens

Allergens are not limited to food ingredients. Certain medications such as antibiotics and non-steroidal anti-inflammatory drugs can cause what is known as drug allergy. Insect venom, airborne mold spores, dust mites, pet hair, pollens from trees, grasses or weeds and perfumes can also trigger allergic reactions. Additionally, exposure to certain substances in the work-environment known as occupational allergens such as nickel, latex and chemicals including but not limited to ethanol, chemicals in cosmetics and skin care products, detergents, drain cleaners, etc. provoke contact allergy or allergic contact dermatitis. **Figure 1-1** illustrates a few recognized sources of allergens in the environment.

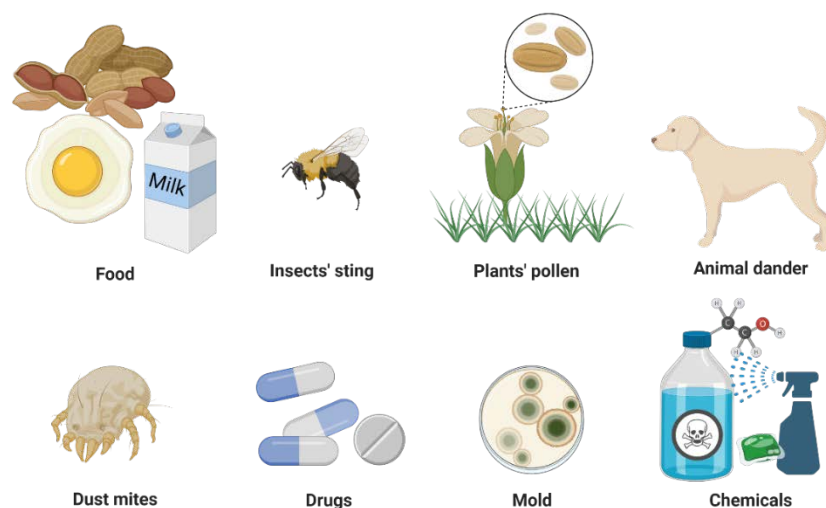


Figure 1-1 Different sources of allergens that enter the body through airways and gastrointestinal tract.
Created with BioRender.com.

1.3 Allergy Burden

The 18th century's scientific developments and industrialization lead to a tenfold increase in the world population and rapid urbanization until the beginning of the 21st century. As a result, human lifestyle change especially with regards to nutrition, unusual foodstuff (such as insects) consumption², massive production and usage of chemicals, drugs, cosmetics and skin care products have increased the prevalence of allergic diseases worldwide. There is evidence that the elevated CO₂ levels due to air pollution and climate change increase the pollen yields of many plants³. Changes in rainfall patterns, flooding and dampness along with warmer temperatures in many areas of the world have created ideal conditions for mold and fungal growth, which is an important risk factor for developing allergic fungal sinusitis, asthma, atopic dermatitis and chronic respiratory diseases^{3,4}.

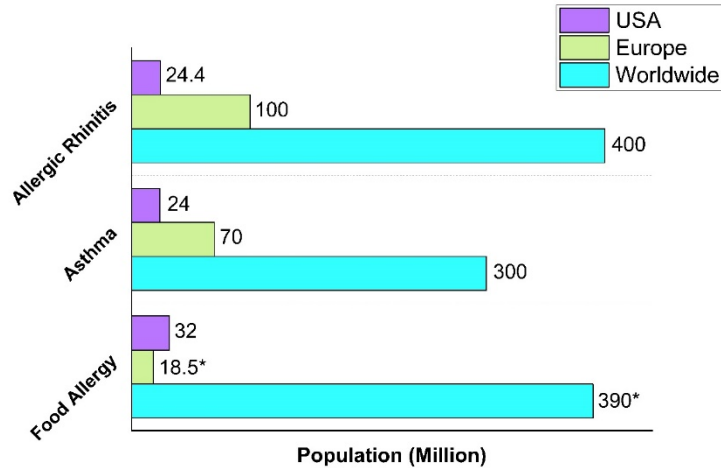


Figure 1-2 Prevalence of asthma and 2 of the most common allergic diseases in the United States^{4,5}, Europe⁶ and worldwide⁴. * Average population calculated from the World Allergy Organization’s (WAO) lowest and highest estimations. According to WAO, 11-26 million members of the European population suffer from food allergy. This number is estimated to be 240-550 million people worldwide. WAO’s data is from 2013 published in White Book On Allergy⁴.

In 2013, the World Allergy Organization (WAO) reported that an estimated 240-550 million people around the globe are affected by food allergy, 300 million suffer from asthma and 400 million from allergic rhinitis (hay fever)^{4,7}. Evidence based on epidemiological studies show that the prevalence of allergic diseases is rising all across the world⁷. World Health Organization (WHO) has expressed its concern about the rising number of asthma patients worldwide, as asthma was among the top five causes of death in high-income countries in 2004 and caused 461000 deaths in 2019. Asthma and allergy are two intertwined conditions that often occur together. Pollen, dust mites, mold spores and animal dander are the sources of substances that trigger both allergic rhinitis and asthma⁸. Food allergens may also trigger asthma symptoms⁹. It is predicted that the number of asthma-affected people around the world will increase to 400 million by 2025. Asthma and Allergy Foundation of America estimates that 60 percent of American asthma patients suffer from allergic asthma, which is induced by an immune response in the airways to a variety of airborne allergens¹⁰. Epidemiological studies in Europe show that chronic allergic diseases affect more than 150 million people on this continent. The European Academy of Allergy and Clinical Immunology (EAACI) considers allergy as a public health concern of growing proportions, as it predicts that with the current trend more than half of the European population will develop at least one type of allergy by 2025⁶. The graph in **Figure 1-2** shows the prevalence of asthma and allergic diseases in USA, Europe and worldwide in 2013.

Allergy has indeed a major negative impact on the patients’ life quality including physical and mental well-being, social relations, educational and career progression, and productivity. Since the onset of the most allergic diseases is during the early years of life, children and youth suffer most from the impaired life quality. In Europe, more than 100 million days of absence from school and work due to asthma and hay fever are recorded every year⁶. The economic burden of the allergic diseases on the national health care systems in EU is estimated to be between 55-151 billion Euro per year⁶. In the United States, more than 24 billion US Dollars is spent annually on tackling food allergy in children alone¹¹.

Unlike the developed countries, large well-designed epidemiological studies on allergy prevalence in the developing and low-income countries are scarce^{2,12}. With that said, it is difficult to make an accurate evaluation of the socio-economic burden of the allergic diseases in other continents. However, it is probably not far from reality to assume that in the small economies, the financial hardship of managing allergy is unendurable. An estimation of annual economic burden of asthma in India has been made by Koul *et al.* to be 487.2 billion Indian Rupee equal to about 6.7 billion US Dollars in 2018¹³. Considering that the majority of the Indian citizens are not covered by the public health insurance, the financial burden is mostly imposed on the patients who may not afford seeing a physician for a proper diagnosis and treatment.

According to EAACI, 45% of the allergy cases in Europe are not properly diagnosed⁶. A study among the US adults show that 1 out of 5 American adults believe that they suffer from food allergy, whereas only 1 out of 20 refer to physicians to get a proper clinical diagnosis⁵. Early accurate diagnosis of allergy and the causative allergen(s) is crucial for receiving exposure prevention guidelines and an effective treatment. Furthermore, getting a diagnosis as close as possible to the onset of the allergic disease is vitally important for avoiding further complications, improving the patients' quality of life and for cutting down the expenditure on medications, acute medical services, and paid sick leave from work and school.

1.4 Type I Hypersensitivity Reactions

The immunological hypersensitivity reactions, also known as allergic reactions, were classified into four types depending on the antigen and the immune reaction mechanism. Type I-III allergic reactions are antibody-mediated, although different classes of antibodies are involved. Type IV allergic reactions are mediated by T cells. In type I allergy, IgE antibodies are the main immune reactants activating the mast cells. In the context of this thesis, type I immune responses are the most relevant and will be discussed in more details in the following.

Type I immediate hypersensitivity reaction can be divided into i) sensitization with the first-time exposure to allergen (**Figure 1-3 A-C**), and ii) activation or early-phase reaction upon re-exposure to allergen (**Figure 1-3 D**). Sensitization of the tissue-resident mast cells and the blood immune cells, known as basophils, is a symptom-free process in which these immune cells are armed with allergen-specific IgE antibodies. The first time that an allergy prone individual is exposed to an allergen, the allergen passes through the airways or cleaves the epithelial cell tight junctions and enters the mucosa where it is collected and processed by immature dendritic cells (**Figure 1-3 A**). The processed allergen is then carried by the now mature dendritic cells to the local lymph node and is presented to naive T cells. These T cells differentiate into helper T cells (T_H2) with the aid of previously produced cytokines (interleukin 4 and 13 produced primarily by mast cells, eosinophils, and basophils). The activated T_H2 cells produce additional cytokines and in the presence of stimulatory molecules interact with B cells whose role is to rearrange the gene segments that encode allergen-specific IgE antibody production (**Figure 1-3 B**). The B cells eventually differentiate into antibody producing plasma cells travelling back to the site where the allergens entered the mucosa and producing IgE antibodies. IgE antibodies diffuse into the lymphatic vessels and are distributed throughout the body by the blood circulation. In the blood, the IgE binds to basophils, and when it reaches the interstitial fluid (ISF) in the tissues, it binds to high affinity IgE receptors ($F_{c\epsilon}RI$) on the membrane of the mast cells, sensitizing them to react to allergens re-entering the body (**Figure 1-3 C**). Later re-exposure to the allergen leads to an early-phase reaction which involves activation of the mast cells upon binding of an allergen to two adjacent IgE molecules (**Figure 1-3 D**). The activated mast cells degranulate immediately releasing inflammatory mediators such as histamine, heparin, serotonin, tryptase, chymase, a few other cytokines and growth

factors into the ISF. Among the released mediators, histamine is the primary cause of symptoms associated with the early-phase reaction. Smooth muscle contraction, expansion of blood vessel diameter (vasodilation), increased blood vessel permeability, elevated local blood flow, itching, sneezing, mucus production, coughing as well as the wheal and flare which appear within minutes of allergen exposure are all caused by histamine^{14–20}.

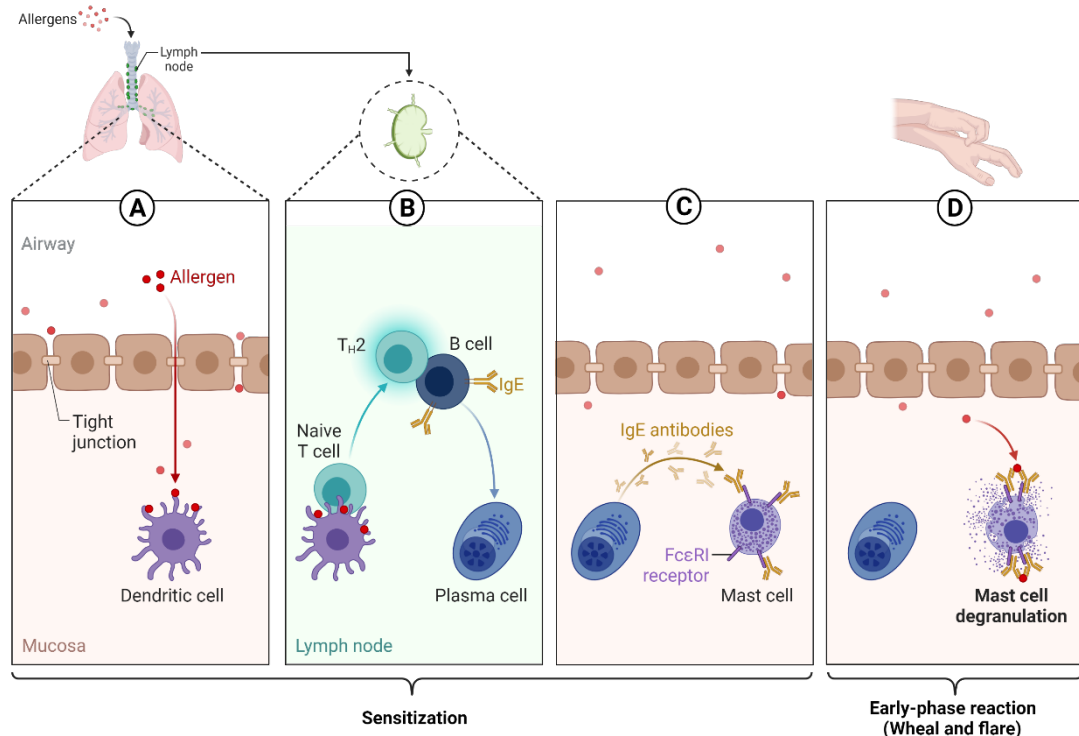


Figure 1-3 The role of mast cells in type I immediate hypersensitivity reactions, which can be divided into sensitization (first time exposure to allergen) and activation or early-phase reaction (re-exposure to allergen); A) the allergen enters the mucosa and is processed by immature dendritic cells; B) the processed allergen is then carried to the local lymph node and is presented to naive T cells, which differentiate into helper T cells (T_H2). The activated T_H2 cells interact with B cells which eventually differentiate to antibody producing plasma cell; C) plasma cells travel back to the site where the allergens entered the mucosa and produce IgE antibodies. In the tissues, IgE antibodies bind to high affinity IgE receptors (F_cεRI) on the membrane of the mast cells, sensitizing them to react to allergens re-entering the body; D) a later re-exposure to the allergen leads to an early-phase reaction. The allergen binds to two adjacent IgE antibodies on mast cells initiating release of histamine which causes the wheal and flare symptom to appear within minutes of allergen exposure. Created with BioRender.com.

1.5 Clinical Type I Allergy Screening and Diagnosis

In the clinical settings, the allergy diagnosis begins with documenting the medical history of the patient followed by a physical examination. Thereafter, *in vivo* skin tests and *in vitro* allergen-specific IgE antibody tests in whole blood are used to identify the specific immune responses. In this section, the two most common clinical practices for the diagnosis of allergic diseases are presented, and the advantages and shortcomings of each are briefly discussed.

In vivo skin prick test

Since the late 1950s, the Skin Prick Test (SPT) has been the gold standard of clinical allergy diagnosis. **Figure 1-4** displays the SPT procedure performed on an adult's forearm. In this method, sterile metal

lancets with a 1-mm long pricker (needle) are used to puncture the epidermis, which is the outermost layer of the skin. This is done at 90° through drops of allergen extracts or control solutions that are placed on the skin in marked rows on the forearms or between the shoulders on the back with 2-5 cm distance between each test site. To assess the histamine reactivity, a positive control test is done by pricking the skin through an allergen-free histamine-containing drop. As negative control, the skin is also pricked through drops of blank diluent that is used to prepare the allergens' extracts. The negative control helps to identify false positive tests, which may appear as non-allergic inflammation of the skin due to the applied pressure, also known as dermatographism. On the test spots, the allergens enter the skin through the opened pathway reaching the skin's immune cells in the upper dermis. If the patient is allergic to the administered substance, the IgE antibodies on the sensitized mast cells capture the allergen and degranulate, releasing histamine and other biomarkers into the ISF. Within 15-20 minutes, the released histamine induces a secondary inflammatory response in the tissue. Red itchy inflamed spots, known as wheal (swollen spot) -and-flare (erythema, redness) appear in the tested area. The accurate assessment and the interpretation of SPT can only be done by an allergologist or by trained medical personnel measuring the diameter of the wheals. If the wheal diameter is larger than 3 mm, the test is considered positive.^{21,22}

The SPT is a quick and readily accessible tool to diagnose type I allergy in patients with allergic rhinitis, food and drug allergy and asthma, and has been the primary clinical diagnostic method for allergy screening, because of its simplicity, low cost and reliability when performed by trained professionals^{7,21-23}. However, like any other diagnostic tool, the SPT has also its limitations.

For instance, the SPT cannot be carried out during pregnancy and on patients with skin trauma, severe eczema and dermatographism. In elderly and small children, the wheal-and-flare may hardly be visible. There are also a few drugs, such as antihistamines and tranquilizers that can inhibit histamine reactivity consequently resulting in false negative SPT. This is due to the fact that SPT does not rely on the assessment of the primary event of histamine release, but rather evaluates the secondary inflammatory tissue response, which is the consequence of histamine release. As mentioned earlier, the test sites should be at least 2 cm apart to avoid that the drops of different allergens merge. This means that the number of tests that can be performed on each forearm is limited to maximum 10-12 for an adult and even less when performed on children. Often, the skin of the upper back is also used to screen for allergic reactions to larger numbers of suspected allergens. Being pricked many times on the forearms and on the back can be irritating especially for infants. Another challenge associated with SPT are the variations in the interpretation of the results by different professionals. A few factors have been recognized to cause variations in the test results. Factors including the allergens' quality as well as quantity, pricker's height and thickness, the angle at which the skin is pricked, and the pressure applied to the lancet have been identified as sources of variability and were optimized to improve the accuracy as well as the reproducibility of the test results. Despite the efforts to standardize the SPT, variations in defining and measuring the wheals remain an issue since the assessment is done qualitatively by visual inspection^{7,21,22}. Attempts have been made to overcome this challenge by automating the SPT reading²⁴. Technologies such as 2D²⁵ and 3D²⁶ scanners, Laser Doppler Flowmetry (LDF)²⁷ for quantifying the blood flow in the skin tissue, photography²⁸ with a digital camera, thermography²⁹ and skin impedance³⁰ measurements have been implemented to automate the wheal measurement. However, most of the aforementioned methods suffer from poor precision and require expensive equipment. Besides, the currently available technologies are unable to perform simultaneous measurement of multiple wheals and therefore make the test analysis quite tedious²⁴. In conclusion, a low-cost and precise diagnostic tool addressing the limitations of the SPT could be favorable.

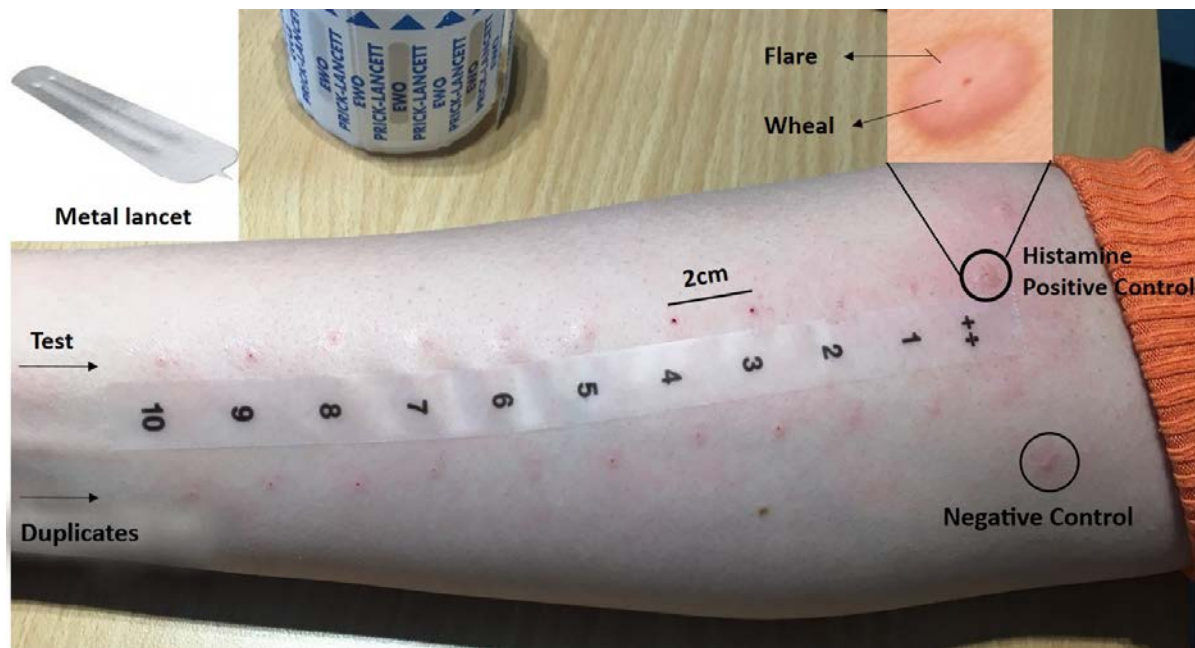


Figure 1-4 Skin prick test on the forearm using metal lancets with a 1- mm pricker; extracts of 10 potential allergens are administered in duplicates through the skin surface on both sides of the test grid (numbered tape) with a histamine-introduced positive control and a negative control puncture on the top.

In vitro tests

In vitro tests can be categorized into cell-based and serum-based analysis. In the cell-based analysis, either the amount of histamine released due to degranulation of the activated basophils in whole blood sample is quantified fluorometrically, or the specific IgE receptor expression on the cell surface is analysed by flow cytometry^{7,31}. The cell-based analysis is rarely used in clinical diagnosis, because its reproducibility is subject to change as the analysis primarily depends on the number of viable basophil cells in the sample. Besides, the difficulty of performing the test and the insufficient sensitivity outgrow the added value provided by the test⁷.

One of the early serum-based tests which were developed in the late 1960s comprised the calculation of total serum IgE with a solid-phase immunoassay, where IgE antibodies were captured between bound anti-IgE antibodies and the secondary anti-IgE antibodies with a label³². A normal threshold was defined for the total amount of IgE antibodies, and the IgE levels in the serum sample of the patients were compared with the normal threshold. IgE levels higher than the normal value were associated with allergic diseases, whereas with observation of low or normal amount of IgE antibodies, the presence of IgE-mediated allergy was rejected. Later, it became evident that high levels of IgE are not a specific indication for allergy and can be observed in patients with other disorders as well. In addition, low and normal IgE levels do not necessarily rule out type I allergy. Another major drawback with the total serum IgE test was the difficulty with defining normal IgE thresholds, as the amount of IgE in the serum is very much age dependent as well³².

Next, the more specific serum-based immunoassays emerged, in which the allergen-specific IgE antibodies in the sample were captured between unrefined natural allergens (conjugated to a solid or liquid-phase support) and labelled anti-IgE antibodies^{7,33} as illustrated in **Figure 1-5**. The analytical performance of specific IgE immunoassays has been improved in time.

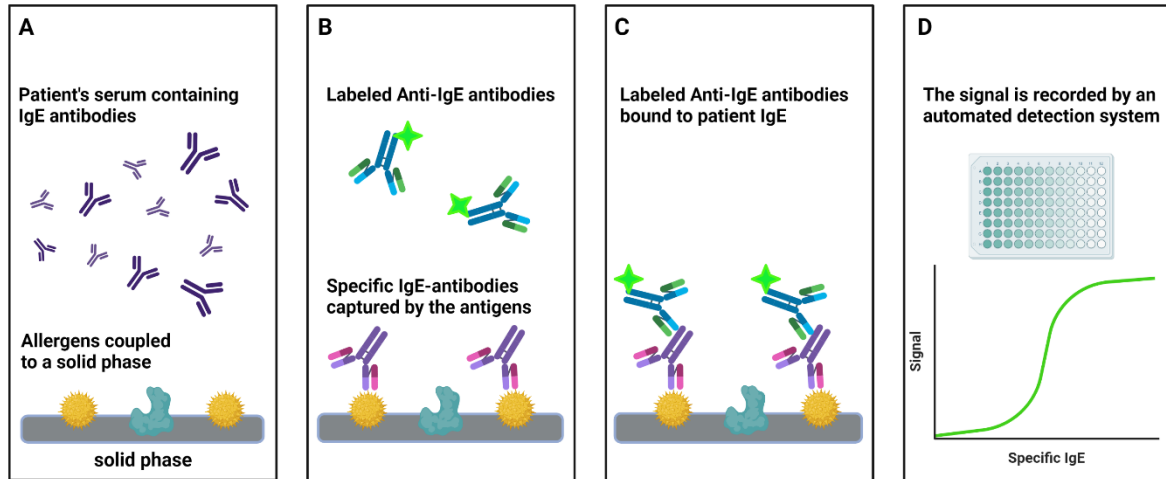


Figure 1-5 Allergen-specific IgE antibody test by a solid-phase immunoassay. A) Allergens (antigen) are coupled to a solid phase support and is exposed to the patient's serum containing IgE antibodies; B) specific IgE antibodies are captured by the antigens while labeled anti-IgE antibodies are added to the reaction container; C) labeled anti-IgE antibodies bind to the patient IgE; D) the label creates a signal which is recorded by the signal detection system. Created with BioRender.com

In clinical practice, *in vitro* detection of specific IgE antibodies in serum specimen of individuals with history of exposure to certain allergens is considered a complementary diagnostic tool for type I allergy screening^{7,21,33,34}. Allergen-specific IgE antibody tests are suitable for patients who cannot endure the SPT or have high risk of anaphylaxis. The qualitative immunoassays are ideal for rapid screening with the aim to rule in and rule out the causative allergens that trigger immune response in an individual. The possibility of multiplexing with small volumes of sample and reagents is another strong argument that makes IgE immunoassays a convenient laboratory practice. The quantitative assays which can indicate the degree of sensitization, are also a good tool for monitoring the efficacy of allergen immunotherapy. However, when unrefined natural allergens are used in the assay, a positive result does not necessarily mean that the patient is allergic to that substance. This is a major challenge that particularly undermines the selectivity of the IgE antibody test for food allergy diagnosis. An allergenic substance is composed of a few allergenic and non-allergenic protein components. Often allergenic proteins with identical structures and epitopes (binding sites) can be found in different food or substances³³. An individual who is allergic to a certain protein may show positive IgE antibody tests to food and substances that contain proteins with similar characteristics. For instance, many people who suffer from hay fever are allergic to certain fruits and vegetables, because many of the proteins found in fruits and vegetables are like the allergenic ones in birch and grass pollen. The so called cross-reactivity issue has been addressed by developing molecular allergy tests in which the unrefined natural allergen is replaced by recombinant allergenic proteins^{33,35}. The identification, the cloning and the mass production of allergenic proteins is a complex expensive process which adds to the cost of the immunoassay tests. Usually, the analysis of the test results takes a day, which is quite long compared to the SPT which is a rather immediate test for type I allergy screening. Moreover, for performing and analyzing molecular allergy tests, an advanced laboratory setting is required which may not be easily accessible in rural areas and in the developing and low-income countries. Thus, the need for a low-cost quantitative allergy test that has the accuracy and specificity of the quantitative *in vitro* tests while it is as simple and as rapid as the SPT and allows multiplexing, has remained unmet.

1.6 Skin Structure and Physiology

Understanding the skin structure and physiology is important for developing a new allergy test. The primary function of the skin, which is the body's largest organ and interface with the environment, is to protect the internal organs from external physicochemical injuries. The skin facilitates the adsorption of vitamin D from the sun, meanwhile it safeguards the body from the harmful ultraviolet radiation. Other vital functions of the skin include water, temperature, and electrolyte regulation. Moreover, acidic pH values (4-6)¹⁰⁸ of the skin surface combat the invading organisms such as microbes and viruses. As the first organ that is exposed to environmental hazards, the skin is armed with an immunological defense mechanism against pathogens^{109,110}.

To fulfill its key roles, the skin displays different cell types that are distributed across the skin in three main layers: epidermis, dermis and subcutaneous tissue also called the hypodermis¹¹¹ (**Figure 1-6**). Each of the layers has its own structure and function. The middle skin layer, dermis, is composed of an extracellular matrix mainly containing collagen and elastic fibers which give structure, strength, and elasticity to the skin. The dermis also contains a rich network of sensory nerves, tiny blood vessels, sweat and oil glands as well as hair follicles. In addition, four main types of cells reside in the dermis, including fibroblasts, dermal dendritic cells, macrophages, and mast cells¹¹².

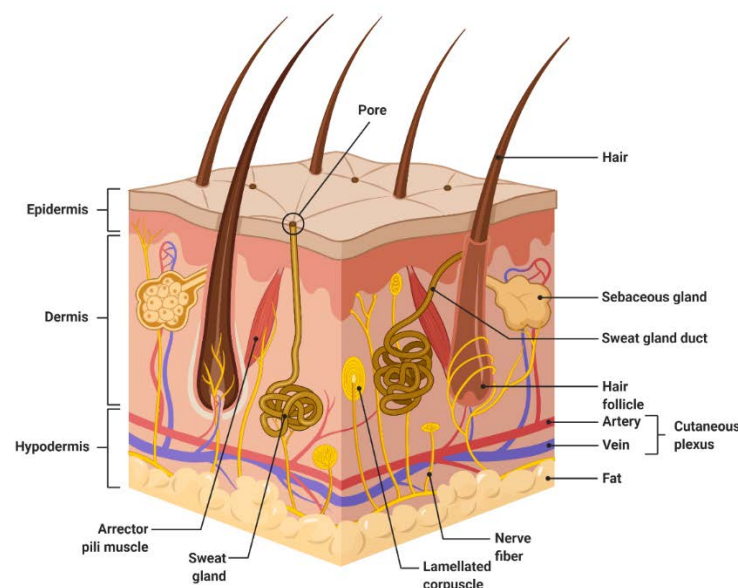


Figure 1-6 Schematic of skin cross section illustrating the three main layers: epidermis the outermost layer, dermis the middle layer and subcutaneous tissue (fat) or hypodermis as the innermost layer. Created with BioRender.com

Mast cells and allergic inflammation biomarkers

Mast cells, along with dendritic cells, are the first players in the body's line of defense against threats from the external environment including allergens and invading pathogens and are therefore located near the surfaces that are exposed to the environment including the skin, the airways, and the gastrointestinal tract. Human mast cells derive from immature stem cells in the bone marrow that differentiate to blood cell types. The immature mast cells circulate in the blood and migrate to different tissues in the whole body where they eventually differentiate and reach their final maturation. In the skin, the mast cells reside in the upper dermis beneath epithelial tissue near blood

vessels, nerves, mucus producing glands and hair follicles. Regardless of age and gender, the mast cell density in the lower arm skin varies between 56 and 64 cells/mm²¹¹⁶. Intact mast cells can be recognized under the microscope by their round or oval shape and the densely packed small granules within the cytoplasm. The diameter of the smallest mast cells is 8-10 μm , while the largest mast cells have a diameter of 16-20 μm ¹¹⁷. The secretory granules of mast cells contain preformed mediators such as histamine, heparin, serotonin, tryptase, chymase and a few newly generated mediators including prostaglandin D₂, leukotriene C₄ and platelet-activating factor. The plasma membrane of the mast cell has immunoglobulin E (IgE) receptors, known as F_{cε}RI, which bind to the F_c region of circulating IgE. Upon cross-linking of two adjacent IgE-F_c receptor complexes by binding to the same foreign antigen (called allergen), the mast cell is activated and releases mediators (degranulation) into the ISF that fills the spaces between cells^{14,18,118,119} (see **Figure 1-7**). The aforementioned mediators are theoretically useful biomarkers for the clinical diagnosis of type I hypersensitivity reactions. However, except histamine and tryptase, other granule-derived mediators are either technically difficult to measure or are not specific for mast cell activation¹²⁰. For instance, leukotriene C₄ and platelet-activating factor are produced by numerous other types of cells and therefore their detection does not specifically indicate mast cell activation.

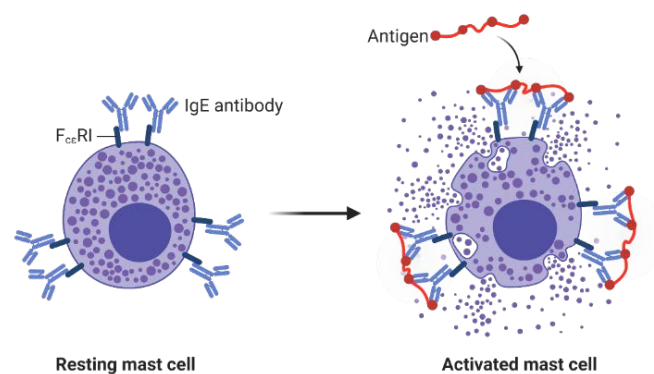


Figure 1-7 Resting mast cell granules contain histamine and other inflammatory mediators. Crosslinking of two F_c receptors and binding of foreign antigen (i.e., allergen) to membrane-bound IgE antibodies cause degranulation of activated mast cell. Created with BioRender.com

Interstitial fluid as a carrier of allergic inflammation biomarkers

As mentioned previously, the skin mast cells reside in the upper dermis and upon activation release biomarkers into the dermal ISF. Among the body fluids such as urine, saliva and sweat the composition of the ISF, which surrounds the cells in tissues and makes up three-quarters of the body's total (14-17 L) extracellular fluids, is the closest to the blood but does not have the blood matrix complexity. ISF is filtered along the capillaries from the blood plasma, diffuses through the endothelial cell wall, fills the interstitial compartment between the blood vessels and the cells and flows towards the lymphatic vessels where it enters the blood stream again. During the journey from the blood capillaries to the lymph nodes, the ISF carries nutrients from the blood to the cells and the waste products from the cells to the blood. Moreover, ISF transports signaling molecules between the cells, metabolites and electrolytes to tissues and organs and antigens and cytokines to lymph nodes. Unlike the blood, the concentrations of large proteins such as albumin and globulin in ISF are minimal, which is an advantage when detection of small molecules in low concentrations is of interest. In addition, analysis of the ISF

provides local information about the tissue because the cells secrete certain biomarkers into the ISF that are otherwise scarce in the blood or other body fluids^{36,98,121-129}. Knowing the content of the dermal ISF is crucial for identifying the biomolecules that might interfere with the detection of allergic inflammation biomarkers such as histamine. The main constituents of ISF are listed in **Figure 1-8**. Since ISF contains very little buffering molecules such as hemoglobin and albumin, even mild metabolic disorder conditions can cause remarkable pH changes in ISF. pH variations between 6.6 to 7.6 have been observed¹³⁰.

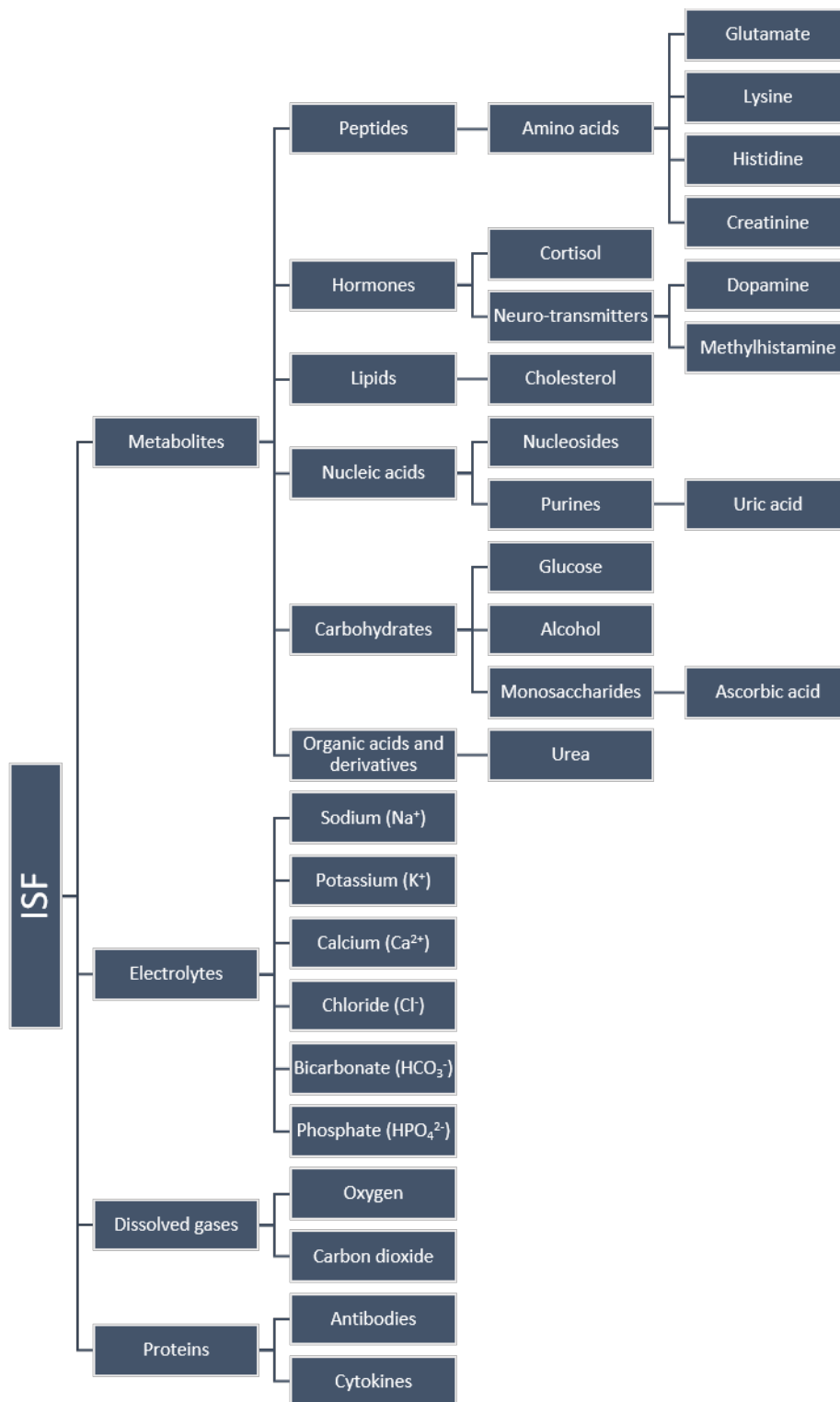


Figure 1-8 Main constituents of interstitial fluid.

1.7 Dermal Microneedle Sensors as A New Generation of Diagnostic Tools for Type I Allergy Screening

Microneedles for dermal drug delivery and sensing

Over the past few decades, the technological innovations in the field of health care have been focused on personalization and decentralization of biomedical diagnosis³⁶. As a class of wearable devices, microneedle (MN)-based dermal patches have been developed and implemented for minimally invasive drug and vaccine administration^{37–42}, bio-signal recording^{43–51}, biofluids extraction^{52–56}, biomarkers capturing⁵⁷ and for the real-time monitoring of disease biomarkers^{57–64}, metabolites^{55,65–75}, electrolytes^{64,76,77} and therapeutic drugs^{78–81}. In the field of allergy, the MNs have been used for therapeutic applications including immunotherapy by allergen delivery⁸² and treatment of atopic dermatitis by delivering anti-inflammatory drug compounds⁸³. To this date, no MN sensor has been reported for allergy diagnosis, whereas there are numerous studies on glucose monitoring with wearable MN-based sensors^{84–88}. Progress has even been made in closing the loop between diabetes diagnosis and therapy by developing a MN patch as a combined glucose sensor and insulin delivery device^{79,89–96}.

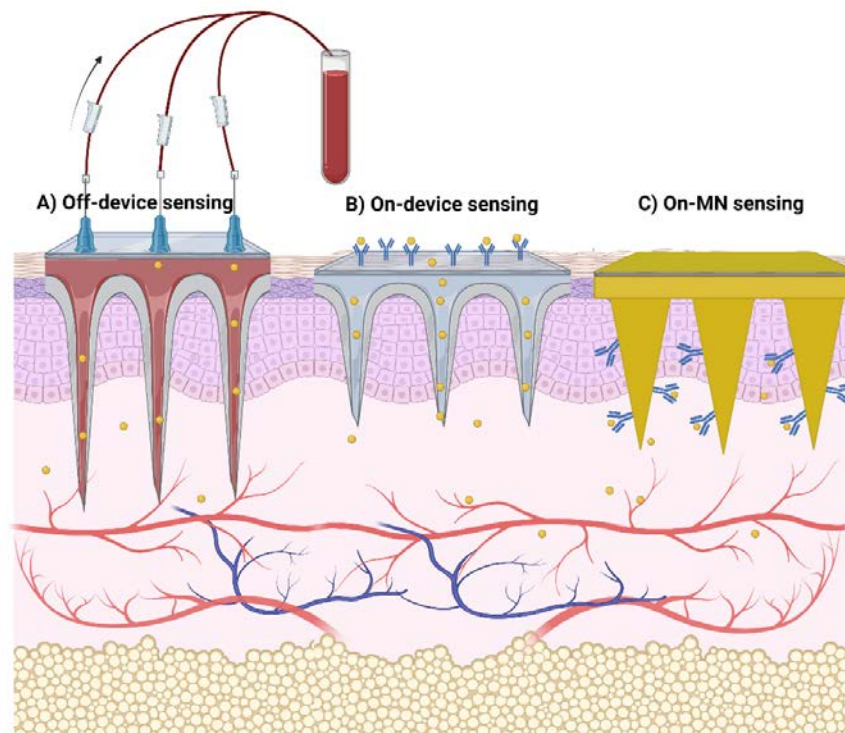


Figure 1-9 Schematic illustration of skin cross section and three different transdermal microneedle sensor configurations: A) hollow microneedles for fluid extraction and off-device sensing of analyte; B) hollow microneedles for fluid extraction combined with an on-device sensing unit; C) solid microneedles coated for on-microneedle sensing in the skin. Created with Biorender.com

Among the signal transducers implemented in MN sensors including optical^{69,97}, mass-based^{58,59} and electrochemical⁹⁸ transduction, the latter is the most advantageous mainly due to the low cost of components, ease of miniaturization and scalability of the fabrication³⁶. Depending on the mode of transdermal sensor operation, MNs are manufactured in different configurations and a variety of materials. Hollow, porous, and swellable MN configurations are used for off-device and on-device

sensing where the biofluids, such as blood and ISF, containing the target analyte are extracted from the skin and transferred to a separate compartment either off the MN device (**Figure 1-9 A**) or integrated within the device (**Figure 1-9 B**) for analysis. Solid MNs either fully fabricated of biocompatible conductive materials or coated with a conductive layer are used for on-MN sensing (**Figure 1-9 C**) in the skin. For on-MN sensing, often the surface of the solid MN is modified with a specific biorecognition element (e.g. enzyme and antibody/antigen) which captures the target analyte, thus eliminating the need for transdermal fluid sampling^{98,99}.

Pyrolytic carbon microelectrodes

The research group of Professor Stephan Sylvest Keller, the Biomaterial Microsystems group, is internationally leading in design and fabrication of pyrolytic carbon electrodes with high aspect ratio microstructures for bioelectrochemistry. Pyrolytic carbon is a conductive, biocompatible and chemically inert material which is obtained by pyrolysis of organic polymers at high temperatures in inert atmosphere¹⁰⁰⁻¹⁰³. Pyrolytic carbon electrodes with high aspect ratio 3D micro structures that are impossible to obtain with metals, have been fabricated from SU-8 precursor templates for electrochemistry^{104,105}, real-time electrochemical detection of dopamine from human neural stem cells¹⁰⁶ and electrochemical analysis of alkaline phosphate activity in cell cultures¹⁰⁷. **Figure 1-10** shows scanning electron microscopy (SEM) images of a few pyrolytic carbon microelectrodes with high aspect ratio 3D structures that have been previously developed in the Biomaterial Microsystems group.

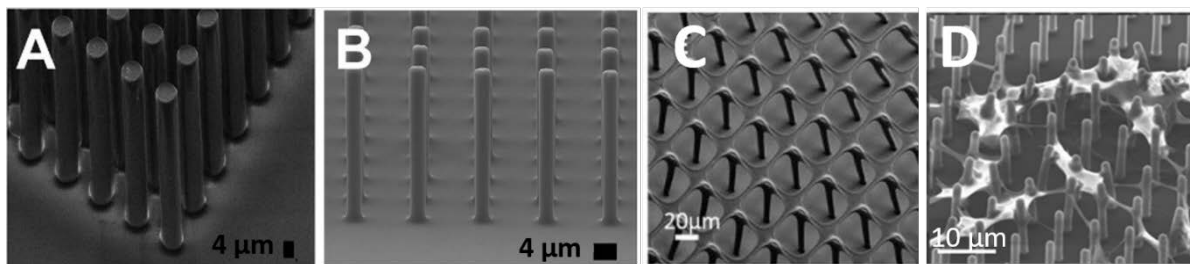


Figure 1-10 SEM images of A) micropillars SU-8 precursor (before pyrolysis); B) pyrolytic carbon micropillars; C) suspended 3D pyrolytic carbon structures; D) neural stem cells grown on pyrolytic carbon micropillars¹⁰³⁻¹⁰⁶.

InstaPatch - Instantaneous monitoring of allergic reactions in the skin

In the InstaPatch research project led by Professor Stephan Sylvest Keller at DTU Nanolab the aim was to develop a novel allergy test to address some of the limitations of the SPT by instantaneous and quantitative monitoring of allergic reactions in the skin. The core idea was to introduce intradermal microneedle (MN) sensors based on pyrolytic carbon as a new generation of diagnostic tools for allergy screening. This was done in collaboration with DTU Bioengineering, DTU Food, the Allergy Clinic of Copenhagen University Hospital at Herlev and Gentofte and Malmö and Cardiff universities. The project was co-funded by LEO foundation, Copenhagen Center for Health Technology (CACHET), DTU Nanolab and the Independent Research Fund Denmark (DFF-FTP).

Like the insulin delivery and monitoring device, which was mentioned earlier, the envisioned InstaPatch allergy test comprised of a dermal sensor patch with arrays of MNs (**Figure 1-11 A**) that both serve the allergen delivery and the sensing of allergic reactions in the skin (**Figure 1-11 B and C**). More specifically, it was proposed to develop a miniaturized patch for allergy testing with arrays of MN

electrodes either fully made of pyrolytic carbon or partially coated with carbon for combined dermal delivery of allergens and electrochemical sensing of allergy biomarkers in the skin.

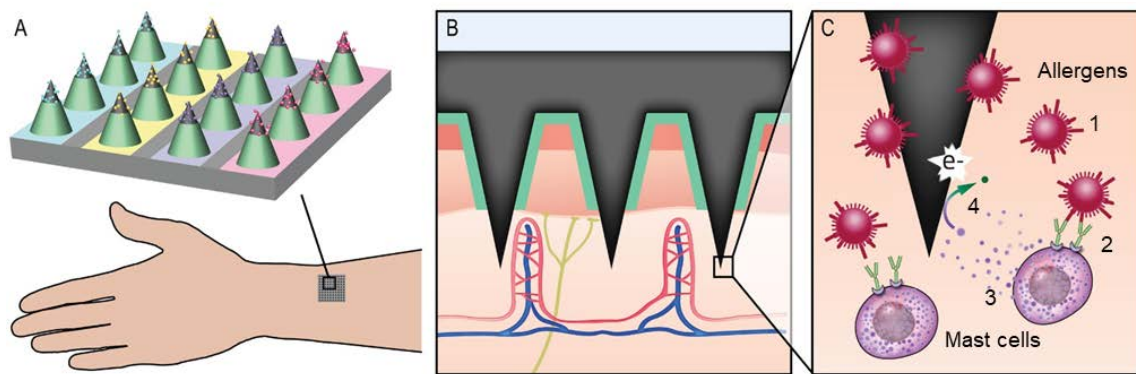


Figure 1-11 Schematic illustration of the InstaPatch MNs. Image provided from funding application by S.S. Keller.

While the SPT qualitative assessment is based on observing consequences of the immunoreaction (wheal and flare) initiated by the histamine release, the electrochemical MN sensor patch enables quantitative and direct monitoring of the allergic inflammation biomarkers as they are released from the skin mast cells into the ISF. The potential advantages are more comfort, higher accuracy, and fewer false negatives. Unlike the SPT, the InstaPatch test does not require interruption of anti-histamine treatments because the biomarkers are caught immediately at the vicinity of the activated mast cells in the site of the reaction. Miniaturization of the pricking needles allows for including multiple tests in the confined area of a few mm², which is particularly an advantage for allergy screening of children or patients with skin lesions. Moreover, automated monitoring makes the InstaPatch test an ideal diagnostic tool that can be used by less experienced users or in a non-clinical setting.

The main research activities within the framework of the InstaPatch project were divided into three sub-projects; i) microfabrication of pyrolytic carbon MNs, ii) electrochemical sensor development for the *in vitro* detection of allergic inflammation biomarkers using pyrolytic carbon as electrode material, iii) test of allergen delivery and mechanical stability of pyrolytic carbon MNs and *in vivo* testing of the sensor.

1.8 Ph.D. Project Scope, Objectives and Deliverables

The aim of this Ph.D. project, which was defined within the framework of the InstaPatch research project, was to develop an electrochemical (bio)sensor for the detection of allergy biomarkers. The main hypothesis was that the pyrolytic carbon microelectrodes can be used as an electrochemical transducer for the quantitative analysis of the allergic reaction. In this Ph.D. project, histamine released by the mast cells in the dermis was chosen as the target biomarker for analysis. The amount of histamine released from the activated mast cells depends on their sizes¹¹⁷, and their density at the site of reaction¹³¹. The maximum amount of histamine released from the smallest mast cells is 2.5±0.5 pg/cell, while this value reaches 10±2.5 pg/cell for the largest mast cells¹¹⁷. *In vivo* human skin study of 21 allergic individuals (allergic to Timothy grass pollen) by Petersen *et al.* (1997) revealed that the release of histamine is a very localized process where the largest amount of histamine can be detected within 1 mm distance from the provocation site. The same study showed that 6-8 minutes after allergen injection, the tissue histamine level reaches its highest value about 600 nM and after 20 minutes it drops to about 200 nM¹³².

Based on the background knowledge and boundary conditions introduced above, the main objectives of this Ph.D. project were defined as:

- i. test of hypothesis: demonstrating that pyrolytic carbon microelectrode could be implemented as a transducer for electrochemical histamine sensing
- ii. (bio)sensor development: enabling quantitative electrochemical histamine analysis

Desired (bio)sensor performance criteria:

Calibration characteristics: as explained before, the concentration of histamine at its release peak is about 600 nM in the allergen-provoked tissue. Then, this value gradually drops to about 200 nM after 20 minutes. Thus, measuring concentrations in the range of at least 200-600 nM is the main performance requirement.

Operational conditions: the (bio)sensor should be able to detect histamine at 37°C (internal body's temperature) and in ISF pH level 6.6-7.6.

Response time: as explained earlier, histamine release reaches its peak within 6-8 minutes from allergen injection and decreases by 70% after 20 minutes. Hence, the (bio)sensor should be able to generate a signal within 10-20 minutes from the time that histamine is released

Selectivity and reliability: histamine detection in biologically relevant media such as mast cell medium and/or ISF should be enabled. The (bio)sensor should be able to exclusively measure histamine in nM concentration range in the complex matrix of a biological sample. Based on the detection mechanism of the (bio)sensor and on the sample matrix, interfering molecules will be identified.

Reproducibility and stability: the operational stability of the developed (bio)sensor in the aforementioned conditions (pH, temperature, sample matrix,...) should be such that in 20-30 minutes of uninterrupted use, the electrochemical signal remains at least 3 times greater than the drift¹³³. Moreover, the (bio)sensors prepared in the same way, should respond similarly to a certain concentration of histamine in the given conditions.

- iii. Proof-of-concept histamine measurement from activated mast cells.

The overall objective of the Ph.D. project is schematically illustrated in **Figure 1-12**.

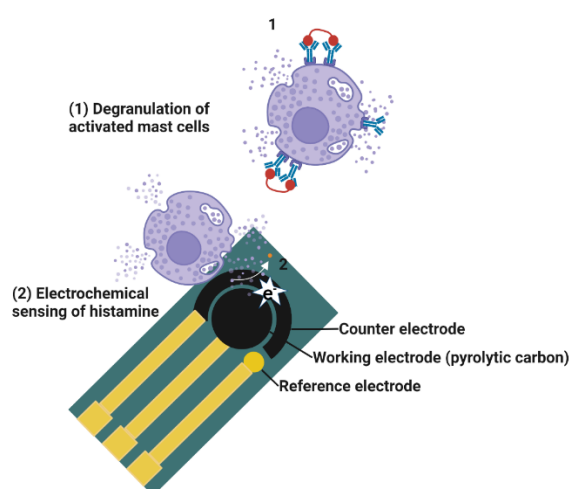


Figure 1-12 Schematic illustration of the main project objectives: electrochemical histamine detection from activated mast cells using pyrolytic carbon microelectrodes. Created with Biorender.com.

1.9 Structure of the Thesis

The Ph.D. project was divided into three main iterations, each consisting of four main types of activity: design, fabrication, characterization, and testing. Different tasks were defined within each type with the overall purpose of meeting one of the three main project objectives at the end of each iteration. **Chapter 2** presents the theoretical backgrounds of the electrochemical techniques that are used throughout the thesis to characterize and test the (bio)sensors. Thereafter, the structure of the thesis follows the iterations.

Iteration 1- Fabrication of pyrolytic carbon for electrochemical histamine detection

In the first iteration, the focus was to produce the pyrolytic carbon microelectrode that could be implemented as a transducer for electrochemical histamine sensing. This was initiated by fabricating batches of 2D and 3D pyrolytic carbon microelectrodes using a previously optimized process flow which is explained in detail in **Chapter 3**. The chapter also includes sections about microelectrode design modification and the electrochemical characterization of the fabricated electrodes. Next, a few setups were designed and fabricated for the electrochemical measurements on the pyrolytic carbon microelectrodes and for sensor development. The design and fabrication process of the setups as well as the outcomes are explicitly discussed in **Chapter 4**. A literature survey on the state-of-the-art of electrochemical histamine sensing was conducted, which can be found in **Chapter 5**.

Iteration 2- Electrochemical histamine detection in nM range

Much of the project time (about 90% if not more) was allocated to the second iteration, therefore it represents a large part of this thesis including two papers containing the main results. A second-generation enzymatic biosensor was developed on by modification of 3D pyrolytic carbon with an electrocatalyst, which enables indirect histamine detection by analysis of the by-products of the enzymatic reaction. 3D sensor configurations more closely resembled the 3D MN design in the final sensor platform. The optimized procedures for the modification of the pyrolytic carbon surface with the electrocatalyst, and for the enzyme immobilization as well as the biosensor mechanism are explained in **Chapter 6**. The experiments that were carried out to select the best enzyme for biosensor construction are also included in this chapter. A great deal of optimization was required to be able to obtain reliable and reproducible data from the sensors. The sensor optimization process and the obtained results are published and available in **Paper I in Appendix A**. To enhance the sensitivity of the biosensors, a novel electrochemical transduction method was developed, which is presented in **Paper II (manuscript) in Appendix B**.

Iteration 3 - Proof-of-concept histamine measurement from activated mast cells

The proof-of-concept measurements of histamine released from the activated mast cells are presented at the end of **Paper II**. Finally, the main conclusions drawn from this work and the future perspectives are summarized in **Chapter 7**.

Chapter 2. Electrochemistry and Electrochemical Methods

In this chapter, the main concepts of electrochemistry are introduced. Furthermore, the theory related to the electrochemical methods applied in this thesis is briefly presented.

2.1 Electrochemistry

Electrochemistry is the science of studying chemical reactions by electricity. Common between the chemical reactions and the electricity is the flow of electrons. As a result of a spontaneous chemical reaction, electrons are transferred between two ionic species. The species that loses electrons is said to be oxidized, while the species that gains the electrons is reduced. Direct electron exchange between the oxidizing and the reducing chemical species is known as homogeneous electron transfer (**Figure 2-1 b**). If the electron exchange takes place through solid conducting materials defined as electrodes and connected to an external electrical circuit, the electron transfer is heterogeneous (**Figure 2-1 c**). By placing a potentiostat in series with the electrodes in the circuit, it is possible to study the spontaneous chemical reactions near the electrodes via the current produced by the heterogeneous electron transfer. The potentiostat can also be used as a source of electrical energy to induce electron transfer between two electro-inactive species that otherwise would not undergo spontaneous chemical reactions with each other.

2.2 Electrochemical Cell

An electrochemical cell consists of at least two electrodes separated by an ionic conductor defined as electrolyte. The electrodes are made of different conducting materials such as solid metals, carbon and semiconductors. The electrolyte usually consists of a liquid solution with low resistance containing ionic species such as Na^+ and Cl^- in either an aqueous or non-aqueous solvent. The transport of charge across the electrode takes place by the movement of electron-hole pairs, while the movement of ions facilitates the charge transport in the electrolyte. The energy required to move the charge through the external circuit between the electrodes is called the cell potential. Electrochemical techniques, which will be discussed later in this chapter, have been developed to study the processes and factors that affect the transport of charge at the electrode/electrolyte interface. Although the overall chemical reaction taking place in an electrochemical cell consists of two independent half-reactions each taking place at one electrode, most of the time only one of these reactions is of interest. The schematic diagram in **Figure 2-1 a** shows a standard three-electrode electrochemical cell connected to a potentiostat. The electrodes are named after their functions; working electrode (WE), reference electrode (RE) and auxiliary or counter electrode (CE). The WE is a solid conductive material such as gold, platinum, carbon near which the half reaction of interest is studied. An electrical potential applied to the WE is always adjusted with respect to the RE which has a constant potential during the experiments. A few of the most commonly used REs are Standard Hydrogen Electrode (SHE) also called Normal Hydrogen Electrode (NHE), which is the internationally accepted primary reference (the potential of all other REs are measured and quoted with respect to NHE or SHE), Saturated Calomel Electrode (SCE) with potential of 0.242 V vs. SHE and Silver coated with Silver Chloride (Ag/AgCl) in saturated KCl solution with a potential of 0.197 V vs. SHE. Since the RE has a constant potential, any potential change in the cell is considered to be related to the WE interface. The CE closes the circuit and the electrons flow between the WE and the CE. To avoid that the CE limits the current flowing between WE and CE, the CE is preferably selected from highly conductive materials, if possible, more conductive than the WE material, and with an active surface area of at least ten times larger than the one of the WE. Platinum is the most used CE material.

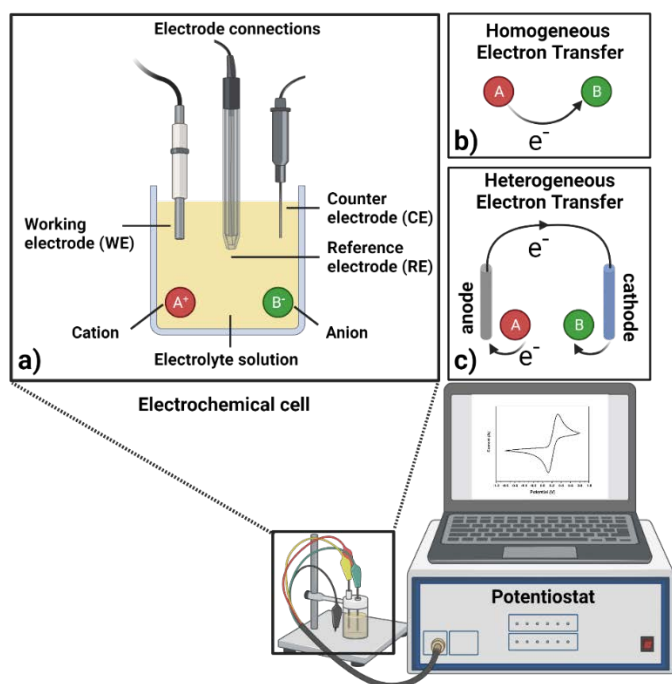


Figure 2-1 Schematic diagram of a) three-electrode electrochemical cell; b) homogeneous electron transfer; c) heterogeneous electron transfer. Created with Biorender.com.

Redox reactions

Applying a potential to the WE means that the energy level of its electrons is perturbed. **Figure 2-2** is the schematic representation of the redox reactions of a dissolved electroactive species (substance A) at the electrode-electrolyte solution interface when a negative or a positive perturbation potential is applied to the WE. When a negative potential is applied to the WE, the electrons gain energy. If the energy is high enough, the electrons will leave the electrode and move to the lowest vacant molecular orbit of the species in the electrolyte solution. This flow of electrons from the electrode to the solution generates a reduction current (cathodic) in the external circuit between the WE and the CE which is recorded by the potentiostat. The reverse flow of electrons from the solutes in the electrolyte solution to the electrode occurs when a positive potential is applied to the WE. In this case, the energy level of the electrons at the WE are lowered and the electrons of the species in the electrolyte solution will transfer to the more favorable energy levels in the WE. The flow of electrons from the electrolyte solution to the electrode generates an oxidation current (anodic). The reduction and oxidation (redox) of different chemical species at the interface of an electrode-solution only occurs at certain potentials called the standard potential, E^0 , which is usually reported for a half-reaction. By convention all half-reactions are written as reductions. Therefore, using the term 'standard reduction potential' for E^0 is more precise. If more than one type of electroactive species is present in the solution, the substance with the most positive E^0 will be reduced first when the potential of the WE is shifted towards more negative values. When the WE potential becomes more positive, the substance with most negative E^0 will be oxidized first. E^0 is used when the activities of all species in the cell are unity. By convention the standard potential of the hydrogen electrode (SHE) is assigned as zero ($E^0=0$ for SHE). For every reaction of interest, E^0 is the difference between the potential of the reaction and the potential of SHE, given that the activities of reactants and products are unity.

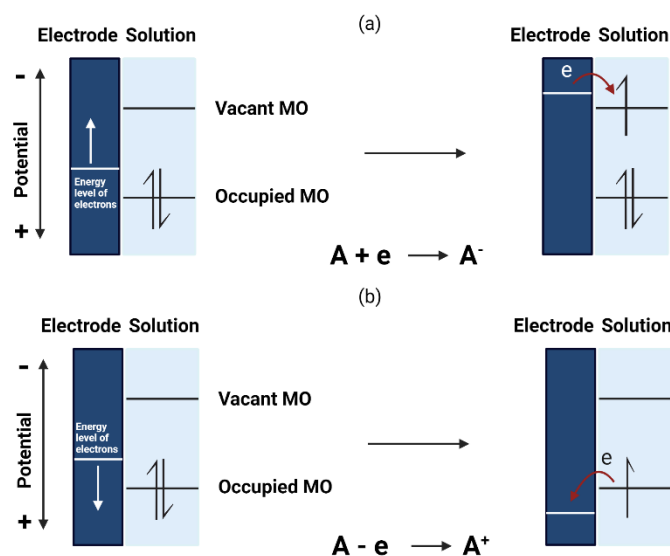


Figure 2-2 Schematic representation of (a) reduction and (b) oxidation process of a dissolved electroactive species (substance A) at the electrode-electrolyte solution interface when a negative or a positive potential is applied to the WE. The molecular orbitals (MO) shown in the solution are the lowest vacant MO and the highest occupied MO of the species A. Recreated by BioRender.com from Allen J. Bard textbook of Electrochemical Methods.

Faradaic and non-faradaic electrode processes

Processes at electrodes that cause an external flow of current are not limited to the redox reactions at the electrode-solution interface. In fact, electrode processes are divided into faradaic and non-faradaic types. Redox reactions that involve electron transfer across the electrode-solution interface and are governed by the Faraday's law of electrolysis, which suggests that the amount of chemical reactions induced by current is proportional to the amount of charge that passes through the electrode-electrolyte boundary, are called faradaic processes. Non-faradaic processes such as adsorption and desorption of solutes to and from the electrode generate an external current flow, even though charge does not cross the interface. Changes in the area and the potential of the electrode and the solution composition give rise to non-faradaic processes at the electrode-electrolyte interface. The current that is generated by the movement of ions and electrons in the electrolyte solution is called charging current. When the concentrations of electroactive species that undergo redox reactions are very low in the solution, the charging current can be much larger than the faradaic current. Another term for the charging current is 'capacitor current'. The reason for this naming is that the electrode-solution interface behaves like a capacitor, which is described by a model called the 'electric double layer' illustrated in **Figure 2-3**. When a negative or positive potential is applied to an electrode, a very thin layer ($< 0.1 \text{ \AA}$) of electric charge (q^M ; M for metal) is built up on the surface of the electrode due to excess or deficiency of electrons, respectively. The charged surface of the electrode attracts ions of opposite charge from the solution. The excess of either cations or anions at the electrode surface generates a non-zero charge in the solution (q^S), which balances the charge of the electrode at all times ($q^M = -q^S$). The charged electrode and the oppositely charged ions next to it define the electric double layer (EDL) which can be considered as an array of oriented dipoles at the electrode-solution interface. The EDL constitutes of different layers. As mentioned, the nearest layer to the surface of the electrode consists of neutral molecules as well as anions and cations of solvent

and solute that are specifically adsorbed by van der Waals and electrostatic forces. This tinny adsorbed inner layer is referred to as the Helmholtz layer and the plane that goes through the electric centers of the specifically adsorbed ions is called the inner Helmholtz plane (IHP). The next layer is the diffuse part of the EDL, where solvated ions are nonspecifically adsorbed to the electrode by long-range electrostatic forces. The plane that passes through the electric centers of the nonspecifically adsorbed ions closest to the electrode is termed as the outer Helmholtz plane (OHP). The diffuse part of the double layer expands from the OHP to the bulk of the solutions and has a typical thickness of 0.3-10 nm, although the thickness depends on the total ionic concentration in the solution and the balance between attraction toward the electrode and the random placement due to thermal agitation in the solution. The outermost part of the EDL is the bulk solution which has a different concentration of species, which are produced or consumed at the vicinity of the electrode surface. The capacitance of the EDL is denoted by C_d . In reality, the electrode-solution interface is not an ideal capacitor but has also somewhat resistor characteristics. The internal resistance of the solid electrode and the solution resistance must be taken into consideration in modeling of the EDL.

Electrochemical cells with faradaic processes can either be galvanic (also called voltaic) or electrolytic depending on whether the chemical reaction takes place spontaneously or not. In galvanic cells the chemical reactions occur spontaneously at the electrodes connected externally by a conductor, whereas in electrolytic cells the reactions require an external voltage to be initiated. Galvanic cells are employed in the fields of fuel cells for the conversion of chemical energy to electrical energy. Electrolytic cells are often used for electrolytic synthesis of chemicals and electroplating.

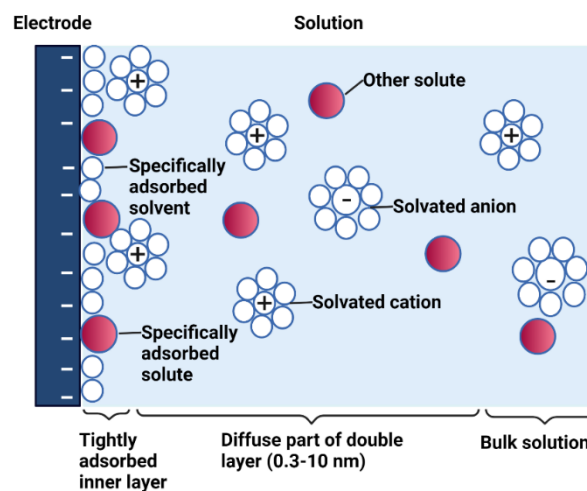


Figure 2-3 The electric double layer model of the electrode-solution interface.

In electrolytic cells, the faradaic current is directly proportional to the reaction rate at the electrode. The current i is the number of coulombs of electric charge Q flowing per second:

$$i = \frac{dQ}{dt} \left(\frac{\text{coulombs (C)}}{s} \right)$$

2-1

$$\frac{Q}{nF} \frac{\left(\frac{C}{\text{mol}}\right)}{\left(\frac{C}{\text{mol}}\right)} = N(\text{mol electrolyzed})$$

2-2

where n is the stoichiometric number of electrons involved in the electrode reaction, F is the Faraday constant ($96,485 \text{ C mol}^{-1}$) and N is the number of moles of reactant. The reaction rate at the electrode can be written as a function of current:

$$\text{Reaction Rate} \left(\frac{\text{mol}}{\text{s}}\right) = \frac{dN}{dt} = \frac{i}{nF}$$

2-3

Since the reactions taking place at the electrode are heterogeneous, usually current density j is used instead of the current and therefore the reaction rate is described in units of mol s^{-1} per unit area (most frequently cm^2):

$$\text{Reaction Rate} \left(\frac{\text{mol}}{\text{s cm}^2}\right) = \frac{i}{nFA} = \frac{j}{nF}$$

2-4

Figure 2-4 shows the pathway of a general electrode reaction. For an electrode reaction as described in equation 2-5 to occur, a few rate determining steps must be considered.



2-5

Where O is an oxidant and R is a reducing agent. The first step is the mass transfer. There are three modes of mass transfer from the bulk to the electrode surface region and vice versa. In other words, the reactant molecule (O) in the bulk solution has three ways to reach the surface of an electrode: (1) diffusion through a concentration gradient; (2) convection, which is the movement of bulk fluid by physical means such a stirring or boiling; and (3) migration, which is the attraction or repulsion of an ion by a charged surface¹³³.

In complex processes, intermediate chemical reactions prior or right after the electron transfer are quite common. A series of homogeneous electron transfers, protonations, dimerization or heterogeneous reactions such as catalytic decomposition on modified electrode surfaces are examples of intermediate chemical reactions that might be required for the conversion of O to R . Other surface reactions such as adsorption, desorption, electrodeposition and electron transfer at the electrode surface are also factors that affect the electrode reaction rate and the current. When the rates of all steps in a reaction pathway are the same, a steady-state current is obtained. The rates of electron transfer and adsorption at the electrode surface are potential dependent.¹³³⁻¹³⁵ **Figure 2-4** illustrates a general electrode reaction pathway.

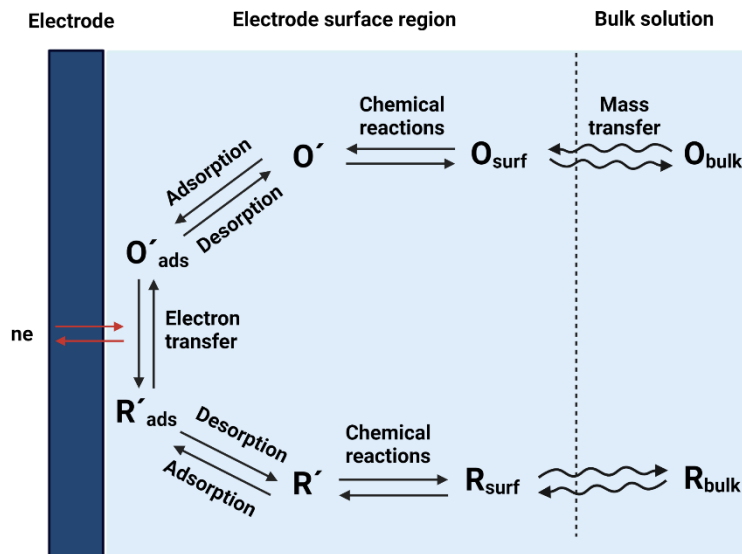


Figure 2-4 Factors affecting electrode reaction rate and current, regenerated by BioRender.com from Allen J. Bard textbook of Electrochemical Methods.

Nernst equation

If a chemical reaction at equilibrium is disturbed by changing the conditions, such as changing the concentration of reactants or products, the equilibrium shifts in the opposite direction to counteract this change. In an electrochemical cell with a cathode and an anode (two half-cells) connected by an external conductor or a salt bridge, the net driving force of the reaction also known as the net cell voltage is the difference between the potentials of the two electrodes:

$$E_{cell} = E_c - E_a$$

2-6

where E_c is the potential of the electrode at which the cathode reaction (reduction) occurs and E_a is the potential of the electrode at which the anodic reaction (oxidation) takes place. If the net cell voltage E_{cell} is positive, the net cell reaction goes spontaneously in the forward direction and if E_{cell} is negative, then the net cell reaction moves spontaneously in the reverse direction. The potential of each half-cell written as a reduction reaction as in equation 2-5 is obtained by the Nernst equation.

The Nernst equation giving the half-cell potential E versus the SHE for the half-reaction in equation 2-5 is

$$E = E^0 - \frac{RT}{nF} \ln \frac{A_{Red}}{A_{Ox}}$$

2-7

Where E^0 is the standard reduction potential ($A_R=A_O=1$), R is the gas constant ($8.314 \text{ J (K mol)}^{-1}$), T is the absolute temperature (K), n is the number of electrons in half-reaction, F is the Faraday constant ($96,485 \text{ C mol}^{-1}$) and A_i is the activity of species i .

Replacing the natural logarithm by base 10 logarithm and inserting the temperature $T=298.15 \text{ K}$ (25.00°C) into equation 2-7, results in the more commonly used form of the Nernst equation:

$$E = E^0 - \frac{0.05916 (V)}{n} \log \frac{A_{Red}}{A_{Ox}}$$

2-8

The standard potential E^0 is used for a galvanic cell when all activities of reactants and products are unity. For solute species i , the activity is $A_i = \gamma_i(C_i/C^0)$, where C_i is the concentration of species i , C^0 is the standard concentration (usually 1M) and γ_i is the activity coefficient which is unitless. In reality, activity coefficients are almost always unknown. To avoid this problem, the biochemists often replace the standard reduction potential in the Nernst equation by the formal potential, $E^{o'}$, which is the reduction potential at physiological conditions (pH=7) and incorporates the activity coefficients of the oxidized and the reduced species. Moreover, implementing $E^{o'}$ in the Nernst equation is not limited to the condition when the activities of all species are at unity.

Whenever protons (H^+) are involved in a redox reaction such as in biochemical reactions or when either reactants or products are acids or bases, the reduction potentials are pH dependent. E^0 is used when pH=0 ($A_{H^+} = 1$). However, in biological redox reactions pH 0 is not relevant and that is where $E^{o'}$ applies under specific conditions including the pH, ionic strength, and concentration of the involved species. Using the formal potential, the Nernst equation or the electrode potential (at 25°C) can be rewritten as logarithmic function of reactant and product concentrations^{133,135}:

$$E = E^{o'} - \frac{0.05916}{n} \log \frac{C_{Red}}{C_{Ox}}$$

2-9

2.3 Electrochemical Methods

Electrochemical methods are used to study the behavior and the response of an electrochemical system to an applied excitation or perturbation. In an electrochemical experiment, certain parameters potentially influencing the behavior of an electrochemical cell such as temperature, pH, pressure, bulk concentration of electroactive species, electrode material, electrode geometry and surface conditions are kept constant while other important parameters including electrical variables such as potential, current and charge are closely observed. For example, for investigating the electrode reactions in voltammetric techniques, the current is plotted as a function of the applied potential. In potentiometry, the potential is determined as a function of concentration of electroactive species while the current is set to zero in the cell. In the following sections, the electrochemical techniques used throughout this thesis are discussed theoretically.

Cyclic voltammetry

In cyclic voltammetry, a triangular potential waveform (**Figure 2-5 A**) is applied to the WE and the resulting current from the oxidation and reduction processes of molecular species at the electrode-solution interface is plotted as a function of the applied potential (**Figure 2-5 B**). This plot is known as cyclic voltammogram. There are two conventions commonly used for recording a cyclic voltammogram: the US convention and the IUPAC convention. The latter has been used throughout this thesis and is the base of the theoretical discussion in this section. Cyclic voltammetry is performed in a three-electrode cell consisting of a WE, a CE and a RE all immersed in an electrolytic solution containing redox active species. The redox reactions at the WE are studied from the cyclic voltammograms. As the potential vs. time plot in **Figure 2-5 A** shows, the potential of the WE vs. RE is swept linearly from an initial value E_1 to a switching potential E_2 at a certain potential per second

which is known as the sweep rate or the scan rate. Then, the direction of the linear sweep is reversed, and the potential is swept back to its initial value. This cycle might be repeated many times until a stability in the system is observed. The initial and the switching potential values are chosen in such a way that the linear sweep passes the formal potential ($E^{\circ'}$) of the redox active species of interest. The cyclic voltammogram in **Figure 2-5 B** displays the recorded current (y-axis) data vs. the applied potentials (x-axis) for a reversible reaction (equation 2-5) that is fast enough to maintain equilibrium concentrations of reactant (O) and product (R) at the electrode surface. As it can be seen, the redox peak currents ($i_{p,a}$ and $i_{p,c}$) have equal magnitudes in a reversible process. In the IUPAC convention, potentials become more positive along the (positive) x-axis and oxidation currents are defined as positive.

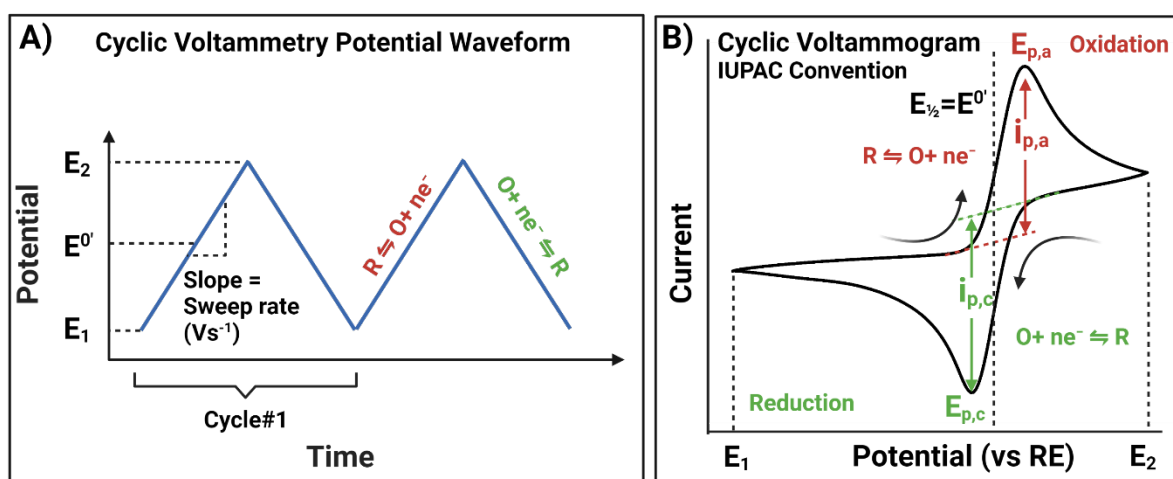


Figure 2-5 Cyclic voltammetry: A) triangular potential waveform; B) current-potential response (cyclic voltammogram) of an electrochemically reversible system.

When no potential is applied to the WE, the concentrations of redox active species (O and R) in the solution near the electrode are uniform and equal to the bulk concentration. Upon application of a potential, a stagnant volume of solution with different concentrations of species from the bulk, known as the Nernst diffusion layer, is formed at the electrode surface and continues to grow throughout the potential scan. Depleted redox species are replenished through this layer by diffusion, regardless of the overall mode of mass transfer in the bulk solution. The Nernst equation predicts how the concentration of redox active species near the electrode changes as the potential is linearly swept back and forth. The current flow also varies as the redox active species are consumed or produced.

At the initial potential usually, no electrochemical reaction occurs. As the potential is ramped positively (anodically), $[R]$ is steadily consumed near the electrode as it is oxidized to O . According to the Nernst equation, when the potential reaches the formal potential ($E = E^{\circ'}$), which is experimentally estimated to be midway between the two peak potentials ($E^{\circ'} \approx E_{1/2} = (E_{p,a} + E_{p,c})/2$) also known as half-wave potential), R will be oxidized to O until $[R] = [O]$, and equilibrium is achieved. With further increase of the potential to more positive values ($E = E_{p,a}$), additional amount of R is transferred to the surface of the electrode by diffusion from the bulk solution. At this point, the peak anodic (oxidation) current ($i_{p,a}$) is observed. If there were no diffusion limitations, the measured current would level off at the top of the anodic wave as the potential is scanned past this point. But in real systems, the diffusion is typically too slow to replenish the consumed species (R) near the electrode. Hence, upon sweeping the potential to more positive values, the rate of diffusion of R from the bulk solution to the electrode surface becomes significantly lower, resulting in a drop in the current level.

While R species are consumed at the electrode surface, O species are produced and its concentration $[O]$ at the electrode surface is increased, satisfying the Nernst equation. At the switching potential, the scan direction is reversed, and the potential is swept negatively (cathodically). The oxidized species O present at the electrode surface are reduced back to R as the applied potential becomes more negative. At half-wave potential, the concentrations of the redox couple are equal. Thereafter, the reduction current of O is increased until it reaches its maximum at the peak cathodic current ($i_{p,c}$) where the potential is $E = E_{p,c}$. After this point and until the potential is back to its initial value, the current is again limited by diffusion. As the oxidized species is depleted and the diffusion rate is too low to replenish the consumed species, the cathodic current decays back toward its initial value.

The two peaks of the cyclic voltammogram are separated due to the diffusion of the redox active species to and from the electrode. If the redox process is chemically and electrochemically reversible, the difference between the anodic and cathodic peak potentials, known as peak-to-peak separation ΔE_p is

$$\Delta E_p = |E_{p,a} - E_{p,c}| = \frac{2.22 RT}{nF} = \frac{57.0}{n} \text{ (mV) (at } 25^\circ\text{C)}$$

2-10

where $E_{p,a}$ and $E_{p,c}$ are the potentials at which the peak anodic and peak cathodic currents are observed and n is the number of electrons in the half-reaction.

Chemical reversibility indicates the stability of the reactant upon oxidation or reduction and whether it can be regenerated in the reverse reaction. Electrochemical reversibility is an indication for the ease of electron transfer between the electrode and the redox species. Vanished anodic or cathodic peaks in the cyclic voltammogram and larger peak-to-peak separations than ΔE_p of an ideally reversible system (Nernstian system in equation 2-10) are indicative of sluggishness of electron transfer processes and that there is a high barrier to electron transfer.

For electrochemically reversible reactions involving freely diffusing redox species, the Randles–Sevcik equation (2-11) predicts the peak current, i_p (A), which is proportional to the concentration of redox active species, C (mol L⁻¹), and the square root of the scan rate ν (V s⁻¹):

$$i_p = (2.69 \times 10^8) n^{3/2} A C D^{1/2} \nu^{1/2}$$

2-11

where n is the number of electrons in the half-reaction, A (m²) is the electroactive surface area of the electrode and D is the diffusion coefficient of the redox active species (m² s⁻¹). For a higher scan rate, the size of the diffusion layer is smaller, and the peak current is higher. According to equation 2-11, the plot of i_p vs. $\nu^{1/2}$ is linear for a reversible process. Eventual deviations from linearity indicate either that the process is electrochemically quasi-reversible or that the electron transfer occurs via surface-adsorbed species. If the redox active species are adsorbed on the surface of the electrode, the peak current varies linearly with ν .

Faradaic processes are so far the only contributors to the peak current i_p in the cyclic voltammogram discussed in this section. However, the constant change of the potential of the WE also induces a constant capacitive current, which alternates between positive and negative values depending on the potential sweep direction. This capacitive current i_{cap} is directly proportional to the potential scan rate. In the absence of redox processes in the potential window of the cyclic voltammetry, the

voltammogram would only trace the capacitive current and would have a rectangular shape without distinguishable peaks.^{136,137}

In this thesis, cyclic voltammetry is implemented for:

- i. the characterization of electrochemical behavior of the pyrolytic carbon microelectrodes,
- ii. studying the electrode surface modifications (oxygen plasma treatment of pyrolytic carbon)
- iii. studying direct histamine oxidation on the pyrolytic carbon
- iv. the investigation of catalytic properties of electrodeposited Prussian blue film

Chronoamperometry

Amperometry is a general term used to refer to electrochemical techniques, in which a current is measured as a function of an independent variable which is typically time or the electrode potential. Amperometry combined with standard chemical processes and setups such as stirred batch reactors and flow injection systems enables quantitative electroanalysis of chemical reactions.

Chronoamperometry is a variant of amperometry, in which a potential is applied to the electrode and the resulting current vs. time is observed. In this technique, a step of constant reducing or oxidizing potential (vs. the RE) is applied by the potentiostat to the WE to drive the reduction or oxidation reaction of an electroactive species. The potential is varied from a value E_1 below the species formal potential at which no faradaic reaction occurs to a potential E_2 above the species formal potential at which the electroactive species at the electrode immediately undergoes either reduction or oxidation (**Figure 2-6 A**). At E_2 all the species are consumed at the electrode surface and the concentration of reactant becomes equal to zero at the electrode. The value of the constant potential required to drive the oxidation or reduction of an electroactive species can be determined from the cyclic voltammogram of the species of interest by calculating the formal potential using the anodic and cathodic peak potential values. A slightly more negative potential than the calculated formal potential must be applied to the WE to drive the reduction and a more positive potential than the calculated formal potential must be imposed for the oxidation of the species. This is to ensure that lack of potential as driving force is not limiting the reaction. However, the added potential value must be small enough to avoid simultaneous reduction or oxidation of other electroactive species that might be present in the solution.

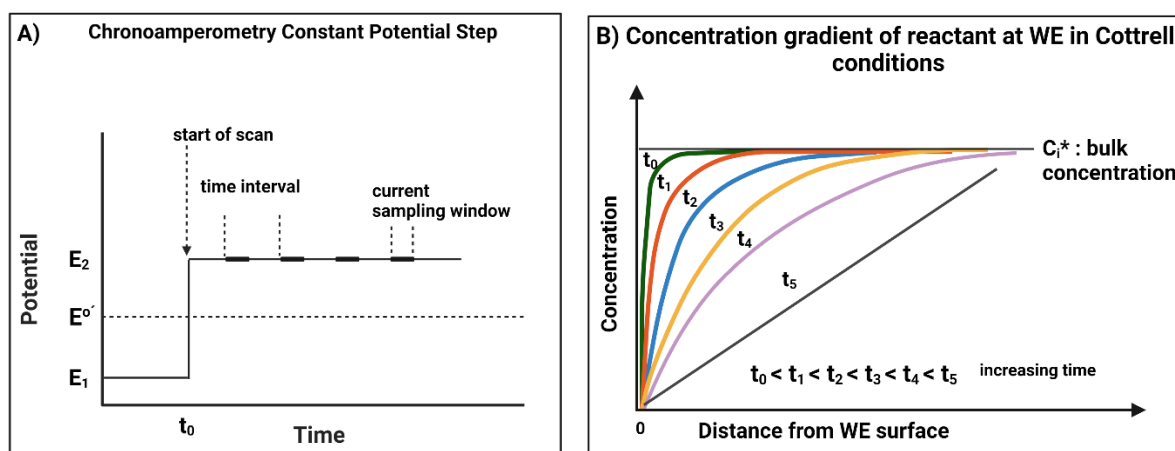


Figure 2-6 Profiles of A) applied potential step in chronoamperometry; B) reactant concentration gradient at the electrode surface in Cottrell conditions.

Once the activation energy of the reaction is provided, a cathodic or anodic current starts to flow between the WE and the CE, which is sampled at a fixed time interval. This current will flow as long as the reactant is consumed. If the potential is not a limiting factor for the reaction, the electron transfer is controlled by mass transport to the electrode surface. In an unstirred solution without convection, the faradaic current is limited by diffusion of electroactive species to the electrode surface. The reactant molecule is rapidly depleted at the electrode surface while its concentration at distance from the electrode remains the same as in the bulk C_i^* . This creates a concentration gradient leading to diffusion of more reactant molecules from the bulk towards the electrode surface. As the time passes, this diffusion layer continues to grow from the electrode into the bulk solution as illustrated in **Figure 2-6 B** and the resulting gradient is less steep. As a result, the flux of diffusing molecules is getting smaller and smaller with time and the current gradually decays as shown in **Figure 2-7**.

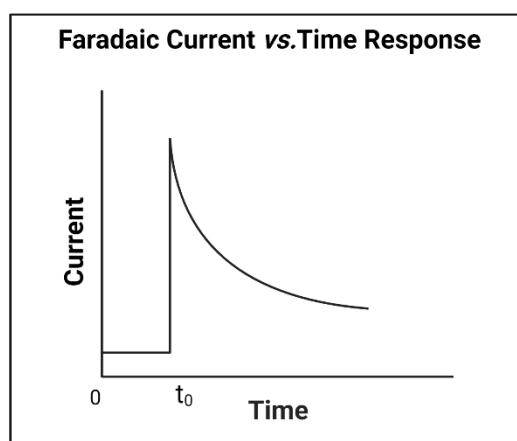


Figure 2-7 Result of chronoamperometry; faradaic current flow vs. time plot.

For a planar electrode with linear diffusion, the magnitude of the current i_d (A) is dependent on the concentration of the reduced or oxidized species and follows the Cottrell equation:

$$i(t) = i_d(t) = \frac{nFAD_i^{1/2}C_i^*}{\pi^{1/2}t^{1/2}}$$

2-12

where n is the number of electrons involved in the half-reaction, F is the Faraday constant ($C \text{ mol}^{-1}$), A (m^2) is the electrode area, D_i is the diffusion coefficient of the electroactive species i ($\text{m}^2 \text{ s}^{-1}$), C_i^* is the bulk concentration of the electroactive species i (mol L^{-1}) and t is the time (s).

The Cottrell equation describes the time dependence of the current with the current decaying with $t^{-1/2}$ as illustrated in **Figure 2-7**. Furthermore, the current as a function of time reflects the concentration gradient in the vicinity of the electrode surface.

Direct proportionality of the current and the concentration of the reduced or oxidized substance promotes chronoamperometry as a simple and reliable analytical technique for the quantification of various substances if their diffusion coefficients and the electrode area are known. Moreover, the careful choice of the applied potential establishes chronoamperometry as an ideal tool for selective identification of a specific electroactive species in solutions with complex matrices. Because diffusion is the only mode of mass transport under Cottrell experimental conditions, chronoamperometry is

also used to determine the diffusion coefficient of electroactive species or the active electrode surface area when the concentration is known. Since stirring is not required, chronoamperometry can be used with a few μL of solution.¹³⁵

When the solution is stirred or there is a movement in the solution, convection changes the kinetics of the charge transfer at the electrode surface. Mass transport mode and rate changes, the diffusion layer becomes thinner, and current does not follow the Cottrell equation any longer. In this case, one-dimensional mass transport to an electrode along the x-axis can be described by the Nernst-Planck equation¹³⁷:

$$J_i(x) = -D_i \left[\frac{\partial C_i(x)}{\partial x} \right] - \left(\frac{z_i F}{RT} \right) D_i C_i \left[\frac{\partial \varphi(x)}{\partial x} \right] + C_i v(x)$$

2-13

where J_i ($\text{mol cm}^{-2} \text{s}^{-1}$) is the flux of species i , D_i ($\text{cm}^2 \text{s}^{-1}$) is the diffusion coefficient, $\varphi(x)$ is the potential at a distance x from the electrode surface, v (cm s^{-1}) is the velocity of a volume element of the solution moving in the x direction, C_i (mol cm^{-3}) is the bulk concentration of species i , z_i (C) is the charge of species i , F (C mol^{-1}) is the Faraday constant, R (J (K mol)^{-1}) is the gas constant and T (K) is the absolute temperature. In this equation, the first term contains the concentration gradient related to the diffusion, the second term expresses the migration, and the third term is the convection due to the stirring of the solution. Considering that current is directly proportional to the flux, one can obtain the current from the Nernst-Planck equation. However, solving equation 2-13 mathematically is not straightforward and the solution depends on the experimental conditions.

In this thesis chronoamperometry is used for:

- i. Prussian blue electrodeposition on the pyrolytic carbon
- ii. Prussian blue-catalyzed hydrogen peroxide sensing
- iii. Enzymatic histamine detection

Furthermore, stirred batch amperometry is used for Prussian blue-catalyzed hydrogen peroxide sensing (Paper I).

Open circuit potentiometry

Due to the separation of charge a potential develops across an electrode-electrolytic solution interface or at the junction of two electrolytic solutions segregated by a boundary. Generally, potentiometry involves the measurement of the WE (indicator electrode) interfacial potential versus a RE with stable potential. At the electrode-solution interface, electron exchange between the inert electrode and a species in solution raises or lowers the potential energy of electrons in the electrode to match the energy of electrons in the species in solution (thermodynamic equilibrium). According to the Nernst equation (2-7), the electrode potential is normally directly proportional to the logarithm of the activity (or concentration) of the electroactive species in the solution. The cell potential is equal to the difference between the WE and RE potential ($E_{\text{cell}} = E_{\text{WE}} - E_{\text{RE}}$). Potentiometry of solutions containing redox active species is performed without disturbing the equilibrium arrangement of ions in the electrical double layer. If a current flows between two points in the system, the potential difference is reduced, the equilibrium is disturbed and the electrode potential would change, resulting in false potential measurements. Therefore, the voltage measuring instrument or the potentiostat should be

equipped with a high input impedance ($10^{12}\Omega$) to accomplish the potential measurement with as low a current as possible.^{138,139}

The Open Circuit Potential (OCP) is the potential between two points with no current flowing because the circuit is open, as the name suggests. Open circuit potentiometry involves the measurement of the potential that is assumed to be a result of the WE reaching an equilibrium with an analyte in solution. Unlike amperometry, open circuit potentiometry allows for nondestructive electroanalysis, which may be important in probing small volumes, due to zero current passage through the cell. Coupled with surface-bound enzymes or nanoparticles, this technique has been used for the calibrated detection of various analytes^{140,141}.

Recently, it has been demonstrated that open circuit potentiometry is a useful tool in studying enzyme kinetics and provides similar information as amperometry and voltammetry¹⁴². This technique is independent of electrode size and mass transfer effects. Open circuit potentiometry is used in this thesis as an alternative technique to stirred batch amperometry for hydrogen peroxide sensing.

Chapter 3. Microelectrode Fabrication

This chapter presents the design and fabrication process of 2D and 3D pyrolytic carbon microelectrodes, which were used in this thesis. In addition, the chapter includes a brief discussion of the electrochemical properties of the fabricated electrodes, which were obtained by cyclic voltammetry.

3.1 Carbon Microelectromechanical Systems

The term 'Micro-Electro-Mechanical Systems' (MEMS) is generally used to denote microscale devices with dimensions from well below one micron to several millimeters with both mechanical and electrical components including microstructures, microsensors, microactuators and microelectronics all integrated onto the same chip, which is usually made of silicon. MEMS have diverse applications in multiple markets such as electronics (e.g., disk drive heads), communications (e.g., radio frequency components in mobile phones), automotive (e.g., air bag sensors), medical (e.g., blood pressure sensors and pacemakers) and environmental monitoring (e.g., bio/chemical sensors) to name a few. Micro- and nanosized electromechanical structures are fabricated on a silicon substrate by addition of thin layers of materials with methods such as sputtering, evaporation and chemical vapor deposition, photolithography for pattern definition and subtraction of materials with top-down approaches such as reactive ion etching. Other microfabrication techniques such as soft lithography have enabled the use of polymeric materials for development of MEMS devices with 3D features. Further combining the polymer microfabrication techniques with pyrolysis has opened up for a new class of MEMS known as carbon-MEMS (C-MEMS)^{143,144}. Carbon is biocompatible and more environmental-friendly than other materials. It has versatile mechanical and electrochemical properties that make it an ideal material for the development of MEMS. C-MEMS are obtained by thermochemical decomposition (pyrolysis) of organic polymer precursors at 600-3000°C in inert atmosphere^{143,145}. The precursor structures are patterned on a silicon substrate by a microfabrication technique. Photolithography is the preferred technique for patterning the carbon-containing photoresists due to its high resolution and reproducibility. In this technique, light with a specific wavelength (violet or ultraviolet light) passes selectively through a patterned mask placed over the photoresist deposited on a substrate. For a negative photoresist, the pattern to be fabricated is designed as transparent areas on the mask while the rest is covered by chromium blocking the light passage. The absorbed photons initiate a cross-linking reaction in the exposed areas of the photoresist, making them less soluble in a chemical developer. The unexposed photoresist is removed from the substrate during the chemical development leaving only the cross-linked polymeric features^{101,146,147}. During the pyrolysis process, the patterned polymeric precursor is decomposed at elevated temperatures and all its noncarbon elements gradually evaporate leaving behind only carbon.

Carbon can form covalent bonds with various elements including itself. Elemental carbon exists in several forms (allotropes) including graphite, graphene, diamond, buckyballs, carbon nanotubes, amorphous and glassy carbon (or glass-like), each of which has its own mechanical, chemical, electrical and thermal properties¹⁴⁴. Carbon resulting from pyrolysis of photoresist is glass-like with a smooth and shiny surface. Studies suggest that carbon atoms in both sp^2 and sp^3 hybridization states are present in the glassy carbon microstructure; sp^2 hybridized carbon atoms arrange themselves in a network of interwoven ribbons of graphitic planes, while sp^3 hybridized carbon atoms make up irregular (amorphous) domains^{144,146,148,149}. Properties that make glassy carbon an attractive material for bioelectrochemical applications include it being electrically conducting, chemically inert over a wide range of electrical potentials, impermeable to gases and highly resistant to strong acids and bases. Glassy carbon has also a low surface energy and a nonreactive surface which is an advantage when it is used in biological environments. However, the rich carbon chemistry also allows for surface modification with active groups when needed^{101,143,145,150}. In this chapter, the design and fabrication process of pyrolytic carbon microelectrodes used throughout the Ph.D. project are presented.

3.2 Pyrolytic Carbon Microelectrode Design

In the first iteration of the project, 2D and 3D pyrolytic carbon microelectrodes in three-electrode-chip configuration, previously designed (named as 2D-C4Bio and 3D-C4Bio) in the group, were replicated and used for the initial sensor development experiments. The schematic design of these electrodes and the optimized process flow for their fabrication is presented here.

2D pyrolytic carbon in three-electrode-chip configuration

The schematic in **Figure 3-1** shows the design of the 2D pyrolytic carbon in three-electrode-chip configuration. The overall design of the chip resembled the commercial DropSens electrodes¹⁵¹. A circular working electrode (WE) with a diameter of 4 mm and an area of 12.5 mm² surrounded by a ring-like counter electrode (CE) with an area of 25.2 mm² was patterned on a 10x30 mm² chip (**Figure 3-1 A**). A gold pseudo-reference electrode (RE) with an area of 0.8 mm², gold leads and contact pads for the connection of the electrode to the potentiostat were deposited as shown in **Figure 3-1 B**. As illustrated in **Figure 3-1 C**, a passivation layer confined the electrode area and protected the leads from delamination and chemical reactions.

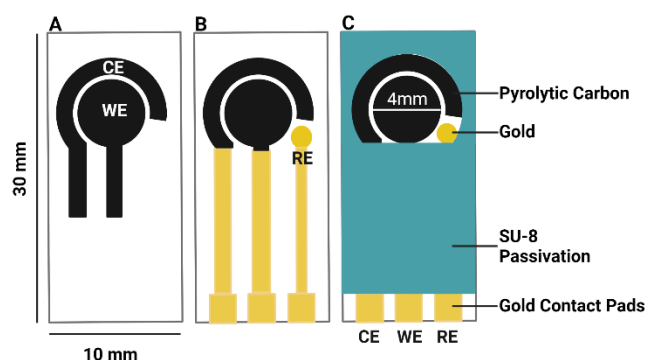


Figure 3-1 Schematic design of 2D pyrolytic carbon in three-electrode-chip configuration; A) pyrolytic carbon layer; B) gold pseudo RE, leads and contact pads; C) SU-8 passivation layer. Created with Biorender.com.

3D pyrolytic carbon in three-electrode-chip configuration

The schematics in **Figure 3-2 A-C** show the design of the 3D pyrolytic carbon in three-electrode-chip configuration. The chip had the same dimensions and the same electrode configuration as the 2D ones. The only differences between the 3D and the 2D microelectrode chips were the total surface area of the pyrolytic carbon WE and the material used to pattern the CE, RE, the leads and the contact pads. Platinum was used to pattern the CE, the pseudo RE as well as the leads and the contact pads for the connection of the electrode to the potentiostat (**Figure 3-2 B**). The circular WE with the diameter of 4 mm (**Figure 3-2 C**) had an additional 284 micropillars made of pyrolytic carbon (**Figure 3-2 D**).

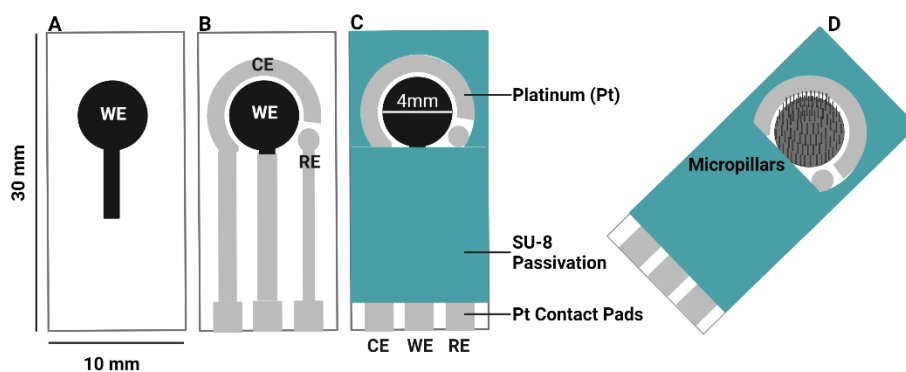


Figure 3-2 Schematic design of 3D pyrolytic carbon in three-electrode configuration; A) pyrolytic carbon WE; B) Pt CE, pseudo RE, leads and contact pads; C) SU-8 passivation layer; D) micropillar structures. Created with Biorender.com

3.3 Pyrolytic Carbon Microelectrode Fabrication

2D microelectrode fabrication

The pyrolytic carbon microelectrodes were fabricated by photolithography with the negative epoxy photoresist SU-8 followed by pyrolysis. The fabrication process flow of the 2D microelectrodes is illustrated in **Figure 3-3**. In the first step, an insulating silicon oxide layer with the thickness of 600 nm was grown on a 4-inch silicon wafer (**Figure 3-3 A**). Thereafter, SU-8 2035 was spin coated on the wafer in two cycles using a RCD8 spin coater (Karl-Süss, Germany) with a spread cycle at 1000 rpm for 10 s at an acceleration of 200 rpm s^{-1} and a thinning cycle at 5000 rpm for 120 s using 1000 rpm s^{-1} , resulting in a film with a thickness of 15-17 μm (**Figure 3-3 B**). The SU-8 was soft-baked for 15 min at 50°C on a programmable hotplate (Harry Gestigkeit GmbH, Germany) with a temperature ramp of 2°C min^{-1} to remove the solvent. Next, the 2D WE and the CE design was patterned on the photoresist-coated wafer by UV (wavelength 365 nm) exposure through a chromium photomask on a MA6 mask aligner (Karl-Süss, Germany) with a total exposure dose of $2 \times 250 \text{ mJ cm}^{-2}$ (**Figure 3-3 C**). The exposed areas were cross-linked in a post-exposure-bake (PEB) similar to the soft-bake (SB) but with a duration of 2 hours. The unexposed SU-8 photoresist was removed by development in fresh PGMEA (SU-8 developer) for 2x5 min (**Figure 3-3 D**), followed by IPA rinsing and drying in N_2 atmosphere at room temperature. After drying, the samples were flood exposed with a dose of $2 \times 250 \text{ mJ cm}^{-2}$. A hard-bake step of 15 hours at 90°C was performed to harden and dry out the SU-8 microstructures. In the next step after the photolithography, the SU-8 samples were pyrolyzed for 5 hours at 1100°C in N_2 atmosphere in a high temperature furnace (PEO-04, ATV Technologies, Germany) (**Figure 3-3 E**). The SU-8 microstructures shrink during the pyrolysis process, resulting in a flat smooth surface with the thickness of 2 μm in case of the 2D microelectrodes. After obtaining pyrolytic carbon, 150-nm thick Au leads and contact pads with a 15 nm titanium (Ti) adhesion layer were patterned by e-beam metal deposition through a shadow mask (**Figure 3-3 F**). Finally, the complete electrode chip except the pyrolytic carbon WE, the CE, the Au pseudo-RE and the contact pads were passivated by a 5 μm thin SU-8 layer (**Figure 3-3 G**). The passivation layer was used to confine the sensing area to the pyrolytic carbon surface and at the same time to protect the metal and carbon from delamination. The wafer was diced into 14 electrode chips with a dimension of $10 \times 30 \text{ mm}^2$ (**Figure 3-3 H**).

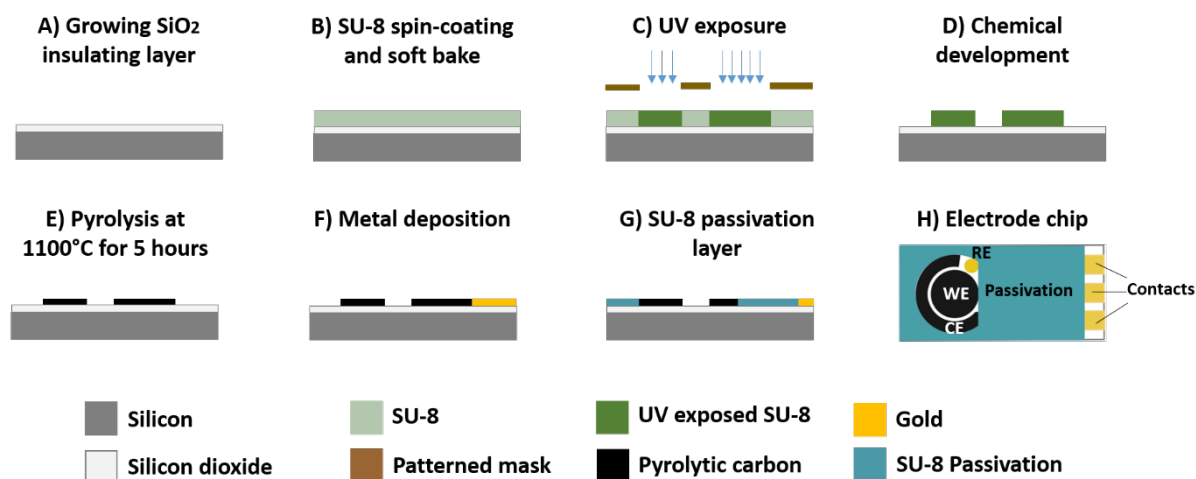


Figure 3-3 Schematic representation of the process flow for the fabrication of 2D pyrolytic carbon microelectrodes.

Figure 3-4 shows the fabricated 2D pyrolytic carbon microelectrode chips ($10 \times 30 \text{ mm}^2$) with integrated pyrolytic carbon CE and Au pseudo-RE.



Figure 3-4 2D pyrolytic carbon in three-electrode-chip configuration with integrated CE (pyrolytic carbon) and pseudo RE (Au) and leads and contact pads (Au). Each chip had a dimension of $10 \times 30 \text{ mm}^2$. Reprinted from Yasmin Mohamed Hassan's Ph.D. thesis¹⁵².

3D microelectrode fabrication

Fabrication of the 3D pyrolytic carbon microelectrodes consisted of two photolithography steps followed by pyrolysis. **Figure 3-5** shows the schematic illustration of the process flow for the fabrication of these electrodes. The first photolithography step with SU-8 2035 defined the flat circular base of the pyrolytic carbon WE (**Figure 3-5 A-B**) and was identical to the one for the 2D electrodes. An additional step of SU-8 photolithography defined 284 micropillars on top of the flat circular base. For this, SU-8 2075 was dispensed and spin-coated (500 rpm , 30 s , 50 rpm s^{-1} and 1000 rpm , 60 s , 100 rpm s^{-1}) followed by a SB for 6 hours at 50°C . A second spin-coating of SU-8 2075 was performed to obtain the final thickness of approximately $500 \mu\text{m}$, followed by a SB for 12 hours (**Figure 3-5 C**). The pattern of the micropillars was transferred by UV exposure through a chromium photomask with a total dose of $4 \times 250 \text{ mJcm}^{-2}$ using the mask aligner followed by a PEB for 10 hours at 50°C (**Figure 3-5**

D). Next, the uncross-linked SU-8 was removed in a chemical development bath containing PGMEA (**Figure 3-5 E**). Compared to the 2D electrodes, the 3D electrodes spent a longer time in the chemical developer (2x40 min), since the 500- μm thick unexposed SU-8 layer required longer time to dissolve. The pyrolysis process and parameters were the same as used for the 2D microelectrodes. A 3D pyrolytic carbon WE with $225 \pm 1 \mu\text{m}$ high and $68 \pm 2 \mu\text{m}$ wide (diameter) pillars were obtained as shown in **Figure 3-5 F**. The CE, the pseudo-RE, the leads and the contact pads were defined by Pt deposition up to 150 nm through a shadow mask (**Figure 3-5 G**). The fabrication process flow was finished by adding an SU-8 passivation layer to the microelectrodes (**Figure 3-5 H**) and dicing the wafer into $10 \times 30 \text{ mm}^2$ chips (**Figure 3-5 I**) just as it was done for the 2D microelectrodes.

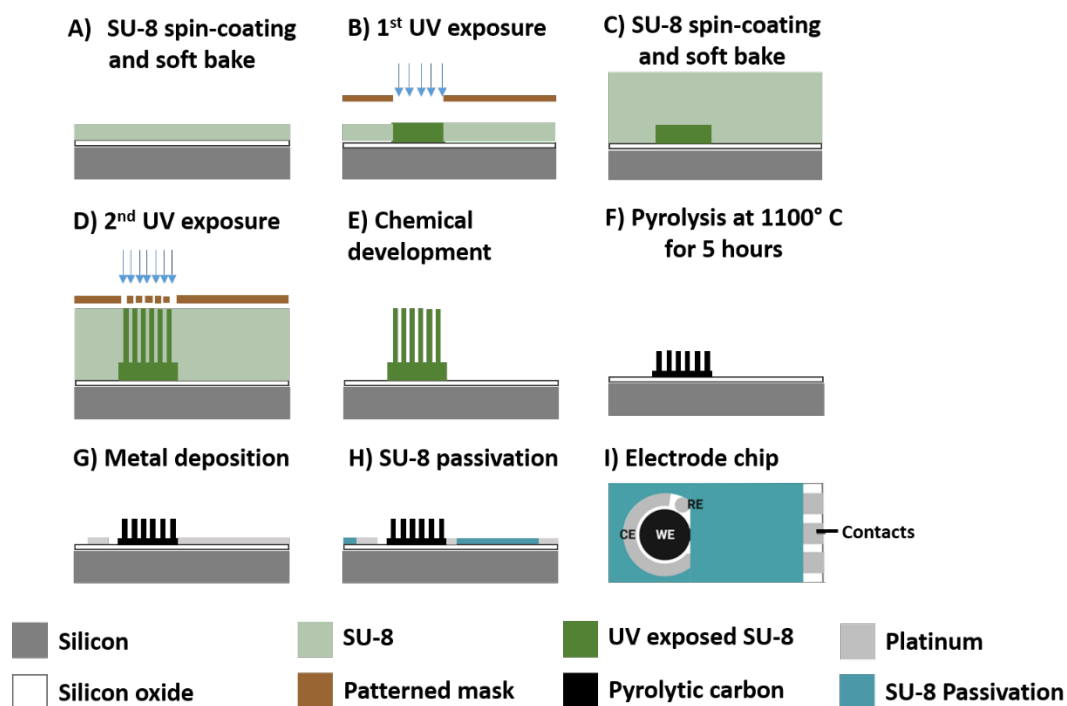


Figure 3-5 Schematic illustration of the process flow for the fabrication of the 3D pyrolytic carbon microelectrodes.

Figure 3-6 shows the optical (A) and SEM (B) images of the 3D pyrolytic carbon consisting of 284 micropillars.

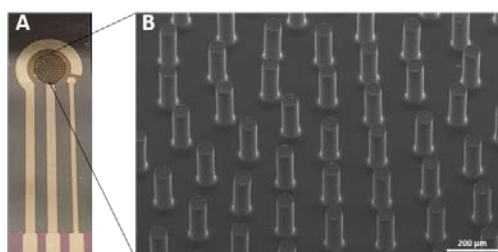


Figure 3-6 Image A) $10 \times 30 \text{ mm}^2$ pyrolytic carbon microelectrode chip (3D) with integrated Pt CE, RE, leads and contact pads; B) SEM of pyrolytic carbon micropillars as the WE (scale bar: $200 \mu\text{m}$).

3.4 Electrochemical Characterization of 2D and 3D Pyrolytic Carbon

Electrochemical properties of both the 2D and the 3D pyrolytic carbon WEs were obtained by cyclic voltammetry in 10 mM $\text{K}_3\text{Fe}(\text{CN})_6/\text{K}_4\text{Fe}(\text{CN})_6$ in phosphate buffered saline (PBS) pH 7.4 in the potential window between -1.0/+1.0 V at a scan rate of 50 mV s^{-1} . For the sake of comparison, the cyclic voltammograms were recorded using external standard Pt CE and Ag/AgCl in 3M KCl RE.

Figure 3-7 represents the cyclic voltammograms of the fabricated 2D and 3D pyrolytic carbon microelectrodes. Comparison of the $\text{Fe}^{+3/+4}$ oxidation and reduction peaks on both types of electrodes tells us that the 3D microelectrode yielded almost twice as high peak currents compared to the 2D microelectrode. The Fe^{+3} oxidation peak on the 2D pyrolytic carbon WE produced $271.62 \pm 17.47 \mu\text{A}$ of current, whereas this value was $634.74 \pm 20.71 \mu\text{A}$ on the 3D electrodes. This can be explained by the fact that the 3D microelectrode with 284 micropillars provided a larger active surface area for electrochemistry than the flat 2D surface. As mentioned earlier in this chapter, the geometrical surface area of the 2D pyrolytic carbon WE was 12.5 mm^2 . For calculating the geometrical surface area of the 3D pyrolytic carbon WE, the surface area of 284 carbon micropillars with the dimensions of $225 \mu\text{m}$ in height and a diameter of $68 \mu\text{m}$ had to be added to the area of the flat pyrolytic carbon base (12.5 mm^2), which resulted in a total of 26.2 mm^2 . Finally, equation 2-10 was used to calculate the peak potential separations (ΔE_p) of the pyrolytic carbon electrodes which were $171.34 \pm 17.72 \text{ mV}$ and $299.84 \pm 8.16 \text{ mV}$ for the 2D and 3D electrodes, respectively.

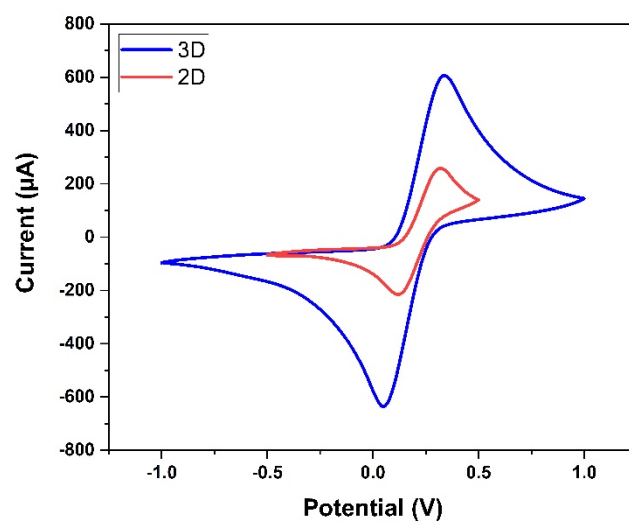


Figure 3-7 Cyclic Voltammograms of 2D (red) and 3D (blue) pyrolytic carbon microelectrodes in 10 mM $\text{K}_3\text{Fe}(\text{CN})_6/\text{K}_4\text{Fe}(\text{CN})_6$ in PBS pH 7.4 .Scan rate 50 mV s^{-1} vs. standard Ag/AgCl in 3M KCl RE. External Pt CE was used to record the data.

3.5 Microelectrode Design Modification

Although it is more convenient to have miniaturized CE and RE integrated on the same chip than using bulky external electrodes, it was decided to implement an external Ag/AgCl (in 3M KCl) standard RE instead of the integrated Pt and Au pseudo-REs for the biosensor development. Generally, the pseudo-REs suffer from the lack of thermodynamic equilibrium and their potentials are not stable/constant during the electrochemical measurements, especially when immersed in strong acidic and alkaline solutions. Similarly, the on-chip CE was replaced by an external Pt CE. Preferably, the surface area of the CE must be 10 times larger than that of the WE. In brief, the overall reason that we decided to go for external CE/RE was more stable measurements, and the fact that the CE area could be larger for an off-chip CE than for the on-chip version. Hence, the design of the microelectrode chips were modified accordingly. **Figure 3-8** shows the modified design of the 3D pyrolytic carbon in the single-electrode-chip configuration. Internal CE and pseudo-RE were eliminated, so each pyrolytic carbon microelectrode chip would serve as a single WE. However, the design of the 3D carbon structures remained unaltered. Finally, the microelectrode chips were shortened in length (16 mm) to be able to include more microelectrode chips on each wafer. 6-inch wafers were used to increase the fabrication process efficiency and to reduce the cost. Each 6-inch wafer included 84 microelectrode chips.

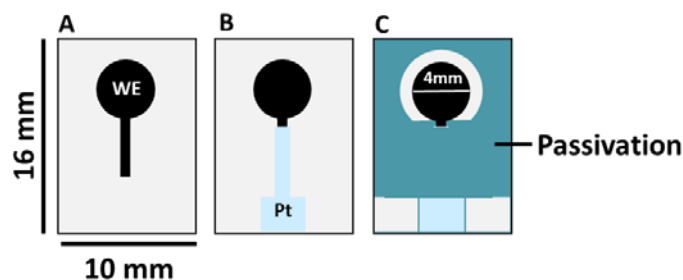


Figure 3-8 Final design of 3D pyrolytic carbon microelectrodes in the single-electrode-chip configuration.

Figure 3-9 shows a modified 3D pyrolytic carbon WE with 284 micropillars. These microelectrodes were fabricated by Long Quang Nguyen and Jesper Yue Pan and were used to obtain the results presented in Paper I and II. More details about the fabrication of the 3D microelectrodes can be found in Paper I.

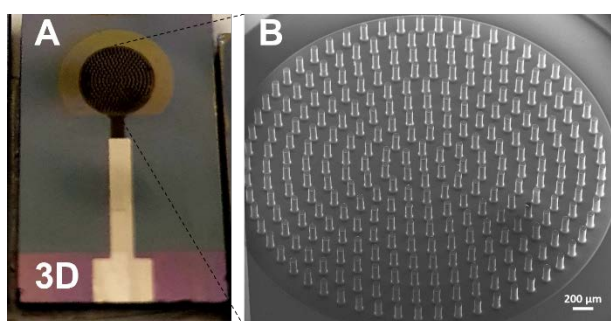


Figure 3-9 Modified pyrolytic carbon microelectrode in the single-electrode-chip configuration; A) 3D pyrolytic carbon WE chip (10x16 mm); B) SEM of 284 pyrolytic carbon micropillars.

Chapter 4. Fabrication of Electrochemical Cell

This chapter entails the ideas and the technologies that were exploited to innovate electrochemical cells specifically developed for pyrolytic carbon electrodes with a variety of dimensions, configurations, and applications. The starting point of this process was the optimization of the polymeric setup that was previously fabricated by CO₂ laser ablation and used by former group members^{152,153} for electrochemical characterization of pyrolytic carbon electrodes.

4.1 Polymeric Setup With Magnetic Clamps for an Individual Three-Electrode-Chip

The inherited polymeric setup made of two laser-cut poly-methyl-methacrylate, PMMA, plates (5 mm thick) that were clamped together by magnetic force is illustrated in **Figure 4-1**. As the schematics in **Figure 4-1 A** show, the setup was composed of two PMMA plates, named as the 'bottom plate' with a pocket (20x10x1 mm) for electrode placement and a 'top plate' with an opening and a trench for the O-ring. The opposite poles of eight cubic gold-plated magnets (5 mm) with adhesive force of 11.8 N per magnet placed in engraved pockets on four corners of each plate provided a magnetic force to clamp the two plates together. As it can be seen in **Figure 4-1 B**, the opening in the top plate created a well (300 μ L) above the microelectrodes with the pyrolytic carbon WE with integrated CE and Au pseudo-RE. This provided access to the microelectrode surface, while the O-ring placed between the two plates prevented the liquid from leakage and confined the active area of the electrode. Since the design of the pyrolytic carbon microelectrode chip was similar to the commercial screen-printed DropSens electrodes, a commercially available connector from DropSens enabled electrical connection between the on-chip microelectrodes and the potentiostat.

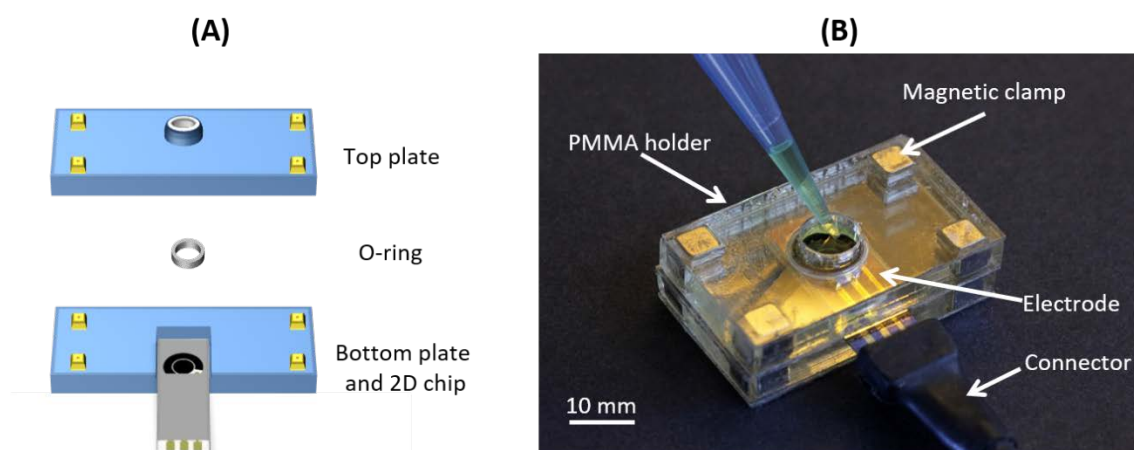


Figure 4-1 Laser-cut PMMA electrode holder with magnetic clamp and DropSens connector previously developed by former group members ^{152,153}.

The simple design of the setup combined with magnetic clamping allowed for quick and effortless replacement of microelectrode chips. As a result, more than one microelectrode could be characterized or used for electrochemical measurements in a relatively short time. However, a few major challenges appeared frequently when using the setup. Although this simple setup was cheap, fast and easy to replicate, it was often unstable on the laboratory desk when connected to the commercial DropSens connector. This was due to its small dimensions (20x30 mm) and light weight compared to the heavy connector and the long cable attached to it. It was observed that the connector cable created a torque making the setup to topple over, if not fixed to the desk by tape. Being unsteady, the connection was often poor, and the fragile silicon microelectrode chip broke from the last insertion point into the connector. Another challenge that very often led to electrode breakage before the measurement, was the strong magnetic force that made it difficult to control the two PMMA plates when they were close to each other. The uncontrollable clamping force would move the

setup and displace the microelectrode chip from the engraved pocket, causing either breakage or misplacement of the microelectrode chip. Another reoccurring trouble was that the round O-ring would fall off from its place on the top plate or was misplaced over the microelectrodes during clamping. This caused primarily leakage and variations in the confined electrode area. Last, the cubic magnets would move out of the engraved pockets if not somehow fixed in place.

Having taken all the aforementioned challenges with the primary PMMA setup into consideration, the design was optimized as it is displayed in **Figure 4-2**. In the primary setup, a few millimeters of the microelectrode chip where the contact pads were patterned protruded the edge of the clamped PMMA plates on one side for insertion into the connector. This increased the risk of chip breakage, as part of the chip was not supported by the PMMA substrate. In the revised design, the pocket for the placement of the microelectrode chip was moved inwards to the middle of the bottom PMMA plate providing full support for the entire chip length. The size of the PMMA plates was increased in two dimensions to 80 mm to increase the stability of the setup on the laboratory desk while the thickness of the plates remained unchanged at 5 mm. In order to be able to clamp and separate the top and bottom plates in a more controlled manner, two handgrips on two sides of each PMMA plate were included in the design. To fix the O-ring in place, the circular O-ring was redesigned with two wing-like supporting extensions that were gripped by two pin-like microstructures engraved on the bottom side of the top plate. The O-ring shape was cut out of a silicone sheet with a thickness of 1 mm with the CO₂ laser. The eight cubic magnets were replaced by fourteen gold-plated ring magnets (supplied by supermagnete, Germany) with outer and inner diameters of 6 and 2 mm respectively and an adhesive force of 14.9 N per each magnet. To be able to counteract the strong magnetic force and to control the assembly of top and bottom plates, the magnets were placed on the non-contacting sides of the two plates meaning the bottom side of the bottom plate and the top side of the top plate. For placing the ring magnets, the PMMA plates were not cut completely through, but were just engraved. 4 mm deep cavities with pin-like microstructures with a diameter of 2 mm in the middle were created to hold the magnets in place.

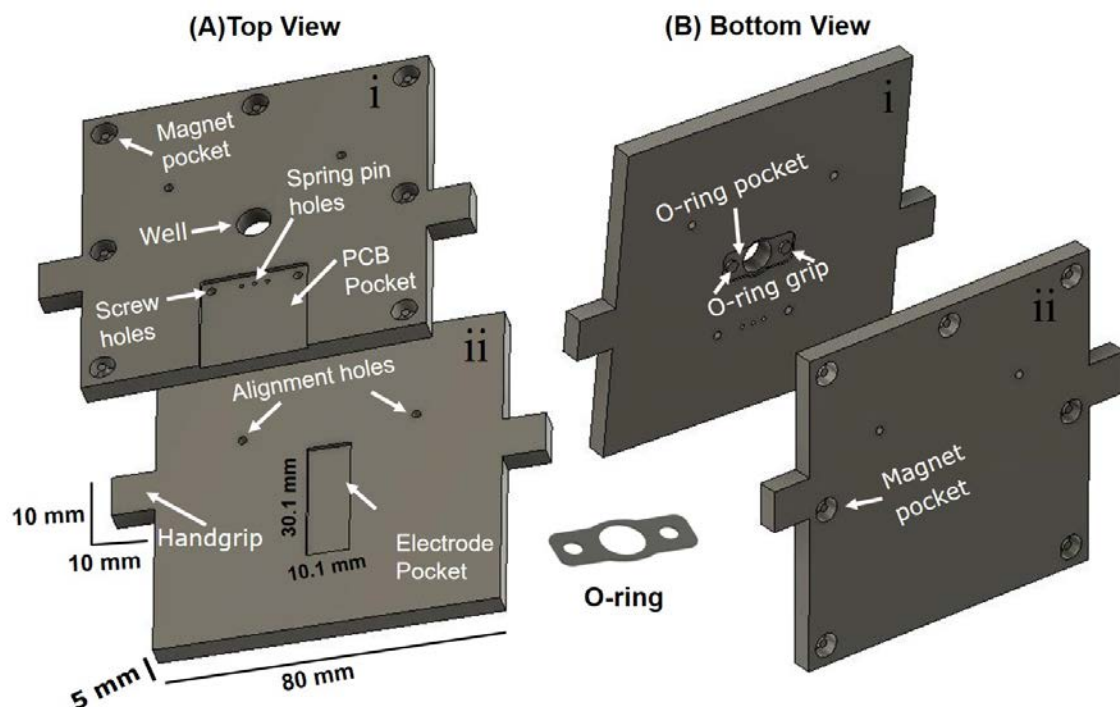


Figure 4-2 Schematic design of the micromilled PMMA setup with magnetic clamp and PCB for microelectrode chips with integrated CE and RE.

A Printed Circuit Board (PCB) was designed to interface the microelectrode chip with the potentiostat. Three separate copper leads along the leads and the contact pads of the microelectrode chip were patterned on the PCB by removing the material in between the leads and elsewhere on the board mechanically using a micromilling tool. 1-mm diameter holes were drilled on both end of each lead. On one side, three gold-coated spring pins and on the other side three wires were soldered. The wires provide connection to the cables (WE, CE & RE) of the potentiostat, while the spring pins in touch with the contact pads of the microelectrode chip provide connection to the WE as well as the integrated CE and RE. An engraved pocket with three pin holes and two screw holes were incorporated on the top PMMA plate for mounting the PCB. The resulting optimized setup can be seen in **Figure 4-3**.

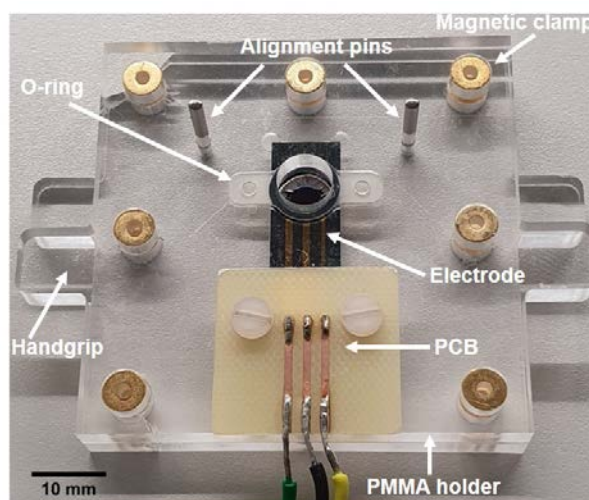


Figure 4-3 Micromilled PMMA setup assembled.

The optimized setup was stable and robust. It was used for microelectrode characterization and simple electrochemical measurements. No wobbling, no leakage and no loose connection was observed. The only thing that could be optimized in this revised version of the PMMA setup was the sharp corners. The strong magnetic force resulted in cracking of two of the corners of the PMMA plates. This could be optimized by moving the magnet cavities inwards away from the corners of the plates and by including curved corners in the design. The PMMA setup was fabricated using micromilling technique, which entails removing bulk material by mechanical cutting tools to create complex features at the microscale¹⁵⁴. The micromilling fabrication method is highly reliable when high precision is needed. Thus, the method has been vastly used to create microfluidic devices. However, for fabricating the PMMA setup with magnetic clamp, obtaining precision in microscale was not crucial as the dimensions of different features were from 1 mm and above. Since features had to be created on both sides of two PMMA plates, the design and fabrication process of the setup was very time consuming. It took about two weeks to create one setup including design phase, micromilling machine programming, test and failure corrections, PCB fabrication, soldering of pins and wires, O-ring cutting and assembling. Replication of the setup took 1½-2 days. Moreover, in the initial design of the setup the possibility of multiplexing, stirring, and using external RE or CE in combination with the pyrolytic carbon WE were not considered.

4.2 Glass Beaker With a Designed Cap for Electrode Insertion

As mentioned in the previous chapter, at some point during the project it was decided to use external Pt CEs and standard RE that are shown in **Figure 4-4**. For this purpose, a cap was designed for a 5 mL glass beaker with an aperture for fitting the pyrolytic carbon WE, an opening for spiral Pt wire CE or for flat CE (Silicon coated on both sides with Pt), an opening for RE insertion and a vent hole for pipetting of samples. Initially, the cap was cut out of a 5-mm thick PMMA sheet by CO₂ laser. After changing the microelectrode chip configuration and dimensions where integrated CE and pseudo-RE were removed and chip length was reduced from 30 to 16 mm, the cap height had to be increased to about 15 mm for immersion of the microelectrode chip into the solution in glass beaker. For this modified design of the cap 3D printing was implemented. The design and the fabrication of the cap for a glass cell is explicitly explained in Paper I.

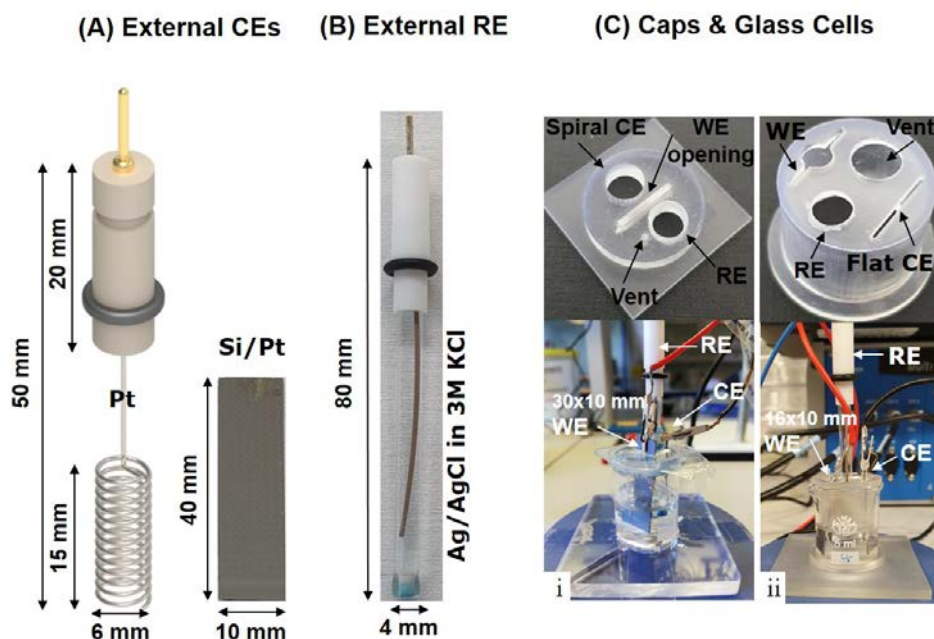


Figure 4-4 Components of the glass cell including (A) external Pt CEs, (B) external RE and (C) designed caps for electrode insertion and 5mL glass beakers on a supporting plate.

4.3 3D Printed Multi-Electrode Cell

Although the glass beaker in combination with a designed cap was a fast and easy-to-build electrochemical cell with the possibility of stirring and implementing external CE and standard RE, it did not allow for multiplexing or simultaneous measurements on several microelectrodes. The protocol for electrochemical sensor preparation was a lengthy and time-consuming process. The preparation of each single sensor would take about 4 hours, while the storage of the sensors considered as non-negligible because loss of sensitivity was observed. In these circumstances, statistical data collection in a timely manner was immensely challenged. To address the challenge, multi-electrode cells enabling a variety of configurations and applications including simultaneous sensor preparation were envisioned. Among the polymer fabrication techniques available, additive manufacturing by stereolithography was considered as the most convenient for rapid prototyping of the envisioned multi-electrode cells. This section includes the descriptions of the main iterations for multi-electrode cell fabrication by 3D printing.

Additive manufacturing by stereolithography

Additive manufacturing, commonly known as 3D printing, was used to prototype and create the electrochemical cell and measurement setups for multiple electrodes. Additive manufacturing technology comprises layer-by-layer creation of a 3D object. The object is designed using 3D modeling softwares such as Autodesk Fusion 360, AutoCAD or SolidWorks. The design file is then imported into the 3D printing software, which uses specific algorithms to divide the model into layers. The software also set ups the print layout and orientation and creates support structures of various thicknesses and densities for optimal printing. While in thermal printing, a continuous filament of thermoplastic material is extruded and solidifies layer-by-layer, in stereolithography (SLA) technology a laser beam is used to initiate a controlled photopolymerization process by curing a photosensitive liquid resin into hardened plastic objects. **Figure 4-5 A** schematically shows the main composition of a SLA printer and the bottom-up process of printing a 3D object. In this configuration, the build platform is immersed

into a photosensitive resin tank. The laser beam is focused on a X-Y scanning mirror, which rotates to reflect and move the laser beam across the build platform. The photopolymerization process begins on the platform when the laser beam illuminates the nearby liquid resin. The resin molecules absorb the energy of the laser beam photons, to make chemical bonds with neighboring molecules. The beam diameter and the precision of its movement across the platform, defines the resolution of the printer. In the bottom-up process, the printing starts with the lowest layer of the object on the build platform and thereafter the layers are formed gradually on top of that. The post-print treatments include the removal of the unhardened resin from the print in an isopropyl alcohol (IPA) wash bath (**Figure 4-5 B**) and the final annealing of the printed object in a heated UV chamber (**Figure 4-5 C**).

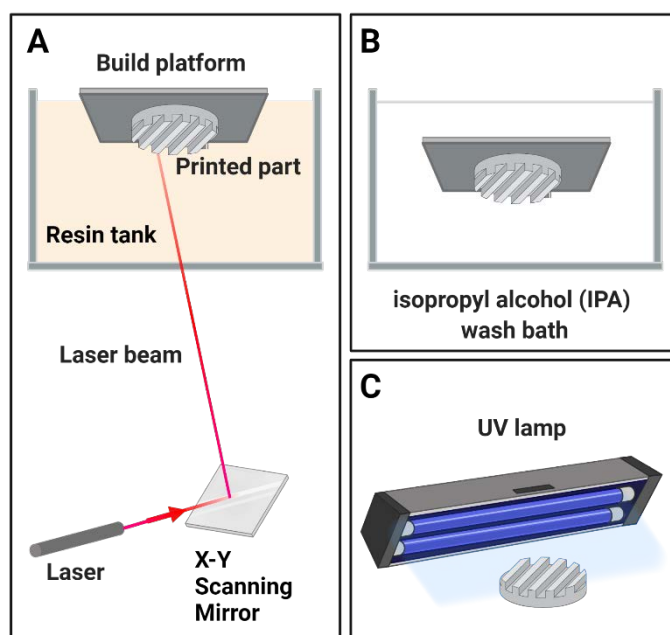


Figure 4-5 Schematic illustration of bottom-up additive manufacturing process based on stereolithography consisting of A) layer-by-layer laser initiated photopolymerization, B) rinsing and C) post-curing in heated UV chamber.

First-generation 3D printed multi-electrode cell with magnetic clamp

The schematic design in **Figure 4-6** shows different components of the first-generation 3D printed electrochemical cell. The design was inspired by the glass cell, consisting of a beaker (20 mL), a square bottom plate as a holder of four pyrolytic carbon WEs, an O-ring for sealing the WEs and a cap for insertion of an external CE (spiral wire in **Figure 4-4 A**) and a standard RE (**Figure 4-4 B**) shared by the four WEs. For printing the O-ring, Flexible resin (formlabs) which mimics the properties of rubber was used. The cap, the beaker and the WE holder were made of Clear resin (formlabs). The beaker and the WE holder were clamped by eight cubic magnets (adhesive force 11.8 N per magnet). The biggest challenge was the leakage. The magnetic force was not large enough to retain the beaker, the O-ring and the WE holder tightly together. A less crucial yet troublesome issue was the positioning of the cap, which was unstable and loosely fitted on the beaker.

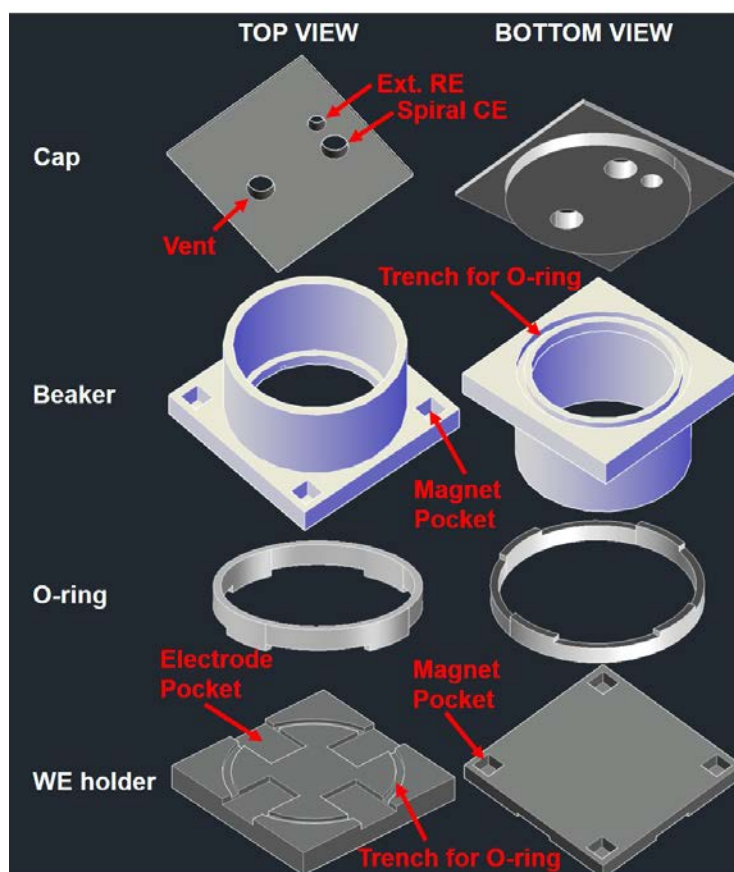


Figure 4-6 Initial design of the components of the first-generation 3D printed multi-electrode cell with four magnetic clamps (total of 8 magnets).

To solve the leakage problem, the clamping was fortified by increasing the number of the magnets to a total of 24 in the second design iteration displayed in **Figure 4-7**. It was observed that a large liquid column (> 20 mL) above the WEs caused leakage into their surroundings. Therefore, the bottom of the beaker was partially closed and the liquid column above each WE was confined to a well (300 μ L) which was sealed by a round rubber O-ring. To secure the cap on the beaker, a trench was incorporated in the cap design.

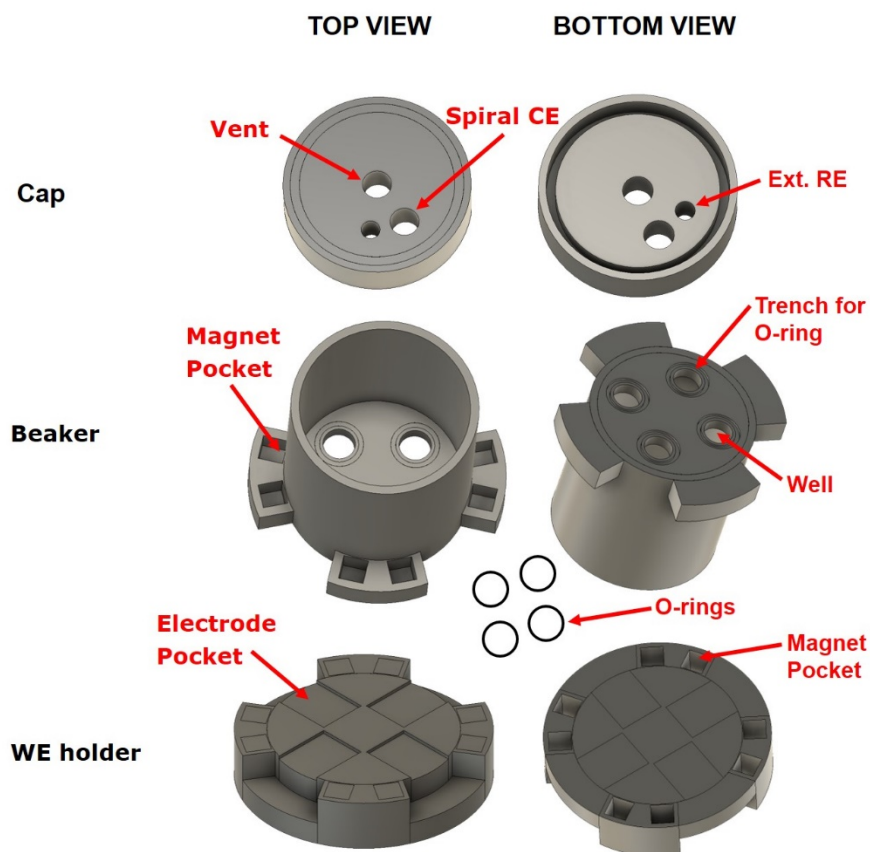


Figure 4-7 Optimized design of the components of the first-generation 3D printed multi-electrode cell with eight magnetic clamps (total of 24 magnets).

The assembled 3D printed multi-electrode cell with magnetic clamp is pictured in **Figure 4-8** containing water. No leakage was observed in the first printed copy of the cell, and it was used for the characterization of the pyrolytic carbon microelectrodes by cyclic voltammetry. No remarkable disturbance caused by the magnetic field was observed in the cyclic voltammograms of the microelectrodes. However, statistical data and further electrochemical investigations such as studying the impedance of the microelectrodes in the 3D printed cell with magnetic clamp are required to confirm the initial observation, indicating that the magnetic field did not affect the electrochemical processes in the cell. Furthermore, it was decided to abandon the magnetic clamp for two major reasons: i) leakage in replicated cells, ii) inability to implement magnetic stirring in the cell as the strong magnetic field created by the magnetic clamps would have damaged the stirrer and agitate the rotation of a magnetic stirring bar.



Figure 4-8 Assembled optimized first-generation 3D printed multi-electrode cell with four pyrolytic carbon WEs.

Second-generation 3D printed multi-electrode cell with magnetic stirring

The electrochemical sensor preparation process with Prussian blue electrodeposition on the pyrolytic carbon microelectrodes required magnetic stirring. For this purpose, the magnetic clamp was replaced by 8 screws in the design of the 3D printed multi-electrode cell as shown in **Figure 4-9 A-D**. The magnet pockets were replaced by 2-mm screw holes (8 in the WE holder and 8 around the beaker). The beaker and the WE holder were fixed together using 2-mm screws and bolts. Compared to the magnets which allowed for instant clamping and separation of the two main cell components, loosening and tightening the screws and bolts required about 5-7 minutes of manual work to assemble or to separate the components of the cell. Despite this drawback, the screws secured the cell from leakage. The design was reliably reproducible. No leakage was observed from several 3D printed copies of the cell replicated randomly at different times using 2 different formlabs 3D printers. As shown in **Figure 4-9 E**, a magnetic stirrer bar placed in the center of the bottom of the beaker in between the WE wells provided the stirring possibility in the 3D printed multi-electrode cell. A cap with a large opening in the middle, allowed for insertion of the magnetic stirrer bar, for visual inspection of the cell and to have better control on the placement of the external electrodes. The cell was successfully used for batch microelectrode characterization and sensor preparation in a timely manner. By using the multi-electrode cell in combination with a multichannel potentiostat with four channels, the sensor preparation capacity was increased four times as four sensors could be prepared simultaneously. More explicit information about the design of the multi-electrode cell is included in Paper I.

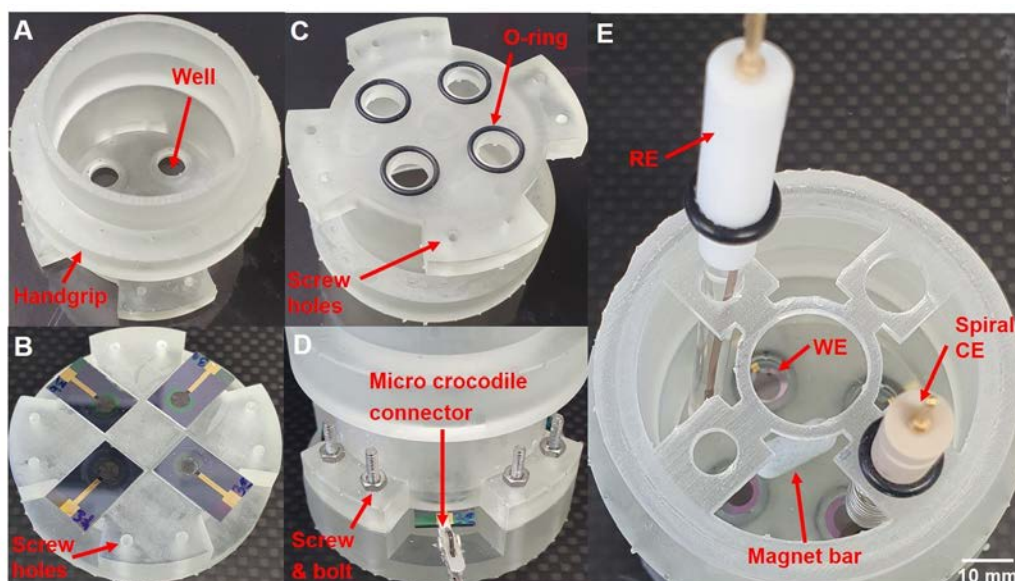


Figure 4-9 Components of second-generation 3D printed multi-electrode cell with magnetic stirring for batch sensor preparation; pictures show (A) top view of beaker with 4 wells, (B) WE holder with 8 screw holes, (C) bottom view of beaker with 4 rubber O-rings and 8 screw holes, (D) side view of the assembled parts fastened by screws and bolts and (E) top view of the assembled setup with external CE and RE and magnetic stirring.

Figure 4-10 includes a few caps that were designed for different applications and electrode configurations. The cap in **Figure 4-10 A** was designed for a common external spiral CE and a common RE connected to all four WEs. A small vent was included for pipetting of solution. In **Figure 4-10 B** and C, openings for four sets of flat CE and RE were included such that each individual pyrolytic carbon WE had its own CE and RE. A wide opening in the center of the designed cap in **Figure 4-10 B** allowed for insertion of a magnetic stirrer bar. The four vents in **Figure 4-10 C** were incorporated for pipetting samples into four separated wells. The cap in **Figure 4-10 D** was designed for insertion of four spiral CEs and a common RE. The cap in **Figure 4-10 E** was specifically equipped with an inlet in the middle for nitrogen purging such that the nitrogen pipe could be fixed on the screw-like inlet and the flow of nitrogen gas would be divided radially in all directions inside the beaker. **Figure 4-10 F** shows the cap that was designed for a cell with four separate wells, allowing each well and each individual WE to have its own flat CE and RE.

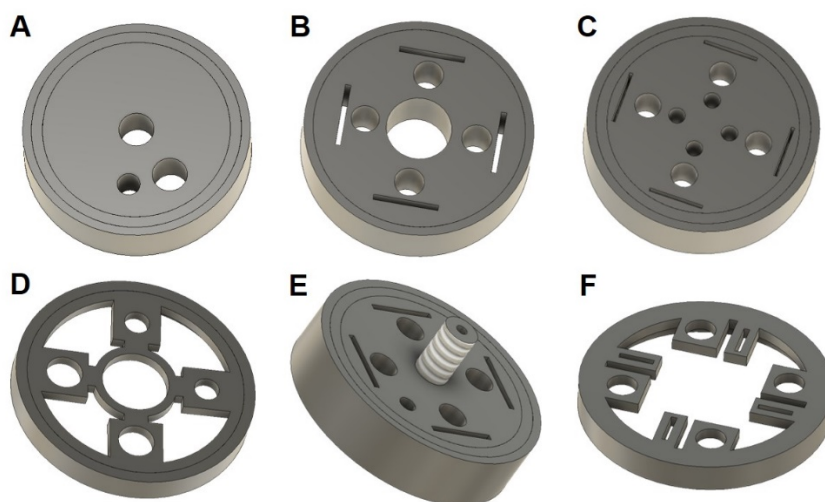


Figure 4-10 Designed caps for (A) single external CE (spiral) & RE shared between four WEs; (B) four individual REs and flat CEs and a large vent for magnet bar insertion; (C) four individual REs and flat CEs and small vents for pipetting into separate wells; (D) four individual spiral CEs and a common RE; (E) nitrogen purging; (F) four separate wells.

Third-generation 3D printed multi-electrode cell for static cell-based measurements

In vitro detection of histamine released from activated mast cells did not require magnetic stirring, as either the mast cell supernatant containing histamine would be added into the well where pyrolytic carbon WE was located, or the mast cells sedimented on the pyrolytic carbon inside the well would be stimulated to release histamine directly on the microelectrode surface or in its vicinity. Therefore, for static cell-based measurements, the design of the 3D printed multi-electrode electrochemical cell was adjusted by lowering the volume of the beaker and separating the four WE wells by two crossing walls which equally divide the beaker into four identical compartments with a volume of 2 mL each as shown in **Figure 4-11**.

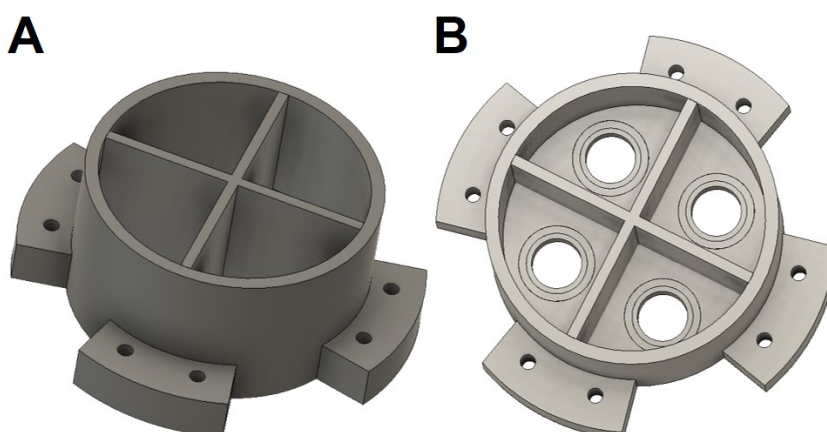


Figure 4-11 Design of the 3rd-generation 3D printed multi-electrode cell with (A) crossing walls dividing the beaker to (B) four identical yet separate WE wells.

Figure 4-12 shows the 3D printed multi-electrode cell that was used for histamine detection in mast cell supernatant, the results of which are presented in Paper II.



Figure 4-12 Assembled 3rd-generation 3D printed multi-electrode cell with 4 separate WE wells for static cell-based histamine measurements.

Chapter 5. Electrochemical Histamine Sensing

This chapter presents the state-of-the-art of electrochemical histamine sensing. The historical story of histamine discovery is also touched upon in this chapter. In addition, a brief review of different types of electrocatalysts for electrochemical hydrogen peroxide detection is included. Finally, the chapter is concluded with a short discussion of Prussian Blue structure and electrochemical properties as an electrocatalyst for hydrogen peroxide oxidation and reduction.

5.1 Histamine

Histamine is chemically classified as a 'biogenic' amine, an organic nitrogen-containing derivative of ammonia, which means that it is not only a natural constituent of human body, but it is also commonly found in animals, plants and other living organisms such as bacteria and fungi. For the first time, histamine was isolated from a plant fungus (ergot) by an English physiologist, Sir Henry Hallett Dale, in 1910. Dale *et al.* conducted fundamental animal studies to investigate the biological actions of histamine when injected as a stimulating drug to different organs of different species. Among others, they observed a shock-like reaction by animals to injected doses of histamine ¹⁵⁵. Further investigations led to identification of histamine in human liver and lung tissue extracts by Best *et al.* in 1927, and eventually the active role of histamine in allergy and anaphylactic shock were demonstrated ¹⁵⁶. These early discoveries on histamine actions in animals and the human body motivated other scientists to search for antihistamines at the same time as they were trying to understand histamine's chemical structure, origin and fate in the body. In 1952, Riley and West concluded that histamine is stored in tissue mast cells, as they observed a strong positive correlation between histamine content and tissue resident mast cell populations. Another experimental observation which supported their conclusion was that using the compound 48/80 as histamine release stimulator left behind disrupted mast cells ¹⁵⁷. Compound 48/80 is a polymer composed of p-methoxy-N-methyl phenylethylamine crosslinked by formaldehyde. It was first introduced by Paton in 1951 as histamine liberator ¹⁵⁸ and since then, it has been widely used as a selective mast cell stimulator in animal studies and tissue models for non-IgE-directed mast cell activation and degranulation ¹⁵⁹.

In 1956, Schayer described the formation and metabolic pathways of histamine in the body ¹⁶⁰. Both processes (formation and metabolism) are catalyzed by enzymes. Histamine is formed by the decarboxylation of the amino acid L-histidine catalyzed by histidine decarboxylase (HDC) enzyme. Histamine metabolism, which inactivates the histamine actions in the body, takes place in two ways either inside the cells or in the extracellular space. The intracellular pathway involves methylation of the imidazole ($C_3H_4N_2$) ring catalyzed by histamine N-methyltransferase (HMT) enzyme. The extracellular pathway entails oxidative deamination of the primary amino group (NH_2) by diamine oxidase (DAO) enzyme in the presence of molecular oxygen and water, which leaves behind histamine metabolites including imidazole-4-acetaldehyde ($C_5H_6N_2O$), ammonia (NH_3) and hydrogen peroxide (H_2O_2) ¹⁶¹. Histamine formation and metabolic pathways are illustrated in **Figure 5-1**.

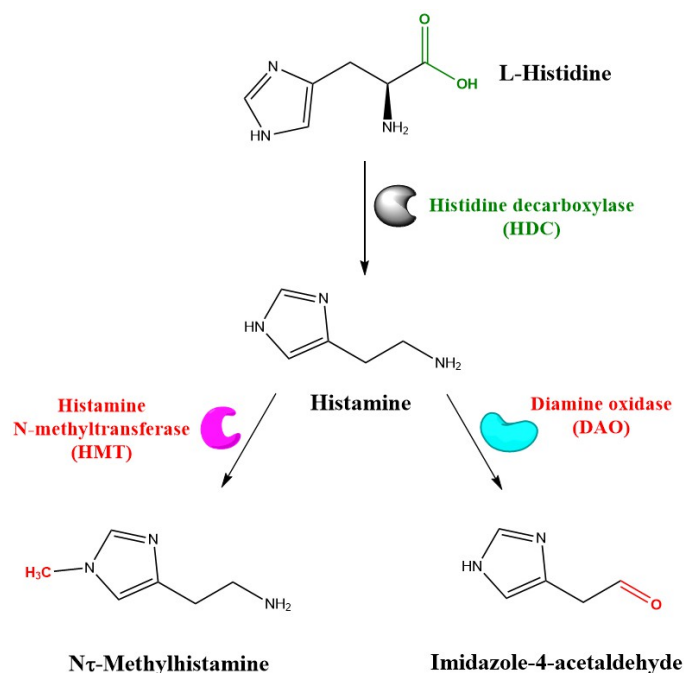


Figure 5-1 Physiological pathways of histamine formation from L-histidine and histamine metabolism catalyzed by DAO or HMT enzymes.

5.2 Historical Evolution of Electrochemical Histamine Sensors

The fundamental studies on histamine during the early 20th century have established the building blocks of the vast knowledge that we have today about the pathophysiological roles of histamine in anaphylaxis and allergy¹⁶², neurotransmission and brain functions¹⁶³, neurological diseases¹⁶⁴ such as sclerosis, schizophrenia, Alzheimer's and Parkinson's diseases^{165,166} as well as its key role in controlling gastric acid secretion¹⁶⁷. While histamine plays a pivotal role in regulating sleep-wakefulness cycles¹⁶⁸, a high level of histamine in the human body causes histamine poisoning. High levels of histamine can enter the bloodstream through the gastrointestinal tract by consumption of spoiled food. Histamine is formed in improperly preserved fish, cheese, wine, meat and fermented food due to uncontrolled bacterial growth^{169,170}. Therefore, the detection of histamine has relevance and importance for both biomedical and food quality control applications. Literature reporting electrochemical histamine detection in food samples are abundant^{170–183,183–193}. However, only the literature concerning the biomedical application of histamine sensors and biosensor is covered in this section.

As illustrated in **Figure 5-2**, the last two decades of the 20th century was the birth period of the first electrochemical sensors developed in the attempt to detect histamine. Prior to this date, the fluorometric assay had been widely utilized to measure the histamine released from tissue resident or isolated mast cells. In 1986, a Japanese group reported successful *in situ* detection of histamine liberated from mast cells by a constructed histamine-sensitive membrane electrode where the electric potential was measured versus an Ag/AgCl RE by potentiometry¹⁹⁴. About a decade later, the UK-based group of Loughran and Turner in collaboration with a US scientist developed an amperometric biosensor for the detection of histamine using electrodes built of graphite foils. The electrodes were modified by a bacterial enzyme, methylamine dehydrogenase (MADH), as the biorecognition element which catalyzes the oxidation of methylamine to formaldehyde and ammonia¹⁹⁵. In the same year

(1995), Pihel *et al.* succeeded in measuring histamine in real-time as it was released from a single rat peritoneal mast cell by implementing a carbon fiber microelectrode (CFME) at 1 μm distance from the cell ¹⁹⁶. Fast scan cyclic voltammetry (FSCV) with a triangle potential waveform from +0.1 to +1.4 V swiped at a scan rate of 800 V s^{-1} was used to analyze the electrochemical oxidation of histamine at the carbon fiber. The authors reported a primary anodic peak for histamine at +1.3 V vs saturated calomel electrode (SCE) and a secondary anodic peak at +0.9 V vs SCE.

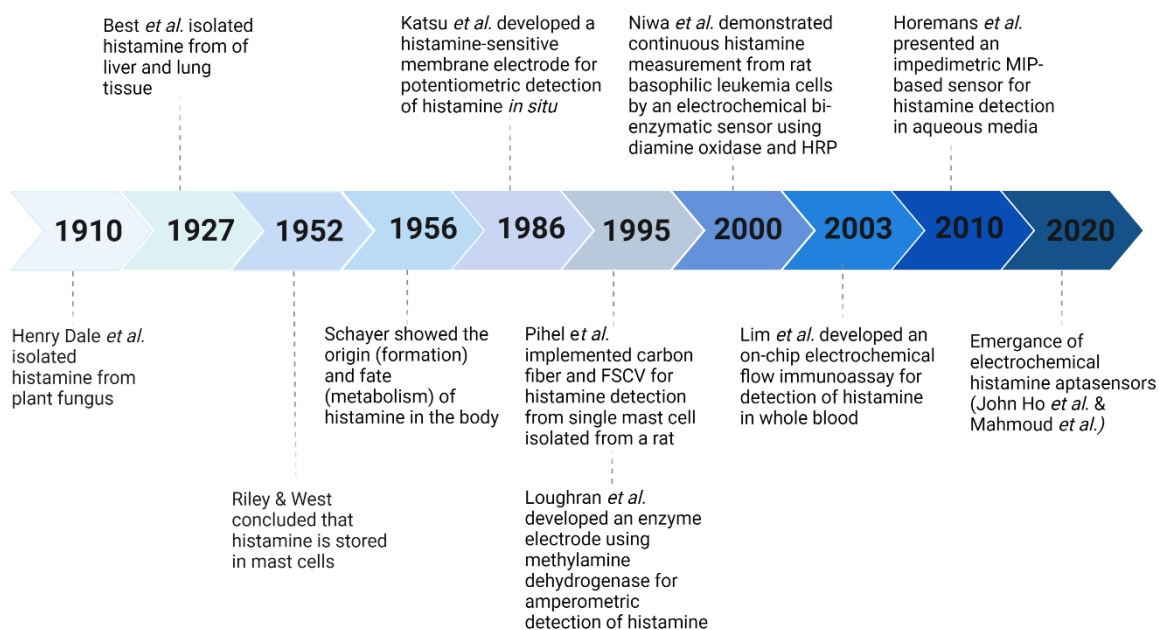


Figure 5-2 Timeline of histamine discoveries and electrochemical histamine sensors.

At the beginning of the new millennium, another Japanese group presented a bi-enzymatic histamine biosensor constructed by modifying a glassy carbon (GC) electrode with a bilayer composed of recombinant histamine oxidase (HO) and horseradish peroxidase (HRP) entrapped in bovine serum albumin (BSA) and osmium-gel respectively ¹⁹⁷. HO oxidizes histamine resulting in formation of H_2O_2 . HRP reduces the H_2O_2 at 0 V vs. Ag/AgCl. Having coupled the biosensor with a microfabricated capillary unit, they were able to sample the extracellular solution and to measure histamine continuously from a small mast cell colony. In another attempt, the same sensor was combined with a microdialysis sampling probe and used to measure histamine released from rat basophilic leukemia cells (RBL-2H3) down to concentrations of 23 nM ¹⁹⁷. In 2003, Lim *et al.* (Japan) proposed a microfabricated on-chip electrochemical flow immunoassay system with a multichannel matrix column where antigen-antibody complexes were separated from the unreacted antihistamine immunoglobulin G (IgG) antibody on the basis of differences in isoelectric points ¹⁹⁸. The flow-cell system was equipped with GC electrode, Pt CE and Ag/AgCl RE and was coated with a cation-exchange resin which enabled isoelectric separation of proteins. IgG antibody was conjugated with ferrocenemonocarboxylic acid (Fc) which oxidizes at 395 mV vs. Ag/AgCl. Histamine conjugated with BSA was added to the reaction mixture which competed with the target histamine in whole blood sample. When the mixture was passed through the multichannel matrix column, free Fc-IgG and histamine-Fc-IgG complex were selectively trapped, while the eluted species passed through the flow cell where the current due to oxidation of Fc on the histamine-BSA-Fc-IgG antibody complex at 395 mV was monitored. Histamine in concentration range of 200 – 2000 ng mL^{-1} (2 – 20 μM) was detected

in whole blood samples of symptomatic individuals allergic to cedar pollen. In the past decade, molecularly imprinted polymers (MIPs) have been investigated by different research groups for the detection of histamine mostly in food samples^{172,199}. MIP is an inert synthetic polymer with imprinted nanocavities that act as recognition element of a biosensor. The target molecule is used as template for imprinting nanocavities in the polymer. Horemans *et al.* (2010) mixed histamine with functional monomers. After the stabilization and eventual crosslinking of monomers, the histamine was removed from the polymer particles. A thin layer of another polymer, serving as immobilization layer for MIPs, was spincoated on aluminium electrodes. Then, the MIP particles were applied to the polymer by a stamp and thermally embedded in this layer. Nanocavities on MIP particles selectively rebind to histamine, changing the impedance of the sensor. At a frequency of 213 Hz, the impedimetric MIP-based sensor responded to 0-12 nM histamine in aqueous media²⁰⁰. In 2017, Akhoundian *et al.* incorporated MIPs into a carbon paste electrode and were able to detect histamine in spiked human serum samples²⁰¹. Cyclic voltammogramic responses to different concentrations of histamine were obtained in samples containing hexacyanoferrate (III) as mediator and the limit of detection (LOD) of 74 pM was achieved. Finally, histamine aptasensors are the newest class of electrochemical biosensors that have emerged in the more recent years²⁰²⁻²⁰⁴. Aptamers are synthetic DNA or RNA sequences randomly generated against a specific target molecule. Aptamers are immobilized on an electrode surface as a biorecognition element with selective affinity for the target molecule of interest. Mahmoud *et al.* (2020) constructed a dual-recognition MIP/aptasensor on a GC electrode and tested the response of the biosensor to histamine in blood plasma samples by two different techniques including differential pulse voltammetry (DPV) and electrochemical impedance spectroscopy (EIS) which yielded LODs of 0.15 and 0.11 nM respectively²⁰³. A few other examples of electrochemical histamine sensors and biosensors intended for biomedical applications are summarized in **Table 5-1**.

Table 5-1 Examples of electrochemical histamine sensors and biosensors for biomedical applications. *The values are converted from ng mL⁻¹ to molar concentrations for the sake of comparison.

Sensor type	Electro-chemical method	Electrode material	Linear range	LOD	Sample Matrix	Remarks	Reference
Direct oxidation	FSCV	CFMEs		1.4 μM	Physiological buffer containing Tris-HCl, NaCl, KCl, glucose, CaCl ₂ and MgCl ₂ pH 7.4	Histamine detection from single mast cells from rats at 1 μm distance from the cell surface	Pihel <i>et al.</i> 1995 ¹⁹⁶
Direct oxidation	LSV/CV	Boron-doped diamond thin-film	0.5 – 100 μM	1 μM	Phosphate buffer KH ₂ PO ₄ /K ₂ HPO ₄ pH 7.1		Sarada <i>et al.</i> 2000 ²⁰⁵
Direct oxidation	LSV	GC		10 μM	Phosphate buffer KH ₂ PO ₄ /K ₂ HPO ₄ pH 7.1		Sarada <i>et al.</i> 2000 ²⁰⁵
Direct oxidation	FIA/ Amperometry	Boron-doped diamond thin-film	0.5 – 100 μM	500 nM	Phosphate buffer KH ₂ PO ₄ /K ₂ HPO ₄ pH 7.1	Sensitivity: 4 nA μM ⁻¹	Sarada <i>et al.</i> 2000 ²⁰⁵
Direct oxidation	FIA/ Amperometry	Boron-doped diamond thin-film	1 – 40 μM	2.76 μM	Oxygenated Dulbecco modified Eagle's media (DMEM) high-glucose buffer solution pH 7.4	Direct measurement in segment of stomach tissue of male guinea pigs, Sensitivity: 0.25 nA μM ⁻¹	Bitziou <i>et al.</i> 2008 ²⁰⁶
Direct oxidation	FSCV	CFMEs	1 – 20 μM	1 μM	Tris-buffer pH 7.4 for <i>in vitro</i> studies	<i>In vivo</i> studies in mouse brain cells, sensitivity: 0.354 ± 0.032 nA μM ⁻¹	Samaranayake <i>et al.</i> 2015 ²⁰⁷
Direct oxidation	SWV	Electroactive polymer film (catalyst) on GC	5 – 200 μM*	0.28 μM	PBS pH 7	Measured spiked histamine in diluted human urine	Degefu <i>et al.</i> 2014 ²⁰⁸
Enzymatic (AO)	FIA/ Amperometry	Graphite modified by redox polymer	10 – 200 μM	2.2 μM	Phosphate buffer pH 7	Sensitivity: 6.8 mA M ⁻¹ cm ⁻²	Niculescu <i>et al.</i> 2000 ²⁰⁹
Enzymatic (MADH)	Amperometry	Graphite foil	0 – 200 μM	4.8 μM	Phosphate buffer pH 7.5 containing KCl		Loughran <i>et al.</i> 1995 ¹⁹⁵
Enzymatic (MADH)	Amperometry	Gold	25 μM – 4 mM	25 μM	Potassium phosphate buffer containing KCl pH 7.5		Zeng <i>et al.</i> 2000 ²¹⁰
Bi-Enzymatic (HO & HRP)	Amperometry	Carbon	0.1 – 100 μM	23 nM	PBS buffer and extracellular solution	Measured histamine release from a small colony of rat basophilic leukemia cells (RBL-2H3)	Niwa <i>et al.</i> 2000 ¹⁹⁷
Enzymatic (HO)	Amperometry	Carbon	28 – 2700 nM*	11.3 nM	Buffer and cell supernatant	Rat basophilic leukemia (RBL-2H3) cells	Iwaki <i>et al.</i> 2002 ²¹¹
Enzymatic (HmDH)	Amperometry	GC	2 – 30 μM	2 μM	Potassium phosphate buffer pH 7	Sensitivity: 0.17 μA μM ⁻¹ cm ⁻²	Yamada <i>et al.</i> 2008 ²¹²

Enzymatic (HmDH)	Amperometry	Cup-stacked carbon nanofibers on GC	0.3 – 300 μ M	0.1 μ M	Britton Robinson buffer pH 9.4	Measured histamine release from rat basophilic leukemia cell line RBL-2H3	Komori <i>et al.</i> 2021 ²¹³
Antigen-Antibody Affinity (immunosensor)	EIS	Ultra thin Graphene oxide	0.1 – 1 μ M	0.1 μ M	PBS buffer pH 7		Delle <i>et al.</i> 2015 ²¹⁴
Competitive Immunosensor	CV	Graphene	0.01 – 10 nM*	5 pM*	$\text{Fe}(\text{CN})_6^{3-/4-}$ solution containing KCl	Human serum	Yang <i>et al.</i> 2015 ²¹⁵
On-chip flow immunosensor	CV	GC	2 – 20 μ M*	2 μ M*	Whole blood	Histamine & cedar pollen allergen in whole blood were detected	Lim <i>et al.</i> 2003 ¹⁹⁸
MIP	EIS	Aluminium	0 – 12 nM	< 1 nM	Aqueous solution		Horemans <i>et al.</i> 2010 ²⁰⁰
MIP	EIS	Aluminium	0 – 12 nM	2 nM	PBS neutral pH	Performance of the sensor is pH dependent	Bongaers <i>et al.</i> 2010 ²¹⁶
MIP	EIS	Aluminium	0 – 400 nM	50 nM	PBS buffer pH 5	Analyzed histamine concentration of mildly acidic bowel fluid samples of several test persons	Peeters <i>et al.</i> 2013 ²¹⁷
MIP	CV	Carbon paste	0.1 – 7 nM* 7 – 400 nM*	74 pM*	Solution of hexacyanoferrate (III) and KCl	Histamine spiked to human serum samples were measured	Akhoundian <i>et al.</i> 2017 ²⁰¹
Histamine-selective membrane	Potentiometry	Poly(vinyl chloride) substrate		< 0.1 mM	Physiologically balanced salt solution containing NaCl, KCl, CaCl_2 , glucose and HEPES-NaOH	Measured secreted histamine from rat peritoneal mast cells	Katsu <i>et al.</i> 1986 ¹⁹⁴
Histamine-selective electroactive membrane	Potentiometry	Graphite	1 μ M – 100 mM*	0.5 μ M*	Aqueous solution	Sensor tested in synthetic serum sample	Amini <i>et al.</i> 1999 ²¹⁸
MIP/Aptasensor Dual-recognition	DPV	GC	0.46 – 35 nM	0.15 nM	Phosphate buffer containing $[\text{Fe}(\text{CN})_6]^{3-/4-}$ as redox probe	Detected histamine in human blood plasma	Mahmoud <i>et al.</i> 2020 ²⁰³
MIP/Aptasensor Dual-recognition	EIS	GC	0.35 – 35 nM	0.11 nM	Phosphate buffer containing $[\text{Fe}(\text{CN})_6]^{3-/4-}$ as redox probe	Detected histamine in human blood plasma	Mahmoud <i>et al.</i> 2020 ²⁰³

5.3 State-Of-The-Art of Electrochemical Histamine Sensing for Biomedical Applications

The state-of-the-art electrochemical histamine sensors are classified according to their types, applications, transduction techniques and electrode materials in a chart in **Figure 5-3**. In general, the majority of the published research in electrochemical histamine sensing can be divided into two main categories: i) chemical sensors recording the histamine oxidation directly on the electrode, ii) enzymatic biosensors detecting the histamine oxidation indirectly via monitoring of the metabolites of the histamine degradation by the enzyme.

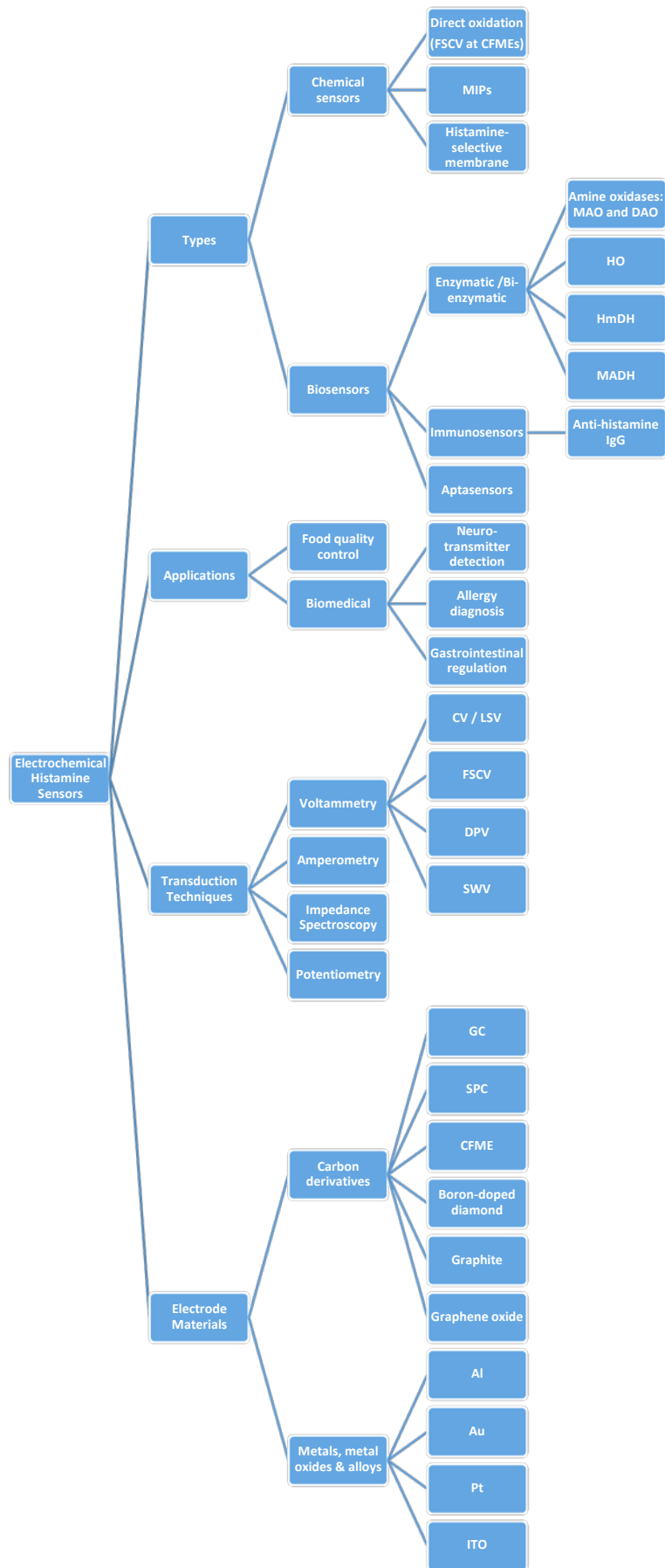


Figure 5-3 Overview of the state-of-the-art electrochemical histamine sensors.

Cyclic voltammetry and techniques related to it such as FSCV, linear sweep voltammetry (LSV), square wave voltammetry (SWV) and differential pulse voltammetry (DPV) are the electrochemical techniques used to develop chemical sensors for direct histamine detection, while amperometry combined with flow injection analysis (FIA) system is the most established technique for histamine detection by enzymatic biosensors.

Chemical Sensors

Among voltammetric techniques for direct histamine oxidation measurements, FSCV at CFMEs is the most frequently explored technique. In CV, constant sweeping of the potential causes a capacitive current, the amplitude of which is directly proportional to the area of the electrode (equation 2-11). When CV is performed on conventional electrodes such as 2D electrodes with an area of a few mm² for the detection of tiny traces of electroactive species in a complex sample, the capacitive background current masks the faradaic current from the redox reactions of the target species. In addition, the amplitude of the capacitive current increases with scan rate. At high scan rates (100 V s⁻¹ or faster) the amplitude of the capacitive current is much larger than the faradaic current²¹⁹. Therefore, ultramicroelectrodes having at least one dimension smaller than 25 μm such as Pt wires embedded in glass or resin and CFMEs are more convenient tools for the voltammetric detection of very low concentrations of electroactive substances. Electrochemical sensors relying on FSCV with CFMEs, pioneered by Wightman's group, have been utilized for *in vivo* studies of neurotransmitters including histamine^{220,221}. The FSCV technique has high sensitivity and rapid temporal response which makes it a versatile tool for real-time *in vivo* monitoring of exocytosis from a single cell²²². Two major challenges with these types of sensors are interference from substances in the sample that have similar oxidation peak potentials and electrode fouling which reduces the sensitivity²²³. Oxidation of histamine in aqueous solution at carbon electrodes requires a potential of at least 1.1 V vs Ag/AgCl²²⁴. At this potential, other molecules present in the biological samples such as H₂O₂ and tertiary amines also undergo oxidation²²³. Selectivity has been obtained by fine tuning the parameters of the potential waveform and introducing new waveform shapes^{223,225}. Histamine oxidation is an irreversible reaction and the oxidation product undergoes an oxidative electropolymerization on the carbon that fouls the electrode, reducing sensitivity of the sensor. Histamine oxidative electropolymerization has been explained and illustrated (**Figure 5-4**) by Puthongkham *et al.* who suggested Nafion coating of the carbon in order to alleviate the electrode fouling²²⁴.

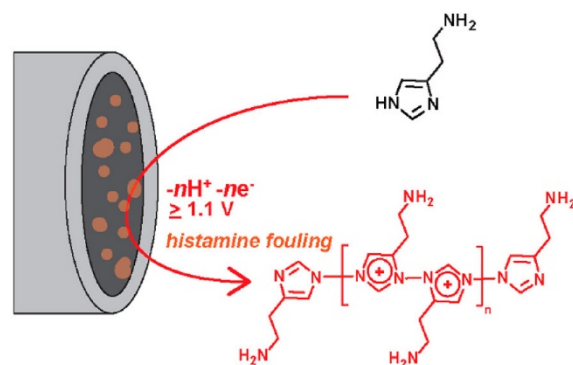


Figure 5-4 Mechanism of histamine oxidation and electropolymerization of the histamine oxidation product at carbon electrodes which fouls the electrode surface. Reprinted from reference ²²⁴.

Enzymatic Biosensors

Compared to the chemical sensors relying on direct histamine oxidation, enzymatic histamine biosensors show better selectivity and operate at lower potentials. Amine oxidases (AO) including monoamine oxidase (MAO) and DAO have been immobilized to construct electrochemical histamine biosensors ^{226–229}. They mediate oxidative deamination of histamine to imidazole-4-aldehyde and require copper and a quinone as cofactors. However, these enzymes are not specific to histamine. Other biogenic amines such as tyramine, putrescine and spermidine are catabolized by AOs ²³⁰. More histamine-specific enzymes including histamine oxidase (HO) ²¹¹, histamine dehydrogenase (HmDH) ^{213,231} and methylamine dehydrogenase (MADH) ²¹⁰ have been used. LODs in low μM -range comparable to those of chemical sensors were obtained. The major challenges with enzymes are loss of functionality when immobilized, a decline of the enzyme activity and poor stability when pH and temperature conditions are not optimal. Moreover, since the enzymatic histamine biosensors rely on the detection of the enzymatic reaction by-products, there is a need for additional electrode modification with another enzyme or an electrocatalyst that mediates the by-product oxidation or reduction. H_2O_2 is the by-product of histamine degradation by oxidases including DAO. In the following, the electrocatalysts for H_2O_2 detection are reviewed.

5.4 Electrocatalysts for Electrochemical Detection of H_2O_2

H_2O_2 is an electroactive molecule, which undergoes a two-electron reaction process at different pH levels and its oxidation or reduction can be studied quantitatively in real-time by electroanalysis ²³². An electrochemical H_2O_2 sensor converts the chemical reaction into an electrical signal proportional to the amount of oxidized or reduced H_2O_2 in the sample. Non-electrocatalytic or direct detection of H_2O_2 redox is straightforward and effortless, but it has major impediments. Due to slow electron transfer kinetics at most electrode materials, high over-potential is required to overcome the H_2O_2 oxidation potential and drive the reaction ²³³. A highly conductive and noble electrode material is required to facilitate the electron transfer while at the same time it is not oxidized itself. On a Pt electrode, H_2O_2 is oxidized at potentials above +0.6 V vs Ag/AgCl ²³⁴. At this potential, many other

species in biological samples such as uric acid, ascorbic acid and bilirubin also undergo oxidation, which causes interference and compromises selectivity²³². Moreover, the amplitude of the H₂O₂ reduction current on Pt electrodes is 10 times lower compared to the current produced due to oxygen reduction, meaning that the detection of H₂O₂ by its reduction in the presence of oxygen is practically impossible²³⁵.

In order to accelerate the electron transfer kinetics, to lower the required over-potential for H₂O₂ redox reaction and to minimize the possible interference in sensing, electrodes have been modified with a number of electrocatalysts (see **Figure 5-5**) including biological catalysts found in nature (e.g. enzymes)²³⁶ and synthetic ones (e.g. alloys, metal complexes, etc.)²³⁷⁻²³⁹. A number of non-enzyme proteins as well as redox enzymes such as horseradish peroxidase (HRP)^{240,241}, catalase^{242,243} and heme proteins (e.g. hemoglobin, myoglobin, etc.)²³⁶ have been immobilized to mediate the electron transfer between H₂O₂ and the electrode.

The advantage of using enzymes and non-enzyme proteins as bioelectrocatalysts is their very high selectivity and good sensitivity to low concentrations of H₂O₂. However, the bottleneck problems associated with using protein based and enzymatic electrocatalysts are: (i) high cost of proteins and enzymes, (ii) instability, denaturation and loss of catalytic activity with changes in temperature, pH, humidity and the electrolytes in the measuring buffer, (iii) loss of catalytic activity due to wrong orientation of the enzyme during immobilization, (iv) time-consuming sensor preparation protocols and (v) low reproducibility due to all above mentioned reasons in addition to the difficulty of long-term storage^{233,236}.

Research has been focused on designing efficient electrocatalysts with abundant active sites that can maximize the charge transfer at the electrode surface. Noble metals such as Au, Pt and Pd, and their alloys (e.g. AuAg, PtPd) in the form of nanostructures and nanoparticles^{238,244-248}, metal oxides (MnO₂, TiO₂, etc)²⁴⁹ and metal complexes (ferric hexacyanoferrate, metallophthalocyanines, etc)²⁵⁰, organic and polymeric materials such as redox dyes and conductive polymers²⁵¹ as well as carbon-based nanomaterials (carbon nanotubes, graphene, doped carbon, etc)²⁵² have been explored as H₂O₂ catalysts. Moreover, different nanostructures such as nanoparticles, nanowires, nanotubes, nanofibers and free-standing 3D structures have been developed for more efficient electrocatalytic performance resulting in more sensitive H₂O₂ detection^{253,254}. Often the aforementioned nanomaterials are incorporated onto the surface layer of an electrode to create a sensing element for detection of H₂O₂. Increased active surface area, enhanced electron transfer kinetics and low over-potential are the common advantages of the tailored nanomaterials. As a result, highly sensitive sensors with LODs down to a few nM have been developed. However, each of these materials and composites has its own pitfall.

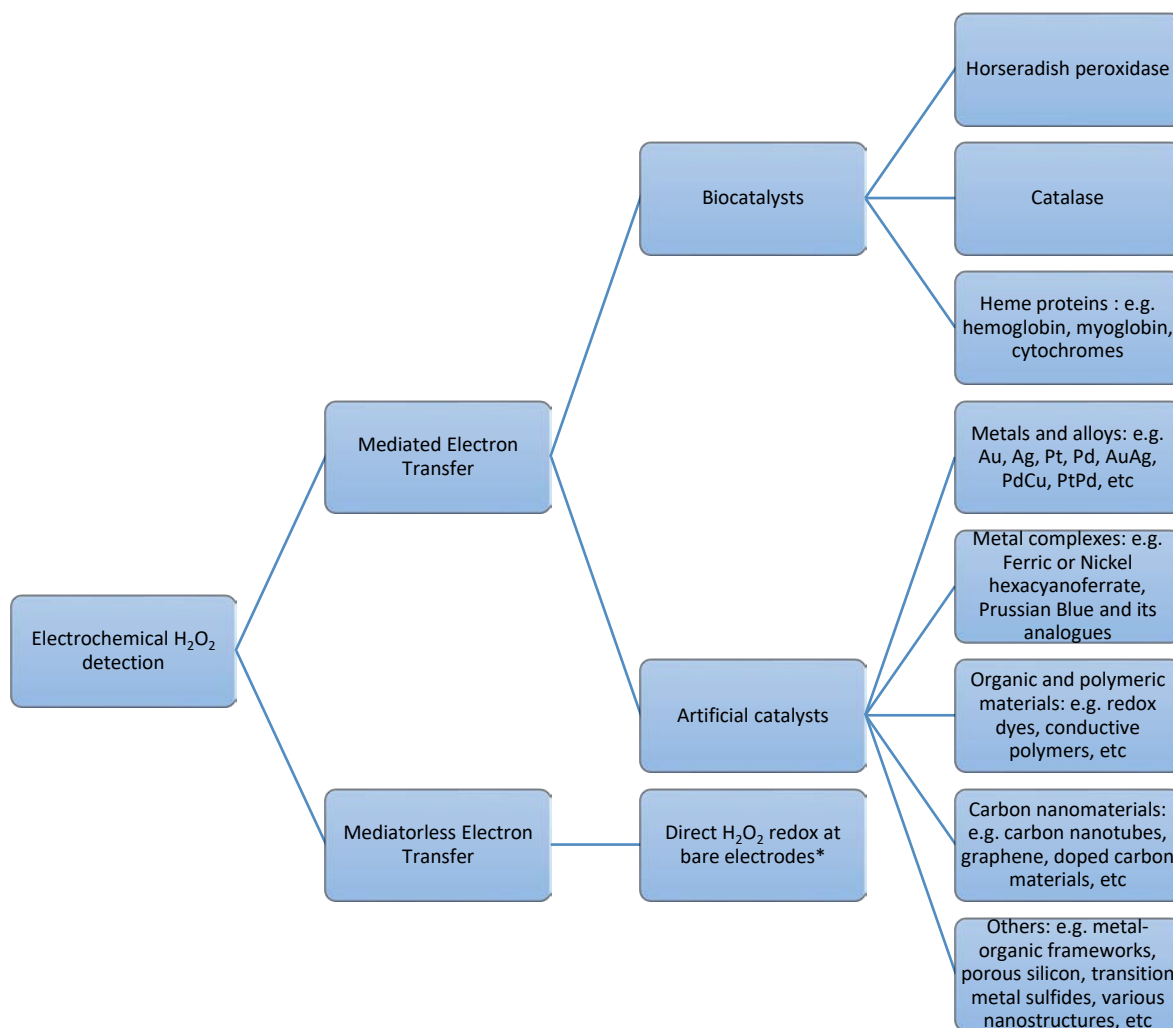


Figure 5-5 Overview of electrochemical H₂O₂ detection methods and electrocatalysts. * Reduction detection in the presence of O₂ is impossible and oxidation happens only at high over-potentials, causing large parasitic anodic current.

Noble metals such as Au and Pt are excellent conductors and charge collectors and due to their low toxicity, high surface area and rich surface functionalization chemistry they are generally good sensing materials which enhance the electrochemical performance. The electrochemical H₂O₂ sensors based on the bimetallic/alloys are more sensitive than the monometallic sensors. Slow kinetics and fouling as the result of adsorption at bare metals make these types of sensors less sensitive. Apart from their short supply and high cost, noble metals and their alloys/bimetallic nanoparticles suffer from lack of specificity^{232,238}.

Transition metals and transition metal oxides, such as cobalt oxide, copper oxide, manganese oxide, exhibit good electrocatalytic activity towards H₂O₂ as they are able to have multiple oxidation states and adsorb other substances onto their surface^{255–258}. Various nanostructures of these materials have

been synthesized, which have the advantages of enhanced mass transport, unique electrical and chemical properties such as high current density and good wettability in aqueous samples. The morphology of porous oxide layers can be controlled during synthesis to tailor pore size and connectivity and increase the surface area. With these advantages, sensors based on transition metal oxides display fast electron transfer kinetics, low background charging current and high sensitivity, but usually require high over-potential as catalysts ²³².

Carbon nanomaterials, such as carbon nanotubes, and other carbon derivatives, in particular graphene have been immensely exploited for sensing applications either as substrate material or as electrocatalyst. Excellent electrical and thermal conductivities, large specific surface area, inert electrochemistry and wide potential window have established carbon-based nanomaterials as promising sensing elements. High specific active surface area as well as interconnected and multiple electron paths provide unique catalytic properties and significant improvement in sensitivity of the sensor ^{237,252,259,260}.

Despite the abundance and the low price of carbon, the main limiting factor in using carbon-based nanomaterials as electrocatalysts mediating H₂O₂ oxidation/reduction is the need for a suitable base electrode, which can support the binding of the separately produced electrocatalysts. In most cases, the carbon-based electrocatalysts are synthesized in a separate process than the base electrode, which means that they have to be transferred and incorporated onto the substrate electrode. Polymeric binders enable adhesion between particles, but this complicates the fabrication process, increases the cost and reduces the stability and reproducibility of such sensors. Increased internal resistance, blocked active sites and interfering side reactions during electrochemical measurements are other undesirable aspects of using polymeric binders ^{237,252,259,261,262}.

Conducting polymers have also been used to modify metallic and carbon-based electrodes to lower the over-potential required for H₂O₂ oxidation/reduction at the electrode/electrolyte interface. Modification of electrodes with organic or inorganic polymers or poly-electrolytes can take place by self-assembly. In fact, the sensitivity of such sensors highly depends on how well the polymer attaches to the electrode surface. A good binding and firm attachment of the polymer to the electrode surface is essential for mediating the redox transformations of H₂O₂. The shape, the morphology and the material of the base electrode and its compatibility with the type of polymer defines the quality of the binding. Moreover, the selectivity of these sensors relies on the exclusion mechanism of the polymer. The ability of the polymer layer to exclude other molecules than H₂O₂ either by size or by charge-repulsion determines the selectivity of the sensor. Conductive polymers have also been employed as supporting substrate for decorating electrodes with other electrocatalytic nanomaterials. However, the major drawback of using organic or inorganic polymers as redox mediator is the time-consuming and complicated sensor construction process. Toxic materials are also not suitable for the sensors developed for biomedical applications such as cell-based measurements ²⁵¹.

Among the metal complexes, Prussian blue (PB) and its analogues, which is a metal hexacyanoferrate, have been extensively used as an electrocatalyst for oxidation/reduction of H₂O₂ ^{235,263–265}. The reduced form of PB, which is called Prussian white (PW), catalyzes the reduction of O₂ and H₂O₂ at very low potential (0 V versus Ag/AgCl) ²⁶⁶. Furthermore, the oxidized form of PB, known as Berlin Green (BG), has a catalytic activity for the oxidation of H₂O₂ at potentials above 0.6 V versus Ag/AgCl ²⁶⁷. Efficiency-wise, the catalytic activity of PB has been reported to be more than 1000 times higher compared to Pt ²³⁵ and of similar order of magnitude as the enzyme peroxidase ²⁶⁸. Since 1999, when the mechanism of H₂O₂ reduction at PB was explained for the first time by Karyakin *et al.* ²⁶⁹, numerous examples of electrochemical sensors and biosensors based on PB have emerged ^{264,270–272}. Biocompatibility of PB justifies its use as a suitable candidate for the field of clinical analysis. PB can

harmlessly pass through the body and it has been approved by U.S. Food and Drug Administration (FDA) as antidote for thallium poisoning²⁷³. Electrodes can be modified with PB by electrodeposition which requires minimal equipment. The low cost and ease of synthesis of PB makes it an ideal electrocatalyst for commercialization and mass production of H₂O₂ sensors. While there are numerous examples, where thin films of PB have been deposited on electrodes of different materials such as Au²⁷⁴, Pt²⁷⁵, GC^{276,277} and screen-printed carbon (SPC)^{270,278}, there has not been any example of depositing PB on pyrolytic carbon for H₂O₂ sensing application.

5.5 Prussian Blue Crystal Structure and Electrochemical Properties

PB is a metal complex with a face-centered cubic lattice structure containing low-spin (Fe²⁺) and high-spin (Fe³⁺) iron atoms with cyanide bridges in between. Historically, the terms ‘soluble’ and ‘insoluble’ were used to denote the PB structure with and without intercalated potassium (K⁺) ions respectively²⁶⁴. The atomic composition ratio of Fe³⁺/Fe²⁺ in the synthesized PB film determines its electrochemical properties and stability. This ratio is nearly 1 in soluble PB and larger than 1 in insoluble form where one quarter of the Fe²⁺ sites is missing²⁷⁹. The vacancies in the insoluble PB are occupied by water molecules coordinated to octahedral Fe³⁺ atoms²⁸⁰. **Figure 5-6** shows the lattice structure of the insoluble form of PB.

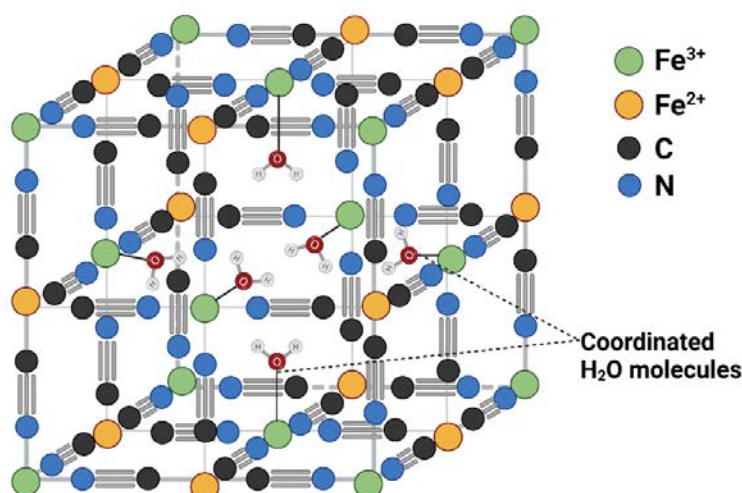


Figure 5-6 Face-centered cubic lattice structure of the ‘insoluble’ PB with coordinated water molecules. Created with Biorender.com

The zeolitic structure of the PB can also accommodate uncoordinated water molecules and alkali ions such as Na⁺ or K⁺²⁸¹. While K⁺ promotes the electrochemical activity of PB, all group II cations such as Na⁺, H⁺ and Ca²⁺ have blocking effects²⁸². The structure of the soluble PB in its reduced state contains only the Fe²⁺ atoms (all Fe³⁺ are reduced to Fe²⁺) and the reversibly intercalated K⁺ ions which compensate the charge as depicted in **Figure 5-7**. The open framework of the PB only allows the low-molecular-weight species such as O₂ and H₂O₂ to diffuse into the lattice gap where they are reduced^{283,284}. The catalytic activity of PB for the H₂O₂ reduction was reported to be about 100 times greater than its catalytic activity towards O₂²⁸⁵. The combination of low potential and size-exclusion of interfering molecules identifies PB as a highly selective electrocatalyst for H₂O₂ reduction such that it is also known as ‘artificial peroxidase enzyme’²⁸⁶.

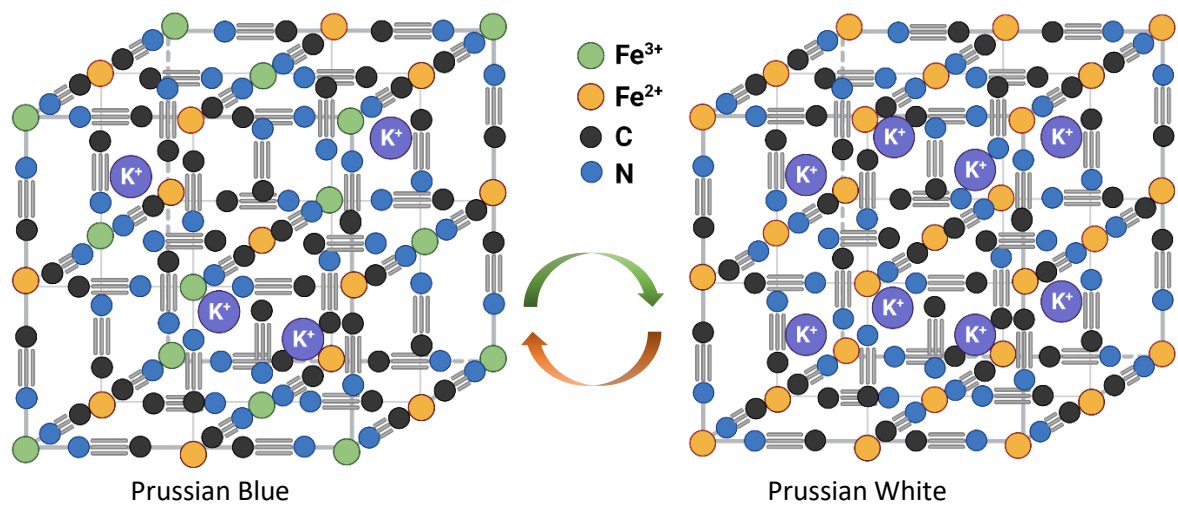


Figure 5-7 Lattice structure of 'soluble' PB and its reduced form PW with reversibly intercalated K⁺ ions.
 Created with Biorender.com

Chapter 6. Enzymatic Histamine Biosensing with Prussian Blue-Modified Pyrolytic Carbon Microelectrodes

This experimental chapter starts by presenting the design of the enzymatic biosensor for histamine detection and the overall strategy for its optimization. Next, the optimized protocols for the biosensor construction, including the Prussian Blue electrodeposition and enzyme immobilization, are described. Additionally, the results of a few pre-studies of enzymes are included.

6.1 Biosensor Design

Based on the discussions of the previous chapter, the aim was to rather design a biosensor for histamine detection by pyrolytic carbon than a chemical sensor. Like GC, the oxidation of histamine directly at the pyrolytic carbon was observed at a potential of 1.2 V, which could easily drive the co-oxidation of interfering biomolecules. FSCV with the pyrolytic carbon microelectrodes was neither possible as the large surface area of the microelectrode (26.2 mm²) caused a large charging current which masked the small faradaic current from histamine oxidation, making the detection of histamine in nM and μ M range nearly impossible.

Therefore, it was decided to develop an enzymatic biosensor using DAO as the receptor for histamine, and a non-enzymatic electrocatalyst in the form of PB for H₂O₂ detection. Commercially produced DAO was easily accessible from different source organisms such as bacteria, yeasts, various plants, and animals. Modification of microelectrodes with PB was also simple, required minimal equipment and had the scalability potential. The mechanism of quantitative histamine measurement with the constructed enzymatic biosensor is schematically demonstrated in **Figure 6-1**.

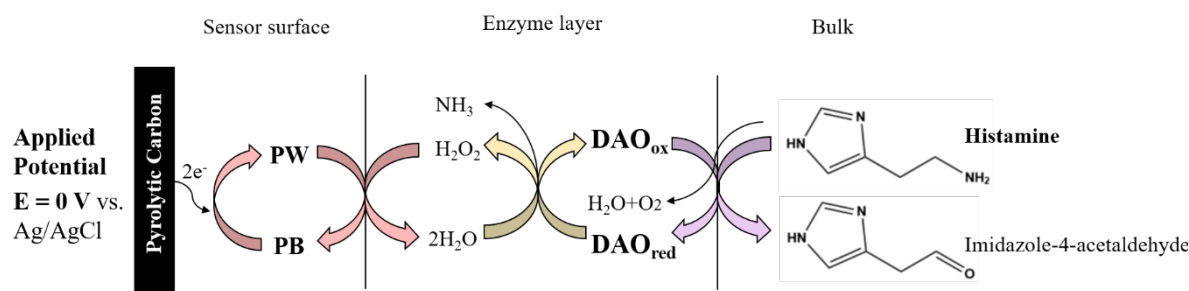


Figure 6-1 Mechanism of histamine detection with PB/DAO-modified pyrolytic carbon microelectrodes.

In an aqueous solution, histamine is oxidized to imidazole-4-acetaldehyde in the presence of dissolved molecular oxygen (O₂) by DAO as a result of which, H₂O₂ and NH₃ are produced. At an applied potential of 0 V vs Ag/AgCl, PB film is at its reduced form (PW) which catalyzes the reduction of H₂O₂ to water. PB and all its redox forms act as 3D electrocatalysts where small molecules can diffuse rapidly in and out. H₂O₂ is able to diffuse into the PW zeolitic structure through the open channels of about 0.32 μ m²⁸⁷ and is completely reduced to water before diffusion out of the crystal. Upon reduction, each H₂O₂ molecule gains two electrons from the PW film causing its partial oxidation to PB. Regeneration of the PW film generates a reduction current which passes through the external circuit, is recorded by the potentiostat and used for quantification of the histamine present in the sample.

6.2 Biosensor Optimization Strategy

To detect histamine in range of 200-600 nM, the designed biosensor was optimized in several steps. The flow chart in **Figure 6-2** illustrates the approach to biosensor optimization. In the first place, the PB film electrodeposition on pyrolytic carbon microelectrodes was optimized for the sake of reproducibility. A detailed description of the PB film electrodeposition optimization can be found in Paper I included in Appendix A. Secondly, electrochemical H₂O₂ detection with the PB-modified

electrodes was established by stirred batch amperometry. The results of amperometric H_2O_2 detection are also presented in Paper I. Next, to improve the H_2O_2 detection limit with PB, a novel electrochemical method was developed as an alternative for stirred batch amperometry. The novel electrochemical H_2O_2 measurement method, which was a combination of potentiometry and chronoamperometry, is described in Paper II in Appendix B. Thereafter, the procedure of enzyme immobilization on the PB-modified pyrolytic carbon microelectrodes was optimized. For this purpose, stirred batch amperometry was implemented as the standard method. The results are included in Paper II. Then, the histamine detection in buffer was established using the alternative method of measurement plus the optimized PB electrodeposition and enzyme immobilization protocols. The obtained results are discussed in Paper II. Eventually, the electrochemical detection of the histamine released from activated mast cells was also demonstrated by the optimized biosensor in Paper II.

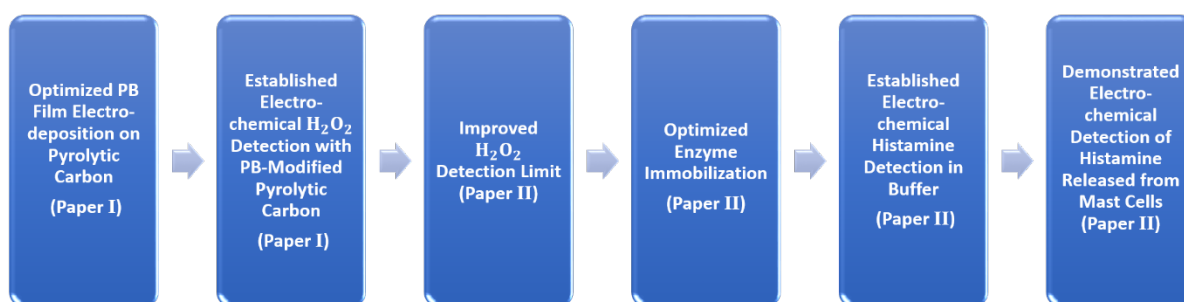


Figure 6-2 Process of optimizing the designed enzymatic biosensor for histamine detection.

Table 6-1 gives an overview of the electrochemical techniques, WEs and electrochemical setups used in each step of the biosensor optimization procedure. The optimized experimental protocols for the preparation of the biosensor are provided in the following sections. The outcome of a few preliminary studies that were conducted on the DAO enzymes obtained from animal and plant sources are also included at the end of this chapter.

Table 6-1 Electrochemical techniques, WEs and setups used in each step of biosensor optimization process

Procedure	Electrochemical Techniques	Working Electrode	Electrochemical Cell
Optimization of PB Film Electrodeposition on Pyrolytic Carbon (Paper I)	Chronoamperometry Cyclic Voltammetry	2D pyrolytic carbon single-electrode chips 3D pyrolytic carbon single-electrode chips	2 nd generation 3D printed multi-electrode cell with magnetic stirring
Electrochemical H ₂ O ₂ Detection with PB-Modified Pyrolytic Carbon (Paper I)	Stirred Batch Amperometry	2D pyrolytic carbon single-electrode chips 3D pyrolytic carbon single-electrode chips	5 mL glass cell with printed cap
Improvement of H ₂ O ₂ Detection Limit (Paper II)	Developed a novel method: combination of Open Circuit Potentiometry and Chronoamperometry	3D pyrolytic carbon single-electrode chips	5 mL glass cell with printed cap
Optimization of Enzyme Immobilization (Paper II)	Stirred Batch Amperometry	3D pyrolytic carbon single-electrode chip	5 mL glass cell with printed cap
Electrochemical Histamine Detection in Buffer (Paper II)	Combination of Open Circuit Potentiometry and Chronoamperometry	3D pyrolytic carbon single-electrode chips	5 mL glass cell with printed caps
Electrochemical Detection of Histamine Released from Mast Cells (Paper II)	Combination of Open Circuit Potentiometry and Chronoamperometry	3D pyrolytic carbon single-electrode chips	3 rd generation 3D printed multi-electrode cell with separate compartments for static measurements

6.3 Prussian Blue Film Electrodeposition

Traditionally, PB film was either formed chemically on electrode surfaces by co-precipitation of ferrocyanide, $[\text{Fe}^{2+}(\text{CN})_6]^{4-}$, and ferric ions (Fe^{3+})²⁸⁸ or by electrodeposition of ferricyanide, $[\text{Fe}^{3+}(\text{CN})_6]^{3-}$, and ferrous ions (Fe^{2+}) from an aqueous solution containing equimolar amounts of potassium ferricyanide, $\text{K}_3\text{Fe}(\text{CN})_6$, and ferric chloride (FeCl_3)^{235,268,289}. Metal and semiconductor substrates such as Pt, Au, GC, graphite and SPC have been modified by PB films using the aforementioned methods^{266,271,277,290–297}. Novel methods that were more recently exploited include self-assembly^{276,298}, template-assisted²⁹⁹, aerosol deposition²⁷⁵, hydrothermal processes³⁰⁰ and oxidative print light synthesis³⁰¹.

Efforts to modify the pyrolytic carbon with PB films by the co-precipitation method at room temperature from an aqueous solution of potassium ferrocyanide and ferric chloride were not successful. On the contrary, electrodeposition of PB films on pyrolytic carbon was reproducible and H₂O₂ detection with the PB-modified pyrolytic carbon electrodes was successfully demonstrated.

As mentioned earlier, a detailed description of the PB film electrodeposition procedure on the pyrolytic carbon, its optimization process and the obtained results can be found in Paper I included in Appendix A. What follows here is an overview of the optimized procedure illustrated in **Figure 6-3**, **Table 6-2** and **Table 6-3**.

Figure 6-3 displays the setup used for the batch preparation of PB-modified pyrolytic carbon microelectrodes. The setup consists of (A) a 3D-printed cell with four pyrolytic carbon electrodes in the bottom placed on a compact magnetic stirrer, (B) a potentiostat for initiating the electrodeposition by applying a potential and (C) a computer connected to the potentiostat for monitoring the results.

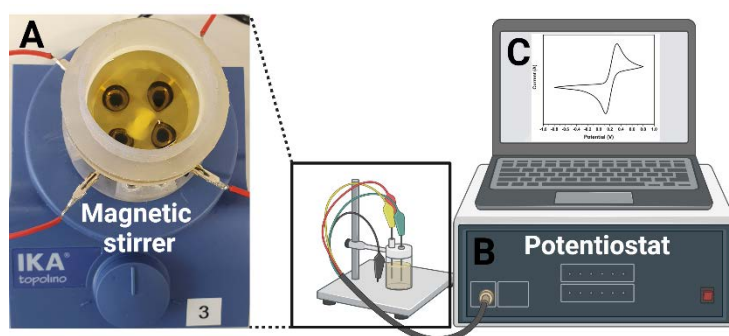


Figure 6-3 Setup used for the batch preparation of PB-modified pyrolytic carbon microelectrodes consisting of A) 3D-printed multi-electrode cell on magnetic stirrer; B) potentiostat; C) computer for monitoring the process.

The modification process of pyrolytic carbon with PB film consisted of six steps³⁰²:

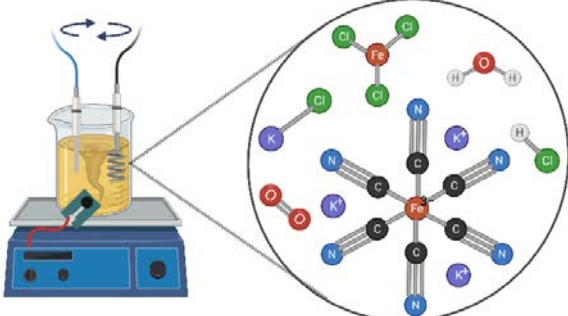
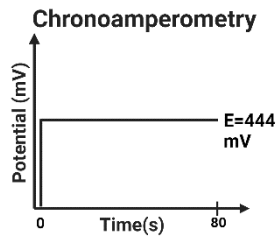
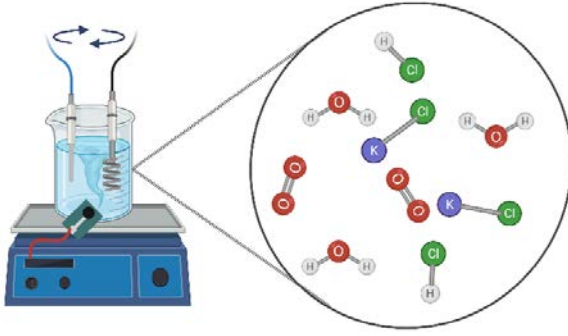
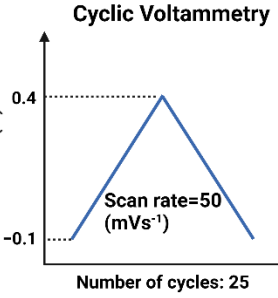
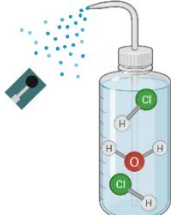
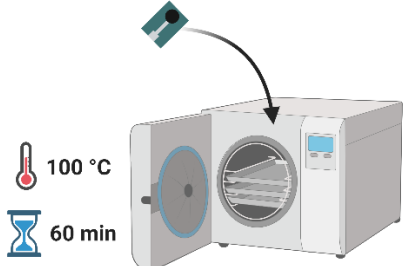
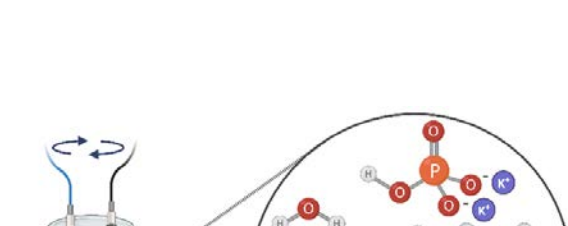
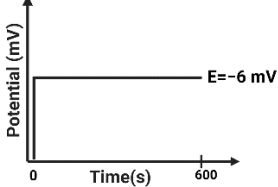
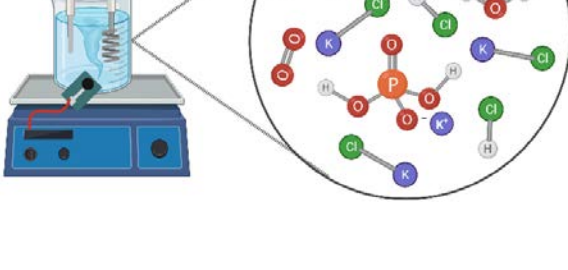
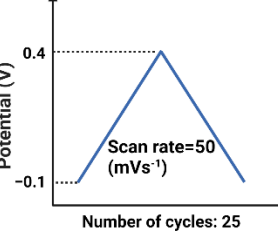
1. Electrodeposition of the PB from the growth solution
2. Activation of the PB film in salt solution
3. Rinsing of the electrodes to remove the salt residues
4. Annealing of the PB film
5. Conditioning
6. Stabilization in phosphate buffer

The chemical solutions required in each step are listed in **Table 6-2**. The procedures applied upon the pyrolytic carbon microelectrodes including the modes and the parameters implemented by the potentiostat in each step are schematically illustrated in **Table 6-3**.

Table 6-2 Requirements including chemical solutions for each step of electrode modification with PB film.

	1. Electro-deposition	2. Activation	3. Rinsing	4. Annealing	5. Conditioning	6. Stabilization
Requirements	2.5mM FeCl_3 2.5mM $\text{K}_3\text{Fe}(\text{CN})_6$ 0.1M KCl 0.1M HCl	0.1M KCl 0.1M HCl	0.1M HCl	Convection oven / Furnace	0.05M K_2HPO_4 0.05M KH_2PO_4 0.1M KCl pH adjusted to 5.5 using HCl	0.05M K_2HPO_4 0.05M KH_2PO_4 0.1M KCl pH adjusted to 5.5 using HCl

Table 6-3 Procedures and parameters applied to the microelectrodes in each step of PB film synthesis.

Step	A: Applied to the Pyrolytic Carbon Microelectrode	B: Applied by the Potentiostat
1) Electro-deposition	 <p>The diagram shows a microelectrode in a beaker with a yellow solution, connected to a potentiostat. A circular inset shows the chemical structure of Prussian Blue, a complex of iron (Fe), nitrogen (N), carbon (C), and potassium (K) ions.</p>	<p>Chronoamperometry</p>  <p>Potential (mV) vs Time (s). The potential is constant at $E=444$ mV for 80 seconds.</p>
2) Activation	 <p>The diagram shows a microelectrode in a beaker with a blue solution, connected to a potentiostat. A circular inset shows the chemical structure of Prussian Blue, a complex of iron (Fe), nitrogen (N), carbon (C), and potassium (K) ions.</p>	<p>Cyclic Voltammetry</p>  <p>Potential (V) vs Number of cycles: 25. The scan rate is 50 (mVs⁻¹). The potential ranges from -0.1 V to 0.4 V.</p>
3) Rinsing	 <p>The diagram shows a microelectrode being rinsed with water from a bottle.</p>	NA
4) Annealing	 <p>The diagram shows a microelectrode being placed in an oven. The temperature is 100 °C and the time is 60 min.</p>	NA
5) Conditioning	 <p>The diagram shows a microelectrode in a beaker with a blue solution, connected to a potentiostat. A circular inset shows the chemical structure of Prussian Blue, a complex of iron (Fe), nitrogen (N), carbon (C), and potassium (K) ions.</p>	<p>Chronoamperometry</p>  <p>Potential (mV) vs Time (s). The potential is constant at $E=-6$ mV for 600 seconds.</p>
6) Stabilization	 <p>The diagram shows a microelectrode in a beaker with a blue solution, connected to a potentiostat. A circular inset shows the chemical structure of Prussian Blue, a complex of iron (Fe), nitrogen (N), carbon (C), and potassium (K) ions.</p>	<p>Cyclic Voltammetry</p>  <p>Potential (V) vs Number of cycles: 25. The scan rate is 50 (mVs⁻¹). The potential ranges from -0.1 V to 0.4 V.</p>

The electrode modification process was monitored by keeping the recorded current under surveillance in each step. **Figure 6-4 A** shows the current transient recorded during the PB electrodeposition from the growth solution which contained equimolar amounts of $K_3Fe(CN)_6$ and $FeCl_3$. The mixture of $K_3Fe(CN)_6$ and $FeCl_3$ has a yellowish color (see the solution inside the cell in **Figure 6-3 A**) and is chemically stable unless a potential of about 400 mV vs. Ag/AgCl is applied upon it to reduce the Fe^{3+} ions of $FeCl_3$ to Fe^{2+} , which in a one-to-one combination with $[Fe^{3+}(CN)_6]^{3-}$ ions form the PB crystal. Duncan *et al.* suggested that in fact Turnbull's blue is synthesized in this way, which has the same structure as the PB³⁰³. The recorded negative current was indicative of Fe^{3+} reduction to Fe^{2+} at the electrode surface during the 80 s of electrodeposition at an applied potential of 444 mV vs Ag/AgCl. It was observed that the convection created by the magnetic stirring could enhance the electrodeposition. Acidic environment (pH 1-2) was also essential for a good electrodeposition. The acidity of the growth solution is required to prevent hydrolysis of Fe^{3+} by hydroxyl (OH^-) ions instead of cyanide bridges (CN). Hydrolysis results in irregular and unstable PB film²³⁵.

While some studies^{234,266,304} suggested that adding KCl to the growth solution is essential for charge compensation, others³⁰⁵ suggested that KCl should be avoided in the growth solution as its presence weakens PB films. In fact, postulates on the structure of the freshly electrodeposited PB film are contradictory. According to Itaya *et al.*, the freshly electrodeposited PB is of insoluble form³⁰⁶, whereas Buser *et al.* claimed that the formation of purely insoluble PB film in the presence of even slightest amount of K^+ ions is impossible³⁰⁷. Perhaps, the crystalline structure that is formed during the film electrodeposition is a hybrid between the soluble and the insoluble PB. As mentioned before, the soluble form of PB has reversibly intercalated K^+ ions in its open lattice structure. Thus, it can be concluded that the insoluble PB was transformed to the soluble form during the activation step by cycling in KCl solution at scan rate of 50 mV s^{-1} in the potential window between -0.1 and +0.4 V vs Ag/AgCl where the reversible redox reaction of high-spin irons $Fe^{3+/2+}$ occurs. The K^+ ions are essential for charge compensation upon PB reduction²³⁵. The cathodic peak of the cyclic voltammogram in

Figure 6-4 B depicts the PW formation. It was observed that the cathodic peak slightly increased after each cycle indicating the progressive transformation of the insoluble PB into the soluble PB. Wang *et al.* concluded that probably a composition intermediate between the insoluble and soluble PB is obtained after 30–50 cycles³⁰⁴.

I. Oh *et al.* proved that 56% (w/w) of the fresh PB film is water³⁰⁸. Moreover, studies^{281,308,309} suggest that the complex 3D network of PB films might contain chloride impurities and occluded ions such as free $Fe(CN)_6^{4-}$. It has been confirmed quantitatively that the transformation of the insoluble PB film to soluble form is an irreversible process, in which free anions and some of the water molecules are lost meanwhile K^+ ions enter the PB film structure³⁰⁸. During the annealing, more water molecules exit the PB structure leading to a more stabilized film on the electrode.

According to a study by Mattos *et al.* of the PB film stability on GC, conditioning the film at -50 mV vs SCE (-6 mV vs Ag/AgCl) for 600 s in KCl-containing phosphate buffer (pH 5.5) after drying would improve its stability³⁰². The current transient in **Figure 6-4 C** recorded during the conditioning step, shows that after a few seconds of applying the reducing potential, the curve reached a stable plateau at 0 V indicating null passing current. Although the reason for this empirical observation has not been investigated or explained in detail, one can argue that keeping the PB film at this potential ensures

the full structural transformation from the insoluble to soluble form. At this potential, all Fe^{3+} ions are reduced to Fe^{2+} while K^+ ions enter the structure to maintain the electroneutrality of the film. The null passing current indicates that the PW was fully formed after a few seconds, leaving no high spin irons in the film structure. The cyclic voltammogram (**Figure 6-4 D**) obtained in the same buffer after conditioning the film displays highly reproducible PB/PW redox peaks confirming that a reasonably stable film structure was obtained.

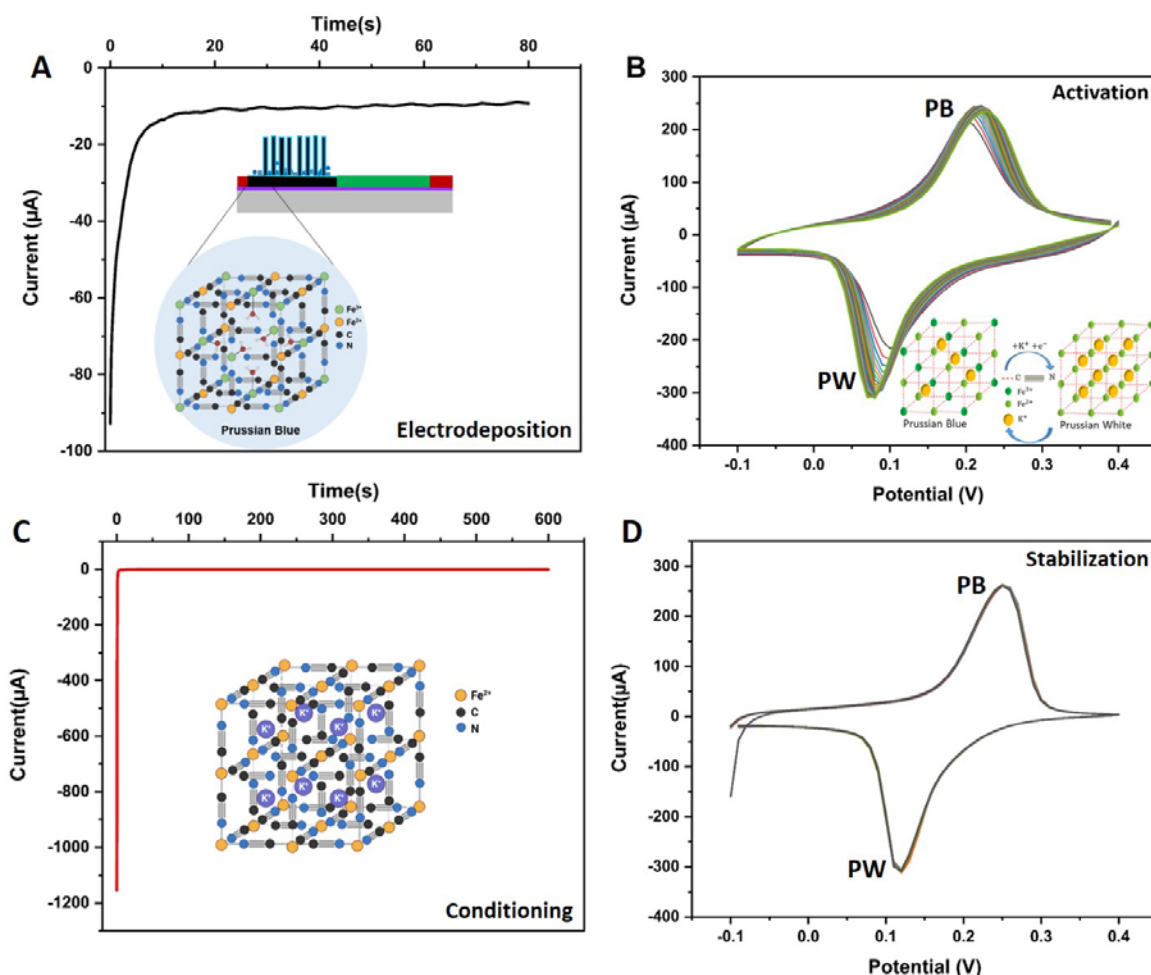


Figure 6-4 Currents recorded by the potentiostat to monitor the electrode modification process in A) PB film electrodeposition, B) film activation, C) conditioning and D) stabilization steps.

Literature suggests that the electrodeposited PB film is most stable in acidic conditions, and at pH values higher than 6.4 PB shows very low stability which is believed to be caused by the strong interaction between ferric ions and hydroxyl ions (OH^-) leading to destruction of PB and leakage from the electrode surface²⁸⁷. The same was confirmed empirically about the electrodeposited PB films on the pyrolytic carbon. Stability of the PB film was evaluated in KCl-containing phosphate buffer at different pH values between 5.5 and 7.4 by cyclic voltammetry. PB film on the pyrolytic carbon was most stable in phosphate buffer pH 5.5. The results can be found in Paper I in Appendix A. KCl-containing phosphate buffer with pH adjusted to 5.5 was selected as the working solution for H_2O_2 detection.

6.4 Enzyme Layer Construction

Unlike PB, most enzymes have optimum pH around the neutral or in the basic range, and the activity of the enzymes is declined in acidic environment. Before constructing the enzyme layer on the PB-modified pyrolytic carbon, a preliminary study was conducted on two commercially available DAO products to evaluate their activity and functionality at pH 5.5, the ideal pH for PB. In addition, the products were assessed in terms of their content and purity for immobilization. The outcome of the pre-studies on enzymes are presented and discussed in this section.

Diamine Oxidase selection

DAO was formerly named 'histaminase' as it was initially believed to catalyze only the histamine oxidation. But the name was changed as it became evident that the enzyme is able to catalyze the oxidative deamination of other primary amines. It is also known as 'copper-containing amine oxidase' as it belongs to the family of amine oxidase enzymes which require copper as a cofactor. The copper atom is essential for catalytic oxidation of amines at the active site of the enzyme. Moreover, the amine oxidation reaction is facilitated by another organic cofactor identified as 2,4,5-trihydroxyphenylalanine quinone (topa quinone, TPQ) which serves as the site of substrate binding. DAO can be found in different species including bacteria, fungi, various plants, animals, and human. The best known DAO enzymes for research use have been purified from lentil (*Lens esculenta*) and pea (*Pisum sativum*) plants, also from the kidney, intestine and placenta of mammals^{310–313}.

In this Ph.D. project, commercially available DAO enzymes from two different source species were characterized and compared for biosensor construction. Solid DAO from porcine kidney and liquid DAO from *Pisum sativum* were provided by Sigma-Aldrich (Denmark) and IBEX Pharmaceuticals (Canada) respectively. DAO is a homodimer of two identical subunits composed of 642 amino acids in total. The crystal structure of DAO enzyme from *Pisum sativum* is schematically demonstrated in **Figure 6-5**. According to the suppliers, each subunit of DAO from *Pisum sativum* had a nominal molecular weight of 73 ±3 kDa, and the molecular weight of each subunit of DAO from porcine kidney was 87 kDa. Enzymatic activity of DAO from *Pisum sativum* was reported to be 2672 units per mL while the activity of DAO from porcine kidney was ≥ 0.05 unit per mg of solid enzyme. One active unit was defined as being able to oxidize 1.0 μmole of putrescine per hour at pH 7.2 at 37 °C.

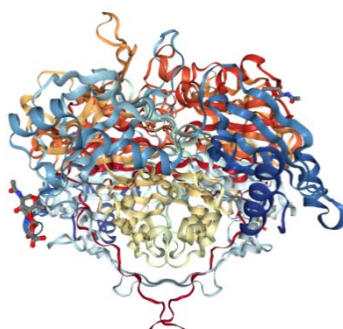


Figure 6-5 Crystal structure of a eukaryotic (pea seedling) copper-containing amine oxidase at 2.2 Å resolution³¹⁴.

The most favorable pH for the activity of DAO from *Pisum sativum* is 7.2, and in the range between 6.3 and 7.4 for the DAO from porcine kidney. The enzymatic activity of both DAO products towards histamine at pH 5.5 and 7.2 was evaluated by a fluorometric assay. Moreover, spectrophotometry was performed to assess the protein concentration of the purchased DAO products.

Spectrophotometric determination of protein concentration

In terms of energy, the electromagnetic wave can be seen as a beam of energy particles, known as photons. When a protein molecule adsorbs a photon, energy-wise it is elevated to an excited state. As it can be seen in the electromagnetic spectrum of **Figure 6-6 A**, the molecule can go through rotation, vibration, electronic excitation and ionization as the energy of the adsorbed photon is increased. In spectrophotometry, the absorbance of visible light and the ultraviolet radiation by the sample is studied. The energy of the photon (E) has a direct relation with the frequency (ν) of the electromagnetic wave:

$$E = h\nu \quad 6-1$$

where h is Planck's constant. The energy has also an inverse relation with the wavelength (λ):

$$E = h\frac{c}{\lambda} \quad 6-2$$

where C is the speed of light in vacuum. When visible light travels through a medium, its speed is reduced to C/n with n being the refractive index of the medium. Matters other than vacuum have refractive index larger than 1, meaning that the visible light propagates more slowly through almost all matters than through the vacuum. During the traverse, the wavelength of the transmitted light changes, while the frequency remains constant. When the protein molecules in the medium adsorb the photons of light, the intensity (I_0) of the incident beam, which is defined as the energy per second per unit area of the light beam, drops. **Figure 6-6 B** demonstrates the main components of a spectrophotometer, where visible light from a continuous source is passed through a monochromator, which selects a narrow band of wavelengths from the incident beam. The monochromatic light passes through a cuvette with a light path length (l) of 1 cm. The cuvette is filled with a solution containing the sample. If some of the light is absorbed by the sample, the transmitted light will have a lower intensity (I) than the initial value. Beer-Lambert's law describes the key principle of the spectrophotometry as a relation between the optical density (OD) or absorbance (A) and the concentration (c) of the light-absorbing species in the sample:

$$A = \epsilon lc \quad 6-3$$

where ϵ is the molar absorptivity or extinction coefficient which has the units of $M^{-1} cm^{-1}$. Since l , the light path length is expressed in cm and c is usually given in moles per liter (M), the absorbance is a dimensionless value. Molar absorptivity of a substance is an indication for the degree of light absorption at a certain wavelength. Proteins normally absorb ultraviolet radiation at the wavelength of 280 nm. To analyze the absorbance of a compound by spectrophotometry, the intensity of the monochromatic light that traverses a reference cuvette containing pure solvent or blank buffer is measured and defined as I_0 in the first place. Next, the reference cuvette is replaced by the sample-containing cuvette and the intensity of the light after passing through the sample is measured by the detector and nominated as I . Transmittance (T) is defined as the fraction of the light that passes through the sample cuvette and strikes the detector:

$$T = \frac{I}{I_0} \quad 6-4$$

The pure solvent or the blank buffer usually absorbs some light. In addition, the reference cuvette usually causes minor absorbance, reflection and scattering of light. By measuring the light intensity as it goes through the reference cuvette, we compensate for the non-zero baseline. If no light is absorbed by the sample, transmittance is at maximum, meaning that the intensity of the light after passing through the sample-containing cuvette is equal to the baseline intensity ($I = I_0$). Absorbance can be also obtained by:

$$A = \log\left(\frac{I_0}{I}\right) \quad 6-5$$

Given the extinction coefficient of the light-absorbing substance in the sample and the path length of 1 cm, the concentration is calculated by applying the absorbance value to equation 6-3.³¹⁵⁻³¹⁷

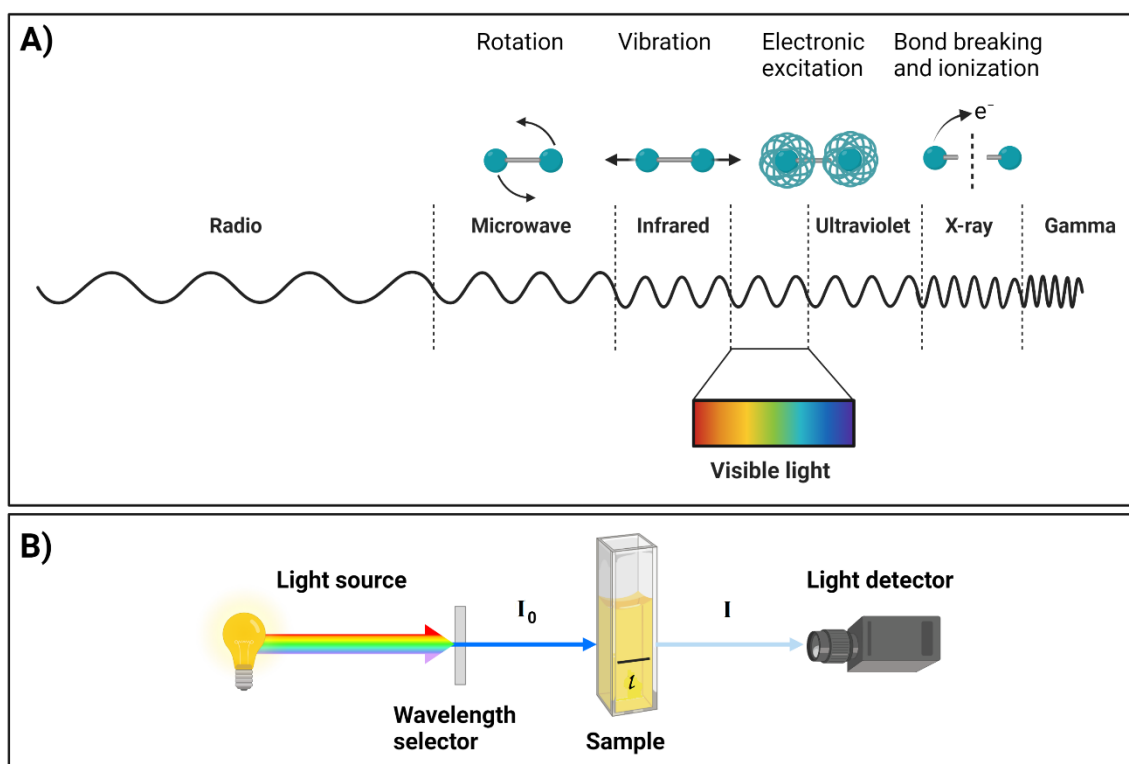


Figure 6-6 Schematic illustration of spectrophotometry; A) Electromagnetic spectrum and molecular excitation states when absorbing a photon of light in each region of the spectrum, B) main components of a spectrophotometer. Created with Biorender.com

For the determination of protein concentration of DAO products, a 10 mg mL⁻¹ solution of DAO from porcine kidney was prepared in PBS. Thereafter, tenfold serial dilutions (1:10, 1:100) were made by adding 100 μ L of DAO stock solution to 900 μ L PBS. The DAO from pea plant was received in liquid form and the concentration was unknown. Therefore, the enzyme solution as it was received was used as the stock and was diluted in PBS to prepare the tenfold serial dilutions such as it was done for DAO from porcine kidney. Furthermore, PBS was used as blank and BSA standard as reading control. 1 mL of each sample was applied in cuvettes, and OD or absorbance at 280 nm was gained 3 times for each sample by the spectrophotometer.

The plot in **Figure 6-7 A** shows the average OD values obtained for each enzyme dilution. Obviously, the 1:10 dilutions which contain more proteins absorb more light than the 1:100 dilutions. Knowing the percent solution extinction coefficient ($\epsilon_{percent}$) of DAO from porcine kidney which is $12.8 \text{ (g/100mL)}^{-1} \text{ cm}^{-1}$, the protein concentration of the diluted enzyme samples were calculated in terms of mg mL^{-1} by implementing an adjustment factor of 10 to Beer-Lambert's law as follows:

$$\text{concentration in } \frac{\text{mg}}{\text{mL}} = \left(\frac{A}{\epsilon_{percent}} \right) \times 10 \quad 6-6$$

Equation 6-6 was also used to calculate the protein concentration of the diluted DAO samples from the plant. Since the extinction coefficient of the DAO from *Pisum sativum* was unknown, its $\epsilon_{percent}$ was assumed to be approximately 10. This is a common practice for obtaining a rough estimation of protein concentration of a sample whose extinction coefficient is unknown, as most protein extinction coefficients ($\epsilon_{percent}$) range from 4.0 to 24.0³¹⁸. As the bar plots in **Figure 6-7 B** demonstrate, the protein concentration of 1:100 and 1:10 dilutions of the plant-derived DAO were about 0.1 and 1 mg mL^{-1} respectively. Taking the dilution factors into account, the concentration of the stock solution of DAO from the plant was estimated to be 10 mg mL^{-1} . From the protein concentration values obtained for the dilutions of DAO from porcine kidney, the actual amount of protein in the 1 mL stock solution appeared to be between 5-8 mg, even though a 10 mg mL^{-1} solution was prepared. This result revealed that the solid DAO product from porcine kidney contained some other substances in addition to the enzyme. Comparison of the OD and the estimated protein concentrations of 1:10 dilutions of the two DAO products indicates that the DAO product from the plant (*Pisum sativum*) contains more enzyme than the DAO from porcine kidney.

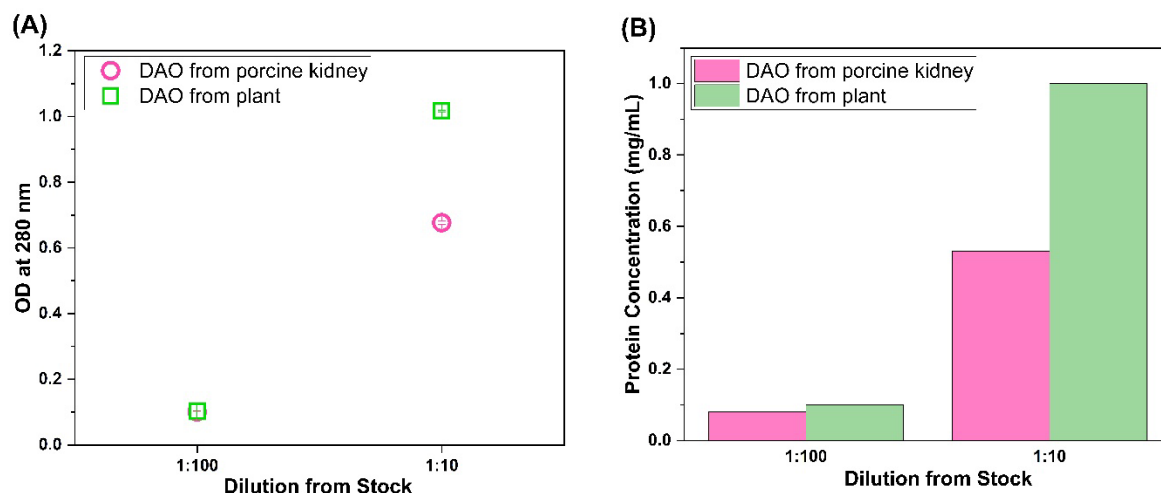


Figure 6-7 Spectrophotometric characterization of commercial DAO products from porcine kidney and *Pisum sativum* by determination of (A) optical density or absorbance of the samples at wavelength of 280 nm and (B) protein concentrations of tenfold dilution series.

DAO activity and histamine degradation at different pH levels

Fluorometry, which is based on the same principle as spectrophotometry, was used to evaluate the enzyme activity in different pH conditions. Fluorometry enables quantitative analysis of biological analytes that either are naturally fluorescent or are labeled with dyes that only emit fluorescence

when the analyte is bound to the target of interest. Fluorophores absorb light of a specific excitation wavelength (from ultraviolet region to visible light spectrum) and emit light of reduced energy and longer wavelength (from visible light to the near infrared region). Fluorometers measure the fluorescent intensity, which correlates with the number of biomolecules within the sample.³¹⁷

In this experiment, a fixed amount of fluorescently labelled histamine was mixed in tubes with different concentrations of DAO from the porcine kidney (supplied by Sigma-Aldrich) and the plant-derived DAO (supplied by IBEX Pharmaceuticals) such that the final concentrations were as listed below from 1 to 4:

- 1) 1000 $\mu\text{g mL}^{-1}$ DAO + 250 ng mL^{-1} Histamine
- 2) 100 $\mu\text{g mL}^{-1}$ DAO + 250 ng mL^{-1} Histamine
- 3) 10 $\mu\text{g mL}^{-1}$ DAO + 250 ng mL^{-1} Histamine
- 4) 1 $\mu\text{g mL}^{-1}$ DAO + 250 ng mL^{-1} Histamine
- 5) PBS + 250 ng mL^{-1} Histamine

Both the DAO and the histamine solutions were prepared in PBS at two different pH levels; pH 5.5 which was most favorable for the PB and pH 7.2 optimal for the enzyme activity. The samples were incubated at 37°C for 1 hour in Eppendorf tubes, and thereafter were loaded in duplicates in a microtiter plate coated with glass microfibers which adsorb the undegraded histamine³¹⁹. **Table 6-4** shows the design of the 96-well microtiter plate, which included blanks (PIPES buffer + 7% HClO_4) and histamine standards (std) too. Control samples containing histamine mixed with blank PBS at different pH levels (number 5 in the above list) were also included in the plate design. After another 30 minutes of incubation at 37°C, the plate was washed and the amount of adsorbed histamine in each well was measured fluorometrically by a HISTAREADER® (RefLab).

Table 6-4 Plate design for the assessment of DAO activity and histamine degradation at different pH levels.

Blank	Blank	Blank	Blank	Blank	Blank	Blank	Blank	Blank	Blank	Blank	Blank
Blank	Blank	Blank	Blank	Blank	Blank	Blank	Blank	Blank	Blank	Blank	Blank
std	1	1	1	1	1	1	1	1	x	x	x
std	2	2	2	2	2	2	2	2	x	x	x
std	3	3	3	3	3	3	3	3	x	x	x
std	4	4	4	4	4	4	4	4	x	x	x
std	5	5	5	5	5	5	5	5	x	x	x
std	PBS pH 7.2	PBS pH 7.2	PBS pH 5.5	PBS pH 5.5	PBS pH 7.2	PBS pH 7.2	PBS pH 5.5	PBS pH 5.5	x	x	x
	DAO (porcine/Sigma) in PBS pH 7.2		DAO (porcine/Sigma) in PBS pH 5.5		DAO (plant/IBEX) in PBS pH 7.2		DAO (plant/IBEX) in PBS pH 5.5				

The graph in **Figure 6-8** was constructed by averaging the amounts of adsorbed histamine measured in duplicates for each DAO product. The amounts of adsorbed histamine indicate how well the different concentrations of each DAO enzyme were able to degrade histamine at pH 5.5 and pH 7.2.

As it can be seen from the control samples (histamine in blank PBS, shown as 0.0 $\mu\text{g mL}^{-1}$ DAO concentration on the graph), about 55-65 ng mL^{-1} histamine was adsorbed in the absence of enzymes. The amounts of adsorbed histamine in the wells where histamine was incubated with 1 $\mu\text{g mL}^{-1}$ of porcine DAO product from Sigma, did not show any difference from those of the control samples. On the contrary, 1 $\mu\text{g mL}^{-1}$ of the plant DAO from IBEX was able to degrade some histamine at both pH levels, which can be seen on the graph as a slight decrease in the amounts of adsorbed histamine relative to the controls. While 10 $\mu\text{g mL}^{-1}$ of plant DAO at the ideal pH (7.2) was able to degrade more than half of the histamine, porcine DAO required a tenfold increase in the concentration to be able to break down a similar amount of histamine at optimal pH. Moreover, 1000 $\mu\text{g mL}^{-1}$ of the plant DAO at pH 5.5 degraded nearly the entire histamine, whereas the porcine DAO lost its activity considerably in acidic PBS.

In conclusion, the obtained results indicated that the plant DAO product from IBEX Pharmaceuticals contained more active enzymes than the porcine DAO from Sigma-Aldrich. These results confirmed the outcome of the spectrophotometry experiment which suggested that a 10 mg mL^{-1} plant DAO solution contained more active enzyme than a porcine DAO solution with a similar concentration. Additionally, plant DAO was able to maintain its activity to a remarkable degree at a non-optimal pH in the acidic range. However, larger amount of enzyme was required at pH 5.5 to degrade histamine compared to the case where the pH was near neutral.

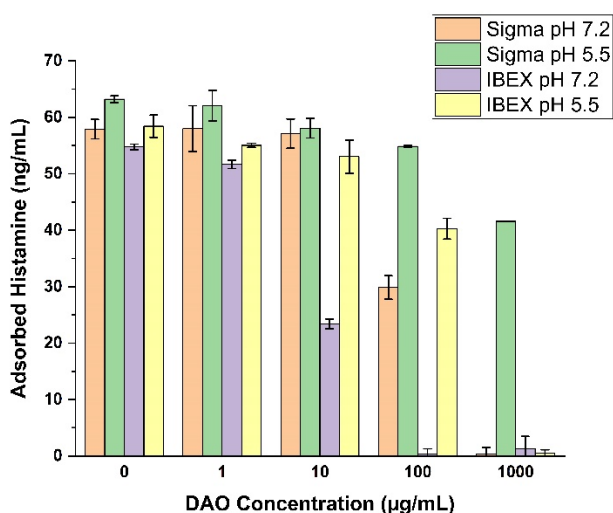


Figure 6-8 Results of fluorometric assessment of DAO activity at different pH levels, presenting the concentration of undegraded histamine adsorbed to the glass microfibers in a microtiter plate as a function of DAO concentration.

Evaluation of DAO purity by gel electrophoresis

Since the results of spectrophotometry and enzyme activity test indicated that DAO from porcine kidney might contain fewer active enzymes and more impurities than the plant DAO, gel electrophoresis was performed to evaluate the purity of the two DAO products.

Sodium dodecyl sulfate-polyacrylamide gel electrophoresis (SDS-PAGE) was performed in which negatively charged proteins are forced to move through gel pores by an applied electric field, and thereby are separated according to their molecular weight. As illustrated in **Figure 6-9**, the method is roughly comprised of three main steps including: A) sample preparation and loading onto a

polyacrylamide gel, B) electric field application to the gel and protein separation, and C) protein staining and gel analysis.

Sample preparation contains heating the proteins with SDS to 95 °C for 5 minutes, or alternatively 70 °C for 10 minutes. SDS is an ionic detergent, which destructs complex interactions in protein structures and causes protein denaturation. Heating helps to break the hydrogen bonds in the secondary and tertiary structures of the proteins. Reducing chemicals might be added to the sample buffer to cleave the disulfide bridges. In brief, proteins unfold and are negatively charged in the presence of SDS at high temperatures during the sample preparation step. Then, when the sample is cooled down to room temperature, it is loaded onto a dedicated well in the polyacrylamide gel, which was previously immersed in electrophoresis buffer in the electrophoresis apparatus. In addition to the samples, proteins of known molecular weights which serve as size markers are usually loaded onto the first or the last well of the gel. The molecular weight size markers allow the estimation of the sizes of the proteins in the actual samples, and thereby the protein content of the samples can be identified.

Thereafter, the power supply is connected, and an electric field is applied to the gel. Typically, the gel is in a vertical position in the electrophoresis chamber with anode (positive electrode) placed at the bottom and cathode (negative electrode) at the top. In response to the electric field, the negatively charged and denatured protein molecules move through the gel towards the positive electrode. Polyacrylamide gel acts like a sieve and determines how fast the proteins move through its matrix. Different proteins are separated based on their size and molecular weight. Large-molecular-weight molecules are slowed down in regions of the gel with a higher percent concentration, while smaller protein molecules migrate to the bottom of the gel.

For the analysis of the gel, the proteins are either stained in the gel (analytical coloring) or transferred to a membrane and detected with antibodies (western blotting). Staining is required because proteins are not detected in visible light, and the dye allows for visualization of the separated proteins.³²⁰

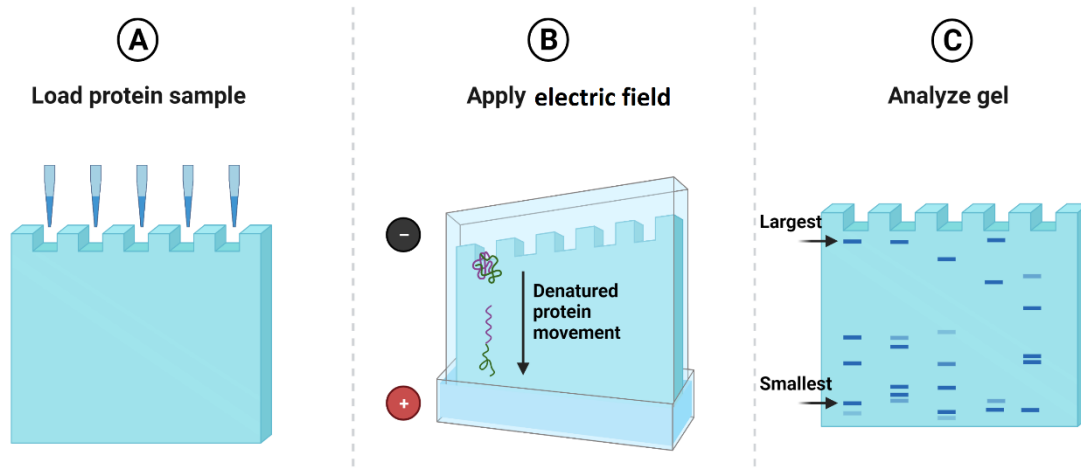


Figure 6-9 Schematic illustration of SDS-PAGE procedure. Created with Biorender.com

In the designed SDS-PAGE analysis in this project, two different batches (named DTU & LMA) of DAO from porcine kidney supplied by Sigma-Aldrich and a batch of plant DAO from *Pisum sativum* supplied by IBEX Pharmaceuticals were evaluated in terms of their enzyme purity for immobilization purpose. The gel containing the separated proteins from DAO products is displayed in **Figure 6-10**. The samples

were stained with blue dye for visual analysis. The colored ladders going down along the first well to the left are the molecular weight size markers. Two concentrations were tested per each enzyme product; dark blue ladders contained 25 μg protein per well and light blue ladders contained 2.5 μg protein per well.

As mentioned before, DAO from *Pisum sativum* has a molecular weight of about 146 kDa, and DAO from porcine kidney has a molecular weight of 170 kDa. As it can be seen, both products from Sigma and IBEX contained DAO ($\sim 146\text{-}170$ kDa), though the batches of enzyme from porcine kidney (DTU, LMA) supplied by Sigma had a significant number of impurities of lower molecular weight proteins. The product derived from *Pisum sativum* plant supplied by IBEX had remarkably more active DAO enzymes and less impurities compared to the products derived from porcine kidney.

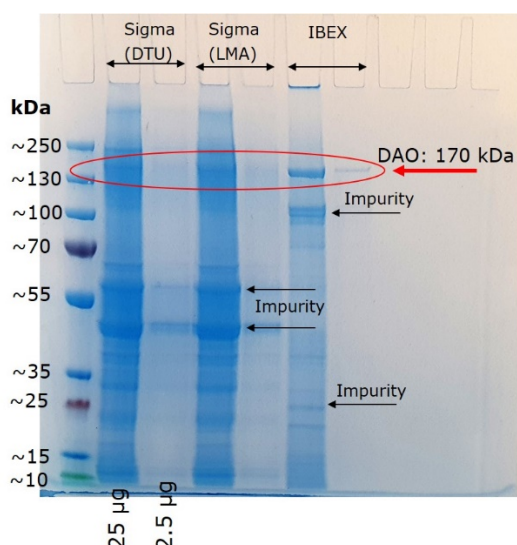


Figure 6-10 DAO enzyme purity test by SDS-PAGE analysis.

In conclusion, it was decided to use the DAO from *Pisum sativum* plant for immobilization and construction of histamine biosensor, as the product had more active enzymes and less impurities compared to the DAO from porcine kidney. Moreover, the enzymatic activity of the product was sufficiently preserved at pH 5.5 which was optimal for PB stability.

DAO immobilization

After the pyrolytic carbon WE on the microfabricated electrode chips described in chapter 3 was modified with a thin film of PB, 10 mg mL^{-1} DAO from *Pisum sativum* in a PBS solution containing 0.5% BSA as the spacer molecule and 1% glutaraldehyde (GA) as the cross-linker^{321,322}, was drop-cast on the electrode and left for 30 minutes at room temperature (22-25°C) to dry and immobilize. The schematic illustration of the constructed enzymatic biosensor can be seen in Figure 6-11. Then, the biosensors were rinsed with PBS to remove the unbound molecules, and were used immediately for histamine detection, the results of which are included in Paper II in Appendix B.

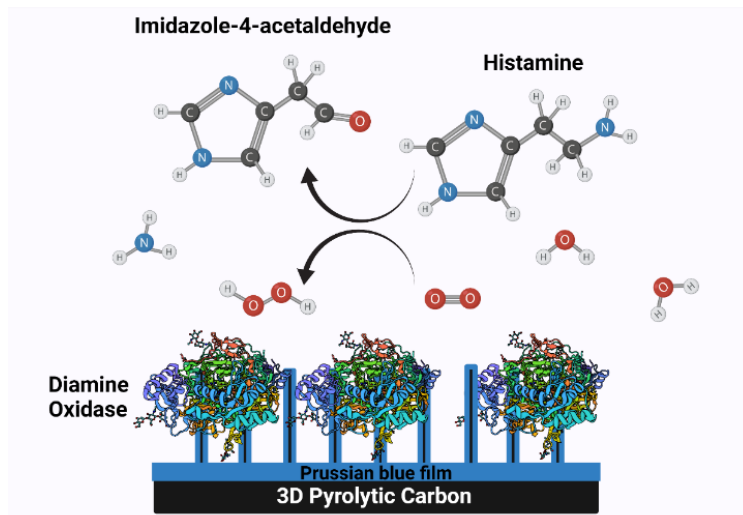


Figure 6-11 Schematic illustration of the constructed enzymatic histamine biosensor by DAO immobilization on PB-modified 3D pyrolytic carbon microelectrode. Created with Biorender.com

Chapter 7. Conclusion and Outlook

This chapter will conclude the study by summarizing the major achievements in relation to the project objectives defined in chapter 1 and by discussing the value and contribution of this Ph.D. dissertation to the research fields of allergy, CMEMS and electrochemical sensing thereof. It will also review the limitations of the study and propose opportunities for future research.

This Ph.D. project aimed at developing an electrochemical sensor by using 3D pyrolytic carbon for the quantitative analysis of type I allergic reactions. The main hypothesis was that the pyrolytic carbon microelectrode in MN configuration can be used as an electrochemical transducer for the detection of allergy biomarkers released from the mast cells in the dermis. Being the primary allergy biomarker, histamine was chosen as the sensing target. Knowledge of the skin cellular structure and physiology, ISF content as well as allergy and histamine release mechanism shaped the requirements and the boundary conditions of this research. Accordingly, the main success criteria for the sensor's performance were defined as being able to measure histamine in ISF in the concentration range of 200-600 nM at pH levels of 6.6 -7.6 within 10-20 minutes.

3D pyrolytic carbon microelectrodes with micropillar structures resembling the MN design were fabricated in a two-step photolithography process followed by pyrolysis. The optimized microfabrication process allowed for excellent control of the dimensions of the pyrolytic carbon micropillar structures resulting in highly reproducible 3D microelectrodes. Histamine biosensor was constructed by immobilizing a layer of DAO enzymes, purified from *Pisum sativum* (pea plant), on the microelectrodes. DAO would catalyze the oxidation of histamine in the presence of molecular oxygen and generate H_2O_2 and ammonia as the reaction by-products. Because the concentration of the produced H_2O_2 is directly proportional to the histamine concentration, the quantification of H_2O_2 would enable quantitative analysis of unknown amounts of histamine. However, the H_2O_2 reduction at carbon in the presence of oxygen is impossible. In addition, the H_2O_2 oxidation at carbon occurs at high potential values because of the slow electron transfer kinetics. At these high potentials, other biological substances in the ISF also co-oxidize. To avoid these challenges, the pyrolytic carbon microelectrodes were modified with PB film as an electron transfer mediator which catalyzes the reduction of H_2O_2 at 0 V vs. Ag/AgCl. Although there are many examples of PB film incorporation on carbon derivatives for H_2O_2 sensing in literature, this work is the first ever investigation of PB electrocatalytic activity on the pyrolytic carbon.

To increase the sensor preparation capacity, a multi-electrode electrochemical cell was designed and fabricated by additive manufacturing. Simultaneous PB film electrodeposition on four microelectrodes in the 3D printed cell made the procedure of sensor preparation more efficient in terms of the required time and material. The process of PB film electrodeposition on the pyrolytic carbon was optimized and assessed by amperometry in stirred phosphate buffered, which resulted in highly reproducible results. Linear amperometric response to 0.3–8 μM H_2O_2 in phosphate buffer pH 5.5 which is the optimum pH for PB, and LOD as low as 160 nM were obtained with 98% confidence by PB-modified 3D pyrolytic carbon microelectrodes. In addition, the sensitivity of the PB-modified 3D pyrolytic carbon for the amperometric quantification of H_2O_2 in stirred buffer was above $1 A M^{-1} cm^{-2}$, which is the maximal possible sensitivity of carbon electrodes in FIA systems. In the first place, the sensors owe their high sensitivity to the 3D microstructures which provide an electrocatalytically large active surface area for H_2O_2 reduction. Secondly, the strong convective transportation of the analyte molecules to the active sites at the electrode enhances the measured current in stirred environments.

Stirred batch amperometry was also implemented for the optimization of the enzyme immobilization on the PB-modified 3D pyrolytic carbon microelectrodes. The optimum amounts of DAO enzyme, BSA as the spacer molecule and GA as the cross-linker were determined by assessing the amperometric responses of at least three identically prepared biosensors to 1 mM histamine.

Nevertheless, the strong convection in a magnetically stirred solution does not mimic the natural convection in the laminar flow of the ISF in the extracellular environment of the dermis. Moreover, amperometry which measures the charge passage through the electrode as it is produced, did not provide the required sensitivity in the ISF microenvironment. The biosensors which were constructed

by using the optimized PB electrodeposition and enzyme immobilization protocols, hardly showed any visible amperometric response to 10 μM histamine in stirred phosphate buffer. Therefore, a so-called 'capacitive' method for the detection of low concentrations of histamine on PB/DAO-modified 3D pyrolytic carbon microelectrodes was developed. The 3D zeolite-like structure of the PB film with its open framework, channels and cavities allows reversible insertion/extraction of alkali-metal cations like K^+ and small molecules such as H_2O and H_2O_2 , and thereby can store and release charge upon reduction and oxidation analogous to charge/discharge cycles of a capacitor. The capacitive method was a combination of two techniques run in sequence during the measurements: i) single step potential chronoamperometry, and ii) open circuit potentiometry. The first technique charged the PB film on the electrode by reducing it to PW. The charge accumulation on the PW/enzyme-modified electrode was analogous to charging a capacitor. The second technique recorded the discharge of the film initiated by H_2O_2 reaction with PW at an open circuit. H_2O_2 would oxidize PW to PB imposing a positive shift in OCP. Upon oxidation, the PW film would lose electrons to H_2O_2 reducing it to H_2O . The amount of the lost charge from the film was then assessed by integrating the recharging current recorded by chronoamperometry in the next step. The hypothesis of this electrochemical transduction concept was that the slow discharge and the rapid recharging of the PB film could enhance the signal and allow measuring lower H_2O_2 concentrations than what was detected by amperometry.

Two types of data were acquired by the capacitive method which could be used to analyze the concentration of the reduced H_2O_2 , and thereby to quantify the amount of histamine in the sample. These two types of data were the OCP shifts recorded during the discharge cycle and the corresponding recharge currents. While recharge currents were recorded for the H_2O_2 concentrations above 1 μM by chronoamperometry, potentiometry showed an outstanding sensitivity to H_2O_2 concentrations in 0.1-1 μM range in the presence of dissolved oxygen, which competes with the H_2O_2 in reacting with the PB. For H_2O_2 detection, LOD of 71 nM was achieved by potentiometry which is less than half the LOD obtained by stirred batch amperometry. Histamine measurement in phosphate buffer at pH 5.5 in the concentration range between 100 nM and 1 mM was established, and the LOD of 363 nM was obtained from the potentiometric data. Thereafter, the proof-of-concept measurements of 90 ng mL^{-1} and 1684 ng mL^{-1} histamine (equal to about 800 nM and 15 μM respectively) released from activated LAD2 human mast cells in cell supernatant in static conditions were demonstrated by the capacitive method. The measurement of each histamine-containing sample by the capacitive method took just about 19 minutes including the time required to establish a stable baseline.

Since H_2O_2 is the common reaction by-product of oxidase enzymes, the capacitive H_2O_2 detection with PB can be interesting for the researchers who employ oxidase enzymes as recognition element of their biosensors. The sensitivity of the capacitive method in static conditions makes it an ideal transduction technique for on-chip cell-based measurements and for developing *in vivo* electrochemical H_2O_2 sensors and oxidase-based biosensors integrated in dermal microneedle patches or in wearable devices.

To summarize, the following were accomplished in regard to the main objectives of the Ph.D. project:

- 1) Confirmed the main hypothesis of the project regarding the use of 3D pyrolytic carbon as a transducer for electrochemical histamine sensing,
- 2) Developed a quantitative electrochemical histamine biosensor on the 3D pyrolytic carbon,
- 3) Established reproducible histamine detection in the concentration range between 100 nM and 1 mM with LOD=363 nM, though in a phosphate buffer at pH 5.5 at the room temperature,
- 4) Enabled histamine detection in 19 minutes,

- 5) Demonstrated the proof-of-concept measurement of about 800 nM histamine released from activated LAD2 human mast cells in the cell supernatant

Nonetheless, the following studies remained inconclusive due to lack of time, which could be the subjects of future work:

Operational conditions: To avoid the instability of PB, the histamine detection experiments were performed in a phosphate buffer at room temperature (22-25°C) and at pH 5.5, which are the optimum temperature and pH conditions for the PB. However, the evaluation of the biosensor performance in the biologically relevant conditions remained incomplete. Future study should focus on establishing histamine detection at 37°C at neutral pH, which are the internal body's temperature and normal ISF pH level. These biologically relevant temperature and pH conditions are also favorable for the enzymatic activity of DAO towards histamine and could enhance the sensitivity of the biosensor. To achieve this goal, the first and foremost challenge that should be addressed is the instability of the PB.

Stability: The instability of PB, which is caused by the strong interaction between ferric ions (Fe^{3+}) and hydroxyl ions (OH^-) at pH higher than 6.4, leads to the destruction of the $\text{Fe}^{\text{II}}-\text{CN}-\text{Fe}^{\text{III}}$ bonds and leakage of the PB from the electrode surface. The stability of PB seems to be dependent on the deposition method, which defines the structure of the film. Other PB deposition methods than electrodeposition could be investigated on the pyrolytic carbon. Another option for improving the stability of the PB could be the implementation of a biocompatible organic or conductive polymer as a protective layer over the PB film.

Calibration characteristics and reproducibility: Due to the lack of time in the last phase of the project, which was caused by the prolonged quarantines during the COVID-19 pandemics, it was decided to limit the cell-based histamine experiments to a quick proof-of-concept measurement demonstrating the histamine detection in mast cell medium. The lowest concentration which was tested was about 800 nM released from 40×10^3 activated LAD2 human mast cells. Although, the detection of histamine at a concentration less than 1 μM in the cell supernatant at neutral pH was successfully demonstrated, this quick experiment did not meet the initial objective. The objective was to enable histamine detection in biorelevant fluid in the concentration range between 200 and 600 nM. In the future, the histamine release assay should be performed with a smaller number of mast cells to obtain lower concentrations of histamine in the cell supernatants. Thereafter, a few histamine-containing supernatants should be tested at least in triplicates at 37°C to evaluate the response of the biosensor to histamine in the real samples in the desired concentration range in the optimum conditions. To estimate the number of histamine turnover of the immobilized DAO, a calibration curve must be made from the response of the biosensor to different concentrations of H_2O_2 added to a blank (zero histamine) cell supernatant.

Selectivity: In this project, a brief study was conducted by the amperometry to evaluate the selectivity of the biosensor for H_2O_2 reduction in the presence of uric acid and ascorbic acid which are potentially the most interfering substances in the ISF for H_2O_2 detection. No current signal was recorded that could indicate the interference from these substances when they were added to the buffer at excessive amounts. In addition, prior to testing the histamine-containing cell supernatants, stable baselines were obtained in control samples consisting of blank (zero histamine) cell supernatants and the cell stimulating compound 48/80. Stable baselines indicated zero interference from the compound 48/80 and the other constituents of the cell supernatants. Nevertheless, more experiments are required as the complementary to these initial observations

for investigating the selectivity of the biosensor for histamine detection in the presence of, for example, other biogenic amines that might be in the ISF.

Cell-based studies: Eventually, the histamine release assay should be performed directly on the 3D biosensor or at its vicinity to mimic the *in vivo* mast cell degranulation and histamine detection by the pyrolytic carbon MN sensor. Mast cells in their culture medium could be sedimented on the 3D biosensors, placed horizontally in the 3D printed multi-electrode setup, and stimulated by compound 48/80 to release histamine. Finally, the concentration of the released histamine could be identified by correlating the obtained signal to a known concentration on a standard calibration curve constructed for the histamine biosensor.

Bibliography

1. Silverstein, A. M. Clemens freiherr von pirquet: Explaining immune complex disease in 1906. *Nat. Immunol.* **1**, 453–455 (2000).
2. Hossny, E. *et al.* Challenges of managing food allergy in the developing world. *World Allergy Organ. J.* **12**, 100089 (2019).
3. Katelaris, C. H. & Beggs, P. J. Climate change: allergens and allergic diseases. *Intern. Med. J.* **48**, 129–134 (2018).
4. Pawankar, R. *et al.* Allergic diseases and asthma: a global public health concern and a call to action. *World Allergy Organ. J.* **7**, 12 (2014).
5. Gupta, R. S. *et al.* Prevalence and Severity of Food Allergies Among US Adults. *JAMA Netw. open* **2**, e185630 (2019).
6. Bonini, S. News From the European Academy of Allergology and Clinical Immunology. *Allergy Clin. Immunol. Int. - J. World Allergy Organ.* **12**, 0186–0187 (2000).
7. Pawankar, R. & Blaiss, G. W. C. S. T. H. R. F. L. M. S. *World Allergy Organization (WAO) White Book on Allergy: Update 2013. World Allergy Organization* (2013).
8. Guibas, G. V., Mathioudakis, A. G., Tsoumani, M. & Tsabouri, S. Relationship of allergy with asthma: There are more than the allergy ‘eggs’ in the Asthma ‘Basket’. *Frontiers in Pediatrics* **5**, (2017).
9. Foong, R. X., du Toit, G. & Fox, A. T. Asthma, food allergy, and how they relate to each other. *Front. Pediatr.* **5**, 1–6 (2017).
10. Mahmoudi, M. *Challenging cases in pulmonology. Challenging Cases in Pulmonology* **9781441970985**, (2013).
11. Gupta, R. *et al.* Original Investigation 1026 JAMA Pediatrics. **167**, (2013).
12. Boye, J. I. *Food allergies in developing and emerging economies: need for comprehensive data on prevalence rates. Clinical and Translational Allergy* **2**, (2012).
13. Koul, P. & Dhar, R. Economic burden of asthma in India. *Lung India* **35**, 281–283 (2018).
14. Wernersson, S. & Pejler, G. Mast cell secretory granules: Armed for battle. *Nature Reviews Immunology* **14**, 478–494 (2014).
15. Amin, K. The role of mast cells in allergic inflammation. *Respir. Med.* **106**, 9–14 (2012).
16. Brown, J. M., Wilson, T. M. & Metcalfe, D. D. The mast cell and allergic diseases: Role in pathogenesis and implications for therapy. *Clin. Exp. Allergy* **38**, 4–18 (2008).
17. Fontenot, A. P. & Peebles, R. S. Allergy and hypersensitivity. *Curr. Opin. Immunol.* **25**, 736–737 (2013).
18. Galli, S. J., Nakae, S. & Tsai, M. Mast cells in the development of adaptive immune responses. *Nat. Immunol.* **6**, 135–142 (2005).
19. Galli, S. J., Tsai, M. & Piliponsky, A. M. The development of allergic inflammation. *Nature* **454**, 445–454 (2008).
20. Metcalfe, D. D. *et al.* Biomarkers of the involvement of mast cells, basophils and eosinophils in asthma and allergic diseases. *World Allergy Organ. J.* **9**, 1–15 (2016).
21. Heinzerling, L. *et al.* The skin prick test - European standards. *Clin. Transl. Allergy* **3**, 1–10 (2013).
22. Antunes, J., Borrego, L., Romeira, A. & Pinto, P. Skin prick tests and allergy diagnosis. *Allergol. Immunopathol. (Madr)*. **37**, 155–164 (2009).
23. Kwizera, R. *et al.* Skin prick reactivity among asthmatics in East Africa. *World Allergy Organ. J.* **13**, 100130 (2020).
24. Justo, X., Díaz, I., Gil, J. J. & Gastaminza, G. Prick test: evolution towards automated reading. *Allergy Eur. J. Allergy Clin. Immunol.* **71**, 1095–1102 (2016).
25. Poulsen, L. K., Liisberg, C., Bindslev-Jensen, C. & Malling, H. J. Precise area determination of skin-prick tests: Validation of a scanning device and software for a personal computer. *Clin. Exp. Allergy* **23**, 61–68 (1993).
26. Dos Santos, R. V., Mlynek, A., Lima, H. C., Martus, P. & Maurer, M. Beyond flat weals: Validation of a three-

- dimensional imaging technology that will improve skin allergy research. *Clin. Exp. Dermatol.* **33**, 772–775 (2008).
27. Olsson, P., Hammarlund, A. & Pipkorn, U. Wheal-and-flare reactions induced by allergen and histamine: Evaluation of blood flow with laser doppler flowmetry. *J. Allergy Clin. Immunol.* **82**, 291–296 (1988).
 28. Bulan, O. Improved wheal detection from skin prick test images. *Image Process. Mach. Vis. Appl.* **7**, 90240J (2014).
 29. Rokita, E., Rok, T. & Tatoń, G. Thermographic measurements of allergen-induced skin reactions. *IFMBE Proc.* **25**, 120–123 (2009).
 30. Nyrén, M., Ollmar, S., Nicander, I. & Emtestam, L. An electrical impedance technique for assessment of wheals. *Allergy Eur. J. Allergy Clin. Immunol.* **51**, 923–926 (1996).
 31. Sturm, E. M. *et al.* CD203c-based basophil activation test in allergy diagnosis: Characteristics and differences to CD63 upregulation. *Cytom. Part B - Clin. Cytom.* **78**, 308–318 (2010).
 32. Ansoategui, I. J. *et al.* IgE allergy diagnostics and other relevant tests in allergy, a World Allergy Organization position paper. *World Allergy Organ. J.* **13**, (2020).
 33. Van Gasse, A. L. *et al.* Molecular allergy diagnosis: Status anno 2015. *Clin. Chim. Acta* **444**, 54–61 (2015).
 34. Bodtger, U., Jacobsen, C. R., Poulsen, L. K. & Malling, H. J. Long-term repeatability of the skin prick test is high when supported by history or allergen-sensitivity tests: A prospective clinical study. *Allergy Eur. J. Allergy Clin. Immunol.* **58**, 1180–1186 (2003).
 35. Huang, H. J. *et al.* Microarray-Based Allergy Diagnosis: Quo Vadis? *Frontiers in Immunology* **11**, (2021).
 36. Teymourian, H., Tehrani, F., Mahato, K. & Wang, J. Lab under the Skin: Microneedle Based Wearable Devices. *Adv. Healthc. Mater.* **2002255**, 1–19 (2021).
 37. Amjadi, M., Sheykhansari, S., Nelson, B. J. & Sitti, M. Recent Advances in Wearable Transdermal Delivery Systems. *Advanced Materials* **30**, (2018).
 38. Vecchione, R. *et al.* Electro-drawn drug-loaded biodegradable polymer microneedles as a viable route to hypodermic injection. *Adv. Funct. Mater.* **24**, 3515–3523 (2014).
 39. Sullivan, S. P. *et al.* Dissolving polymer microneedle patches for influenza vaccination. *Nat. Med.* **16**, 915–920 (2010).
 40. Dillon, C., Hughes, H., O'Reilly, N. J. & McLoughlin, P. Formulation and characterisation of dissolving microneedles for the transdermal delivery of therapeutic peptides. *Int. J. Pharm.* **526**, 125–136 (2017).
 41. van der Maaden, K., Jiskoot, W. & Bouwstra, J. Microneedle technologies for (trans)dermal drug and vaccine delivery. *J. Control. Release* **161**, 645–655 (2012).
 42. Karande, P. & Mitragotri, S. Transcutaneous Immunization: An Overview of Advantages, Disease Targets, Vaccines, and Delivery Technologies. *Annu. Rev. Chem. Biomol. Eng.* **1**, 175–201 (2010).
 43. Srivastava, A. K., Bhartiya, B., Mukhopadhyay, K. & Sharma, A. Long term biopotential recording by body conformable photolithography fabricated low cost polymeric microneedle arrays. *Sensors Actuators, A Phys.* **236**, 164–172 (2015).
 44. Ren, L. *et al.* Fabrication of a Micro-Needle Array Electrode by Thermal Drawing for Bio-Signals Monitoring. *Sensors* **16**, 908 (2016).
 45. Forvi, E. *et al.* Preliminary technological assessment of microneedles-based dry electrodes for biopotential monitoring in clinical examinations. *Sensors Actuators A Phys.* **180**, 177–186 (2012).
 46. Wang, R., Jiang, X., Wang, W. & Li, Z. A microneedle electrode array on flexible substrate for long-term EEG monitoring. *Sensors Actuators B Chem.* **244**, 750–758 (2017).
 47. Yu, L. M., Tay, F. E. H., Guo, D. G., Xu, L. & Yap, K. L. A microfabricated electrode with hollow microneedles for ECG measurement. *Sensors Actuators, A Phys.* **151**, 17–22 (2009).
 48. Wang, L. F., Liu, J. Q., Yan, X. X., Yang, B. & Yang, C. S. A MEMS-based pyramid micro-needle electrode for long-term EEG measurement. *Microsyst. Technol.* **19**, 269–276 (2013).
 49. Ren, L., Liu, B., Zhou, W. & Jiang, L. A Mini Review of Microneedle Array Electrode for Bio-Signal Recording: A

- Review. *IEEE Sens. J.* **20**, 577–590 (2020).
50. Ren, L. *et al.* Fabrication of Flexible Microneedle Array Electrodes for Wearable Bio-Signal Recording. *Sensors* **18**, 1191 (2018).
 51. Chen, K. Y. *et al.* Fabrication of micro-needle electrodes for bio-signal recording by a magnetization-induced self-assembly method. *Sensors (Switzerland)* **16**, 1–15 (2016).
 52. Prausnitz, M. R., Allen, M. G. & Gujral, I. Microneedle Device for Extraction and Sensing of Bodily Fluids. *Off. Gaz. United States Pat. Trademark Off. Patents* **26** (2008).
 53. Mukerjee, E., Collins, S. D., Isseroff, R. R. & Smith, R. L. Microneedle array for transdermal biological fluid extraction and in situ analysis. *Sensors and Actuators A-physical* **114**, 267–275 (2004).
 54. Xue, P. *et al.* Blood sampling using microneedles as a minimally invasive platform for biomedical diagnostics. *Appl. Mater. Today* **13**, 144–157 (2018).
 55. Chang, H. *et al.* A Swellable Microneedle Patch to Rapidly Extract Skin Interstitial Fluid for Timely Metabolic Analysis. *Adv. Mater.* **29**, (2017).
 56. Huang, Y. Development of an ion concentration measurement device integrated with blood extraction microneedle. *Nami Jishu Yu Jingmi Gongcheng/nanotechnology Precis. Eng.* **13**, (2015).
 57. Ng, K. W., Lau, W. M. & Williams, A. C. Towards pain-free diagnosis of skin diseases through multiplexed microneedles: biomarker extraction and detection using a highly sensitive blotting method. *Drug Deliv. Transl. Res.* **5**, 387–396 (2015).
 58. Caratelli, D., Yarovoy, A., Massaro, A., Lay-Ekuakille, A. & In, P. Design and full-wave analysis of piezoelectric micro-needle antenna sensors for enhanced near-field detection of skin cancer. *Prog. Electromagn. Res.* **125**, A22, 391–413 (2012).
 59. Caratelli, D., Lay-Ekuakille, A. & Vergallo, P. Non-Invasive Reflectometry-Based Detection of Melanoma By Piezoelectric Micro-Needle Antenna Sensors. *Prog. Electromagn. Res.* **135**, 91–103 (2013).
 60. Mishra, R. K., Vinu Mohan, A. M., Soto, F., Chrostowski, R. & Wang, J. A microneedle biosensor for minimally-invasive transdermal detection of nerve agents. *Analyst* **142**, 918–924 (2017).
 61. Ciui, B. *et al.* Wearable Wireless Tyrosinase Bandage and Microneedle Sensors: Toward Melanoma Screening. *Adv. Healthc. Mater.* **7**, 1701264 (2018).
 62. Chandrasekaran, S. & Frazier, A. B. An autonomous microneedle-based bio-analysis system. in *SECOND JOINT EMBS-BMES CONFERENCE 2002, VOLS 1-3, CONFERENCE PROCEEDINGS: BIOENGINEERING - INTEGRATIVE METHODOLOGIES, NEW TECHNOLOGIES* 1644–1645 (2002).
 63. Vasylieva, N., Marinesco, S., Barbier, D. & Sabac, A. Silicon/SU8 multi-electrode micro-needle for in vivo neurochemical monitoring. *Biosens. Bioelectron.* **72**, 148–155 (2015).
 64. Eltayib, E. *et al.* Hydrogel-forming microneedle arrays: Potential for use in minimally-invasive lithium monitoring. *Eur. J. Pharm. Biopharm.* **102**, 123–131 (2016).
 65. Barrett, C., Dawson, K., O'Mahony, C. & O'Riordan, A. Development of Low Cost Rapid Fabrication of Sharp Polymer Microneedles for In Vivo Glucose Biosensing Applications. *ECS J. Solid State Sci. Technol.* **4**, S3053–S3058 (2015).
 66. Yoon, H. S., Lee, S. J., Park, J. Y., Paik, S. J. & Allen, M. G. A non-enzymatic micro-needle patch sensor for free-cholesterol continuous monitoring. *Proc. IEEE Sensors* **2014-Decem**, 347–350 (2014).
 67. Windmiller, J. R. *et al.* Bicomponent Microneedle Array Biosensor for Minimally-Invasive Glutamate Monitoring. *Electroanalysis* **23**, 2302–2309 (2011).
 68. Bollella, P., Sharma, S., Cass, A. E. G. & Antiochia, R. Microneedle-based biosensor for minimally-invasive lactate detection. *Biosens. Bioelectron.* **123**, 152–159 (2018).
 69. Brown, S. *et al.* Minimally invasive technique for measuring transdermal glucose with a fluorescent biosensor. *Anal. Bioanal. Chem.* **410**, 7249–7260 (2018).
 70. Chinnadayala, S. R., Park, I. & Cho, S. Nonenzymatic determination of glucose at near neutral pH values based on the use of nafion and platinum black coated microneedle electrode array. *Microchim. Acta* **185**, 250 (2018).

71. Chua, B., Desai, S. P., Tierney, M. J., Tamada, J. A. & Jina, A. N. Effect of microneedles shape on skin penetration and minimally invasive continuous glucose monitoring in vivo. *Sensors Actuators, A Phys.* **203**, 373–381 (2013).
72. Dardano, P. *et al.* Glucose sensing electrode system based on polymeric microneedles. *SAS 2016 - Sensors Appl. Symp. Proc.* 73–77 (2016). doi:10.1109/SAS.2016.7479821
73. Invernale, M. A. *et al.* Microneedle Electrodes Toward an Amperometric Glucose-Sensing Smart Patch. *Adv. Healthc. Mater.* **3**, 1–5 (2014).
74. Li, C. G. *et al.* One-touch-activated blood multidagnostic system using a minimally invasive hollow microneedle integrated with a paper-based sensor. *Lab Chip* **15**, 3286–3292 (2015).
75. Miller, P. R. *et al.* Multiplexed microneedle-based biosensor array for characterization of metabolic acidosis. *Talanta* **88**, 739–742 (2012).
76. Miller, P. R. *et al.* Microneedle-based transdermal sensor for on-chip potentiometric determination of K⁺. *Adv. Healthc. Mater.* **3**, 876–881 (2014).
77. Zhou, J.-X. *et al.* Monitoring of pH changes in a live rat brain with MoS₂/PAN functionalized microneedles. *Analyst* **143**, 4469–4475 (2018).
78. Xu, B. *et al.* H₂O₂-Responsive mesoporous silica nanoparticles integrated with microneedle patches for the glucose-monitored transdermal delivery of insulin. *J. Mater. Chem. B* **5**, 8200–8208 (2017).
79. Khanna, P., Strom, J. A., Malone, J. I. & Bhansali, S. Microneedle-based automated therapy for diabetes mellitus. *J. Diabetes Sci. Technol.* **2**, 1122–1129 (2008).
80. Cahill, E. M. & O’Cearbhaill, E. D. Toward Biofunctional Microneedles for Stimulus Responsive Drug Delivery. *Bioconjug. Chem.* **26**, 1289–1296 (2015).
81. Ranamukhaarachchi, S. A. *et al.* Integrated hollow microneedle-optofluidic biosensor for therapeutic drug monitoring in sub-nanoliter volumes. *Sci. Rep.* **6**, 1–10 (2016).
82. Shakya, A. K. *et al.* Microneedles coated with peanut allergen enable desensitization of peanut sensitized mice. *J. Control. Release* **314**, 38–47 (2019).
83. Chiu, Y. H., Wu, Y. W., Hung, J. I. & Chen, M. C. Epigallocatechin gallate/L-ascorbic acid-loaded poly-γ-glutamate microneedles with antioxidant, anti-inflammatory, and immunomodulatory effects for the treatment of atopic dermatitis. *Acta Biomater.* **130**, 223–233 (2021).
84. El-Laboudi, A., Oliver, N. S., Cass, A. & Johnston, D. Use of Microneedle Array Devices for Continuous Glucose Monitoring: A Review. *Diabetes Technol. Ther.* **15**, 101–115 (2013).
85. Frontino, G. *et al.* Future perspectives in glucose monitoring sensors. *US Endocrinol.* **9**, 21–26 (2013).
86. Chinnadayala, S. R., Park, K. D. & Cho, S. Editors’ Choice—Review—In Vivo and In Vitro Microneedle Based Enzymatic and Non-Enzymatic Continuous Glucose Monitoring Biosensors. *ECS J. Solid State Sci. Technol.* **7**, Q3159–Q3171 (2018).
87. Sharma, S. *et al.* A pilot study in humans of microneedle sensor arrays for continuous glucose monitoring. *Anal. Methods* **10**, 2088–2095 (2018).
88. Takeuchi, K. & Kim, B. Functionalized microneedles for continuous glucose monitoring. *Nano Converg.* **5**, 28 (2018).
89. Caffarel-Salvador, E. *et al.* Hydrogel-forming microneedle arrays allow detection of drugs and glucose in vivo: Potential for use in diagnosis and therapeutic drug monitoring. *PLoS One* **10**, (2015).
90. Xu, B. *et al.* Microneedles Integrated with ZnO Quantum-Dot-Capped Mesoporous Bioactive Glasses for Glucose-Mediated Insulin Delivery. *ACS Biomater. Sci. Eng.* **4**, 2473–2483 (2018).
91. Xu, B. *et al.* H₂O₂-Responsive mesoporous silica nanoparticles integrated with microneedle patches for the glucose-monitored transdermal delivery of insulin. *J. Mater. Chem. B* **5**, 8200–8208 (2017).
92. Tong, Z. *et al.* Glucose- and H₂O₂-Responsive Polymeric Vesicles Integrated with Microneedle Patches for Glucose-Sensitive Transcutaneous Delivery of Insulin in Diabetic Rats. *ACS Appl. Mater. Interfaces* **10**, 20014–20024 (2018).
93. Lee, H. *et al.* Wearable/disposable sweat-based glucose monitoring device with multistage transdermal drug delivery module. *Sci. Adv.* **3**, e1601314 (2017).

94. Khanna, P., Strom, J. A., Malone, J. I. & Bhansali, S. Microneedle-based automated therapy for diabetes mellitus. *J. Diabetes Sci. Technol.* **2**, 1122–1129 (2008).
95. Lee, H. *et al.* A graphene-based electrochemical device with thermoresponsive microneedles for diabetes monitoring and therapy. *Nat. Nanotechnol.* **11**, 566–572 (2016).
96. Wang, J. *et al.* Core-Shell Microneedle Gel for Self-Regulated Insulin Delivery. *ACS Nano* **12**, 2466–2473 (2018).
97. Anonymous. System and methods for optical sensing and drug delivery using microneedles. *Off. Gaz. United States Pat. Trademark Off. Patents* (2013).
98. Madden, J., O'Mahony, C., Thompson, M., O'Riordan, A. & Galvin, P. Biosensing in dermal interstitial fluid using microneedle based electrochemical devices. *Sens. Bio-Sensing Res.* **29**, 100348 (2020).
99. Liu, G. S. *et al.* Microneedles for transdermal diagnostics: Recent advances and new horizons. *Biomaterials* **232**, 119740 (2020).
100. Amato, L. *et al.* Novel Nanostructured Electrodes Obtained by Pyrolysis of Composite Polymeric Materials. *Electroanalysis* **27**, 1544–1549 (2015).
101. Martinez-Duarte, R. SU-8 photolithography as a toolbox for carbon MEMS. *Micromachines* **5**, 766–782 (2014).
102. Hassan, Y. M. *et al.* High temperature SU-8 pyrolysis for fabrication of carbon electrodes. *J. Anal. Appl. Pyrolysis* **125**, 91–99 (2017).
103. Amato, L. *et al.* Dense high-aspect ratio 3D carbon pillars on interdigitated microelectrode arrays. *Carbon N. Y.* **94**, 792–803 (2015).
104. Hemanth, S., Halder, A., Caviglia, C., Chi, Q. & Sylvest Keller, S. 3D Carbon Microelectrodes with Bio-Functionalized Graphene for Electrochemical Biosensing. (2018). doi:10.3390/bios8030070
105. Hemanth, S., Caviglia, C. & Keller, S. S. Suspended 3D pyrolytic carbon microelectrodes for electrochemistry. *Carbon N. Y.* **121**, 226–234 (2017).
106. Amato, L. *et al.* Pyrolysed 3D-carbon scaffolds induce spontaneous differentiation of human neural stem cells and facilitate real-time dopamine detection. *Adv. Funct. Mater.* **24**, 7042–7052 (2014).
107. Caviglia, C. *et al.* In situ electrochemical analysis of alkaline phosphatase activity in 3D cell cultures. *Electrochim. Acta* **359**, 136951 (2020).
108. Ali, S. M. & Yosipovitch, G. Skin pH: From basic science to basic skin care. *Acta Derm. Venereol.* **93**, 261–267 (2013).
109. Barker, A. *Chapter 8. Skin structure. In Plastic and reconstructive surgery.* (John Wiley & Sons, Ltd., 2015). doi:10.5005/jp/books/11454_50
110. Xu, H., Timares, L. & Elmets, C. A. Host defenses in the skin, Editor(s): Robert R. Rich, Thomas A. Fleisher, William T. Shearer, Harry W. Schroeder, Anthony J. Frew, Cornelia M. Weyand. *Clin. Immunol. Princ. Pract. Fourth Ed. Elsevier* 228–238 (2013). doi:10.1016/B978-0-7234-3691-1.00039-8
111. Honari, G. & Maibach, H. I. *Chapter 1. Skin Structure and Function. Applied Dermatotoxicology* (Elsevier Inc., 2014). doi:10.1016/B978-0-12-420130-9.00001-3
112. Wong, R., Geyer, S., Weninger, W., Guimberteau, J. C. & Wong, J. K. The dynamic anatomy and patterning of skin. *Exp. Dermatol.* **25**, 92–98 (2016).
113. Barbieri, J. S., Wanat, K. & Seykora, J. *Skin: Basic Structure and Function. Pathobiology of Human Disease: A Dynamic Encyclopedia of Disease Mechanisms* (Published by Elsevier Inc., 2014). doi:10.1016/B978-0-12-386456-7.03501-2
114. Wojtowicz, A. M. *et al.* The importance of both fibroblasts and keratinocytes in a bilayered living cellular construct used in wound healing. *Wound Repair Regen.* **22**, 246–255 (2014).
115. Hilliges, M., Wang, L. & Johansson, O. Ultrastructural evidence for nerve fibers within all vital layers of the human epidermis. *J. Invest. Dermatol.* **104**, 134–137 (1995).
116. Weber, A., Knop, J. & Maurer, M. Pattern analysis of human cutaneous mast cell populations by total body surface mapping. *Br. J. Dermatol.* **148**, 224–228 (2003).

117. Schulman, E. S. *et al.* Heterogeneity of human mast cells. *J. Immunol.* **131**, 1936 LP – 1941 (1983).
118. Bischoff, S. C. Role of mast cells in allergic and non-allergic immune responses: Comparison of human and murine data. *Nat. Rev. Immunol.* **7**, 93–104 (2007).
119. Metz, M., Siebenhaar, F. & Maurer, M. Mast cell functions in the innate skin immune system. *Immunobiology* **213**, 251–260 (2008).
120. Schwartz, L. B., Metcalfe, D. D., Miller, J. S., Earl, H. & Sullivan, T. Tryptase Levels as an Indicator of Mast-Cell Activation in Systemic Anaphylaxis and Mastocytosis. *N. Engl. J. Med.* **316**, 1622–1626 (1987).
121. Heikenfeld, J. *et al.* Accessing analytes in biofluids for peripheral biochemical monitoring. *Nat. Biotechnol.* **37**, 407–419 (2019).
122. Niedzwiecki, M. M. *et al.* Human Suction Blister Fluid Composition Determined Using High-Resolution Metabolomics. *Anal. Chem.* **90**, 3786–3792 (2018).
123. Samant, P. P. & Prausnitz, M. R. Mechanisms of sampling interstitial fluid from skin using a microneedle patch. *Proc. Natl. Acad. Sci. U. S. A.* **115**, 4583–4588 (2018).
124. Miller, P. R. *et al.* Extraction and biomolecular analysis of dermal interstitial fluid collected with hollow microneedles. *Commun. Biol.* **1**, (2018).
125. Wiig, H. & Swartz, M. A. Interstitial fluid and lymph formation and transport: Physiological regulation and roles in inflammation and cancer. *Physiol. Rev.* **92**, 1005–1060 (2012).
126. Yao, W. & Ding, G. H. Interstitial fluid flow: Simulation of mechanical environment of cells in the interosseous membrane. *Acta Mech. Sin. Xuebao* **27**, 602–610 (2011).
127. Szegedi, K. *et al.* Cytokine profiles in interstitial fluid from chronic atopic dermatitis skin. *J. Eur. Acad. Dermatology Venereol.* **29**, 2136–2144 (2015).
128. Aukland, K. & Nicolaysen, G. Interstitial fluid volume: local regulatory mechanisms. *Physiol. Rev.* **61**, 556–643 (1981).
129. Marques, M. R. C., Loebenberg, R. & Almukainzi, M. Simulated Fluids. *Dissolution Technol.* **18**, 15–28 (2011).
130. Marunaka, Y. Roles of interstitial fluid pH in diabetes mellitus: Glycolysis and mitochondrial function. *World J. Diabetes* **6**, 125 (2015).
131. Yong, L. C. J. The mast cell: Origin, morphology, distribution, and function. *Exp. Toxicol. Pathol.* **49**, 409–424 (1997).
132. PETERSEN, L. J., CHURCH, M. K. & SKOV, P. S. Histamine is released in the wheal but not the flare following challenge of human skin in vivo: a microdialysis study. *Clin. Exp. Allergy* **27**, 284–295 (1997).
133. Harris, D. C. *QUANTITATIVE CHEMICAL ANALYSIS*. **1**, (W.H. Freeman and Company, 2010).
134. Bagotsky, V. S. *FUNDAMENTALS OF ELECTROCHEMISTRY: SECOND EDITION*. (A JOHN WILEY & SONS, INC., 2005).
135. Bard, A. J. & Faulkner, L. R. *ELECTROCHEMICAL METHODS Fundamentals and Applications*. JOHN WILEY & SONS, INC. (WILEY, 2000).
136. Elgrishi, N. *et al.* A Practical Beginner's Guide to Cyclic Voltammetry. *J. Chem. Educ.* **95**, 197–206 (2018).
137. Scholz, F. *Electroanalytical Methods Guide to Experiments and Applications*. Springer (SPRINGER, 2005). doi:10.10071 978-3-662-04757-6
138. Mabbott, G. A. *ELECTROANALYTICAL CHEMISTRY Principles, Best Practices, and Case Studies*. Hoboken, NJ : Wiley (John Wiley & Sons, Inc., 2020).
139. Wang, J. *Analytical electrochemistry*. (John Wiley & Sons, Inc., 2006).
140. Bakker, E. & Pretsch, E. Modern potentiometry. *Angew. Chemie - Int. Ed.* **46**, 5660–5668 (2007).
141. Ding, J. & Qin, W. Recent advances in potentiometric biosensors. *TrAC - Trends Anal. Chem.* **124**, 115803 (2020).
142. Smith, L. A., Glasscott, M. W., Vannoy, K. J. & Dick, J. E. Enzyme Kinetics via Open Circuit Potentiometry. *Anal. Chem.* **92**, 2266–2273 (2020).

143. Rammohan, A. & Sharma, A. Carbon as a MEMS material. *Mater. Fail. MEMS NEMS* 1–20 (2015). doi:10.1002/9781119083887.ch1
144. McCreery, R. L. Advanced carbon electrode materials for molecular electrochemistry. *Chem. Rev.* **108**, 2646–2687 (2008).
145. Wang, C. & Madou, M. From MEMS to NEMS with carbon. *Biosens. Bioelectron.* **20**, 2181–2187 (2005).
146. Schueller, O. J. A., Brittain, S. T., Marzolin, C. & Whitesides, G. M. Fabrication and Characterization of Glassy Carbon MEMS. *Chem. Mater.* **9**, 1399–1406 (1997).
147. Mardegan, A. *et al.* Optimization of Carbon Electrodes Derived from Epoxy-based Photoresist. *J. Electrochem. Soc.* **160**, B132–B137 (2013).
148. Fitzer, E. & Schäfer, W. The effect of crosslinking on the formation of glasslike carbons from thermosetting resins. *Carbon N. Y.* **8**, 353–364 (1970).
149. Pesin, L. A. & Baitinger, E. M. A new structural model of glass-like carbon. *Carbon N. Y.* **40**, 295–306 (2002).
150. Ranganathan, S. & McCreery, R. L. Electroanalytical performance of carbon films with near-atomic flatness. *Anal. Chem.* **73**, 893–900 (2001).
151. DropSens Screen-Printed Electrodes. Available at: https://www.dropsens.com/en/screen_printed_electrodes_pag.html.
152. Hassan, Y. M. Pyrolysed Carbon Electrodes for Bioelectrochemical Applications. *ph.D. Thesis* (2018).
153. Hemanth, S. Fabrication of three-dimensional carbon microelectrodes for electrochemical sensing Fabrication of three-dimensional carbon microelectrodes for electrochemical sensing. (2017).
154. Guckenberger, D. J. & , Theodorus E. de Groot, Alwin M.D. Wanb, David J. Beebe, and E. W. K. Y. Micromilling: A methof for ultra rapif prototyping of plastic mirofluidic devices. *Lab Chip.* **2**, 2364–2378 (2015).
155. Dale, E. B. Y. H. H. & Laidlaw, P. P. Wellcome Physiological. *J. Physiol.* **41(5)**, 318–344 (1910).
156. C. H. Best, H. H. Dale, H. W. Dudley, and W. V. T. The nature of the vaso-dilator constituents of certain tissue extracts. *J. Physiol.* **62(4)**, 397–417 (1927).
157. RILEY JF, W. G. Histamine in tissue mast cells. *J. Physiol.* **Aug; 117(4)**, 72–73 (1952).
158. PATON, W. D. Compound 48/80: a potent histamine liberator. *Br. J. Pharmacol. Chemother.* **6**, 499–508 (1951).
159. Schemann, M. *et al.* The Mast Cell Degranulator Compound 48/80 Directly Activates Neurons. *PLoS One* **7**, (2012).
160. Schayer, R. W. The Origin and Fate of Histamine in the Body. in *In Ciba Foundation Symposium - Histamine (eds G.E.W. Wolstenholme and C.M. O'Connor)* (WILEY). doi:<https://doi.org/10.1002/9780470718957.ch24>
161. Schwelberger, H. G., Ahrens, F., Fogel, W. A. & Sánchez-Jiménez, F. Histamine metabolism. *Histamine H4 Recept. A Nov. Drug Target Immunoregul. Inflamm.* **9788376560**, 63–101 (2013).
162. Rose, B. Rôle of histamine in anaphylaxis and allergy. *Am. J. Med.* **3**, 545–559 (1947).
163. Schwartz, J. -C, Pollard, H. & Quach, T. T. Histamine as a Neurotransmitter in Mammalian Brain: Neurochemical Evidence. *J. Neurochem.* **35**, 26–33 (1980).
164. Fernández-Novoa, L. & Cacabelos, R. Histamine function in brain disorders. *Behav. Brain Res.* **124**, 213–233 (2001).
165. Moon, J. M., Thapliyal, N., Hussain, K. K., Goyal, R. N. & Shim, Y. B. Conducting polymer-based electrochemical biosensors for neurotransmitters: A review. *Biosens. Bioelectron.* **102**, 540–552 (2018).
166. Baranwal, A. & Chandra, P. Clinical implications and electrochemical biosensing of monoamine neurotransmitters in body fluids, in vitro, in vivo, and ex vivo models. *Biosens. Bioelectron.* **121**, 137–152 (2018).
167. Parsons, M. E. & Ganellin, C. R. Histamine and its receptors. *Br. J. Pharmacol.* **147**, 127–135 (2006).
168. Haas, H. L., Selbach, O. & Sergeeva, O. A. *Sleep and sleep states: Histamine role. The Curated Reference Collection in Neuroscience and Biobehavioral Psychology* (Elsevier, 2016). doi:10.1016/B978-0-12-809324-5.02851-0
169. Yadav, S., Nair, S. S., Sai, V. V. R. & Satija, J. Nanomaterials based optical and electrochemical sensing of histamine: Progress and perspectives. *Food Res. Int.* **119**, 99–109 (2019).

170. Ahangari, H., Kurbanoglu, S., Ehsani, A. & Uslu, B. Latest trends for biogenic amines detection in foods: Enzymatic biosensors and nanozymes applications. *Trends in Food Science and Technology* **112**, 75–87 (2021).
171. Hidouri, S. *et al.* Potentiometric sensing of histamine using immobilized enzymes on layered double hydroxides. *J. Food Sci. Technol.* (2020). doi:10.1007/s13197-020-04795-7
172. Serrano, V. M., Cardoso, A. R., Diniz, M. & Sales, M. G. F. In-situ production of Histamine-imprinted polymeric materials for electrochemical monitoring of fish. *Sensors Actuators, B Chem.* **311**, 127902 (2020).
173. Munir, M. A. *et al.* The Application of Polyurethane-LiClO₄ to Modify Screen-Printed Electrodes Analyzing Histamine in Mackerel Using a Voltammetric Approach. *ACS Omega* **7**, 5982–5991 (2022).
174. Niculescu, M. *et al.* Redox hydrogel-based amperometric bienzyme electrodes for fish freshness monitoring. *Anal. Chem.* **72**, 1591–1597 (2000).
175. Lee, M. Y., Wu, C. C., Sari, M. I. & Hsieh, Y. H. A disposable non-enzymatic histamine sensor based on the nafion-coated copper phosphate electrodes for estimation of fish freshness. *Electrochim. Acta* **283**, 772–779 (2018).
176. Hassan, A. H. A. *et al.* Biomimetic magnetic sensor for electrochemical determination of scombrotoxin in fish. *Talanta* **194**, 997–1004 (2019).
177. Serrano, V. M., Cardoso, A. R., Diniz, M. & Sales, M. G. F. In-situ production of Histamine-imprinted polymeric materials for electrochemical monitoring of fish. *Sensors Actuators, B Chem.* **311**, 127902 (2020).
178. Trevisani, M. *et al.* Biosensing the histamine producing potential of bacteria in tuna. *Front. Microbiol.* **10**, 1–11 (2019).
179. Hu, B., Zhang, N., Li, H. & Sun, C. A non-enzymatic Electrochemical Sensor Based on rGO-PPy for Rapid and Sensitive Determination of Histamine in Meat. *Int. J. Electrochem. Sci.* **16**, 1–13 (2021).
180. Pérez, S., Bartrolí, J. & Fàbregas, E. Amperometric biosensor for the determination of histamine in fish samples. *Food Chem.* **141**, 4066–4072 (2013).
181. Draisci, R. *et al.* Determination of biogenic amines with an electrochemical biosensor and its application to salted anchovies. *Food Chem.* **62**, 225–232 (1998).
182. Koçoğlu, İ. O., Erden, P. E. & Kiliç, E. Disposable biogenic amine biosensors for histamine determination in fish. *Anal. Methods* **12**, 3802–3812 (2020).
183. Parate, K. *et al.* Aerosol-jet-printed graphene electrochemical histamine sensors for food safety monitoring. *2D Mater.* **7**, (2020).
184. Vanegas, D. C. *et al.* Laser scribed graphene biosensor for detection of biogenic amines in food samples using locally sourced materials. *Biosensors* **8**, (2018).
185. Anithaa, A. C., Mayil Vealan, S. B., Veerapandi, G. & Sekar, C. Highly efficient non-enzymatic electrochemical determination of histamine based on tungsten trioxide nanoparticles for evaluation of food quality. *J. Appl. Electrochem.* (2021). doi:10.1007/s10800-021-01608-3
186. Torre, R., Costa-Rama, E., Nouws, H. P. A. & Delerue-Matos, C. Screen-printed electrode-based sensors for food spoilage control: Bacteria and biogenic amines detection. *Biosensors* **10**, (2020).
187. Veseli, A. *et al.* Electrochemical determination of histamine in fish sauce using heterogeneous carbon electrodes modified with rhenium(IV) oxide. *Sensors Actuators, B Chem.* **228**, 774–781 (2016).
188. Rodríguez-méndez, M. L., Gay, M., Apetrei, C. & Saja, J. A. De. Biogenic amines and fish freshness assessment using a multisensor system based on voltammetric electrodes . Comparison between CPE and screen-printed electrodes. *Electrochim. Acta* **54**, 7033–7041 (2009).
189. Herrera-Chacón, A., Dinç-Zor, Ş. & del Valle, M. Integrating molecularly imprinted polymer beads in graphite-epoxy electrodes for the voltammetric biosensing of histamine in wines. *Talanta* **208**, 120348 (2020).
190. Liu, J. & Cao, Y. An electrochemical sensor based on an anti-fouling membrane for the determination of histamine in fish samples. *Anal. Methods* **13**, 685–694 (2021).
191. Compagnone, D., Isoldi, G., Moscone, D. & Palleschi, G. Amperometric detection of biogenic amines in cheese using immobilised diamine oxidase. *Anal. Lett.* **34**, 841–854 (2001).
192. Geto, A., Tessema, M. & Admassie, S. Determination of histamine in fish muscle at multi-walled carbon nanotubes

- coated conducting polymer modified glassy carbon electrode. *Synth. Met.* **191**, 135–140 (2014).
193. Chemnitiu, G. C. & Bilitewski, U. Development of screen-printed enzyme electrodes for the estimation of fish quality. *Sensors Actuators, B Chem.* **32**, 107–113 (1996).
 194. Katsu, T., Kanamitsu, M., Hirota, T., Tasaka, K. & Fujita, Y. IN SITU DETECTION OF HISTAMINE RELEASED FROM MAST CELLS BY USING A HISTAMINE-SENSITIVE MEMBRANE ELECTRODE. *Chem. Pharm. Bull.* **34**, 3968–3970 (1986).
 195. Loughran, M. G., Hall, J. M., Turner, A. P. F. & Davidson, V. L. Amperometric detection of histamine at a quinoprotein dehydrogenase enzyme electrode. *Biosens. Bioelectron.* **10**, 569–576 (1995).
 196. Pihel, K., Hsieh, S., Jorgenson, J. W. & Wightman, R. M. Electrochemical Detection of Histamine and 5-Hydroxytryptamine at Isolated Mast Cells. *Anal. Chem.* **67**, 4514–4521 (1995).
 197. Niwa, O., Kurita, R., Hayashi, K., Horiuchi, T. & Torimitsu, K. Continuous measurement of histamine from rat basophilic leukemia cells. *Sensors and Actuators B-chemical* 43–51 (2000).
 198. Lim, T. K., Ohta, H. & Matsunaga, T. Microfabricated on-chip-type electrochemical flow immunoassay system for the detection of histamine released in whole blood samples. *Anal. Chem.* **75**, 3316–3321 (2003).
 199. Ahmed, S. *et al.* Hierarchical Molecularly Imprinted Inverse Opal-Based Platforms for Highly Selective and Sensitive Determination of Histamine. *ACS Appl. Polym. Mater.* **4**, 2783–2793 (2022).
 200. Horemans, F. *et al.* MIP-based sensor platforms for the detection of histamine in the nano- and micromolar range in aqueous media. *Sensors Actuators, B Chem.* **148**, 392–398 (2010).
 201. Akhoundian, M., Rüter, A. & Shinde, S. Ultratrace detection of histamine using a molecularly-imprinted polymer-based voltammetric sensor. *Sensors (Switzerland)* **17**, (2017).
 202. John Ho, L. S., Fogel, R. & Limson, J. L. Generation and screening of histamine-specific aptamers for application in a novel impedimetric aptamer-based sensor. *Talanta* **208**, 120474 (2020).
 203. Mahmoud, A. M., Alkahtani, S. A., Alyami, B. A. & El-Wekil, M. M. Dual-recognition molecularly imprinted aptasensor based on gold nanoparticles decorated carboxylated carbon nanotubes for highly selective and sensitive determination of histamine in different matrices. *Anal. Chim. Acta* **1133**, 58–65 (2020).
 204. Xu, S., Wu, F., Mu, F. & Dai, B. The preparation of Fe-based peroxidase mimetic nanozymes and for the electrochemical detection of histamine. *J. Electroanal. Chem.* **908**, 116088 (2022).
 205. Sarada, B. V., Rao, T. N., Tryk, D. A. & Fujishima, A. Electrochemical oxidation of histamine and serotonin at highly boron-doped diamond electrodes. *Anal. Chem.* **72**, 1632–1638 (2000).
 206. Bitziou, E., O'Hare, D. & Patel, B. A. Simultaneous detection of pH changes and histamine release from oxyntic glands in isolated stomach. *Anal. Chem.* **80**, 8733–8740 (2008).
 207. Samaranyake, S. *et al.* In vivo histamine voltammetry in the mouse preamillary nucleus. *Analyst* **140**, 3759–3765 (2015).
 208. Degefu, H., Amare, M., Tessema, M. & Admassie, S. Lignin modified glassy carbon electrode for the electrochemical determination of histamine in human urine and wine samples. *Electrochim. Acta* **121**, 307–314 (2014).
 209. Niculescu, M. *et al.* Amine oxidase based amperometric biosensors for histamine detection. *Electroanalysis* **12**, 369–375 (2000).
 210. Zeng, K., Tachikawa, H., Zhu, Z. & Davidson, V. L. Amperometric detection of histamine with a methylamine dehydrogenase polypyrrole-based sensor. *Anal. Chem.* **72**, 2211–2215 (2000).
 211. Iwaki, S. *et al.* Real-time monitoring of histamine released from rat basophilic leukemia (RBL-2H3) cells with a histamine microsensor using recombinant histamine oxidase. *Anal. Biochem.* **304**, 236–243 (2002).
 212. Ryosuke YAMADA, Nobutaka FUJIEDA, Maiko TSUTSUMI, Seiya TSUJIMURA, Osamu SHIRAI, and K. K. Bioelectrochemical Determination at HistamineDehydrogenase-based Electrodes. *Electrochem. commun.* **76**, 600–602 (2008).
 213. Komori, K., Komatsu, Y., Nakane, M. & Sakai, Y. Bioelectrochemical detection of histamine release from basophilic leukemia cell line based on histamine dehydrogenase-modified cup-stacked carbon nanofibers. *Bioelectrochemistry* **138**, 107719 (2021).

214. Delle, L. E. *et al.* Impedimetric immunosensor for the detection of histamine based on reduced graphene oxide. *Phys. Status Solidi Appl. Mater. Sci.* **212**, 1327–1334 (2015).
215. Yang, M., Zhang, J. & Chen, X. Competitive electrochemical immunosensor for the detection of histamine based on horseradish peroxidase initiated deposition of insulating film. *J. Electroanal. Chem.* **736**, 88–92 (2015).
216. Bongaers, E. *et al.* A MIP-based biomimetic sensor for the impedimetric detection of histamine in different pH environments. *Phys. Status Solidi A* **207**, 837–843 (2010).
217. Peeters, M. *et al.* Impedimetric detection of histamine in bowel fluids using synthetic receptors with pH-optimized binding characteristics. *Anal. Chem.* **85**, 1475–1483 (2013).
218. Amini, M. K., Shahrokhian, S. & Tangestaninejad, S. Porphyrins as carriers in poly(vinyl chloride)-based membrane potentiometric sensors for histamine. *Analyst* **124**, 1319–1322 (1999).
219. Robinson, D. L., Hermans, A., Seipel, A. T. & Wightman, R. M. Monitoring rapid chemical communication in the brain. *Chem. Rev.* **108**, 2554–2584 (2008).
220. Hashemi, P., Dankoski, E. C., Wood, K. M., Ambrose, R. E. & Wightman, R. M. In vivo electrochemical evidence for simultaneous 5-HT and histamine release in the rat substantia nigra pars reticulata following medial forebrain bundle stimulation. *J. Neurochem.* **118**, 749–759 (2011).
221. Travis, E. R., Wang, Y. M., Michael, D. J., Caron, M. G. & Wightman, R. M. Differential quantal release of histamine and 5-hydroxytryptamine from mast cells of vesicular monoamine transporter 2 knockout mice. *Proc. Natl. Acad. Sci. U. S. A.* **97**, 162–167 (2000).
222. Tatham, P. E. R., Duchon, M. R. & Millar, J. Monitoring exocytosis from single mast cells by fast voltammetry. *Pflügers Arch. Eur. J. Physiol.* **419**, 409–414 (1991).
223. Puthongkham, P. & Venton, B. J. Recent advances in fast-scan cyclic voltammetry. *Analyst* **145**, 1087–1102 (2020).
224. Puthongkham, P., Lee, S. T. & Jill Venton, B. Mechanism of histamine oxidation and electropolymerization at carbon electrodes. *Anal. Chem.* **91**, (2019).
225. Berger, S. N. & Hashemi, P. Brain chemistry | neurotransmitters. *Encycl. Anal. Sci.* **1**, 316–331 (2019).
226. Torre, R., Costa-Rama, E., Lopes, P., Nouws, H. P. A. & Delerue-Matos, C. Amperometric enzyme sensor for the rapid determination of histamine. *Anal. Methods* **11**, 1155–1158 (2019).
227. Torre, R., Costa-Rama, E., Nouws, H. P. A. & Delerue-Matos, C. Diamine oxidase-modified screen-printed electrode for the redox-mediated determination of histamine. *J. Anal. Sci. Technol.* **11**, 4–11 (2020).
228. Niculescu, M. *et al.* Detection of histamine and other biogenic amines using biosensors based on amine oxidase. *Inflamm. Res.* **50**, 146–148 (2001).
229. Carsol, M. A. & Mascini, M. Diamine oxidase and putrescine oxidase immobilized reactors in flow injection analysis: A comparison in substrate specificity. *Talanta* **50**, 141–148 (1999).
230. Collins, J. F. *Copper nutrition and biochemistry and human (patho)physiology. Advances in Food and Nutrition Research* **96**, (Elsevier Inc., 2021).
231. Takagi, K. & Shikata, S. Flow injection determination of histamine with a histamine dehydrogenase-based electrode. *Anal. Chim. Acta* **505**, 189–193 (2004).
232. Chen, W., Cai, S., Ren, Q. Q., Wen, W. & Zhao, Y. Di. Recent advances in electrochemical sensing for hydrogen peroxide: A review. *Analyst* **137**, 49–58 (2012).
233. Pundir, C. S., Deswal, R. & Narwal, Vinay. Quantitative analysis of hydrogen peroxide with special emphasis on biosensors. *Bioprocess Biosyst. Eng.* **41**, 313–329 (2018).
234. Karyakin, A. A., Karyakina, E. E. & Gorton, L. Prussian-Blue-based amperometric biosensors in flow-injection analysis. *Talanta* **43**, 1597–1606 (1996).
235. Karyakin, A. A. Advances of Prussian blue and its analogues in (bio)sensors. *Curr. Opin. Electrochem.* **5**, 92–98 (2017).
236. Yagati, A. K. & Choi, J. W. Protein Based Electrochemical Biosensors for H₂O₂ Detection Towards Clinical Diagnostics. *Electroanalysis* **26**, 1259–1276 (2014).

237. Shamkhalichenar, H. & Choi, J.-W. Review—Non-Enzymatic Hydrogen Peroxide Electrochemical Sensors Based on Reduced Graphene Oxide. *J. Electrochem. Soc.* **167**, 037531 (2020).
238. Chen, S., Yuan, R., Chai, Y. & Hu, F. Electrochemical sensing of hydrogen peroxide using metal nanoparticles: A review. *Microchim. Acta* **180**, 15–32 (2013).
239. Dhara, K. & Mahapatra, D. R. Recent advances in electrochemical nonenzymatic hydrogen peroxide sensors based on nanomaterials: a review. *J. Mater. Sci.* **54**, 12319–12357 (2019).
240. Su, Y., Zhou, X., Long, Y. & Li, W. Immobilization of horseradish peroxidase on amino-functionalized carbon dots for the sensitive detection of hydrogen peroxide. *Microchim. Acta* **185**, (2018).
241. Zheng, X. *et al.* A hydrogen peroxide biosensor based on horseradish peroxidase/poly(L-leucine)/polydopamine modified glassy carbon electrode. *Russ. J. Electrochem.* **53**, 443–451 (2017).
242. Campanella, L., Roversi, R., Sammartino, M. P. & Tomassetti, M. Hydrogen peroxide determination in pharmaceutical formulations and cosmetics using a new catalase biosensor. *J. Pharm. Biomed. Anal.* **18**, 105–116 (1998).
243. Dramińska, S. & Bilewicz, R. Bionzymatic mediatorless sensing of total hydrogen peroxide with catalase and multi-copper enzyme co-adsorbed at carbon nanotube-modified electrodes. *Sensors Actuators, B Chem.* **248**, 493–499 (2017).
244. Liu, D., Guo, Q., Zhang, X., Hou, H. & You, T. PdCo alloy nanoparticle-embedded carbon nanofiber for ultrasensitive nonenzymatic detection of hydrogen peroxide and nitrite. *J. Colloid Interface Sci.* **450**, 168–173 (2015).
245. Thirumalraj, B., Zhao, D. H., Chen, S. M. & Palanisamy, S. Non-enzymatic amperometric detection of hydrogen peroxide in human blood serum samples using a modified silver nanowire electrode. *J. Colloid Interface Sci.* **470**, 117–122 (2016).
246. Yao, Z., Yang, X., Wu, F., Wu, W. & Wu, F. Synthesis of differently sized silver nanoparticles on a screen-printed electrode sensitized with a nanocomposites consisting of reduced graphene oxide and cerium(IV) oxide for nonenzymatic sensing of hydrogen peroxide. *Microchim. Acta* **183**, 2799–2806 (2016).
247. Sakthivel, K. *et al.* A novel synthesis of non-aggregated spinel nickel ferrite nanosheets for developing non-enzymatic reactive oxygen species sensor in biological samples. *J. Electroanal. Chem.* **820**, 161–167 (2018).
248. Liu, H., Weng, L. & Yang, C. A review on nanomaterial-based electrochemical sensors for H₂O₂, H₂S and NO inside cells or released by cells. *Microchim. Acta* **184**, 1267–1283 (2017).
249. Pan, Y. *et al.* Hierarchical hybrid film of MnO₂ nanoparticles/multi-walled fullerene nanotubes-graphene for highly selective sensing of hydrogen peroxide. *Talanta* **141**, 86–91 (2015).
250. De Tacconi, N. R., Rajeshwar, K. & Lezna, R. O. Metal hexacyanoferrates: Electrosynthesis, in situ characterization, and applications. *Chem. Mater.* **15**, 3046–3062 (2003).
251. Borràs-Brull, M., Blondeau, P. & Riu, J. The Use of Conducting Polymers for Enhanced Electrochemical Determination of Hydrogen Peroxide. *Crit. Rev. Anal. Chem.* **0**, 1–14 (2020).
252. Tiwari, J. N., Vij, V., Kemp, K. C. & Kim, K. S. Engineered carbon-nanomaterial-based electrochemical sensors for biomolecules. *ACS Nano* **10**, 46–80 (2016).
253. Peng, M., Zhao, Y., Chen, D. & Tan, Y. Free-Standing 3D Electrodes for Electrochemical Detection of Hydrogen Peroxide. *ChemCatChem* **11**, 4222–4237 (2019).
254. Neal, C. J. *et al.* Picomolar Detection of Hydrogen Peroxide using Enzyme-free Inorganic Nanoparticle-based Sensor. *Sci. Rep.* **7**, 1–10 (2017).
255. Zhang, X. *et al.* Nickel cobaltite micro-nano structures@PEDOT/graphene hybrid: A synthetic strategy constructed high performance biosensing interface. *Mater. Des.* **186**, 108310 (2020).
256. Liu, J. *et al.* Sensitivity enhancement of electrochemical biosensor via cobalt nanoflowers on graphene and protein conformational intermediate. *J. Electroanal. Chem.* **799**, 270–277 (2017).
257. Huang, B., Wang, Y., Lu, Z., Du, H. & Ye, J. One pot synthesis of palladium-cobalt nanoparticles over carbon nanotubes as a sensitive non-enzymatic sensor for glucose and hydrogen peroxide detection. *Sensors Actuators, B Chem.* **252**, 1016–1025 (2017).
258. Hao, C. *et al.* Preparation and Characterization of Fe₂O₃ Nanoparticles by Solid-Phase Method and Its Hydrogen

- Peroxide Sensing Properties. *ACS Sustain. Chem. Eng.* **4**, 1069–1077 (2016).
259. Eguilaz, M. *et al.* Recent advances in the development of electrochemical hydrogen peroxide carbon nanotube-based (bio)sensors. *Curr. Opin. Electrochem.* **14**, 157–165 (2019).
 260. Liu, F. *et al.* Green synthesis of porous graphene and its application for sensitive detection of hydrogen peroxide and 2,4-dichlorophenoxyacetic acid. *Electrochim. Acta* **295**, 615–623 (2019).
 261. Kumar, J. S., Murmu, N. C. & Kuila, T. Recent trends in the graphene-based sensors for the detection of hydrogen peroxide. *AIMS Mater. Sci.* **5**, 422–466 (2018).
 262. Gulaboski, R., Mirčeski, V., Kappl, R., Hoth, M. & Bozem, M. Review—Quantification of Hydrogen Peroxide by Electrochemical Methods and Electron Spin Resonance Spectroscopy. *J. Electrochem. Soc.* **166**, G82–G101 (2019).
 263. Matos-Peralta, Y. & Antuch, M. Review—Prussian Blue and Its Analogs as Appealing Materials for Electrochemical Sensing and Biosensing. *J. Electrochem. Soc.* **167**, 037510 (2020).
 264. Koncki, R. Chemical sensors and biosensors based on Prussian blues. *Crit. Rev. Anal. Chem.* **32**, 79–96 (2002).
 265. Karyakin, A. A. Prussian blue and its analogues: Electrochemistry and analytical applications. *Electroanalysis* **13**, 813–819 (2001).
 266. Karyakin, A. A., Karyakina, E. E. & Gorton, L. The electrocatalytic activity of Prussian blue in hydrogen peroxide reduction studied using a wall-jet electrode with continuous flow. *J. Electroanal. Chem.* **456**, 97–104 (1998).
 267. Itaya, K., Uchida, I. & Toshima, S. Catalysis of the Reduction of Molecular Oxygen at Mixed Valence Complex Modified Electrodes of Prussian Blue Analogs. *Nippon Kagaku Kaishi* **1984**, 1849–1853 (1984).
 268. Neff, V. D. Electrochemical Oxidation and Reduction of Thin Films of Prussian Blue. *J. Electrochem. Soc.* **125**, 886–887 (1978).
 269. Karyakin, A. A., Karyakina, E. E. & Gorton, L. On the mechanism of H₂O₂ reduction at Prussian Blue modified electrodes. *Electrochem. commun.* **1**, 78–82 (1999).
 270. Ricci, F., Amine, A., Palleschi, G. & Moscone, D. Prussian Blue based screen printed biosensors with improved characteristics of long-term lifetime and pH stability. *Biosens. Bioelectron.* **18**, 165–174 (2002).
 271. De Mattos, I. L., Gorton, L. & Ruzgas, T. Sensor and biosensor based on Prussian Blue modified gold and platinum screen printed electrodes. *Biosens. Bioelectron.* **18**, 193–200 (2002).
 272. Salazar, P. *et al.* Prussian Blue and Analogues: Biosensing Applications in Health Care. *Adv. Biomater. Biodevices* **9781118773**, 423–450 (2014).
 273. Zhang, W. *et al.* Prussian Blue Nanoparticles as Multienzyme Mimetics and Reactive Oxygen Species Scavengers. *J. Am. Chem. Soc.* **138**, 5860–5865 (2016).
 274. Huang, J. *et al.* Optimized deposition time boosts the performance of Prussian blue modified nanoporous gold electrodes for hydrogen peroxide monitoring. *Nanotechnology* **31**, (2020).
 275. Chu, Z. *et al.* Template-free growth of regular nano-structured Prussian blue on a platinum surface and its application in biosensors with high sensitivity. *J. Mater. Chem.* **20**, 7815–7820 (2010).
 276. Tabrizi, M. A. & Lahiji, A. A. S. Self-assembling of Prussian blue nanocubic particles on nanoporous glassy carbon and its use in the electrocatalytic reduction of hydrogen peroxide. *J. Iran. Chem. Soc.* **11**, 1015–1020 (2014).
 277. Ricci, F. *et al.* Investigation of the effect of different glassy carbon materials on the performance of Prussian Blue based sensors for hydrogen peroxide. *Electroanalysis* **15**, 175–182 (2003).
 278. McBeth, C., Paterson, A. & Sharp, D. Pad-printed Prussian blue doped carbon ink for real-time peroxide sensing in cell culture. *J. Electroanal. Chem.* **878**, 114537 (2020).
 279. Sato, O., Tao, J. & Zhang, Y. Z. Control of magnetic properties through external stimuli. *Angew. Chemie - Int. Ed.* **46**, 2152–2187 (2007).
 280. Bueno, P. R. *et al.* Changeover during in situ compositional modulation of hexacyanoferrate (Prussian blue) material. *J. Am. Chem. Soc.* **128**, 17146–17152 (2006).
 281. Agrisuelas, J., García-Jareño, J. J., Gimenez-Romero, D. & Vicente, F. Insights on the Mechanism of Insoluble-to-Soluble Prussian Blue Transformation. *J. Electrochem. Soc.* **156**, P149 (2009).

282. Itaya, K., Uchida, I. & Neff, V. D. Electrochemistry of Polynuclear Transition Metal Cyanides: Prussian Blue and Its Analogues. *Acc. Chem. Res.* **19**, 162–168 (1986).
283. Baggio, B. F. *et al.* Morphology and structure of electrodeposited Prussian Blue and Prussian white thin films. *Materials (Basel)*. **12**, 15–21 (2019).
284. García-Jareño, J. J., Sanmatías, A., Navarro-Laboulais, J. & Vicente, F. The role of potassium and hydrogen ions in the Prussian Blue \rightleftharpoons Everitt's Salt process. *Electrochim. Acta* **44**, 395–405 (1998).
285. Karyakin, A. A., Gitelmacher, O. V. & Karyakina, E. E. Prussian Blue-Based First-Generation Biosensor. A Sensitive Amperometric Electrode for Glucose. *Anal. Chem.* **67**, 2419–2423 (1995).
286. Karyakin, A. A. & Karyakina, E. E. Prussian blue-based 'artificial peroxidase' as a transducer for hydrogen peroxide detection. Application to biosensors. *Sensors Actuators, B Chem.* **57**, 268–273 (1999).
287. Ricci, F. & Palleschi, G. Sensor and biosensor preparation, optimisation and applications of Prussian Blue modified electrodes. *Biosens. Bioelectron.* **21**, 389–407 (2005).
288. Murray, R. W. Chemically Modified Electrodes. *Acc. Chem. Res.* **13**, 135–141 (1980).
289. Piernas Muñoz, M. J. & Castillo Martínez, E. Prussian blue and its analogues. Structure, characterization and applications. *SpringerBriefs Appl. Sci. Technol.* 9–22 (2018). doi:10.1007/978-3-319-91488-6_2
290. Zakharchuk, N. F. *et al.* A comparative study of Prussian-Blue-modified graphite paste electrodes and solid graphite electrodes with mechanically immobilized Prussian Blue. *J. Electroanal. Chem.* **398**, 23–35 (1995).
291. García-Jareño, J. J., Benito, D., Navarro-Laboulais, J. & Vicente, F. Electrochemical behavior of electrodeposited Prussian blue films on ITO electrodes: An attractive laboratory experience. *J. Chem. Educ.* **75**, 881–884 (1998).
292. Haghighi, B., Varma, S., Alizadeh Sh., F. M., Yigzaw, Y. & Gorton, L. Prussian blue modified glassy carbon electrodes - Study on operational stability and its application as a sucrose biosensor. *Talanta* **64**, 3–12 (2004).
293. Jaffari, S. A. & Turner, A. P. F. Novel hexacyanoferrate(III) modified graphite disc electrodes and their application in enzyme electrodes - Part I. *Biosens. Bioelectron.* **12**, 1–7 (1997).
294. Katic, V. *et al.* 3D Printed Graphene Electrodes Modified with Prussian Blue: Emerging Electrochemical Sensing Platform for Peroxide Detection. *ACS Appl. Mater. Interfaces* **11**, 35068–35078 (2019).
295. Marwan, J., Addou, T. & Bélanger, D. Functionalization of glassy carbon electrodes with metal-based species. *Chem. Mater.* **17**, 2395–2403 (2005).
296. Rojas, D. *et al.* Electrodeposited Prussian Blue on carbon black modified disposable electrodes for direct enzyme-free H₂O₂ sensing in a Parkinson's disease in vitro model. *Sensors Actuators, B Chem.* **275**, 402–408 (2018).
297. Komkova, M. A., Pasquarelli, A., Andreev, E. A., Galushin, A. A. & Karyakin, A. A. Prussian Blue modified boron-doped diamond interfaces for advanced H₂O₂ electrochemical sensors. *Electrochim. Acta* **339**, 135924 (2020).
298. Borisova, A. V., Karyakina, E. E., Costlier, S. & Karyakin, A. A. Current-free deposition of prussian blue with organic polymers: Towards improved stability and mass production of the advanced hydrogen peroxide transducer. *Electroanalysis* **21**, 409–414 (2009).
299. Karyakin, A. A. *et al.* Prussian Blue Based Nanoelectrode Arrays for H₂O₂ Detection. (2004). doi:10.1021/ac034859I
300. Zhang, X. *et al.* Preparation, characterization, and property of polyaniline/Prussian blue micro-composites in a low-temperature hydrothermal process. *Appl. Surf. Sci.* **253**, 9030–9034 (2007).
301. Silva, W. O. *et al.* Oxidative Print Light Synthesis Thin Film Deposition of Prussian Blue. *ACS Appl. Electron. Mater.* **2**, 927–935 (2020).
302. De Mattos, I. L., Gorton, L., Ruzgas, T. & Karyakin, A. A. Sensor for hydrogen peroxide based on Prussian Blue modified electrode: Improvement of the operational stability. *Anal. Sci.* **16**, 795–798 (2000).
303. Duncan, J. F. & Wigley, P. W. R. The Electronic Structure of the Iron Atoms in Complex Iron Cyanides. 1120–1125 (1959).
304. Wang, Z. *et al.* Stability improvement of Prussian blue in nonacidic solutions via an electrochemical post-treatment method and the shape evolution of Prussian blue from nanospheres to nanocubes. *Analyst* **139**, 1127–1133 (2014).

305. Rosseinsky, D. R. & Glidle, A. EDX, Spectroscopy, and Composition Studies of Electrochromic Iron(III) Hexacyanoferrate(II) Deposition. *J. Electrochem. Soc.* **150**, C641 (2003).
306. Itaya, K., Uchida, I. & Neff, V. D. *Mixed-Valence Compounds; Theory and Applications in Chemistry. Nato Advanced Study Institutes Series; D. Reidel: Dordrecht, The Netherlands* **19**, (UTC, 1986).
307. H. J. Buser, D. Schwarzenbach, W. Petter, and A. L. The crystal structure of Prussian Blue: Fe₄[Fe(CN)₆]₃.xH₂O. *Inorg. Chem.* **16**, 2704–2710 (1977).
308. Oh, I., Lee, H., Yang, H. & Kwak, J. Ion and water transports in Prussian blue films investigated with electrochemical quartz crystal microbalance. *Electrochem. commun.* **3**, 274–280 (2001).
309. Lundgren, C. A. & Murray, R. W. Observations on the Composition of Prussian Blue Films and Their Electrochemistry. *Inorg. Chem.* **27**, 933–939 (1988).
310. Floris, G. & Finazzi Agrò, A. Amine Oxidases. *Encycl. Biol. Chem. Second Ed.* 87–90 (2013). doi:10.1016/B978-0-12-378630-2.00182-1
311. Medda, R. *et al.* Cu(I)-semiquinone radical species in plant copper-amine oxidases. *FEBS Lett.* **453**, 1–5 (1999).
312. Dooley, D. M. *et al.* Coordination Chemistry of Copper-Containing Amine Oxidases: Nuclear Magnetic Relaxation Dispersion Studies of Copper Binding, Solvent-Water Exchange, Substrate and Inhibitor Binding, and Protein Aggregation. *J. Am. Chem. Soc.* **113**, 754–761 (1991).
313. GLATZ, Z., KOVAR, J., MACHOLAN, L. & PEC, P. (*Pisum sativum*) diamine oxidase contains pyrroloquinoline quinone as a cofactor. *Biochem. J.* **242**, 603–606 (1987).
314. Kumar, V. *et al.* Crystal structure of a eukaryotic (pea seedling) copper-containing amine oxidase at 2.2 Å resolution. *Structure* **4**, 943–955 (1996).
315. Zhang, J. X. J. & Hoshino, K. *Optical transducers: Optical molecular sensing and spectroscopy. Molecular Sensors and Nanodevices* (2019). doi:10.1016/b978-0-12-814862-4.00005-3
316. Yoon, J. Y. Introduction to Biosensors: From Electric Circuits to Immunosensors: Second edition. *Introd. to Biosens. From Electr. Circuits to Immunosensors Second Ed.* 1–331 (2016). doi:10.1007/978-3-319-27413-3
317. Zwinkels, J. C., DeRose, P. C. & Leland, J. E. *Spectral Fluorescence Measurements. Experimental Methods in the Physical Sciences* **46**, (Elsevier Inc., 2014).
318. Fasman, G. D. *Practical Handbook of Biochemistry and Molecular Biology.* (CRC Press, 1989).
319. Stahl Skov, P., Norn, S. & Weeke, B. A new method for detecting histamine release. *Agents Actions* **14**, 414–416 (1984).
320. Drabik, A., Bodzoń-Kuśakowska, A. & Silberring, J. Gel Electrophoresis. in *Proteomic Profiling and Analytical Chemistry: The Crossroads: Second Edition* 115–143 (2016). doi:10.1016/B978-0-444-63688-1.00007-0
321. Sirisha, V. L., Jain, A. & Jain, A. *Enzyme Immobilization: An Overview on Methods, Support Material, and Applications of Immobilized Enzymes. Advances in Food and Nutrition Research* **79**, (Elsevier Inc., 2016).
322. Datta, S., Christena, L. R. & Rajaram, Y. R. S. Enzyme immobilization: an overview on techniques and support materials. *3 Biotech* **3**, 1–9 (2013).

Appendix A: Paper I

doi.org/10.1002/elan.202100387

Hydrogen Peroxide Detection Using Prussian Blue-modified 3D Pyrolytic Carbon Microelectrodes

Sheida Esmail Tehrani,^[a] Long Quang Nguyen,^[a] Giulia Garelli,^[a] Bettina M. Jensen,^[b] Tautgirdas Ruzgas,^[c] Jenny Emnéus,^[d] and Stephan Sylvest Keller^[a]

Abstract: A highly sensitive amperometric Prussian blue-based hydrogen peroxide sensor was developed using 3D pyrolytic carbon microelectrodes. A 3D printed multi-electrode electrochemical cell enabled simultaneous highly reproducible Prussian blue modification on multiple carbon electrodes. The effect of oxygen plasma pretreatment and deposition time on Prussian blue electro-

deposition was studied. The amperometric response of 2D and 3D sensors to the addition of hydrogen peroxide in μM and sub- μM concentrations in phosphate buffer was investigated. A high sensitivity comparable to flow injection systems and a detection limit of $0.16 \mu\text{M}$ was demonstrated with 3D pyrolytic carbon microelectrodes at stirred batch condition

Keywords: Prussian blue · hydrogen peroxide sensor · amperometry · pyrolytic carbon

1 Introduction

Detection of hydrogen peroxide (H_2O_2) is highly relevant for food [1] and pharmaceutical [2] industry, biomedical applications [3], environmental monitoring [4,5], chemical synthesis [6] and sustainable energy [7] production. In biological processes, H_2O_2 is generated as an intermediate molecule [3] and as the catalytic by-product of a large number of enzyme-mediated reactions, including glucose [8], cholesterol [9] and lactate [10] oxidation. Being a reactive oxygen species (ROS), elevated H_2O_2 production in the body is an indication for oxidative stress leading to cell and tissue damage, causing early ageing [11], diabetes [12] as well as Alzheimer's, Parkinson's [13] and cardiovascular [14] diseases. Therefore, highly sensitive and real-time monitoring of H_2O_2 is of significant importance for both clinical and industrial applications.

Among the conventional H_2O_2 detection methods including titrimetry [15], fluorescence [16], spectrophotometry [17], chemiluminescence [18], chromatography [19] and electrochemistry [19–21], the latter is rapid and precise for quantitative analysis combined with the potential for miniaturization and low-cost manufacturing of electrochemical sensors. Since H_2O_2 is an electroactive molecule, undergoing a two-electron reaction process at different pH levels, its oxidation or reduction can be studied quantitatively in real-time by electroanalysis. An electrochemical H_2O_2 sensor converts the chemical reaction into an electrical signal proportional to the amount of oxidized/reduced H_2O_2 in the sample. However, direct electrochemical detection of H_2O_2 has major impediments on the majority of electrode materials. Due to slow electron transfer kinetics, very high overpotentials are required to drive the reaction, which is a challenge in the presence of interfering species usually present in biological samples.

In order to enhance the electron transfer kinetics and lower the required overpotential for the H_2O_2 redox reaction, electrochemical H_2O_2 sensors have been developed by modifying electrodes with enzymatic [2,22–24] and non-enzymatic [25–32] electrocatalysts. The advantage of using non-enzymatic bioelectrocatalysts is their very high selectivity and good sensitivity towards low concentrations of H_2O_2 . However, bioelectrocatalysts are often associated with high costs, instability, loss of catalytic activity and time-consuming sensor preparation. Therefore, research efforts have been dedicated to design efficient enzyme-free electrocatalysts with abundant active sites that can be integrated with suitable conductive substrates to maximize the charge transfer at the electrode/electrolyte interface [21,29,30,33]. Noble metals [34] such as Au, Pt and Pd, and their alloys [29] (e.g. AuAg, PtPd) in the form of nanostructures and nanoparticles, metal oxides (MnO_2 , TiO_2) and metal complexes

- [a] S. Esmail Tehrani, L. Quang Nguyen, G. Garelli, S. Sylvest Keller
National Centre for Nano Fabrication and Characterization (DTU Nanolab), Technical University of Denmark, Ørstedes Plads, Building 347, 2800 Kongens Lyngby, Denmark
- [b] B. M. Jensen
Allergy Clinic, Copenhagen University Hospital at Herlev-Gentofte, Gentofte Hospitalsvej 8, 2900 Hellerup, Denmark
- [c] T. Ruzgas
Biofilms Research Center for Biointerfaces, Department of Biomedical Science, Malmö University, Per Albin Hanssons väg 35, Forskaren Building, 21432 Malmö, Sweden
- [d] J. Emnéus
Department of Biotechnology and Biomedicine (DTU Bioengineering), Technical University of Denmark, Produktionstorvet, Building 423, 2800 Kongens Lyngby, Denmark

 Supporting information for this article is available on the WWW under <https://doi.org/10.1002/elan.202100387>

[35] (ferric hexacyanoferrate, metallophthalocyanines), organic and polymeric materials such as redox dyes and conductive polymers [36], as well as carbon-based [37,38] nanomaterials (carbon nanotubes, graphene, doped carbon) have been explored as H_2O_2 electrocatalysts.

Among the metal complexes, Prussian blue (PB), which is a metal hexacyanoferrate, has been extensively used as an electrocatalyst for H_2O_2 sensing [39–45]. The reduced form of PB, which is called Prussian white (PW), catalyzes the reduction of H_2O_2 at very low overpotential [46]. The zeolite-like structure of PB only allows the small molecule of H_2O_2 to diffuse into the crystal lattice where it is reduced [47]. The combination of low overpotential and size-exclusion of interfering molecules has promoted PB as a highly selective electrocatalyst for H_2O_2 detection. Electrodes can be modified with PB by electrodeposition in a few seconds. The low cost and ease of synthesis of PB has identified it as an ideal electrocatalyst for commercialization and mass production of sensors [48–50].

When considering the electrochemical transducer platform, 3D functional electrodes of various materials and structures could potentially overcome the limitations of traditional thin film electrodes. Outstanding properties such as large electrochemically active surface area, enhanced mass transport and diffusion, excellent accessibility to active sites and fast kinetics at the electrode/electrolyte interface could provide better sensitivity compared to 2D electrodes [51]. 3D pyrolytic carbon electrodes have been fabricated using cleanroom based microfabrication processes, allowing for excellent tailoring ability of electrode geometry, configuration and properties for a specific application [52]. In several studies, enhanced sensitivity for electrochemical biosensing with 3D pyrolytic carbon electrodes has been demonstrated [53–55].

While there are numerous examples, where PB has been electrodeposited on thin film electrodes of different materials such as gold [56], platinum [56,57], glassy [58–60] and screen-printed [61,62] carbon, there has to date not been any report on using pyrolytic carbon as the electrode material for the development of PB-based H_2O_2 sensors.

Here, we present for the first time, an ultrasensitive simple H_2O_2 sensor based on PB-modified 3D pyrolytic carbon electrodes. For this purpose, 3D micropillar electrodes were designed and fabricated.

Additive manufacturing technology, also commonly known as 3D printing, was implemented to create an electrochemical cell suitable for the pyrolytic carbon electrode chips. 3D printing enables rapid prototyping of complex structures with a variety of materials and resolutions. The user-friendly 3D design and print softwares allow fast design alterations and optimization of the product. Compared with the traditional industrial manufacturing technologies such as injection molding and milling, 3D printing is the most cost-efficient and affordable manufacturing technique for small-scale production purposes in particular due to low waste of raw materials

[63]. With the growing popularity of the 3D printers and their falling prices in the recent years, scientists explored different 3D designs and printable conductive materials for sensor fabrication [64,65] or developed 3D printed electrochemical systems for flow- and batch injection analysis [66], sensing and biosensing [67], electrosynthesis [68], water splitting and energy-related applications [63].

With the 3D printed electrochemical cell, the electrodeposition of PB was optimized to enhance the surface coverage, electroactive surface, and stability of the electrocatalyst on the pyrolytic carbon electrode. Finally, amperometric H_2O_2 detection in μM and sub- μM range was investigated.

2 Materials and Methods

2.1 Materials

Hydrochloric acid (HCl) ACS reagent 37 % Sigma Aldrich, hydrogen peroxide (H_2O_2) 35 % Alfa Aesar, potassium chloride (KCl) 99.5 % Merck Millipore, potassium hexacyanoferrate (II) trihydrate ($\text{K}_4\text{Fe}(\text{CN})_6 \cdot 3\text{H}_2\text{O}$) ACS reagent 98.5–102.0 % Sigma Aldrich, potassium hexacyanoferrate (III) ($\text{K}_3\text{Fe}(\text{CN})_6$) ACS reagent ≥ 99.0 % Sigma Aldrich, iron (III) chloride hexahydrate ($\text{FeCl}_3 \cdot 6\text{H}_2\text{O}$) 99.0–102.0 % Millipore, monobasic potassium phosphate (KH_2PO_4) ≥ 99.0 % Sigma Aldrich, dibasic potassium phosphate (K_2HPO_4) ACS reagent ≥ 98 % Sigma Aldrich, 0.01 M Phosphate Buffered Saline (PBS) pH 7.4 (NaCl 0.138 M; KCl -0.0027 M in 1 L distilled H_2O) Sigma Aldrich, 2-propanol (isopropanol) 70 % in H_2O were all purchased from Sigma-Aldrich Denmark A/S. All stock solutions were prepared freshly before each experiment using double distilled water, unless otherwise stated. 6-inch single side polished silicon wafers were acquired from Siegert Wafer, SU-8 2000 series resist from Kayaku Advanced Materials and propylene glycol methyl ether acetate (PGMEA) from micro resist technology GmbH, Germany.

2.2 Pyrolytic Carbon Electrode Fabrication

Electrode chips with pyrolytic carbon electrodes in 2D and 3D configuration were designed and fabricated for this study. The flat 2D working electrode (2DWE) had a geometrical shape of a circle with a diameter of 4 mm and a surface area of 12.6 mm². The 3D working electrode (3DWE) consisted of additional 284 micropillars with a height of 225 μm and a diameter of 68 μm patterned on top of the 2DWE resulting in a total geometrical surface area of 26.2 mm² [55].

The pyrolytic carbon electrodes were fabricated by photolithography with the negative epoxy photoresist SU-8 followed by pyrolysis as illustrated in Figure 1. First, approximately 6 mL of SU-8 2035 were spin coated on a 6-inch silicon wafer with 600 nm silicon oxide insulating layer. The spin coating was performed on a RCD8 spin coater (Karl-Süss, Germany) with a spread cycle at

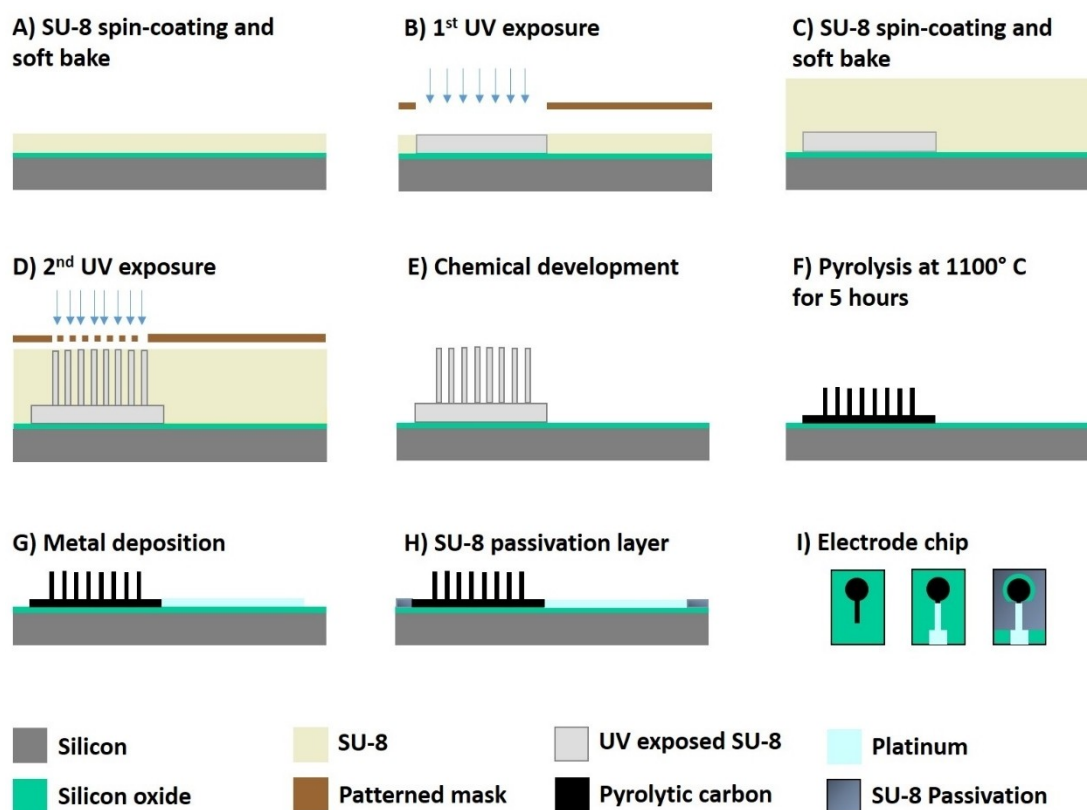


Fig. 1. Schematic representation of 3D pyrolytic carbon electrode fabrication; (A) SU-8 photosensitive resin spin-coated on a silicon wafer with an insulating silicon oxide layer; (B) electrode base patterned in SU-8 by the 1st UV exposure; (C) a thicker SU-8 layer spin-coated over the first layer; (D) micropillars patterned in the thick SU-8 by the 2nd UV exposure; (E) unexposed SU-8 removed during chemical development; (F) 3D pyrolytic carbon formed after 5 hours pyrolysis at 1100°C; (G) Pt lead and contact pad patterned by metal deposition through shadow mask; (H) the silicon chip area including the Pt lead except for the pyrolytic carbon and Pt contact pad passivated by a thin SU-8 layer; (I) Top view of electrode chips after patterning of pyrolytic carbon (left), deposition of metal layer (middle) and patterning of passivation layer (right).

1000 rpm for 10 s at an acceleration of 200 rpm⁻¹ and a thinning cycle at 5000 rpm for 120 s using 1000 rpm⁻¹, resulting in a film with a thickness of 15 μm (Figure 1A). The SU-8 was soft-baked for 15 min at 50°C on a programmable hotplate (Harry Gestigkeit GmbH, Germany) with a temperature ramp of 2°Cmin⁻¹ to remove the solvent. Next, the 2DWE design was patterned on the photoresist-coated wafer by UV exposure on a 365 nm MA6 mask aligner (Karl-Süss, Germany) with a total exposure dose of 2x250 mJcm⁻² (Figure 1B). The exposed areas were crosslinked in a post-exposure-bake (PEB) similar to the soft-bake (SB) but with a duration of 2 hours. For the 3DWE, an additional step of SU-8 photolithography was performed to define the micropillars. SU-8 2075 was dispensed and spin-coated (500 rpm, 30 s, 50 rpm⁻¹ and 1000 rpm, 60 s, 100 rpm⁻¹) followed by a SB for 6 hours at 50°C (Figure 1C). A second spin-coating of SU-8 2075 was performed to obtain the final thickness of approximately 500 μm, followed by a SB for 12 hours. The pattern of the micropillars was transferred by UV exposure with a total dose of 4x250 mJcm⁻² using the mask aligner followed by a PEB for

10 hours at 50°C (Figure 1D). The uncrosslinked SU-8 photoresist was removed by development in PGMEA for 2x40 min (Figure 1E), followed by IPA rinsing and drying in N₂ atmosphere at room temperature. After drying, the samples were flood exposed with the same dose of 4x250 mJcm⁻². The hard-bake step of 15 hours at 90°C was performed for both the 2D and the 3D electrodes to harden and dry out the SU-8 microstructures. Next, the SU-8 samples were pyrolysed for 5 hours at 1100°C in N₂ atmosphere in a high temperature furnace (PEO-04, ATV Technologies, Germany) (Figure 1F) [69]. The SU-8 microstructures shrink during the pyrolysis process, resulting in 225 ± 1 μm high pillars with a diameter of 68 ± 2 μm while the thickness of the 2DWE was reduced to 2 μm. After obtaining pyrolytic carbon, metal leads and contact pads of 150 nm Pt with a 15 nm Ti adhesion layer were patterned by e-beam metal deposition through a shadow mask (Figure 1G). Finally, the complete electrode chip except the pyrolytic carbon WE and the metal contact pads were passivated by a 5 μm thin SU-8 layer (Figure 1H). The passivation layer confines the sensing area to the pyrolytic carbon surface and at the same time

protects the metal and carbon from delamination. The wafer was diced into 84 electrode chips with a dimension of 10×16 mm.

2.3 Design and 3D Printing of Electrochemical Cells

A 3D printed electrochemical cell was used for PB electrodeposition and characterization during electrode preparation. The electrochemical cell allowed performing simultaneous experiments on four pyrolytic carbon electrodes and enabled statistical data collection in an efficient manner. It was designed using Autodesk Fusion 360 3D design software and manufactured by stereolithography (SLA) using a Formlabs3 SLA printer with Clear Resin. The post-treatment included 2 times rinsing of the printed objects in fresh isopropanol for 60 min followed by 12 hours immersion in double distilled water and another 12 hours drying at 22°C . The post-processing of the printed objects was completed by curing in the Form Cure UV chamber at 60°C for 60 min.

The 3D printed electrochemical cell was composed of a base plate, a beaker, and a cap as the three main parts

that were printed separately, as shown in Figure 2A–H. The base plate contains four indentations of $10 \text{ mm} \times 16 \text{ mm} \times 0.6 \text{ mm}$, where four electrode chips can be placed (Figure 2A–B). 8 screw holes with a diameter of 2 mm were included at the circumference to mount the beaker part on the base using $2 \text{ mm} \times 20 \text{ mm}$ screws and bolts. The four symmetrically arranged circular openings in the bottom of the beaker defined four wells above the sensing area of the electrodes (Figure 2C–F). The wells had a diameter of 6.6 mm and depth of 2.9 mm. On the bottom side of the beaker, four narrow trenches contain openings of the wells to accommodate four rubber O-rings (black) to seal the sensing area of the electrode (Figure 2D). The beaker had an inner diameter of 35 mm and a depth of 37 mm. A magnet with the length of 10–12 mm fits into the area between the four wells in the bottom of the beaker if magnetic stirring is required (Figure 2F). A cap with openings for mounting of an external counter- (CE) and a reference electrode (RE) and for pipetting of samples was designed (Figure 2G). The assembly of the three parts with the external CE and RE is displayed in

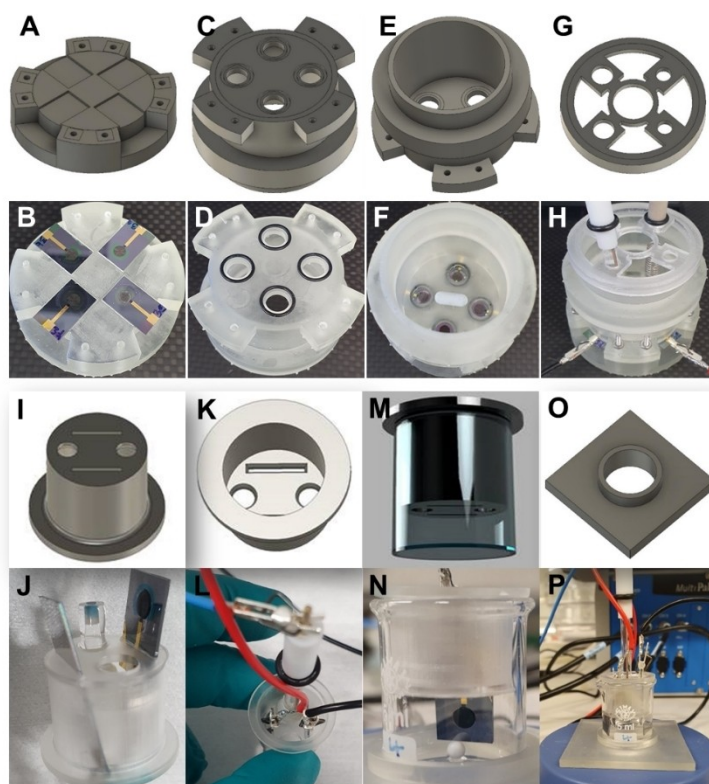


Fig. 2. A) Designed base with four indentations for placing pyrolytic carbon electrode chips; B) 3D printed base with four electrode chips; C) bottom side of the designed beaker with four openings; D) 3D printed beaker with four rubber o-rings to seal the electrodes; E) top view of the designed beaker; F) 3D printed beaker mounted on the base with the electrodes using screws; G) cap designed for insertion of CE and RE into the cell; H) assembled 3D printed electrochemical cell with four electrode chips connected to the potentiostat by micro crocodiles; I) insert design with two apertures for electrode chip and planar CE and two round inlets for RE insertion and sample pipetting; J) 3D printed insert with electrodes; K) top view of the insert with the cavity; L) micro crocodiles inside the cavity providing electrical connection; M) insert designed to fit into a 5 mL glass beaker; N) pyrolytic carbon electrode chip inserted into the glass beaker with the insert; O) foot piece designed to stabilize the small glass beaker during the measurements; P) assembled electrochemical setup for H_2O_2 sensing experiments placed on a compact stirrer and connected to the potentiostat.

Figure 2H. The pyrolytic carbon electrodes were connected to the potentiostat by micro crocodiles.

The actual H₂O₂ sensing experiments were performed with single electrode chips in 5 mL glass beakers to ensure independent measurements. For immersing the sensor chip into the solution inside the glass beaker an insert was designed and 3D printed as shown in Figure 2I–N. It had two 1 mm × 10 mm apertures for the pyrolytic carbon electrode chip and a planar Pt CE (Figure 2I–J). The two round inlets with diameters of 5 mm and 6 mm were devoted to the RE and to sample pipetting, respectively (Figure 2K–L). Micro crocodiles inside the cavity provided connection between the electrodes and the potentiostat. The insert was placed in the glass beaker (Figure 2M–N). A foot piece (Figure 2O) was printed to stabilize the glass beaker on the magnetic stirrer. The assembled electrochemical cell on a compact-size magnetic stirrer (IKA) connected to the potentiostat is pictured in Figure 2P. Multiple 5 mL glass beakers were used in parallel for simultaneous measurements.

2.4 Electrode Pre-treatment and Characterization

The fabricated pyrolytic carbon electrodes were rinsed with isopropanol and distilled water and dried with compressed nitrogen gas. Thereafter, the electrodes were treated by oxygen plasma in a Zepto plasma chamber (Diener Electronic GmbH, Germany) using 40 % of the power corresponding to 120 W for 65 s at 0.6 mbar oxygen pressure.

The electrochemical performance of the plasma-treated electrodes was characterized by cyclic voltammetry in 10 mM K₃Fe(CN)₆/K₄Fe(CN)₆ in PBS pH 7.4 with a potential between −0.8/+0.8 V at a scan rate of 50 mVs^{−1}. Electrodes with reproducible cyclic voltammograms were identified for preparing sensors. A MultiPalmSens4 potentiostat was used to run four simultaneous electrochemical measurements. MultiTrace 4.3 Software was employed for data acquisition. Data treatment and statistical analysis was done using Excel and OriginPro 2018. For each WE, an external Ag/AgCl electrode in 3 M KCl was used as RE, and a silicon chip coated with 15 nm Ti and 150 nm Pt on both sides with a total immersed surface area of approximately 200 mm² was used as a CE.

2.5 Prussian Blue Electrodeposition

Modification of the 2D and 3D pyrolytic carbon electrode surface with PB comprised five steps [70], all performed in the 3D printed electrochemical cell on four electrodes simultaneously. In the first step, the PB was electrodeposited on the pyrolytic carbon in a freshly prepared solution consisting of 2.5 mM K₃Fe(CN)₆, 2.5 mM FeCl₃, 0.1 M HCl and 0.1 M KCl by applying a constant potential of 444 mV vs. Ag/AgCl for varying electrodeposition times of 40, 60, 80 and 100 s. It was observed that if the components of the PB growth solution were mixed and stored before use, the color turned from dark yellow to

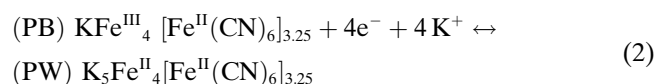
green/blue after approximately 5 hours because the K₃Fe(CN)₆ degraded in acidic solution. Therefore, the four components were prepared separately in distilled water and mixed at the desired concentration immediately before electrodeposition. The growth solution was stirred with a magnet throughout the first step to enhance the PB deposition. In the second step, the electrodeposited PB film was activated in an electrolytic solution containing 0.1 M HCl and 0.1 M KCl by sweeping the potential between 0.4 and −0.1 V (starting at 0.4 V) vs. Ag/AgCl at a scan rate of 50 mVs^{−1} for 25 cycles. As a third step, the electrodes were carefully rinsed with 0.1 M HCl and the PB film was annealed at 100 °C for 1 hour in a convection oven. Next, the modified electrodes were conditioned at −6 mV vs. Ag/AgCl for 600 s followed by 25 cycles between +0.4/−0.1 V at 50 mVs^{−1} in phosphate buffer containing 0.05 M K₂HPO₄/KH₂PO₄ and 0.1 M KCl with pH adjusted to 5.5 using HCl.

2.6 Prussian Blue Characterization

Scanning electron microscopy (SEM Supra, Zeiss, Germany) was used to inspect the integrity of the fabricated micropillars and the PB film deposited on the surface of the pyrolytic carbon electrodes. The electrochemical quality of the PB film after electrodeposition was characterized by cyclic voltammetry in phosphate buffer containing 0.1 M KCl (pH 5.5) in the potential window between −0.1/+0.4 V at a scan rate of 50 mVs^{−1} where the oxidation and reduction of the PW/PB couple occurs. The PB surface coverage Γ on the pyrolytic carbon was calculated using the following equation [56]:

$$\Gamma = \frac{Q}{nFA} \quad (1)$$

where Q is the charge obtained by integrating the cathodic peak current I_c of the cyclic voltammograms of the PB/PW redox reactions (charge consumed for PB reduction), n is the number of electrons per unit cell involved in the redox reaction which is equal to 4 for PB/PW (equation 2) [71], F is the Faraday constant and A is the geometrical area of the electrode. When integrating the I_c , the background (the capacitive current) was subtracted.



In addition, the PB film thickness t was calculated using the equation below [72–74]:

$$t = \Gamma l_0^2 N_A \quad (3)$$

where N_A is Avogadro number and $l_0 = 1.02$ nm is the length of the PB unit cell [75]. Finally, for H₂O₂ detection

the electrodes, which had reproducible cyclic voltammograms for PB/PW redox reactions were selected.

2.7 Hydrogen Peroxide Detection

Phosphate buffer containing 0.05 M K_2HPO_4/KH_2PO_4 and 0.1 M KCl with pH adjusted to 5.5 using HCl was used to record the baseline. Samples were prepared by diluting H_2O_2 (35 %) using the same buffer. The solutions were prepared freshly in dark glasses and were kept on ice ($4^\circ C$) throughout the experiments for the maximum duration of 1 hour to prevent degradation of H_2O_2 due to light and temperature. Amperometry with an applied potential of 0 V, determined from the cyclic voltammograms of the PB/PW redox reaction in phosphate buffer pH 5.5 containing 0.1 M KCl, was used to evaluate the response of the 2D and 3D PB-modified pyrolytic carbon sensors to successive addition of H_2O_2 resulting in concentrations from 0.1 to 10 μM . The H_2O_2 sensing experiments were performed in the 5 mL glass beaker with the insert for immersion of the sensor as well as the RE and CE into 3 mL starting volume of buffer solution. The assembled electrochemical setup was placed on a compact magnetic stirrer. The measurement solution was stirred throughout the experiment using a small magnet (2 mm \times 5 mm). For each concentration of analyte, the average current response of at least three sensors were recorded, the corresponding standard deviations were calculated, and the values were used to construct the calibration curves for 2D and 3D sensors. For this purpose, the current response of each individual sensor to increasing concentrations of H_2O_2 was corrected to the baseline. For each type of sensor, a linear equation, the slope of which indicated the sensitivity of the sensor, was fit to the data points in the dynamic range. The limit of detection (LOD) for each type of sensor was calculated by:

$$LOD = \frac{3 \times SD}{b} \quad (4)$$

where SD is the standard deviation of the current response to the lowest analyte concentration and b is the slope of the linear regression $y = a + bx$.

3 Results and Discussion

3.1 Electrode Pre-treatment and Characterization

The electron transfer at the electrode depends on the conductivity of the electrode material and the active surface area. Any source of physical or chemical contamination on the electrode negatively influences the electron transfer. Furthermore, surface energy and charge influence the wettability of the electrode and mass transport of the electroactive species to the electrode surface. Figure 3A shows representative cyclic voltammograms of microfabricated pyrolytic carbon electrodes in 10 mM $K_3Fe(CN)_6/K_4Fe(CN)_6$ in PBS pH 7.4 recorded at a scan rate of 50 mVs^{-1} . Before the pre-treatment with O_2 plasma, the cyclic voltammograms of the pyrolytic carbon electrodes were flat and no peak was observed. After pre-treatment of the electrodes with O_2 plasma, the cyclic voltammograms for both 2D and 3D electrodes showed clearly distinguishable oxidation and reduction peaks for the redox couple. Mendez-Linan *et al.* investigated the effect of various plasma treatments on the surface properties of pyrolytic carbon [76,77]. O_2 plasma generates a highly activated carbon surface followed by formation of alcohol, carbonyl and carboxyl groups due to oxidation reactions between surface radicals and the active oxygen ions. This results in higher surface energy and enhanced wettability of the carbon surface. Additionally, O_2 plasma efficiently removes potential surface contaminants from the pyrolytic carbon surface. The formal potential for the redox reaction of $K_3Fe(CN)_6/K_4Fe(CN)_6$ is about 230 mV vs. Ag/AgCl reference electrode. Figure 3B and C compare the anodic peak current I_a and the peak potential separation ΔE_p for 2D and 3D pyrolytic carbon, respectively. The 3D pyrolytic carbon electrodes yield an anodic peak current of $I_{a3D} = 480 \pm 25 \mu A$, while the value for the 2D electrodes is $I_{a2D} = 260 \pm 30 \mu A$. The observed increase of the current values with approximately a factor 2

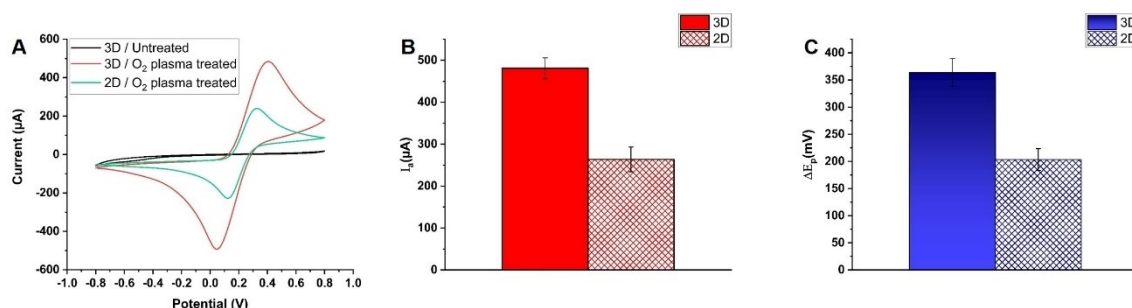


Fig. 3. A) Cyclic voltammograms of untreated as well as O_2 plasma treated 2D and 3D pyrolytic carbon electrodes in 10 mM $K_3Fe(CN)_6/K_4Fe(CN)_6$ in PBS pH 7.4 obtained at scan rate of 50 mVs^{-1} ; comparison of B) anodic peak current I_a and C) peak potential separation ΔE_p for 2D and 3D pyrolytic carbon electrodes ($n = 10$)

between the 2D and 3D electrodes correlates well with the corresponding increase of the electrode surface area due to the addition of the 284 micropillars. Figure 3C shows that the average peak potential separation also increases from 200 mV for the 2D electrodes to about 360 mV for the 3D configuration. This can be attributed to micro-size defects on the 3D electrode surface or the internal resistance of the carbon micropillars.

3.2 Prussian Blue Electrodeposition

The stable mixture of potassium ferricyanide $K_3Fe(CN)_6$ and $FeCl_3$ has a yellowish color. If a potential of about 400 mV vs. Ag/AgCl is applied to reduce the Fe^{3+} of $FeCl_3$ to Fe^{2+} , PB crystals are formed in the presence of ferricyanide $[Fe(CN)_6]^{3-}$. The ideal PB or ferric ferrocyanide ($Fe^{III}_4[Fe^{II}(CN)_6]_3$) cubic unit cell contains low spin iron atoms (Fe^{2+}) coordinated to carbon and high spin iron atoms (Fe^{3+}) coordinated to nitrogen (Figure 4A). The PB crystal structure has interstitial sites and vacancies where counter cations and other small molecules such as oxygen and water can be intercalated. PB with and without potassium ions (K^+) in the crystal structure has been commonly defined as the soluble and insoluble form, respectively [45,75]. In the insoluble PB unit cell, a quarter of the ferrocyanide ($Fe^{II}(CN)_6$) sites are vacant and 14–16 water molecules occupy the empty nitrogen sites of the ferrocyanide and the interstitial vacancies [75], while in the soluble PB unit cell, K^+ ions

occupy half of the vacancies. The synthesis of purely insoluble PB film in the presence of even slightest amount of K^+ ions is impossible [75]. Moreover, the electrochemical activity of the PB film is enhanced in the presence of K^+ ions, because the electron transfer is tightly coupled with the movements of K^+ ions in and out of the PB film, which maintain the electroneutrality of the film during the redox processes [78]. PW, which is the reduced form of PB (Figure 4A), has electrocatalytic activity for H_2O_2 reduction at low overpotential. In the PW unit cell, Fe^{3+} are replaced by Fe^{2+} . The reduction of PB crystal unit cell to PW is a four-electron process which involves K^+ ion uptake per each transferred electron to the film [71]. Therefore it is essential to obtain predominant electrodeposition of electrochemically active PB crystals of the soluble form on the pyrolytic carbon electrodes.

In this study, the first step was electrodeposition of PB crystal films on the pyrolytic carbon WE at a potential of 444 mV vs. Ag/AgCl for variable deposition times. The excessive presence of K^+ ions in the PB growth solution should enhance electrodeposition of the soluble form. Furthermore, acidity of the growth solution (pH 1–2) is required to prevent hydrolysis of ferric ions and avoid that hydroxyl ions replace the cyanide bridges by occupying the valences of iron atoms resulting in irregular and unstable PB films [39]. Preliminary experiments indicated that the horizontal placement of the electrodes in the 3D printed electrochemical cell enhanced the PB electro-

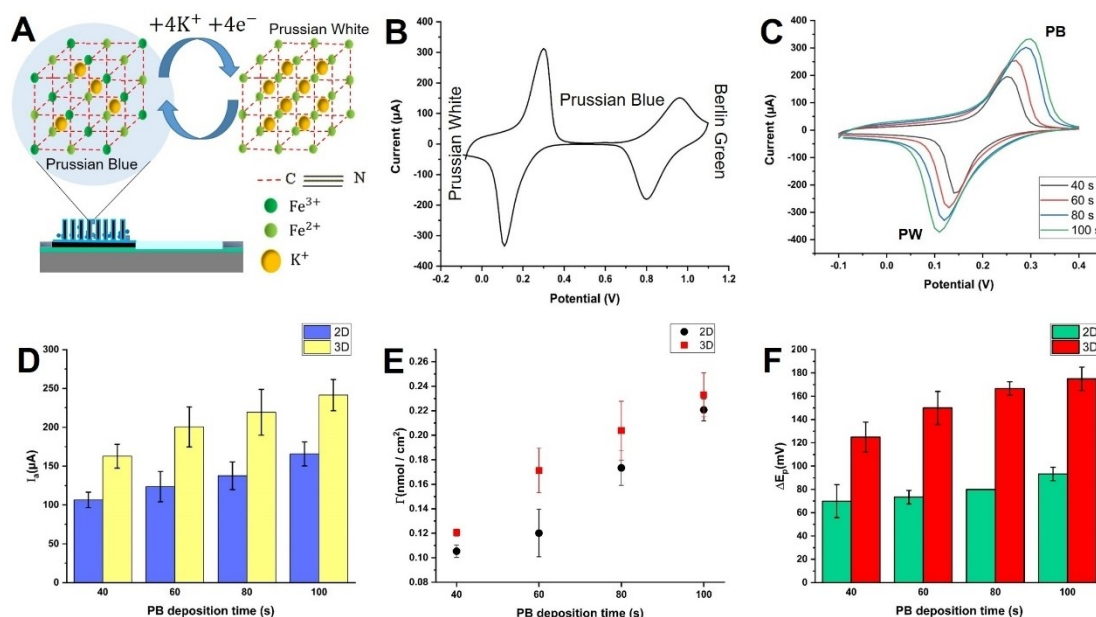


Fig. 4. A) PB unit cell formed during electrodeposition and the PB/PW redox reaction involving four K^+ ions per unit cell interconversion; B) Cyclic voltammograms of the electrodeposited PB film on the 3D pyrolytic carbon electrodes; C) cyclic voltammograms of PB films on 3D pyrolytic carbon electrodes obtained in 0.05 M K_2HPO_4/KH_2PO_4 containing 0.1 M KCl at pH 5.5 and a scan rate of 50 mVs^{-1} after 40, 60, 80 and 100 seconds of electrodeposition followed by activation, annealing and stabilization; D) PB anodic peak current I_a as a function of electrodeposition time for 2D and 3D electrodes; E) estimated PB surface coverage Γ on 2D and 3D pyrolytic carbon as a function of electrodeposition time; F) peak potential separation ΔE_p as a function of electrodeposition time for 2D and 3D pyrolytic carbon ($n=4$).

deposition compared to single electrodes immersed vertically in a beaker (supporting information S1). In the second step of electrode modification, the electrodeposited PB film was activated to further enhance formation of the soluble form of the PB crystal on the electrode surface. For the PB activation, K^+ ions are essential for charge compensation during reduction of PB to PW and most likely to replace water molecules in the crystal structure. A gradual increase in the redox peaks of the cyclic voltammograms as the number of cycles increased from 1–25 was indicative of a fully adsorbed and stable PB film on the pyrolytic carbon electrodes (supporting information S2). In comparison, declining redox peaks and flattened cyclic voltammograms indicated instability of the synthesized film. This observation was considered as a criterion for identifying high quality sensors for further experiments. Next, the residual water molecules were evaporated and the solid PB film on the electrodes was annealed in an oven at 100°C for 1 hour. Prior to annealing of the film, the electrodes were rinsed gently to avoid crystallization of KCl remaining from the solution on the electrodes during evaporation of the water molecules from the synthesized film (supporting information S3). Several studies [59,70,79] suggest using water to rinse PB-modified electrodes prior to drying. However, blue flakes delaminated from the electrode surface when the PB-modified pyrolytic carbon was rinsed gently with water. On the contrary, rinsing with 0.1 M HCl having the same acidity as the PB growth solution did not lead to desorption of the film from the surface. One reason could be the large pH difference between water and the freshly grown PB film, which is in a transition state between the liquid and the solid form and not yet fully adsorbed to the carbon surface. Finally, conditioning and stabilization of the annealed PB film in phosphate buffer containing excessive K^+ (0.1 M KCl) at pH 5.5 were conducted to improve its lifetime and quality [70].

3.3 Prussian Blue Characterization

Figure 4B shows a cyclic voltammogram of the stabilized PB film electrodeposited on the 3D pyrolytic carbon electrode. The cyclic voltammogram was obtained in 0.05 M K_2HPO_4/KH_2PO_4 buffer containing 0.1 M KCl at pH 5.5 and a scan rate of 50 mVs⁻¹. At -0.1 V vs. Ag/AgCl, PB is fully reduced to PW, while at potentials above 0.4 V, the PB is oxidized to Berlin Green. Regardless of the electrode type and the electrodeposition time, the formal potential for the redox reaction of PB/PW on the pyrolytic carbon was approximately 200 mV.

Figure 4C represents cyclic voltammograms of PB films formed on 3D pyrolytic carbon electrodes after 40, 60, 80 and 100 seconds of electrodeposition followed by activation, annealing and stabilization. The two peaks are attributed to the oxidation and reduction of the adsorbed PB/PW film. A longer electrodeposition time clearly resulted in higher anodic and cathodic peak currents

indicating the increasing adsorption of the electrocatalyst on the electrode surface (supporting information S4).

The bar plots in Figure 4D display the extracted anodic peak current of 2D and 3D sensors modified for 40, 60, 80 and 100 seconds. The average current values were obtained from at least four stabilized cyclic voltammograms per each electrode type and PB deposition time. The simultaneous PB modification of multiple pyrolytic carbon electrodes in the 3D printed electrochemical cell was highly reproducible resulting in identical sensors. For both types of pyrolytic carbon electrodes, the anodic peak current increased with increasing electrodeposition time as more PB was adsorbed.

Independently of the deposition time, the 3D carbon electrodes yielded higher currents than the 2D counterparts due to the larger surface area of the electrodes available for PB adsorption. Figure 4E depicts the calculated surface coverage for each electrode type and variable PB deposition time. The surface coverage of the electrodes increased with increasing electrodeposition time due to the formation of a more complete PB layer. Although this trend is similar for 2D and 3D electrodes, the estimated PB surface coverage on 3D electrodes for different deposition times is slightly larger than on the 2D counterparts. It can be speculated that the 3D carbon structures facilitate adsorption and adhesion of PB compared to completely flat carbon surfaces. The estimated mean values of the electrochemically active film thickness for the 2D electrodes after 40 and 60 s of electrodeposition were 0.67 ± 0.03 nm and 0.76 ± 0.12 nm, respectively. For the 3D electrodes these values were 0.77 ± 0.02 nm and 1.0 ± 0.11 nm. The active film thickness reached 1.1 ± 0.09 nm on the 2D and 1.3 ± 0.15 nm on the 3D electrodes after 80 s of electrodeposition, which confirms formation of a continuous PB layer. As the electrodeposition time was increased to 100 s, the film thickness reached 1.41 ± 0.05 nm on the 2D and 1.48 ± 0.11 nm on the 3D electrodes. The length of the PB unit cell is $l_0 = 1.02$ nm, indicating that a complete monolayer was formed for a deposition time of 80 s or more.

In correlation with the increase in the anodic and the cathodic peak currents, larger peak potential separations ΔE_p were observed with increasing PB electrodeposition time (Figure 4F). For the 2D sensors, the highest ΔE_p value measured for 100 s deposition time was around 90 mV, while for the 3D sensors, the ΔE_p reached a value of approximately 170 mV. Larger ΔE_p values are indicative of increased capacitive resistance and decreased electron transfer rate across the modified surface of the electrode. Karyakin *et al.* found that terminating the PB growth at an early nucleation stage resulted in formation of island-like PB nanostructures rather than a continuous film, providing a large electrocatalytically active surface, where the H_2O_2 molecules could diffuse and be reduced [39,80–82]. For pyrolytic carbon electrodes modified with PB, the increase of ΔE_p for prolonged deposition times could be attributed to the formation of a more continuous and condensed PB film with semi-insulating properties

gradually covering the pores in the carbon electrode material and slowing down the electron transfer kinetics at the surface. For the H_2O_2 sensing experiments, a deposition time of 80 s was selected as a compromise between increasing redox peak currents and increasing peak potential separation.

In addition to electrochemical characterization of the PB-modified electrodes, SEM was used to confirm the PB adsorption on the pyrolytic carbon. Figure 5A–C show the 3D pyrolytic carbon electrodes with the micropillars before PB deposition. The intrinsic roughness and porosity of the bare pyrolytic carbon is negligible at micrometer scale (Figure 5A–B) and only at nanometer scale some pores can be identified on the electrode surface (Figure 5C).

Figure 5D–F display the micropillar electrode surface modified with PB with a deposition time of 80 s. The PB was successfully deposited on the top surface and the sidewalls of the 3D pyrolytic carbon micropillars covering the complete electrode surface in a conformal manner. The crystalline structure of PB is clearly visible resulting in nanometer roughness. In some cases cracks were observed in the PB film after annealing and stabilization on both 2D and 3D electrodes (Figure 5E–F). The cracks were even more visible when the deposition time was increased to 100 s. This was attributed to intrinsic stress in the PB film due to crystal formation and extrinsic stress due to the thermal annealing steps. Huang *et al.* [83] optimized PB deposition on nanoporous gold electrodes and reported cracks appearing in the PB layer and eventually delamination of thicker PB films grown with increased deposition time.

The drawback of shorter deposition times (40–60s) was that insufficient PB was formed on the pyrolytic carbon, whereas the challenges associated with longer deposition time (100 s and above) were cracks in the film,

increased instability, loss of catalytic activity and decreased reproducibility. This was another important factor taken into consideration when selecting the optimal deposition time for further H_2O_2 sensing experiments.

During the optimization process, it was observed that factors such as i) cleanliness and moisture level of the electrode surface, ii) the position of the electrodes in the growth solution, iii) a uniform mixing of the precursor molecules during electrodeposition and iv) the freshness of the growth solution were detrimental for successful and reproducible electrodeposition of PB films. Another important observation was that drying the carbon electrode surface by nitrogen after initial characterization and prior to electrodeposition was imperative to obtain stable PB films. To identify eventual variations and defects in the deposited PB films and ensure a high sensor quality, all PB modified electrodes were systematically characterized with cyclic voltammetry before H_2O_2 sensing experiments.

3.4 Hydrogen Peroxide Detection

For H_2O_2 detection, sensors prepared with 80 s PB deposition were tested individually in four separate glass beakers (see supporting information S5). Preliminary experiments demonstrated that the performance of the sensors significantly decreased if H_2O_2 measurements were conducted continuously for extended duration. Similarly, repetitive measurements performed after intermediate washing steps resulted in decay of the electrode properties (see supporting information S6). Unfortunately, stability limitations are a well-known issue for electrochemical sensing with PB [39,74,84]. In the specific case of H_2O_2 sensing, oxygen in the solution, hydroxyl ions and the analyte itself gradually lead to PB degradation. Therefore, each sensor was used only once immedi-

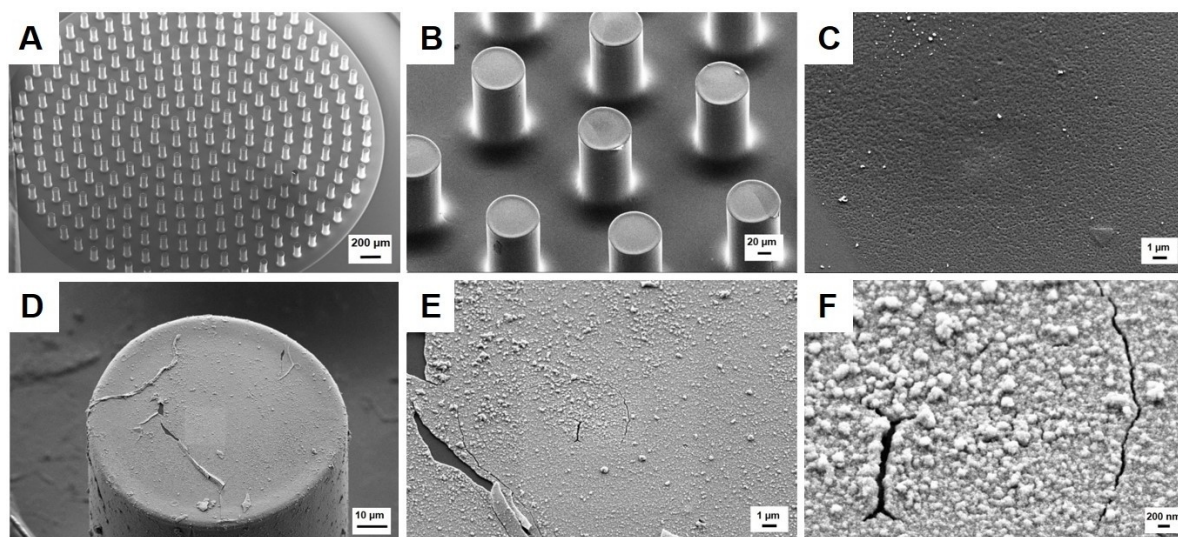


Fig. 5. A–B) bare 3D pyrolytic carbon electrode with micropillars; C) close-up view of the bare pyrolytic carbon surface; D–F) micropillar surface modified with Prussian blue film deposited for 80 s.

ately after preparation and for the maximum duration of 30 min.

A first series of experiments was done in 1–10 μM H_2O_2 concentration range. A typical amperometric response of PB modified 2D and 3D carbon electrodes to μM concentrations of H_2O_2 is presented in Figure 6A. The current response of the 3D sensors was considerably larger than the one of the 2D sensors due to the larger surface area of the electrodes. The corresponding calibration curves of both types of sensors are plotted in Figure 6B demonstrating a good linearity in the μM range ($R^2=0.98$ for the 3D and $R^2=0.99$ for the 2D sensors). The sensitivity of the 3D sensors was $0.2 \mu\text{A}\mu\text{M}^{-1}$, while the sensitivity of the 2D sensors was $0.1 \mu\text{A}\mu\text{M}^{-1}$. This correlates well with an approximately twice as large electrode surface area for the 3D micropillar electrodes compared to the 2D configuration. The corresponding sensitivities for 3D and 2D electrodes calculated based on the current densities were $763 \text{ mAM}^{-1}\text{cm}^{-2}$ and $796 \text{ mAM}^{-1}\text{cm}^{-2}$, respectively. The almost identical values after normalization with the electrode area confirmed that all the PB covered surface contributed equally to the recorded signals. The limit of detection (LOD) calculated from the linear regression of 2D and 3D sensors in μM concentration range were $0.46 \mu\text{M}$ and $0.72 \mu\text{M}$, respec-

tively. The slightly lower LOD for the 2D carbon electrodes was due to larger standard deviations for the measurements with the 3D sensors. The drift in the measured current gradually increasing for continued injections in Figure 6A could be attributed to the onset of PB deactivation and degradation discussed above, among others due to the presence of the analyte in the solution.

In a second series of experiments, H_2O_2 detection in the sub- μM concentration range was investigated. In this range only 3D sensors responded to successive addition of H_2O_2 as illustrated in Figure 6C. The results of H_2O_2 detection in sub- μM range with 2D sensors were inconclusive. A calibration curve in the sub- μM concentration range for the 3D sensors is presented in Figure 6D, showing a good linearity with 98% confidence. The sensitivity was $0.3 \mu\text{A}\mu\text{M}^{-1}$, which was similar to the value determined for the 3D sensors in the previous experiments with μM concentrations. The corresponding sensitivity based on the current density was $1145 \text{ mAM}^{-1}\text{cm}^{-2}$. The LOD calculated based on the linear regression fitted to the data points obtained for the 3D sensors in the sub- μM analyte concentration range was $0.16 \mu\text{M}$. This is comparable with the lowest LODs in buffer that have been reported for carbon-based sensors using exclusively PB as H_2O_2 reduction electrocatalyst without further post

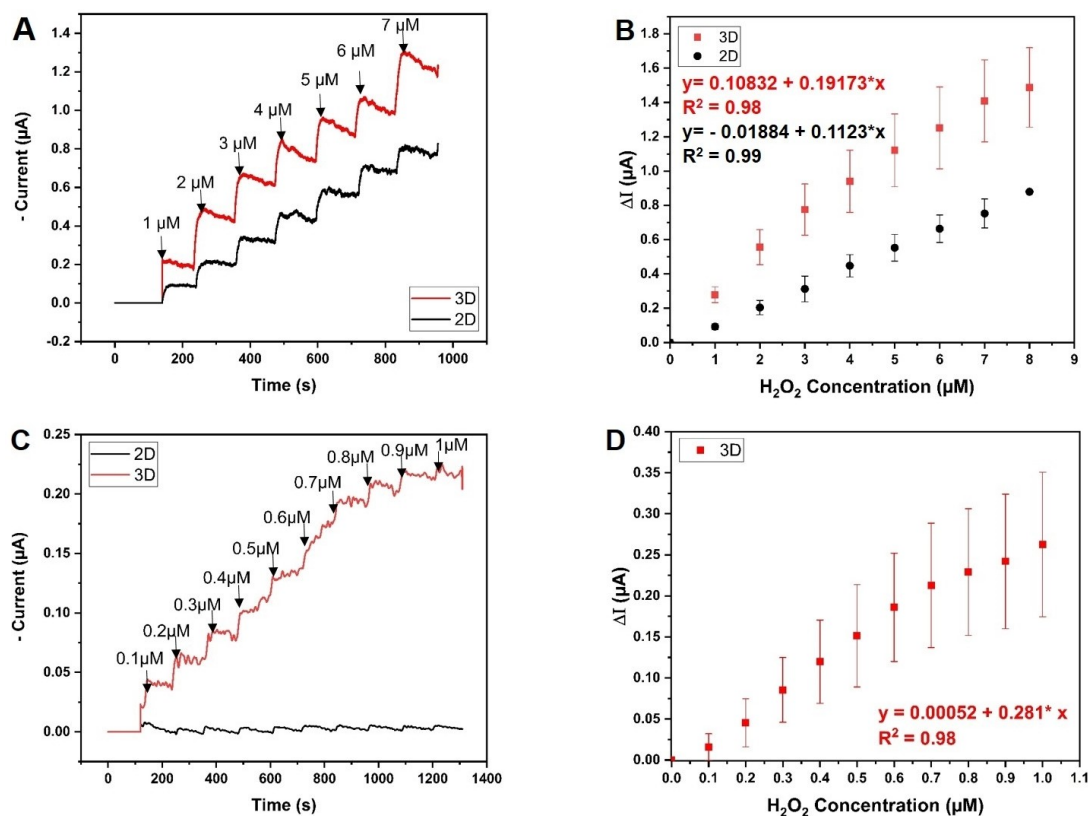


Fig. 6. A) Amperometric current response of 2D and 3D PB -modified pyrolytic carbon electrodes to successive addition of H_2O_2 in μM concentration range; B) baseline corrected calibration curves of 2D and 3D sensors ($n=3$) in μM range; C) amperometric current response of 3D PB-modified pyrolytic carbon electrode to sub μM concentrations of H_2O_2 in comparison with the 2D sensors; D) calibration curve of 3D sensors ($n=7$) in sub- μM concentrations range

treatment steps (see Table 1 and [45]). According to Karyakin *et al.*, the analytical performance of PB-modified electrodes highly depends on the hydrodynamic conditions in which the sensors are tested [39,81,85]. Flow injection analysis systems equipped with a flow-through cell are known to provide the most stable hydrodynamic conditions and the highest sensitivity as the Nernst's diffusion layer is pushed to its lowest limit by the jet force [81]. PB-modified glassy carbon disk electrodes (diameter 1.5 mm) in flow injection analysis system displayed a sensitivity of 600 mA M⁻¹ cm⁻² in phosphate buffer [86]. Theoretically, the maximal possible sensitivity limited by the mass transport of H₂O₂ at the electrodes in a flow injection analysis system is 1000 mA M⁻¹ cm⁻² [87]. In this study, we achieved a comparable sensitivity for 2D and 3D sensors in a stirred batch setup, while the detection limits probably could be further improved using flow injection analysis systems.

4 Conclusion and Future Perspective

We presented for the first time a Prussian blue-based H₂O₂ sensor using pyrolytic carbon as electrode material. 3D pyrolytic carbon electrodes were fabricated using photolithography and pyrolysis. The optimized cleanroom microfabrication processes allow for excellent control of the dimensions of the 3D structures with a high reproducibility. The only modification done to the pyrolytic carbon was oxygen plasma treatment and PB electrodeposition. A 3D printed electrochemical cell was designed and fabricated allowing highly reproducible electrode modification with PB in batch mode on four microelectrode chips in parallel. While numerous researchers combined PB with an additional modification,

e.g. with graphene composite [83] or metal nanoparticles [91,92] to enhance the sensitivity, we were able to achieve a comparable sensitivity and LOD as small as 0.16 μM with PB-modified 3D pyrolytic carbon electrodes without any additional electrode modification. The high sensitivity was attributed to the 3D microstructures, which provided a larger electrocatalytic electrode surface area than the flat 2D electrodes. Considering the sensitivity of the sensor and the simplicity of sensor preparation compared to many sophisticated procedures of electrocatalyst synthesis, the combination of 3D pyrolytic carbon electrodes and PB is recommended when high electrocatalytic activity and rapid H₂O₂ sensor development in batch mode is required.

However, the inherent instability of PB especially at neutral pH, which is a well-known issue, persisted also on pyrolytic carbon when the sensors were repeatedly used. An electrocatalytic activity loss of about 17% at pH 5.5 at ambient temperature was observed within 1 hour of continuous sensor operation in buffer solution (supporting information Figure S7). Therefore, the presented sensor is in the current configuration not suitable for continuous or repeated measurements, but rather for single point analysis. In the future, this challenge could be addressed by using, e.g., conductive polymers as protective layer or by co-synthesis of non-iron hexacyanoferrates [93]. For the sensors to be used in a complex matrix such as a cell medium, the analytical performance including the sensitivity, the reproducibility and the LOD should be evaluated.

Table 1. Comparison of recently developed carbon-based H₂O₂ sensors using exclusively Prussian blue without further modification. *For the sake of comparison, the sensitivity values have been recalculated by the author using the given data in the reference articles.

Sensor Material	Measurement mode	Linear range (μM)	LOD (μM)	Sensitivity (mA M ⁻¹ cm ⁻²)	Sample	Ref
carbon black on screen-printed carbon	Flow injection amperometry	0.2–1000	0.01	660	0.05 M phosphate buffer pH 7.4 containing 0.1 M KCl	[61]
3D printed graphene	batch-injection amperometry	1–700	0.56	57.3	0.1 M phosphate buffer solution pH 7.4 containing 0.1 M KCl	[88]
Screen-printed carbon	i) Steady-state amperometry (aqueous droplet) ii) Periodic flow injection amperometry (vapor)	i) 5–320 ii) 40–320	> 1.5	i) 19* ii) 2*	1 M KCl solution	[62]
3D printed graphene	Stirred batch injection amperometry	1–700	0.11	87*	0.1 M PBS/0.1 M KCl, pH = 7.4	[89]
Boron-doped diamond	Flow injection amperometry			140 330	0.1 M KCl in 0.05 M phosphate buffer, pH = 6.0	[90]
Screen-printed Graphite						
Pyrolytic carbon					Phosphate buffer containing 0.1 M KCl, pH = 5.5	This study
2D	Stirred batch amperometry	1–8	0.46	796		
3D	amperometry	0.3–8	0.16	1145		

Acknowledgments

This research project has been co-financed by Copenhagen Center for Health Technology (CACHET), LEO Foundation and National Center for Nanofabrication and Characterization (DTU Nanolab). The authors are grateful to the mentioned institutes for their financial support. Also thanks to Patama Pholprasit, the process specialist from DTU Nanolab, for her kind help with taking SEM images in figure 5. Jesper Yue Pan's generous help with 3D printing is also greatly acknowledged.

Data Availability Statement

Data related to this study will be published in a publicly accessible repository provided by DTU: www.data.dtu.dk.

References

- [1] B. J. Juven, M. D. Pierson, *J. Food Prot.* **1996**, *59*, 1233–1241.
- [2] L. Campanella, R. Roversi, M. P. Sammartino, M. Tomassetti, *J. Pharm. Biomed. Anal.* **1998**, *18*, 105–116.
- [3] M. Valko, D. Leibfritz, J. Moncol, M. T. D. Cronin, M. Mazur, J. Telser, *Int. J. Biochem. Cell Biol.* **2007**, *39*, 44–84.
- [4] P. R. Gogate, A. B. Pandit, *Adv. Environ. Res.* **2004**, *8*, 501–551.
- [5] O. Legrini, E. Oliveros, A. M. Braun, *Chem. Rev.* **1993**, *93*, 671–698.
- [6] S. Siahrostami, A. Verdager-Casadevall, M. Karamad, D. Deiana, P. Malacrida, B. Wickman, M. Escudero-Escribano, E. A. Paoli, R. Frydendal, T. W. Hansen, I. Chorkendorff, I. E. L. Stephens, J. Rossmeisl, *Nat. Mater.* **2013**, *12*, 1137–1143.
- [7] M. C. Ho, V. Z. Ong, T. Y. Wu, *Renewable Sustainable Energy Rev.* **2019**, *112*, 75–86.
- [8] S. H. Khatami, O. Vakili, N. Ahmadi, E. Soltani Fard, P. Mousavi, B. Khalvati, A. Maleksabet, A. Savardashtaki, M. Taheri-Anganeh, A. Movahedpour, *Biotechnol. Appl. Biochem.* **2021**.
- [9] A. Vrielink, S. Ghisla, *FEBS J.* **2009**, *276*, 6826–6843.
- [10] I. S. Kucherenko, Y. V. Topolnikova, O. O. Soldatkin, *TrAC Trends Anal. Chem.* **2019**, *110*, 160–172.
- [11] T. Finkel, N. J. Holbrook, *Insight Rev. Artic.* **2000**, *408*, 239–247.
- [12] I. C. West, *Diabetic Med.* **2001**, *17*, 171–180.
- [13] B. J. Tabner, S. Turnbull, O. M. A. El-Agnaf, D. Allsop, *Free Radical Biol. Med.* **2002**, *32*, 1076–1083.
- [14] S. Dikalov, K. K. Griendling, D. G. Harrison, *Hypertension* **2007**, *49*, 717–727.
- [15] P. E. A. Boudeville, *Anal. Chem.* **1983**, *55*, 612–615.
- [16] A. Gomes, E. Fernandes, J. L. F. C. Lima, *J. Biochem. Biophys. Methods.* **2005**, *65*, 45–80.
- [17] Y. Zhang, M. Dai, Z. Yuan, *Anal. Methods.* **2018**, *10*, 4625–4638.
- [18] Y. B. Tsaplev, *J. Anal. Chem.* **2012**, *67*, 506–514.
- [19] C. S. Pundir, R. Deswal, Vinay Narwal, *Bioprocess Biosyst. Eng.* **2018**, *41*, 313–329. <https://doi.org/10.1007/s00449-017-1878-8>.
- [20] R. Gulaboski, V. Mirčeski, R. Kappl, M. Hoth, M. Bozem, *J. Electrochem. Soc.* **2019**, *166*, 82–101.
- [21] W. Chen, S. Cai, Q. Q. Ren, W. Wen, Y. Di Zhao, *Analyst.* **2012**, *137*, 49–58.
- [22] M. Baccarin, B. C. Janegitz, R. Berté, F. C. Vicentini, C. E. Banks, O. Fatibello-Filho, V. Zucolotto, *Mater. Sci. Eng. C.* **2016**, *58*, 97–102.
- [23] P. Bollella, L. Medici, M. Tessema, A. A. Poloznikov, D. M. Hushpilian, V. I. Tishkov, R. Andreu, D. Leech, N. Megersa, M. Marcaccio, L. Gorton, R. Antiochia, *Solid State Ionics.* **2018**, *314*, 178–186.
- [24] J. Enomoto, Z. Matharu, A. Revzin, *Methods Enzymol.* **2013**, *526*, 107–121.
- [25] W. A. Alves, I. O. Matos, P. M. Takahashi, E. L. Bastos, H. Martinho, J. G. Ferreira, C. C. Silva, R. H. De Almeida Santos, A. Paduan-Filho, A. M. Da Costa Ferreira, *Eur. J. Inorg. Chem.* **2009**, *15*, 2219–2228.
- [26] B. Amanulla, S. Palanisamy, S. M. Chen, V. Velusamy, T. W. Chiu, T. W. Chen, S. K. Ramaraj, *J. Colloid Interface Sci.* **2017**, *487*, 370–377.
- [27] S. Anjum, Z. Liu, W. Gao, W. Qi, M. R. H. S. Gilani, M. Ahmad, Aziz-Ur-Rehman, G. Xu, *J. Electroanal. Chem.* **2015**, *750*, 74–78.
- [28] S. N. Azizi, S. Ghasemi, N. S. Gilani, *Monatsh. Chem.* **2016**, *147*, 1467–1474.
- [29] K. Dhara, D. R. Mahapatra, *J. Mater. Sci.* **2019**, *54*, 12319–12357.
- [30] X. Chen, G. Wu, Z. Cai, M. Oyama, X. Chen, *Microchim. Acta.* **2014**, *181*, 689–705.
- [31] A. Y. Olenin, *J. Anal. Chem.* **2017**, *72*, 243–255.
- [32] H. Shamkhalichenar, J.-W. Choi, *J. Electrochem. Soc.* **2020**, *167*, 037531.
- [33] R. Ramachandran, S. M. Chen, G. P. Gnana Kumar, P. Gajendran, A. Xavier, N. Biruntha Devi, *Int. J. Electrochem. Sci.* **2016**, *11*, 1247–1270.
- [34] S. Chen, R. Yuan, Y. Chai, F. Hu, *Microchim. Acta.* **2013**, *180*, 15–32.
- [35] N. R. De Tacconi, K. Rajeshwar, R. O. Lezna, *Chem. Mater.* **2003**, *15*, 3046–3062.
- [36] M. Borràs-Brull, P. Blondeau, J. Riu, *Crit. Rev. Anal. Chem.* **2020**, *0*, 1–14.
- [37] M. Eguílaz, P. R. Dalmasso, M. D. Rubianes, F. Gutierrez, M. C. Rodríguez, P. A. Gallay, M. E. J. López Mujica, M. L. Ramírez, C. S. Tettamanti, A. E. Montemero, G. A. Rivas, *Curr. Opin. Electrochem.* **2019**, *14*, 157–165.
- [38] J. N. Tiwari, V. Vij, K. C. Kemp, K. S. Kim, *ACS Nano.* **2016**, *10*, 46–80.
- [39] A. A. Karyakin, *Curr. Opin. Electrochem.* **2017**, *5*, 92–98.
- [40] R. Koncki, *Crit. Rev. Anal. Chem.* **2002**, *32*, 79–96.
- [41] B. Kong, C. Selomulya, G. Zheng, D. Zhao, *Chem. Soc. Rev.* **2015**, *44*, 7997–8018.
- [42] Y. Matos-Peralta, M. Antuch, *J. Electrochem. Soc.* **2020**, *167*, 037510.
- [43] P. Salazar, M. Martín, R. D. O'Neill, P. Lorenzo-Luis, R. Roche, J. L. González-Mora, *Adv. Biomater. Biodevices.* **2014**, *9781118773*, 423–450.
- [44] A. A. Karyakin, *Electroanalysis.* **2001**, *13*, 813–819.
- [45] F. Ricci, G. Palleschi, *Biosens. Bioelectron.* **2005**, *21*, 389–407.
- [46] A. A. Karyakin, E. E. Karyakina, L. Gorton, *Electrochem. Commun.* **1999**, *1*, 78–82.
- [47] M. J. Piernas Muñoz, E. Castillo Martínez, *In: Prussian Blue Based Batteries, SpringerBriefs in Applied Sci. Technol. Springer* **2018**, 9–22.
- [48] W. Gao, S. Emaminejad, H. Y. Y. Nyein, S. Challa, K. Chen, A. Peck, H. M. Fahad, H. Ota, H. Shiraki, D. Kiriya, D. H. Lien, G. A. Brooks, R. W. Davis, A. Javey, *Nature.* **2016**, *529*, 509–514.
- [49] Z. Chu, Y. Liu, W. Jin, *Biosens. Bioelectron.* **2017**, *96*, 17–25.

- [50] Y. Xu, Y. Zhang, X. Cai, W. Gao, X. Tang, Y. Chen, J. Chen, L. Chen, Q. Tian, S. Yang, Y. Zheng, B. Hu, *Int. J. Nanomed.* **2019**, *14*, 271–288.
- [51] M. Peng, Y. Zhao, D. Chen, Y. Tan, *ChemCatChem.* **2019**, *11*, 4222–4237.
- [52] S. Hemanth, C. Caviglia, S. S. Keller, *Carbon* **2017**, *121*, 226–234.
- [53] L. Amato, A. Heiskanen, C. Caviglia, F. Shah, K. Zór, M. Skolimowski, M. Madou, L. Gammelgaard, R. Hansen, E. G. Seiz, M. Ramos, T. R. Moreno, A. Martínez-Serrano, S. S. Keller, J. Emnéus, *Adv. Funct. Mater.* **2014**, *24*, 7042–7052.
- [54] S. Hemanth, A. Halder, C. Caviglia, Q. Chi, S. Sylvest Keller, *Biosensors* **2018**, *8*, 70.
- [55] C. Caviglia, R. P. Carletto, S. De Roni, Y. M. Hassan, S. Hemanth, M. Dufva, S. S. Keller, *Electrochim. Acta.* **2020**, *359*, 136951.
- [56] I. L. De Mattos, L. Gorton, T. Ruzgas, *Biosens. Bioelectron.* **2002**, *18*, 2002193–200.
- [57] Z. Chu, Y. Zhang, X. Dong, W. Jin, N. Xu, B. Tieke, *J. Mater. Chem.* **2010**, *20*, 7815–7820.
- [58] B. Haghighi, S. Varma, F. M. Alizadeh, Sh. Y. Yigzaw, L. Gorton, *Talanta.* **2004**, *64*, 3–12.
- [59] F. Ricci, G. Palleschi, Y. Yigzaw, L. Gorton, T. Ruzgas, A. Karyakin, *Electroanalysis.* **2003**, *15*, 175–182.
- [60] M. A. Tabrizi, A. A. S. Lahiji, *J. Iran. Chem. Soc.* **2014**, *11*, 1015–1020.
- [61] D. Rojas, F. Della Pelle, M. Del Carlo, M. d'Angelo, R. Dominguez-Benot, A. Cimini, A. Escarpa, D. Compagnone, *Sens. Actuators B* **2018**, *275*, 402–408.
- [62] D. Maier, E. Laubender, A. Basavanna, S. Schumann, F. Güder, G. A. Urban, C. Dincer, *ACS Sens.* **2019**, *4*, 2945–2951.
- [63] A. Ambrosi, R. R. S. Shi, R. D. Webster, *J. Mater. Chem. A.* **2020**, *8*, 21902–21929.
- [64] R. M. Cardoso, C. Kalinke, R. G. Rocha, P. L. dos Santos, D. P. Rocha, P. R. Oliveira, B. C. Janegitz, J. A. Bonacin, E. M. Richter, R. A. A. Munoz, *Anal. Chim. Acta.* **2020**, *1118*, 73–91.
- [65] P. S. Sfragano, S. Laschi, I. Palchetti, *Front. Chem.* **2020**, *8*, 1–7.
- [66] R. M. Cardoso, D. M. H. Mendonça, W. P. Silva, M. N. T. Silva, E. Nossol, R. A. B. da Silva, E. M. Richter, R. A. A. Muñoz, *Anal. Chim. Acta.* **2018**, *1033*, 49–57.
- [67] A. L. Silva, G. M. da S. Salvador, S. V. F. Castro, N. M. F. Carvalho, R. A. A. Munoz, *Front. Chem.* **2021**, *9*, 684256.
- [68] S. C. Perry, C. Ponce de León, F. C. Walsh, *J. Electrochem. Soc.* **2020**, *167*, 155525.
- [69] Y. M. Hassan, C. Caviglia, S. Hemanth, D. M. A. Mackenzie, T. S. Alström, D. H. Petersen, S. S. Keller, *J. Anal. Appl. Pyrolysis.* **2017**, *125*, 91–99.
- [70] I. L. De Mattos, L. Gorton, T. Ruzgas, A. A. Karyakin, *Anal. Sci.* **2000**, *16*, 795–798.
- [71] V. D. Ivanov, *Ionics.* **2020**, *26*, 531–547.
- [72] M. I. Prodromidis, A. B. Flown, S. M. Tzouwara-Karayanni, M. I. Karayannis, *Electroanalysis.* **2000**, *12*, 1498–1501.
- [73] M. A. Malik, P. J. Kulesza, R. Włodarczyk, G. Wittstock, R. Szargan, H. Bala, Z. Galus, *J. Solid State Electrochem.* **2005**, *9*, 403–411.
- [74] Z. Wang, H. Yang, B. Gao, Y. Tong, X. Zhang, L. Su, *Analyst.* **2014**, *139*, 1127–1133.
- [75] H. J. Buser, D. Schwarzenbach, W. Petter, A. Ludi, *Inorg. Chem.* **1977**, *16*, 2704–2710.
- [76] L. Méndez-Liñán, M. Pérez-Mendoza, J. I. Paredes, A. Martínez-Alonso, J. M. D. Tascón, M. Domingo-García, F. J. López-Garzón, *Plasma Processes Polym.* **2011**, *8*, 942–950.
- [77] J. I. Mendez-Linan, E. Ortiz-Ortega, M. F. Jimenez-Moreno, M. I. Mendivil-Palma, E. Martínez-Guerra, F. S. Aguirre-Tostado, S. O. Martinez-Chapa, S. Hosseini, M. J. Madou, *Carbon* **2020**, *169*, 32–44.
- [78] J. J. García-Jareño, A. Sanmatías, J. Navarro-Laboulais, F. Vicente, *Electrochim. Acta.* **1998**, *44*, 395–405.
- [79] A. V. Borisova, E. E. Karyakina, S. Costlier, A. A. Karyakin, *Electroanalysis.* **2009**, *21*, 409–414.
- [80] E. A. Puganova, A. A. Karyakin, *Sens. Actuators B* **2005**, *109*, 167–170.
- [81] A. A. Karyakin, E. A. Puganova, I. A. Bolshakov, E. E. Karyakina, *Angew. Chem. Int. Ed.* **2007**, *46*, 7678–7680; *Angew. Chem.* **2007**, *119*, 7822–7824.
- [82] A. A. Karyakin, E. A. Puganova, I. A. Budashov, I. N. Kurochkin, E. E. Karyakina, V. A. Levchenko, V. N. Matveyenko, S. D. Varfolomeyev, *Anal. Chem.* **2004**, *76*, 474–478.
- [83] J. Huang, S. Lu, X. Fang, Z. Yang, X. Liu, S. Li, X. Feng, *Nanotechnology.* **2020**, *31*, 045501.
- [84] F. Ricci, A. Amine, G. Palleschi, D. Moscone, *Biosens. Bioelectron.* **2002**, *18*, 165–174.
- [85] A. A. Karyakin, E. E. Karyakina, L. Gorton, *J. Electroanal. Chem.* **1998**, *456*, 97–104.
- [86] A. A. Karyakin, E. E. Karyakina, *Sens. Actuators B* **1999**, *57*, 268–273.
- [87] T. Ruzgas, E. Csöregi, J. Emnéus, L. Gorton, G. Marko-Varga, *Anal. Chim. Acta.* **1996**, *330*, 123–138.
- [88] R. G. Rocha, J. S. Stefano, R. M. Cardoso, P. J. Zambiasi, J. A. Bonacin, E. M. Richter, R. A. A. Munoz, *Talanta.* **2020**, *219*, 121289.
- [89] V. Katic, P. L. Dos Santos, M. F. Dos Santos, B. M. Pires, H. C. Loureiro, A. P. Lima, J. C. M. Queiroz, R. Landers, R. A. A. Muñoz, J. A. Bonacin, *ACS Appl. Mater. Interfaces.* **2019**, *11*, 35068–35078.
- [90] M. A. Komkova, A. Pasquarelli, E. A. Andreev, A. A. Galushin, A. A. Karyakin, *Electrochim. Acta.* **2020**, *339*, 135924.
- [91] L. Chao, W. Wang, M. Dai, Y. Ma, L. Sun, X. Qin, Q. Xie, *J. Electroanal. Chem.* **2016**, *778*, 66–73.
- [92] L. Wang, Y. Zhang, C. Cheng, X. Liu, H. Jiang, X. Wang, *ACS Appl. Mater. Interfaces.* **2015**, *7*, 18441–18449.
- [93] E. V. Karpova, E. E. Karyakina, A. A. Karyakin, *RSC Adv.* **2016**, *6*, 103328–103331.

Received: July 12, 2021

Accepted: September 10, 2021

Published online on October 12, 2021

ELECTROANALYSIS

Supporting Information

Hydrogen Peroxide Detection Using Prussian Blue-modified 3D Pyrolytic Carbon Microelectrodes

Sheida Esmail Tehrani, Long Quang Nguyen, Giulia Garelli, Bettina M. Jensen, Tautgirdas Ruzgas, Jenny Emnéus, and Stephan Sylvest Keller

Hydrogen Peroxide Detection Using Prussian Blue-Modified 3D Pyrolytic Carbon Microelectrodes

Sheida Esmail Tehrani^a, Long Quang Nguyen^a, Giulia Garelli^a, Bettina M. Jensen^b, Tautgirdas Ruzgas^c, Jenny Emnéus^d, Stephan Sylvest Keller^a

^aTechnical University of Denmark, National Centre for Nano Fabrication and Characterization, Kongens Lyngby, Denmark

^bAllergy Clinic, Copenhagen University Hospital at Herlev-Gentofte, Hellerup, Denmark

^cMalmö University, Department of Biomedical Science & Biofilms – research center for biointerfaces, Malmö, Sweden

^dTechnical University of Denmark, Department of Bioengineering, Kongens Lyngby, Denmark

Supporting information

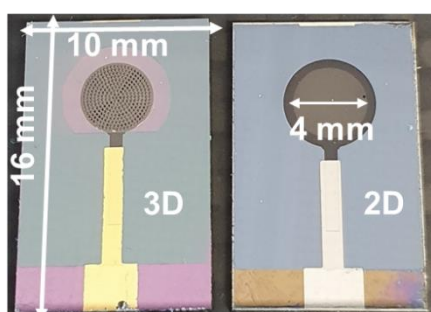


Figure S0: 3D (left) and 2D (right) pyrolytic carbon electrode chips with Au and Pt leads and contact pads respectively.

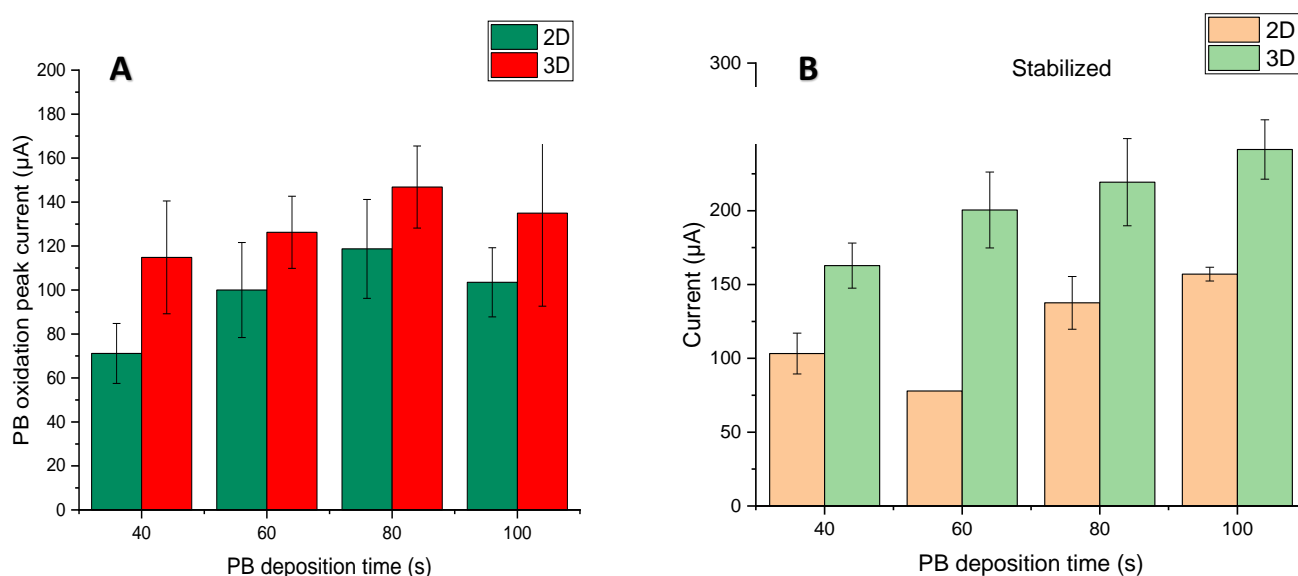


Figure S1: The anodic peak currents obtained from the CVs of A) Prussian blue deposited on pyrolytic carbon in single glass beaker, where the electrode was inserted into the growth solution vertically, B) Prussian blue deposited on pyrolytic carbon in 3D printed electrochemical cell where 4 electrodes were placed horizontally. By comparing the standard deviations ($n=3$) of bar plots in A and B, it can be observed that the Prussian blue film growth on pyrolytic carbon in the 3D printed multielectrode cell was more reproducible. In addition, larger current values of anodic peaks indicate that the Prussian blue electrodeposition and surface coverage on the pyrolytic carbon was significantly enhanced in the 3D printed cell.

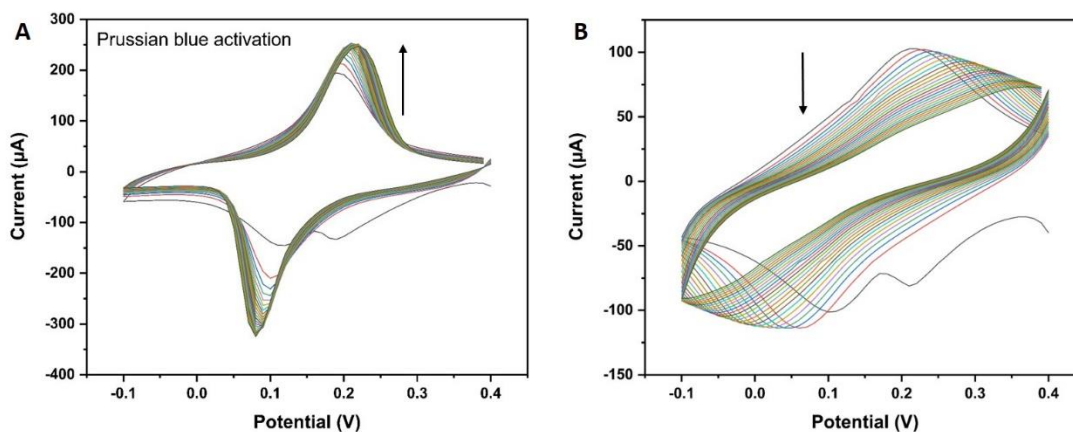


Figure S2: 25 cyclic voltammograms of A) well-grown and fully adsorbed vs. B) an unstable Prussian blue layer. The CVs were obtained at scan rate of 50 mVs^{-1} during the activation of the freshly grown Prussian blue films in 0.1 M HCl containing 0.1 M KCl as electrolyte. Both the anodic and the cathodic peaks of a well-grown and fully adsorbed Prussian blue film gradually increase as the number of potential sweep cycles increase. On the contrary, the declining peaks in B were indicative of an unstable film.

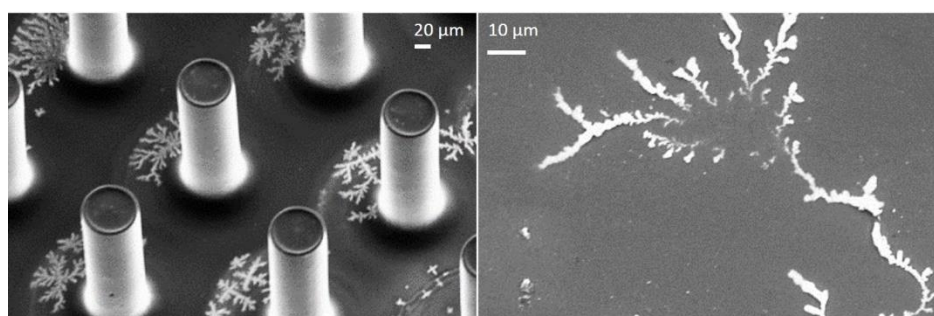


Figure S3: SEM images of 3D Prussian blue-modified electrode that was not rinsed prior to annealing in the oven. The white spots are crystallized KCl.

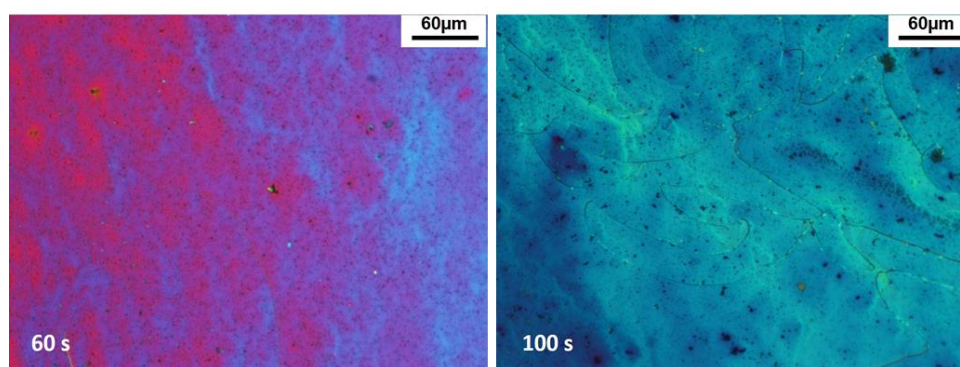


Figure S4: Optical microscopic images of Prussian blue films on the 2D pyrolytic carbon grown after 60 and 100s of electrodeposition. After 60 s of electrodeposition, a very thin film of Prussian blue was formed but parts of the carbon substrate (red spots) remained uncovered. As the electrodeposition time increased to 100 s, a condensed film covered the electrode surface.

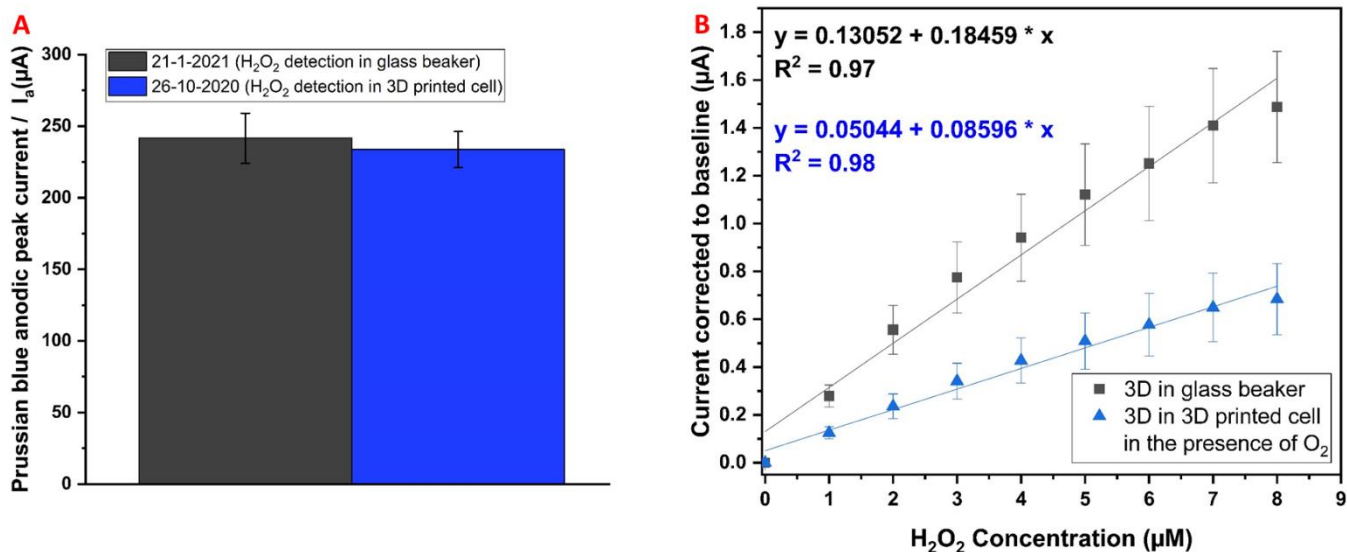


Figure S5: Comparison of two sets (four electrodes per each set) of identical PB-modified 3D sensors that were used to detect 1-10 μM H_2O_2 in 5ml glass beaker and in 3D printed electrochemical cell in stirred phosphate buffer containing 0.1 M KCl pH 5.5; A) similar Prussian blue anodic peak current values (average of 4 sensors) shows that the electrodeposition in 3D printed cell was highly reproducible resulting in identical sets of sensors (the electrodeposition of PB on all electrodes were done in the 3D printed cell); B) calibration curves of the two sets of sensors, where the first set was immersed in 4 separate glass beakers (gray curve) for H_2O_2 sensing while the same experiment (H_2O_2 detection in 1-10 μM range) was performed in the 3D printed cell (blue curve) on the second set of sensors. The results in B, show that the sensitivity of the sensors and the current response was enhanced in the 5ml glass beakers, as the slope of the linear calibration curve in glass beaker is more than twice the slope of the curve in the 3D printed cell. We believe that in the large volume (20 ml) of the 3D printed cell, the stirring magnitude was not sufficient for uniform mixing of the added analyte in the solution. Moreover, the Nernst's diffusion layer thickness upon the sensors that were placed horizontally in small wells on the bottom of the 3D printed cell, was probably increased as the convection was not sufficiently strong to direct the analyte molecules towards the wells. Therefore, the amperometric data presented in the results and discussion section in the main body of the article, was acquired in glass beakers.

Stability of Prussian blue for repetitive H2O2 measurements

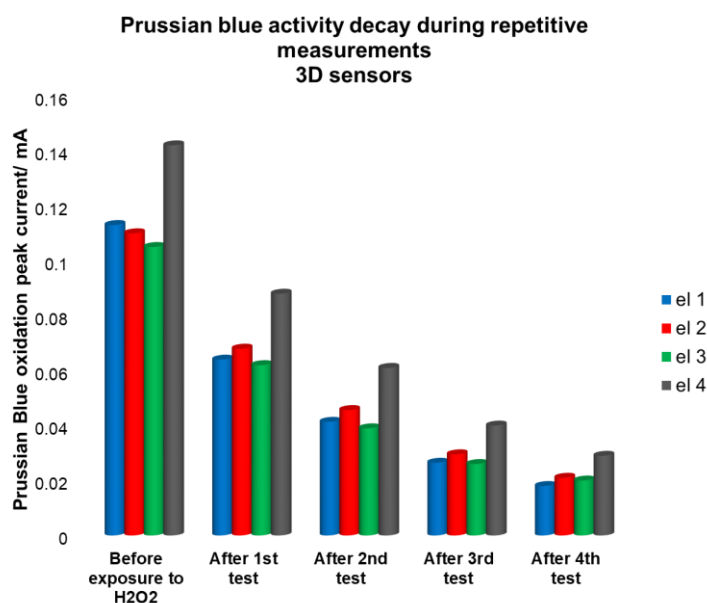


Figure S6: Cathodic peak currents of PB-modified sensors obtained from CVs in blank phosphate buffer containing 0.1M KCl pH 5.5 repeatedly used (in total four times) for H₂O₂ detection. Each test took about 10 minutes. As it can be seen, the PB gradually loses activity, showing that repetitive measurements with the same sensor are not recommended.

Stability of Prussian blue in various conditions

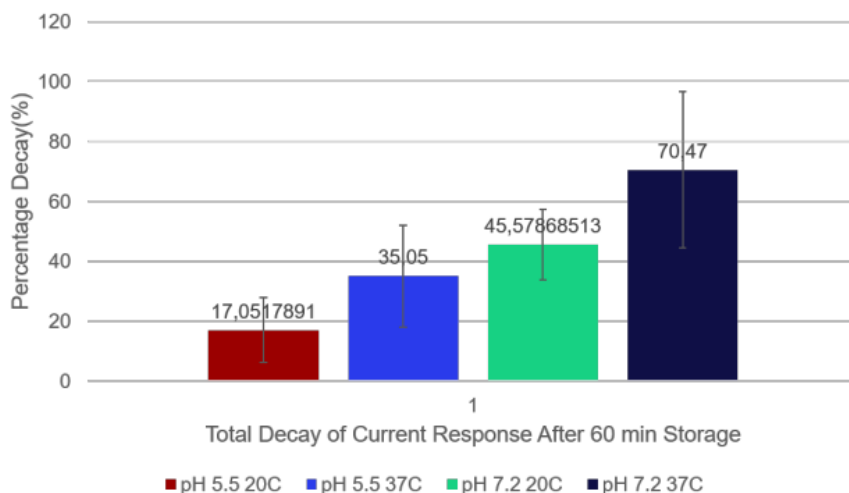


Figure S7: Catalytic activity loss of Prussian blue for electrodes immersed in blank phosphate buffer at different pH and temperature conditions. The degree of the activity loss was quantified by calculating the relative anodic peak current drop in the cyclic voltammograms recorded immediately after immersion and after 1 hour of immersion. Similar to earlier reports in literature, Prussian blue was most stable at ambient temperature and pH 5.5 while a significant decay was observed for neutral pH and 37 C.

Appendix B: Paper II

Capacitive Method as an Alternative Transduction Technique for Developing Prussian Blue-Based Electrochemical Sensors and Biosensors: A Case Study of Enzyme Catalyzed Histamine Oxidation

Sheida Esmail Tehrani^a, Long Quang Nguyen^a, Jesper Yue Pan^a, Bettina M. Jensen^b, Jenny Emnéus^c
Tautgirdas Ruzgas^d, Stephan Sylvest Keller^a

^aTechnical University of Denmark, National Centre for Nano Fabrication and Characterization,
Kongens Lyngby, Denmark

^bAllergy Clinic, Copenhagen University Hospital at Herlev-Gentofte, Hellerup, Denmark

^cTechnical University of Denmark, Department of Bioengineering, Kongens Lyngby, Denmark

^dMalmö University, Department of Biomedical Science & Biofilms – research center for biointerfaces,
Malmö, Sweden

Abstract

As an alternative to the conventional stirred batch amperometry, a novel electrochemical transduction technique for hydrogen peroxide (H₂O₂) detection by Prussian Blue (PB)-based sensors is presented, which has a higher sensitivity and a lower limit of detection (LOD) than what has been achieved with amperometry by the same type of sensors. This technique, which is a combination of open circuit potentiometry and chronoamperometry, owes its sensitivity to the capacitive-like properties of the PB and its ability to accumulate and release charge upon reduction and oxidation. Since H₂O₂ is the common reaction by-product of oxidase enzymes, the capacitive transduction technique can be used for developing PB/oxidase-based biosensors. In this study, histamine biosensor is constructed by immobilizing DAO purified from *Pisum sativum* on a PB-modified 3D pyrolytic carbon electrode. Reproducible measurements of H₂O₂ and histamine in the concentration range between 100 nM and 1 mM in phosphate buffer by the capacitive method are established which resulted in LODs as small as 71 nM and 363 nM, respectively. In addition, a proof-of-concept measurement of 90 ng mL⁻¹ (809 nM) histamine released from activated LAD2 human mast cells is demonstrated in static condition. Given the sensitivity provided in static conditions, the method is ideal for on-chip cell-based measurements and for developing *in vivo* sensors and biosensor.

Keywords

Prussian Blue, Hydrogen peroxide sensor, Histamine detection, Diamine oxidase, Mast cells, Potentiometry, Chronoamperometry, Pyrolytic carbon

1. Introduction

Since Neff [1] explained the electrochemical properties of thin films of Prussian Blue (PB), the iron(III) hexacyanoferrate(II) and its analogs have been extensively explored for energy storage [2,3] and electrochemical sensing [4–6] applications. In the 1990s, Karyakin *et al.* discovered that the electrocatalytic activity of the reduced form of PB, known as Prussian white (PW) or Everitt's salt, was three orders of magnitude higher than the conventionally used platinum electrode for the reduction of hydrogen peroxide (H₂O₂), while the required cathodic potential to drive the reaction was remarkably lower [7–10]. This characteristic of PB appeared especially advantageous for developing highly selective enzymatic biosensors for

biomedical applications as H_2O_2 is a common by-product of oxidase enzymes such as glucose, alcohol- and amine oxidases [4–6,11,12]. Moreover, H_2O_2 reduction on PB-modified electrodes occurs at a cathodic potential of around 0.0 V versus Ag/AgCl minimizing the likelihood of interference from the easily oxidizable species present in complex matrices of biological samples. Many of the developed PB-based enzymatic biosensors for biomedical applications have aimed at detecting glucose in sweat, serum and blood samples [13–16]. A few other target analytes included lactate [17], glutamate [18], cholesterol [19], uric acid [20] and choline [21]. Searching the global scientific databases such as Web of Science using the two keywords, ‘Prussian blue’ and ‘histamine’, indicated a handful of examples of electrochemical PB-based histamine biosensors [22–25]. However, histamine detection in body fluids such as serum, blood or interstitial fluid has not been pursued to date. Histamine plays an important role in the human body as it is the primary allergic inflammatory biomarker that is released from the circulating basophils into the bloodstream and from the tissue-resident mast cells into the interstitial fluid [26–28]. Histamine also acts as a neurotransmitter in the brain, spinal cord and uterus and is involved in many physiological functions [29–33]. The abundance of dietary histamine in the body is associated with histamine intolerance disorder [34,35].

Here, we present for the first time an electrochemical PB-based enzymatic histamine biosensor capable of detecting histamine in mast cell culture medium. In our previous work [36], we demonstrated amperometric detection of H_2O_2 in buffer with 3D PB-modified pyrolytic carbon electrodes. PB electrodeposition on the 3D pyrolytic carbon microelectrodes was optimized and reproducible sensors were obtained. In the current study, we apply the same type of transducer to introduce a novel electrochemical method for measuring the PB-mediated reduction of H_2O_2 in a histamine biosensor based on a capacitive readout. More specifically, diamine oxidase immobilized as biorecognition element on the PB film, degrades the histamine in the sample in the presence of oxygen and generates H_2O_2 as the reaction by-product. While the majority of the developed enzymatic biosensors with PB as a mediator are amperometric, Sasaki *et al.* [37] demonstrated in a recent study that charge-accumulative potentiometry is a more sensitive method for detecting an enzymatic reaction on a PB electrode. Here, we bring forward a new concept that relies on open circuit potentiometry combined with chronoamperometry as the electrochemical measurement technique exploiting a similar concept as what is used for pseudocapacitive energy storage in a microsupercapacitor. One of the advantages of the capacitive method in comparison with the charge-accumulative potentiometry is that the combination of the two techniques (open circuit potentiometry and chronoamperometry) allows for repetitive measurements in the same media, because the chronoamperometry is used in this method to regenerate the sensor and reset the measurement.

2. Materials and methods

2.1. Materials

The chemical reagents required for PB modification of the electrodes, including potassium hexacyanoferrate (III), iron (III) chloride, potassium chloride, hydrochloric acid 37%, monobasic potassium phosphate and dibasic potassium phosphate, were all purchased from Sigma, and the stock solutions were prepared freshly using double distilled water before each experiment. For the initial proof-of-concept experiments, H_2O_2 (35% from Sigma) was diluted

in phosphate buffer. For immobilization of the enzyme layer, $\geq 96\%$ lyophilized bovine serum albumin (BSA) powder and solution grade I glutaraldehyde (GA) (70% in H₂O) from Sigma were dissolved and diluted in phosphate-buffered saline (PBS) pH 7.2 and double distilled water, respectively. Diamine oxidase (DAO) purified from *Pisum sativum* (pea seedling) in liquid form with the enzymatic activity of 2672 U mL⁻¹ was purchased from IBEX Pharmaceuticals Inc., Canada, and used as it was supplied. For histamine detection in buffer, phosphate buffer (0.05 M K₂HPO₄/KH₂PO₄ + 0.1 M KCl) was prepared at pH 5.5 ideal for PB. HCl 37% and NaOH were used to adjust the phosphate buffer's initial pH value (6.8) to acidic and neutral levels, respectively. Histamine (Sigma) stock solutions were prepared in the aforementioned buffers. For *in vitro* histamine detection in the mast cell medium, the supernatant of the activated LAD2 human mast cells containing degranulated histamine at different concentrations was provided by the Allergy Clinic at Copenhagen University Hospital in Gentofte, Denmark. LAD2 mast cell titration and activation were performed in histamine release buffer (HR-buffer) composed of PIPES (RefLab) and 0.5% human serum albumin (CSL Behring, USA). Compound 48/80 (1 mg mL⁻¹, dissolved in sterile water) from Sigma Aldrich was used to induce mast cell degranulation.

2.2. Electrochemical measurements

All electrochemical measurements were performed using a MultiPalmSens4 potentiostat and MultiTrace 4.3 software was used to acquire data. Excel and OriginPro 2018 were employed for data treatment and statistical analysis of the obtained results. A silver wire covered with the silver electrode (Ag/AgCl) in a 3 M KCl solution purchased from Italsens was used as an external reference electrode (RE). Thus, all the potential values reported throughout this article are reported versus Ag/AgCl. A double-sided Pt-coated Si chip with a size of 10 x 40 cm² was used as a counter electrode (CE).

2.3. Electrode fabrication and PB modification

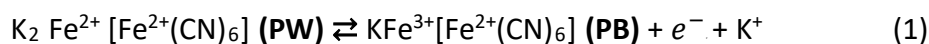
3D pyrolytic carbon microelectrodes with 284 micropillars with a height of 225 μm and a diameter of 68 μm (total geometrical surface area of 26.2 mm²) and metal (Ti+Au) leads (thickness: 150 nm) patterned on a Si chip were used as working electrode (WE). A detailed description of the electrode fabrication process and the method for PB modification can be found in our previous work [36]. Four oxygen-plasma treated WEs were modified simultaneously with PB by applying a potential of 444 mV for 80 s to the WEs immersed in a fresh PB growth solution containing 2.5 mM K₃Fe(CN)₆, 2.5 mM FeCl₃, 0.1 M HCl and 0.1 M KCl. Thereafter, the electrodeposited PB films were activated in a solution consisting of 0.1 M HCl and 0.1 M KCl by sweeping the potential between 0.4 and -0.1 V (starting at 0.4 V) at a scan rate of 50 mV s⁻¹ for 25 cycles. Next, the PB-modified electrodes were rinsed with 0.1 M HCl and annealed at 100°C for 1 hour. Finally, the PB films were conditioned and stabilized at -6 mV for 600 s followed by 25 cycles between +0.4 and -0.1 V at 50 mV s⁻¹ in phosphate buffer containing 0.05 M K₂HPO₄/KH₂PO₄ and 0.1 M KCl with pH adjusted to 5.5 using HCl.

2.4. The concept of H₂O₂ detection with PB-modified 3D electrodes

H₂O₂ is the by-product of enzymatic reactions catalyzed by oxidase enzymes. In these enzymatic reactions, the concentration of the produced H₂O₂ is directly proportional to the concentration of the enzyme's substrate that is being consumed [12]. Therefore, the detection of H₂O₂ is of great importance for the researchers in the biosensor field, who employ oxidase enzymes as the recognition element for their biosensors. In this work, the H₂O₂ sensing with the novel method was optimized in the first place. All the proof-of-concept experiments were performed using H₂O₂ at room temperature (22-25°C) in freshly prepared phosphate buffer as the measurement solution containing 0.05 M K₂HPO₄/KH₂PO₄ and 0.1 M KCl with pH adjusted to 5.5 using HCl 37%. H₂O₂ 35% was diluted in the buffer to desired concentrations and was stored in dark at 4°C until use and fresh samples were prepared each time to exclude effects of eventual H₂O₂ degradation. For the experiments where the dissolved molecular oxygen was removed, the blank phosphate buffer was purged with nitrogen gas for 3 hours while the amount of remaining dissolved oxygen in the buffer was controlled with an optical dissolved oxygen sensor (InLab OptiOX by Mettler Toledo) every hour. H₂O₂ was also prepared in deoxygenated phosphate buffer and the measurement solution was constantly purged during the experiments.

The schematics in **Figure 1** illustrate the concept of H₂O₂ detection with PB-modified 3D pyrolytic carbon WEs by, what we call, the 'capacitive method'. As displayed in **Figure 1A**, the first step involves the application of a reducing potential to the PB-modified WE to convert PB to PW, analogous to charging a capacitor. The PB or ferric ferrocyanide (Fe₄³⁺[Fe²⁺(CN)₆]₃) crystal structure contains low spin iron (Fe²⁺) and high spin iron (Fe³⁺) with carbon and nitrogen (cyanide) bonds in between. The open framework of PB has some interstitial sites and vacancies where countercations such as potassium (K⁺) and small molecule of H₂O₂ can be intercalated. Fe³⁺ ions make up almost half of the total amount of Fe atoms in the PB unit cell ([Fe³⁺]/[Fe^{2+/3+}]⁻¹ = 0.5) [37]. The PB conversion to PW involves the reduction of Fe³⁺ ions to Fe²⁺ by drawing electrons from the electrode, and the insertion of K⁺ ions in the crystal structure of the film. In the second step (**Figure 1B**), the electrical circuit is opened to avoid the flow of charge through the electrode while the potential of the WE versus RE is measured by open circuit potentiometry.

As shown in **Figure 1B**, H₂O₂ oxidizes PW to PB, meaning that Fe²⁺ ions are oxidized to Fe³⁺ by losing electrons to H₂O₂ analogous to discharging a capacitor. This imposes a positive shift in the potential of the WE. As shown below in reaction (1) and (2), the oxidation of a unit cell of soluble PW to PB is a one-electron process [12], while the catalytic reduction of each H₂O₂ molecule to hydroxide ions (OH⁻) involves two electrons [9]. Therefore, the transfer of two electrons per electrocatalytic cycle is postulated.



Unlike the conventional amperometric detection of PB-catalyzed H₂O₂ reduction, in which the lost electrons from the electrocatalyst are instantly substituted and the PW is constantly regenerated, in this technique the loss of electrons escalates in a progressive manner at the open circuit mode.

When the potential is switched on again, the amount of lost charge can be quantified by another step of chronoamperometry as illustrated in **Figure 1C**. A reducing potential is applied to regenerate the PW film and the corresponding reduction current is recorded. Regeneration of PW is analogous to recharging a capacitor, as electrons are drawn from the electrode to reduce the Fe^{3+} ions previously produced because of the PW reaction with H_2O_2 . The integration of the measured current yields the lost charge from the film at open circuit, which is correlated to the amount of reduced H_2O_2 . The main hypothesis of this electrochemical transduction concept is that the slow discharge and the rapid recharging of the PB film enhances the signal and allows to measure smaller concentrations of analyte.

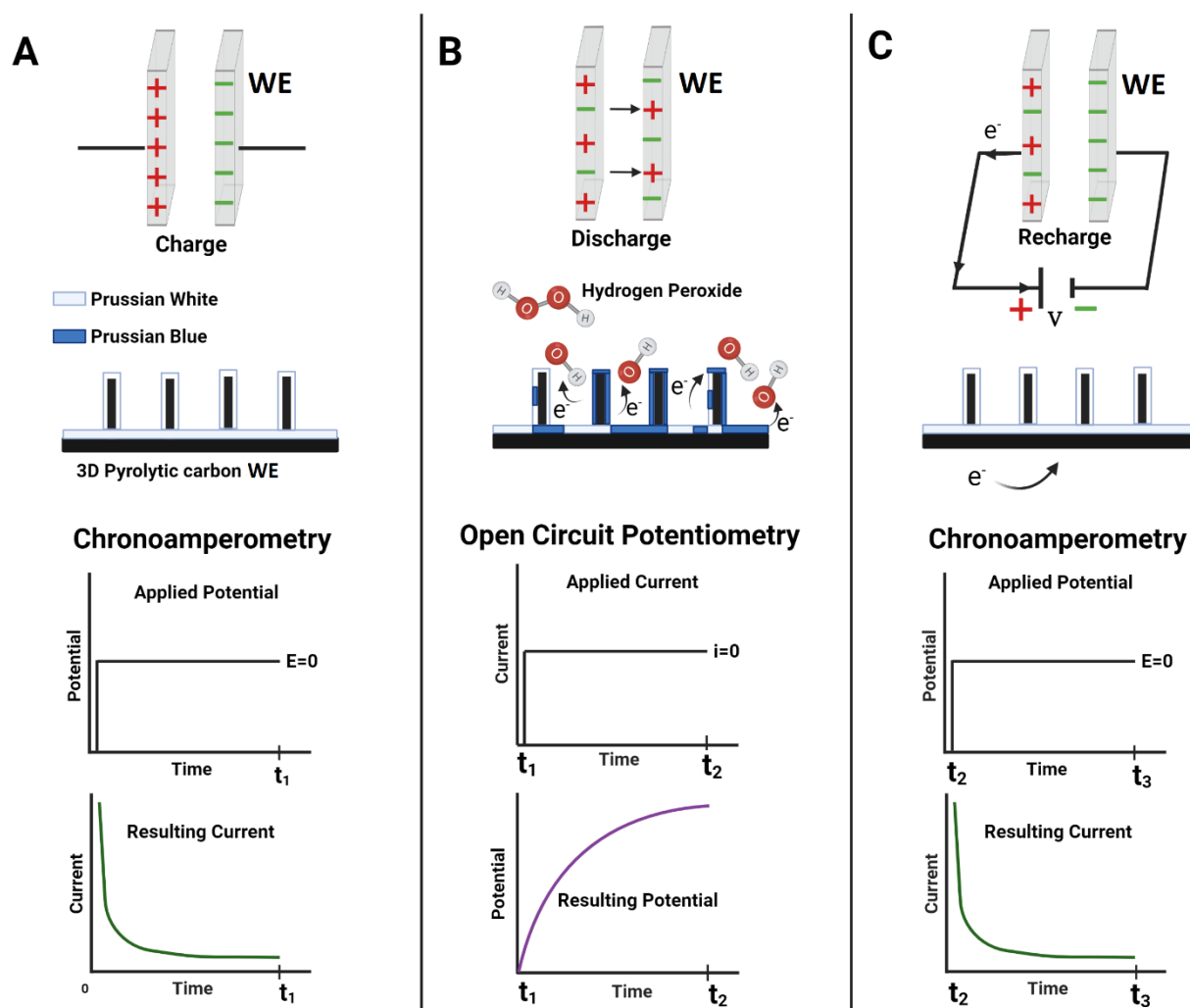


Figure 1 Schematics of the concept of H_2O_2 detection by a 3D pyrolytic carbon WE modified with a PB film, the applied perturbations, the resulting current and potential transients and the analogy of the measurement concept to **A)** charge, **B)** discharge and **C)** recharge of a capacitor.

2.5. Construction of histamine biosensor on PB-modified 3D electrodes

For histamine detection, an enzymatic biosensor was constructed by immobilizing a layer of DAO from *Pisum sativum* as the recognition element on the PB-modified 3D pyrolytic carbon electrodes. As depicted in reaction (3), DAO catalyzes the oxidation of histamine to imidazole-4-acetaldehyde, ammonia (NH₃), and H₂O₂ in the presence of molecular oxygen dissolved in aqueous solution.



Histamine was detected indirectly by the detection of H₂O₂ using the capacitive method.

2.5.1. Determination of the optimum amounts of BSA and GA

DAO was immobilized on the PB-modified 3D pyrolytic carbon WE together with BSA as a spacer molecule and GA as a cross-linker. As mentioned earlier, DAO was supplied in liquid form. The concentration of the DAO stock solution was determined by spectrophotometry, which was 10 mg mL⁻¹. In the optimization process, the concentration of the DAO was kept constant, while the concentrations of BSA and GA were varied one at a time. First, the amount of optimum BSA was found by keeping the DAO and GA concentration constant at 10 mg mL⁻¹ and 0.5%, respectively. Then, similar concentration of DAO together with the optimum amount of BSA were implemented to specify the optimum amount of GA. The optimum amounts of BSA and GA were determined by stirred batch amperometry. The current responses of the biosensors to 1 mM histamine in PBS pH 7.2 were investigated at an applied potential of 0.0 V. Before adding histamine, a stable baseline in blank PBS was obtained for each biosensor. Upon addition of histamine, the maximum current increase from the baseline was evaluated as the best response.

2.5.2. Enzyme immobilization

For the immobilization, the enzymes were used undiluted in the buffer in which the stock was supplied. To avoid repetitive thaw and freeze cycles, the DAO stock solution was aliquoted immediately when received from the supplier and the aliquots were stored at -70° C. For each experiment, a new aliquot was thawed at +4°C and used for immobilization on the same day. In the optimized procedure, 2 μL of DAO solution (10 mg mL⁻¹) was gently mixed in a PCR tube with 1 μL of 0.5% BSA freshly prepared in PBS pH 7.2. Right before immobilization, 1 μL of 1% GA diluted in distilled H₂O was added to the DAO/BSA in the tube and mixed by gentle pipetting without creating air bubbles. Eventually, 4 μL of the DAO/BSA/GA mixture was drop cast on the WE and left at room temperature (22-25°C) for 30 minutes to immobilize. The immobilization and cross-linking process was finished by gently rinsing the electrode with PBS pH 7.2 three times to remove the unbound molecules.

2.6. Histamine detection in buffer

Histamine samples were prepared in phosphate buffer (0.05 M K₂HPO₄/KH₂PO₄) containing 0.1 M KCl pH 5.5 at room temperature which is optimal for PB. Histamine concentrations of

100 nM, 500 nM, 1 μ M, 10 μ M, 100 μ M and 1 mM were tested to determine the dynamic range of the biosensor. Measurements were performed individually on PB/enzyme-modified pyrolytic carbon WEs in separate glass cells. The measurement method comprised of a single potential step chronoamperometry to generate PW ($E=0.0$ V, duration 60 s) followed by open circuit potentiometry for the duration of 120 s in stirred conditions and another single potential step chronoamperometry ($E=0.0$ V, duration 10 s and data acquisition time interval: 1 ms). The method script was run in a blank buffer until a stable baseline was achieved. Histamine samples were added as the circuit was disconnected and stirring was turned on.

2.7. Histamine detection in cell supernatant

4×10^3 and 64×10^4 cells in HR buffer were stimulated by compound 48/80 (1 mg mL^{-1}) to release histamine. After 30 minutes of incubation, the cell remnants were removed by centrifugation, and the histamine-containing supernatants were transferred to a new tube for measurements with the biosensors. The amounts of released histamine were quantified fluorometrically. Supernatants containing 809 nM and 15.24 μ M histamine concentrations were obtained, respectively. Before introducing the histamine-containing samples to the biosensors, baselines were recorded in the blank (cell/histamine-free) HR buffer containing the same amount of compound 48/80 that was used for stimulation of cells, to identify any possible interference in histamine detection from other substances (including compound 48/80) present in the complex matrix of the cell supernatant. Then, the blank HR buffers were removed, and histamine-containing cell supernatants were introduced to the biosensors. The measurement method was constructed exactly in the same way as it was done to measure the histamine in buffer, except that the open circuit potentiometry was extended to 300 s since each biosensor was devoted for single use and therefore, the risk of losing PB electroactivity was minimized. Unlike in previous experiments, the stirring was eliminated, and histamine detection in the cell supernatant was performed in static conditions.

3. Result and Discussion

3.1. Proof-of-concept of H_2O_2 detection with PB-modified 3D electrodes

3.1.1. Concentrations above 1 μ M

Figure 2 represents the typical open circuit potential (OCP) and current responses of a PB-modified pyrolytic carbon electrode as it was exposed to increasing concentrations of H_2O_2 . Before initiating the OCP recording, the deposited PB film was reduced to PW by applying 0 V for 60 s (initial chronoamperometry in **Figure 1A**). The initial chronoamperometry was a preparative step ensuring that most of the PB was converted to PW. Once PW was generated, the electrical circuit was disconnected and the OCP recording was initiated. The open circuit potentiometry step (**Figure 1B**) was initially set to run for 2 minutes and was followed immediately by another single potential step chronoamperometry (0 V for 60 s, **Figure 1C**). This sequential measurement script (single potential step/OCP/single potential step) was repeated for every tested concentration of the analyte on identically prepared sensors. A stable baseline was obtained in a blank phosphate buffer by rerunning the script a few times. H_2O_2 was spiked manually into the buffer at the starting point of the OCP measurement. The solution was stirred during OCP measurement to enhance the mixing of the analyte and the

buffer to ensure that the analyte molecules reach the sensor surface. **Figure 2A** shows the overlapped OCP transients corresponding to different H₂O₂ concentrations. The four repetitions of the blank OCP overlap (curve **a** in **Figure 2A**), indicating a stable baseline. However, the non-zero baseline potential indicates that a competing reaction with another substance rather than H₂O₂ took place at the sensor surface. Since the potential shift from zero was in the positive direction (electrons are drawn from the electrode), this observation was attributed to the reaction of the dissolved oxygen with the PW film. This postulate was confirmed by several complementary experiments where the dissolved oxygen was removed by purging the solution with nitrogen gas. Exposure to 1 μM H₂O₂ caused a positive potential shift (curve **b** in **Figure 2A**) as expected, which is most visible and distinguishable from the blank at the endpoint (at 180 s) of the OCP measurement. The bar plot in **Figure 2B** illustrates the endpoint value of OCP for the tested H₂O₂ concentrations from the same sensors. A tenfold increase in the concentration of the analyte from 1 μM to 10 μM and from 10 μM to 100 μM doubled the potential endpoint. Although further increase of the analyte concentration to 1 mM imposed yet another obvious rise in the potential, the endpoint value after 2 minutes from the start of the reaction did not show a double augmentation. This observation, which is also reflected in the potential curve of 1 mM H₂O₂ in **Figure 2A-e**, is due to the saturation of the reaction at the sensor surface. According to the Nernst equation, the electrode potential is a logarithmic function of the species that undergo oxidation and reduction at the surface. As molecules of H₂O₂ are reduced, Fe²⁺ ions in the PW are oxidized to Fe³⁺. In this case, the Nernst equation for the half-reaction (oxidation of Fe²⁺) can be written as:

$$E = E^{\circ'} + \frac{RT}{nF} \ln \frac{[Fe^{3+}]}{[Fe^{2+}]}$$

where $E^{\circ'}$ is the formal potential of the reaction at pyrolytic carbon, R is the universal gas constant, T is the thermodynamic temperature, n is the number of electrons transferred in the reaction and F is the Faraday constant. The oxidation of Fe²⁺ to Fe³⁺ by H₂O₂ continues until the numbers of Fe²⁺ and Fe³⁺ ions become nearly equal in the film, which means that PW has been fully oxidized and PB is formed. At this point, the electrode potential stabilizes as it reaches a constant value, indicating that no more reactions take place at the electrode surface. The potential curve for 1 mM H₂O₂ (**Figure 2A-e**) shows that saturation was reached after about 20 s from the time that the analyte was introduced. Thereafter the OCP of the electrode remained constant at just above 400 mV.

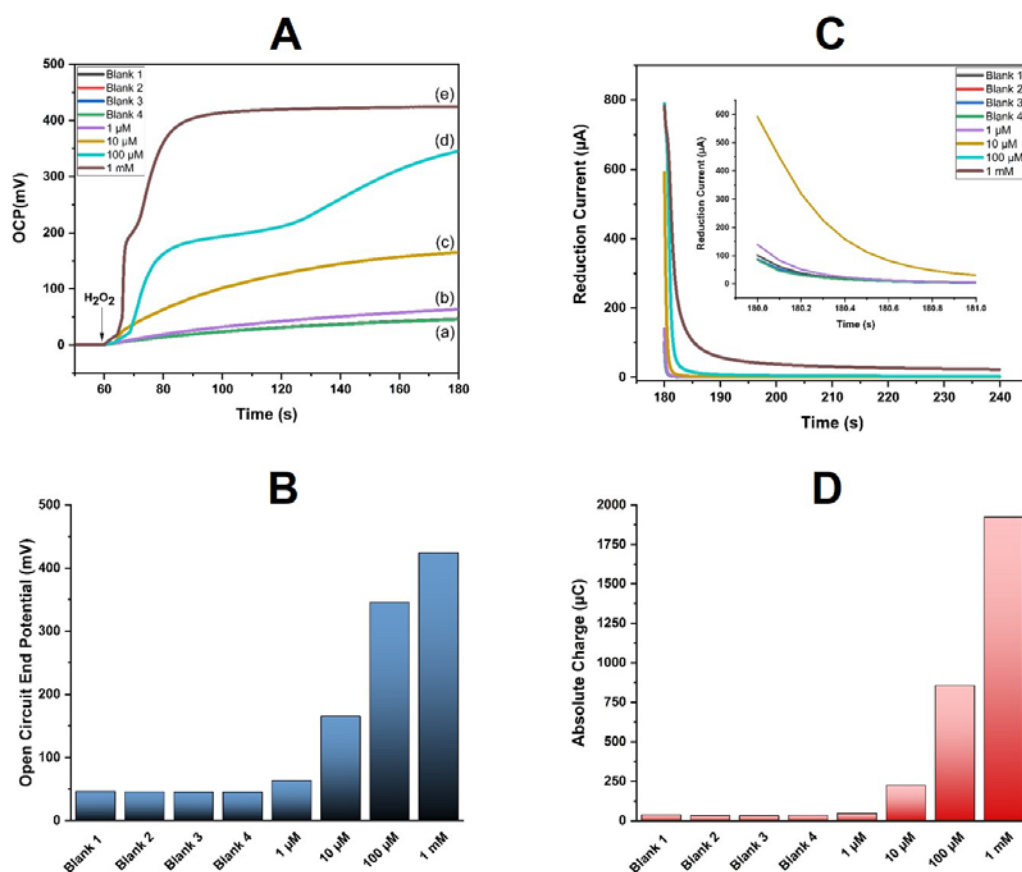


Figure 2 The result of proof-of-concept experiments with H_2O_2 ; **A**) overlapped OCP transients of a PB-modified pyrolytic carbon sensor as it was exposed to (a) blank phosphate buffer, (b) 1 μM , (c) 10 μM , (d) 100 μM and (e) 1 mM H_2O_2 ; **B**) OCP endpoint value after 2 minutes exposure to the analyte; **C**) overlapped current transients following the potentiometry (recharging current of capacitor); **D**) absolute charges calculated by integrating the area under the current responses in the first 10s (t_f : 190s, t_i :180s).

The plot in **Figure 2C** is the overlapped chronoamperometric responses of the sensor to various H_2O_2 concentrations recorded immediately after the potentiometric endpoint for each sample. The stirring was switched off during the current measurement to avoid noise. Once the potential of 0 V was applied, the amount of Fe^{3+} in the PB film, produced because of H_2O_2 reduction in the open circuit mode, was reduced again to Fe^{2+} regenerating the PW film. The resulting reduction current transient follows the Cottrell equation and decays with $t^{1/2}$. The four overlaying blank responses are indicative of the stability of the sensor prior to encountering H_2O_2 , even though the reaction of the film with the dissolved oxygen resulted in a small current. The current response to increasing concentrations of analyte followed the same trend as the OCP. The current response and the area under the current corresponding to the charge increased with increasing concentrations. **Figure 2D** displays the absolute charge values for the blanks and the tenfold increases in the analyte concentration levels. The current changes relative to the baseline were largest in the first few seconds from applying the step of the reducing potential upon the electrode. Therefore, the charge values in plot **D** were recorded during the first 10 s (t_f : 190 s, t_i :180 s). Although, the current curve associated with 1 μM H_2O_2 showed about 50 μA increase in the immediate response compared to the baseline curve (**Figure 2C** inset), the absolute charge value did not show any significant increase compared to the background level. A current increase was not obvious until above

10 μM where a tenfold increase in the analyte concentration generated a doubled charge for each step from 1 μM to 1 mM.

As can be seen in **Figure 2A**, the rate of OCP increase ($\frac{dE_{OCP}}{dt}$) in the given time course is not constant. This is most pronounced from the OCP curves of 100 μM (**d**) and 1 mM (**e**), which showed a linear potential increase during the first 20 s from the start of the reaction and eventually reached a saturation plateau at longer times when all Fe^{2+} ions in the PB film were oxidized. The rate of potential increase within the first 20 s (slope of the linear region of OCP transients) is plotted as a function of H_2O_2 concentration (Log) in **Figure 3**.

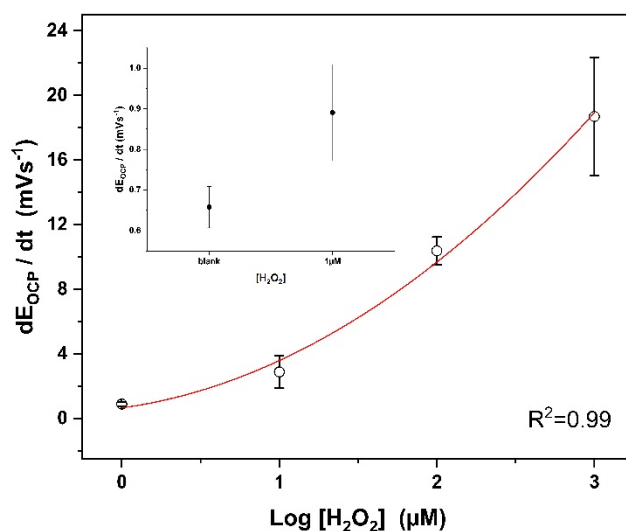


Figure 3 Initial rate of PB-modified pyrolytic carbon potential shift as a function of H_2O_2 concentration. The curve was constructed using the slope of the linear regions (first 20 s) of OCP transients of four ($n=4$) sensors as they were exposed to increasing concentrations of H_2O_2 in the range of 1 μM to 1 mM.

3.1.2. The influence of prolonging open circuit

The plots in **Figure 4** show the effect of varying the period of OCP recording on both the potentiometric and the amperometric responses of identically prepared sensors. The sensors, stabilized in blank phosphate buffer, were exposed to 1 μM H_2O_2 at open circuit for different times varying from 30 to 600 s. As can be seen in **Figure 4A**, the OCP value increased with time, indicating that more reactions took place as the period for potentiometry was extended from 30 to 120 s. As explained before, since the sensors had a non-zero blank response in the presence of dissolved oxygen, the best way of assessing the potentiometric data was to evaluate the growth of the OCP endpoint relative to the baseline OCP recorded at the moment when the reaction of the target analyte (H_2O_2) with PW in the open circuit mode terminates. The bar plots in **Figure 4B** were obtained by subtracting the baseline potentials at 30, 60, 90 and 120 s from the OCP of the sensors exposed to 1 μM H_2O_2 at the same time points ($E_{\text{sample}}(t=30 \text{ s}) - E_{\text{blank}}(t=30 \text{ s})$, $E_{\text{sample}}(t=60 \text{ s}) - E_{\text{blank}}(t=60 \text{ s})$, ...). Keeping the circuit open for longer times allowed more Fe^{2+} ions to be oxidized, thus the potential shift from the background was more pronounced for longer times from the start of the reaction (introduction of H_2O_2). Increasing the open circuit period from 30 to 60 s almost doubled the average potential shift of the sensors from just above 5 mV to 10 mV. Further increase of the

reaction time to 90 and 120 s, resulted in about +2.5 mV potential increase compared to the background. This can be beneficial in static conditions (i.e. no stirring) where diffusion is the rate-limiting factor for the electrode reactions, as allowing longer time would mean that more molecules of analyte reach the active sites of the PW film on the electrode. However, the increasing standard deviations (error bars) of the average potential responses of the sensors with time indicated that the reproducibility of the sensor responses declined with time. Empirically, it was realized that the declining reproducibility of the sensor responses were due to the instability of the deposited electrocatalytic films as they were exposed to H_2O_2 for longer times.

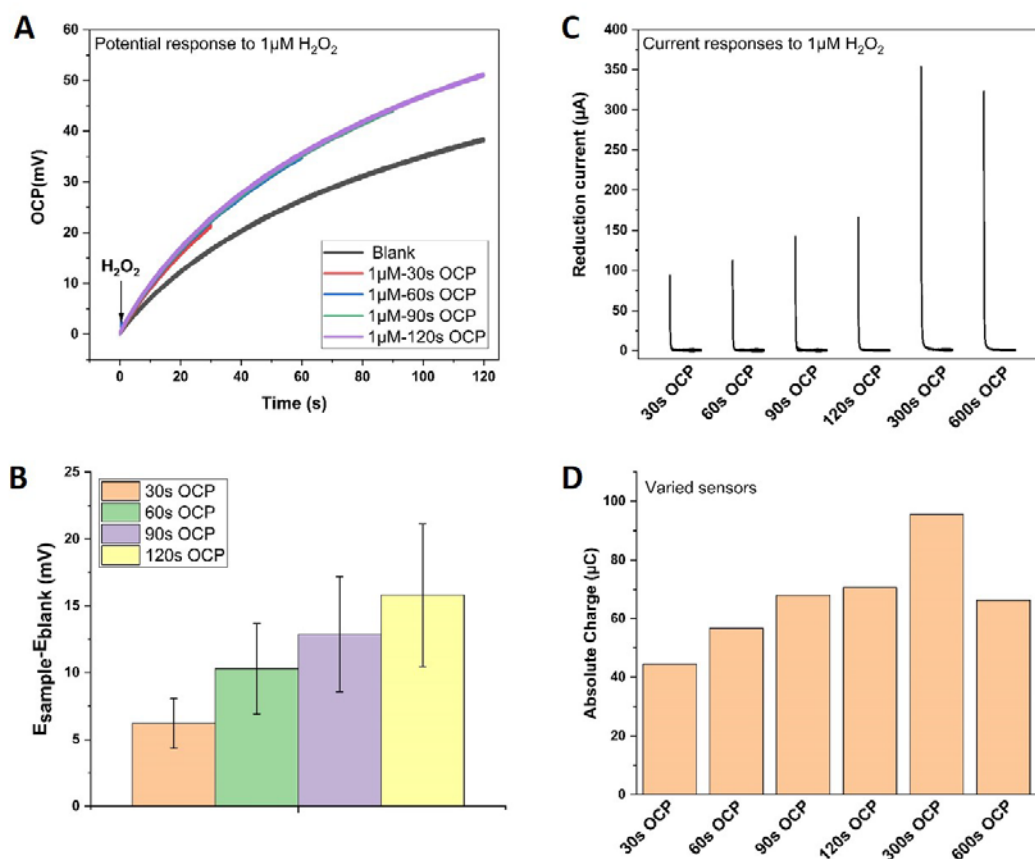


Figure 4 Effect of varying reaction time with H_2O_2 on the potential and current responses; **A)** overlapped OCP transients of four identically prepared sensors as they were exposed to 1 μM H_2O_2 for 30, 60, 90 and 120 s; **B)** potential shift from the baseline (potential in blank buffer) as a result of exposure to 1 μM H_2O_2 for different time lengths ($n=3$); **C)** current responses to 1 μM H_2O_2 after spending 30, 60, 90, 120, 300 and 600 s at open circuit; **D)** absolute charge produced after exposure to 1 μM H_2O_2 at open circuit for different time lengths, charge was obtained by intergrating the area under current responses in C.

Figure 4C demonstrates the reduction currents following the open circuit potentiometry with different time lengths. Extending the period of potentiometry at an open circuit, resulted in an increasing current peak of PB film reduction at 0 V. When potentiometry was given 300 s, the consecutive recharging current showed a sharp response at 350 μA which was twice the current response after 120 s of potentiometry in open circuit mode. These results confirm the potentiometric responses of the sensors. The longer the period of open circuit potentiometry was, the more electrons were lost from the electrocatalytic film because of Fe^{2+} oxidation to Fe^{3+} . Once the circuit was reestablished, more electrons were drawn from the electrode to substitute the lost charge in the film. Thus, higher reduction currents were recorded.

However, when the reaction time at open circuit was extended to 600 s, a current drop was observed. The corresponding charge values that were obtained by integrating the area under the current responses in **Figure 4C**, are presented in **Figure 4D**. The charge followed the same trend as the current, gradually increasing from about 40 μC for 30 s of OCP run to above 90 μC for 300 s. The drop in current and charge after 600 s was probably due to the instability of the PB film as it was exposed to H_2O_2 for an extended period. The cyclic voltammograms of the PB film on the sensors, exposed to 1 μM H_2O_2 for 600 s, showed 50% drop in the PB/PW redox peaks (supporting information **S 1**). Therefore, extending the OCP run time beyond 300 s was not beneficial for enhancing the current response of the sensors. Nevertheless, extending OCP time up to 300 s can be good for detection, at the cost of prolonged measurements.

3.1.3. Concentrations below 1 μM in the presence of dissolved molecular oxygen

For medical diagnosis purposes, usually, detection of H_2O_2 and histamine in μM and sub- μM concentration ranges are of interest. Therefore, in this work, we challenged the developed method with physiologically relevant amounts of H_2O_2 .

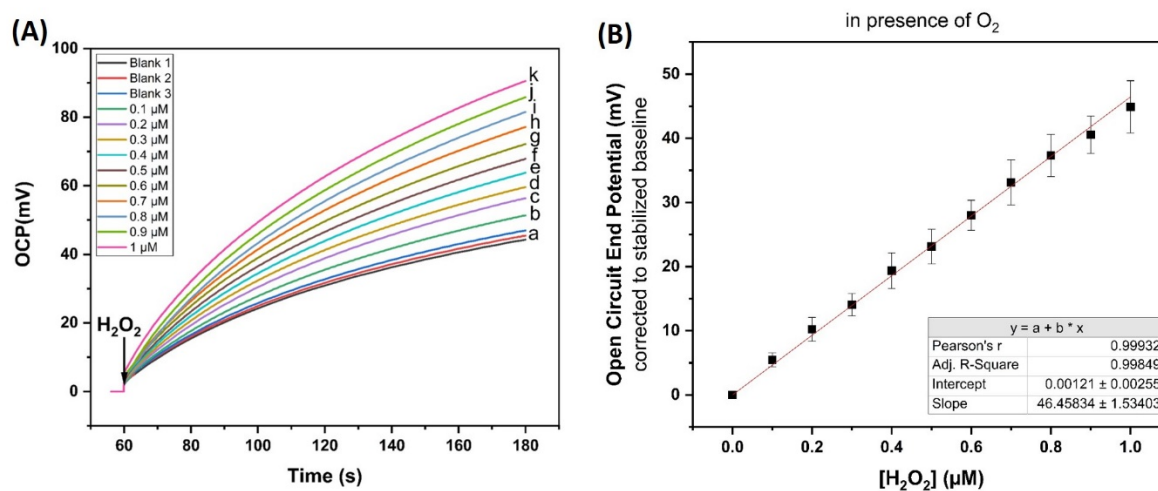


Figure 5 Potentiometric measurement of H_2O_2 in sub- μM concentration range; **(A)** overlapped OCP transients (120 s) of a sensor in a) blank buffer, b) 0.1 μM , c) 0.2 μM , d) 0.3 μM , e) 0.4 μM , f) 0.5 μM , g) 0.6 μM , h) 0.7 μM , i) 0.8 μM , j) 0.9 μM and k) 1 μM H_2O_2 ; **(B)** calibration curve constructed by averaging the shift of open circuit end potential (value at 120 s) of 4 sensors from their stabilized baseline per each tested H_2O_2 concentration in the range of 0.1-1 μM .

The OCP transient in **Figure 5A** represents the potentiometric response of the PB-modified pyrolytic carbon sensors to H_2O_2 (in buffer) with concentrations in the sub- μM range. Since small concentration steps were to be tested, the OCP time length was fixed to 120 s. Three blanks were tested to ensure a stable baseline (**a**: blank 1-3 overlapped). Thereafter, concentrations ranging from 100 nM (**b**) to 1 μM (**k**) were gradually added to the solution. Despite the interference of dissolved oxygen, the OCP demonstrated good behavior with a clear positive shift (~ 5 mV) for each concentration step increase. **Figure 5B** shows the calibration curve based on the OCP data from four sensors. The OCP endpoint values (at 120

s) for each sensor/concentration were normalized to the stabilized baseline of the sensor in blank buffer. Linear regression with $R^2=0.99$ was obtained between 0.1 to 1 μM . The limit of detection (LOD) was calculated to be 71 nM by using the standard deviation of the OCP of the lowest tested concentration (0.1 μM) and the slope of the linear regression. This is about half the LOD that we had previously obtained by stirred batch amperometry for electrodes prepared identically [36]. These experimental results prove that the open circuit potentiometry with PB-modified 3D electrode allows for the detection of small concentrations of H_2O_2 regardless of the competing reaction of the dissolved oxygen with the PB. The current and charge responses of the same sensors from the chronoamperometric step were inconclusive (supporting information **S2**), meaning these measurements did not yield similar sensitivity to sub- μM H_2O_2 as the potentiometry did. We believe that the challenge with the chronoamperometry in the sub- μM range might have arisen from either or a combination of (i) the potentiostat, (ii) the electrode resistance, or/and (iii) the partial decay of the PB. As opposed to the potentiometry which is a slow measurement, the current transient recording by chronoamperometry is a fast-progressing procedure. As the current transients in **Figure 2C** display, the regeneration of PW in the recharging step evolves in less than a few seconds. Thus, the potentiostat should be able to respond rapidly and sample current instantly as the circuit is reconnected and the potential is switched on. If there is a delay between the moment that the potential is applied and when the first data point is recorded, some charge will be lost, or in another words, it will not be captured by the instrument. The shorter this delay, the more precise the measured current will be. This is especially trivial for the detection of very low concentrations of H_2O_2 as the amount of transferred charge is very small. We tried to minimize the lag by setting the current sampling time interval to the minimum possible value. At current sampling time interval of 1ms, we hit the limitations of our equipment. Moreover, the resistance of the pyrolytic carbon electrode and the contacts have huge effects on the current response. The conductivity of the pyrolytic carbon is influenced by many factors including the composition of the polymer precursor and the pyrolysis temperature. For example, any slight changes in the pyrolysis temperature may hamper the carbonization process resulting in incorporation of residual elements in the final pyrolytic carbon which increases the resistance of the electrode. Finally, we believe that the instability of the PB film and its progressive dissolution by the hydroxyl ions could be another reason for the encountered challenge at the low concentrations. If the amount of PB/PW which decays during the experiment is larger than the amount of regenerated PW in the chronoamperometry step, no current response could be recorded beyond the baseline.

3.1.4. The influence of removing dissolved oxygen

To evaluate the influence of the dissolved oxygen on the stability and the sensitivity of the PB-modified sensors, the experiments with H_2O_2 at low concentrations (below 1 μM) were repeated in deoxygenated buffer. Oxygen was removed by purging the buffer with nitrogen gas for 3 hours before starting the experiment. The concentration of the dissolved oxygen was measured every 30 minutes. The freshly prepared buffer contained 8.27 mg L^{-1} of dissolved oxygen. After 1,5 hours, the oxygen concentration in the buffer dropped to 1.15 mg L^{-1} , and eventually this value was 0.59 mg L^{-1} after 3 hours. The sequential measurement script (single potential step/OCP 120s/single potential step) was repeated 6 times on four identically prepared PB-modified pyrolytic carbon sensors in the deoxygenated blank buffer. The charge from the second chronoamperometry step was obtained for each cycle and charge variation

from the previous cycle (ΔQ) was calculated. The background charge variations per each repeated cycle in the presence and the absence of dissolved oxygen can be seen in **Figure 6**. When the dissolved oxygen was removed from the buffer the charge variations decreased drastically and reached zero at the 6th cycle meaning that the baselines of the sensors were stabilized. In the presence of dissolved oxygen, the background charge fluctuated which confirms that the reaction of PB with the dissolved oxygen contributes to nonzero moving baseline.

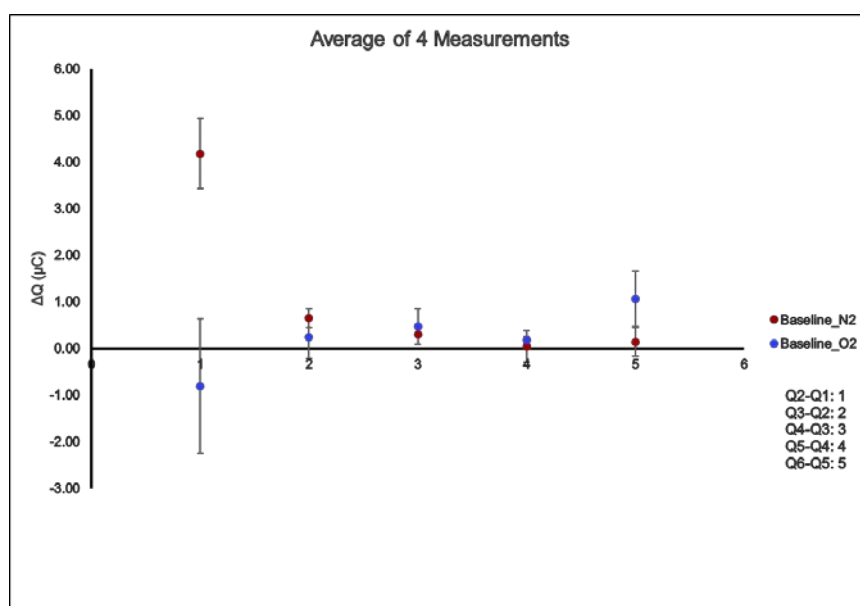


Figure 6 Stabilization of the background charge in the presence and the absence of dissolved oxygen in blank phosphate buffer pH 5.5.

Thereafter, the responses of the sensors to small concentrations of H_2O_2 in deoxygenated buffer were obtained. The calibration curve in **Figure 7** was constructed by calculating the percentage of charge increase relative to the background charge (charge integrated from the current response to blank buffer) per tested H_2O_2 concentration using the following equation:

$$\Delta Q = \frac{Q_{\text{Sample}} - Q_{\text{blank}}}{Q_{\text{blank}}} \times 100$$

As the linear trend of the calibration curve shows, removing oxygen enhanced the current and the corresponding charge responses of the PB-modified pyrolytic carbon sensors to H_2O_2 in the range between 100 nM and 1 μM .

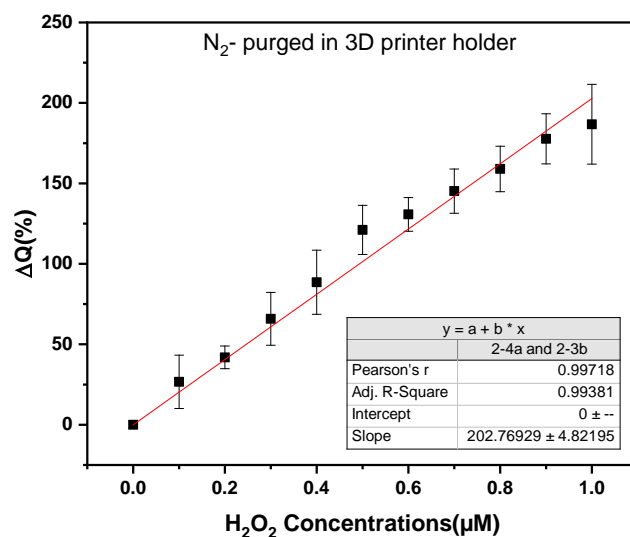


Figure 7 Charge responses to H_2O_2 in deoxygenated phosphate buffer.

When smaller concentrations of H_2O_2 in the range between 10 to 100 nM were tested in the absence of dissolved oxygen, the current responses got into a regime where it was difficult to integrate and quantify the charge. Nevertheless, the open circuit potentiometry, as demonstrated in **Figure 8**, provided sufficient sensitivity. As it can be seen from the linear potential response, it is possible to improve the LOD and increase the sensitivity of the sensors by removing the oxygen and minimizing the influence of PB-oxygen reaction on the background, thereby.

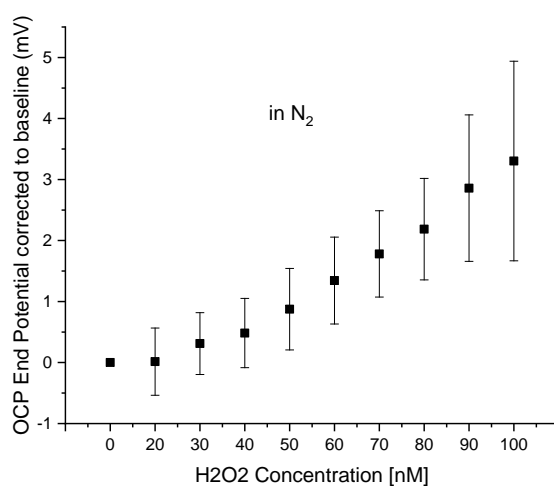


Figure 8 Potentiometric responses to H_2O_2 in the absence of dissolved oxygen.

3.2. Construction of histamine biosensor on PB-modified 3D electrodes

For the construction of the biosensor, DAO was immobilized on the electrode as the recognition element for histamine detection. BSA and GA were added to DAO solution before immobilization. BSA was used as a spacer molecule between the DAO and the GA, whilst GA acted as a cross-linker of the enzymes. Initial experiments indicated that high concentrations of BSA would block the DAO activity and increase the resistance of the biosensor, while low BSA concentrations resulted in a porous and unstable layer. Likewise, when high concentrations of GA were added to the mixture of DAO and BSA, a thick gel-like matter was formed immediately which could obviously not be used for immobilization. Low concentrations of GA also resulted in a loosely bound and unstable enzyme layer which was removed off the electrode surface during electrochemical measurements. Therefore, optimization of the ratio between the DAO, BSA and GA was necessary. As mentioned earlier, the optimization of the enzyme immobilization was performed in the stirred batch amperometry mode. The results are presented in the following section.

3.2.1. Determination of optimum amounts of BSA and GA

The graph in **Figure 9** shows the average current responses of at least three biosensors ($n=3$ per each BSA concentration) to 1 mM of histamine as a function of different BSA concentrations used for enzyme immobilization. The current response of each biosensor to histamine was normalized to the baseline (stabilized current in blank buffer). The best current response from the biosensors was obtained when 0.5% BSA was used in combination with 10 mg mL⁻¹ DAO to construct a recognition layer on the PB-modified pyrolytic carbon. Both a lower (0.25%) and a few higher (1.5%, 3% and 6%) BSA concentrations yielded significantly lower signals.

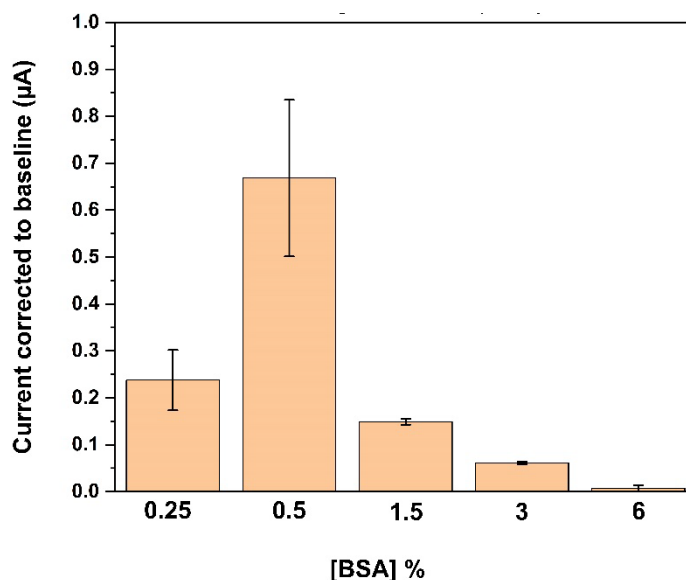


Figure 9 Effect of the concentration of BSA on the amperometric signal for 1 mM histamine. DAO and GA concentrations were 10 mg mL⁻¹ and 0.5%, respectively. Average data \pm SD are indicated ($n=3$).

Next, the optimum amount of BSA was used together with 10 mg mL⁻¹ DAO and different concentrations of GA, to find the optimum amount of cross-linker for immobilization. As

depicted in **Figure 10**, the best current response from the biosensors was obtained when 1% GA was used to cross-link with the DAO and BSA on the PB-modified pyrolytic carbon. Of the two lower (0.25% and 0.5%) and one higher (3%) GA concentrations which were tested, none of them showed as good a signal as the biosensors that were constructed by 1% GA.

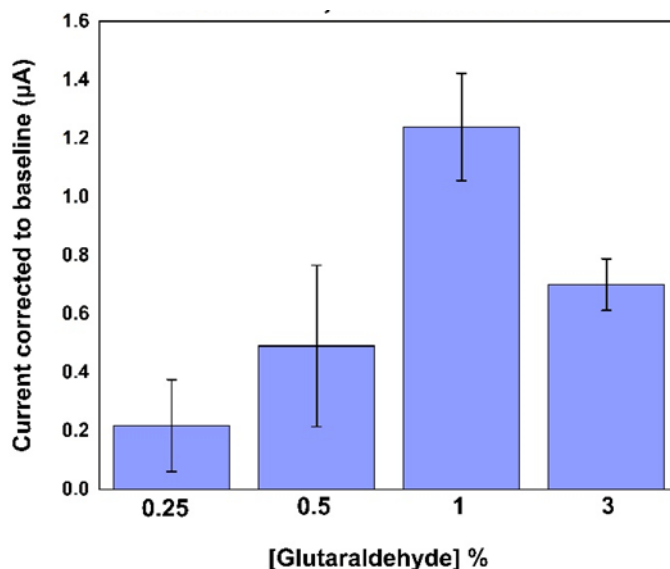


Figure 10 Effect of the concentration of GA on the amperometric signal for 1 mM histamine. DAO and BSA concentrations were 10 mg mL⁻¹ and 0.5%, respectively. Average data ± SD are indicated (n=3).

3.2.2. Enzyme immobilization

After the PB electrodeposition and stabilization on the 3D pyrolytic carbon WE, a 4-µL drop consisting of 2 µL of DAO (10 mg mL⁻¹), 1 µL of 0.5% BSA and 1 µL of 1% GA was drop cast on the electrode over the PB film and left at room temperature (22-25°C) for 30 minutes to immobilize. Afterward, the unbound molecules were gently rinsed off the electrode using PBS pH 7.2. The biosensors were used immediately after preparation.

3.3. Histamine detection in buffer

The calibration curve in **Figure 11** was obtained from the potentiometric responses of five identically prepared enzymatic biosensors to increasing concentrations of histamine. To find the dynamic range, two concentrations in the sub-µM range (100 and 500 nM) and three concentrations above 1 µM with tenfold increase in each step (10, 100, 1000 µM) were tested. For each biosensor, a stable baseline in blank buffer was achieved, which was subtracted from the biosensor signal associated with each tested sample. As previously mentioned, PB is most stable at pH 5.5, therefore the experiments with histamine were performed in phosphate buffer at pH 5.5 to maintain the PB stability for longer times. Although this pH is not ideal for the enzyme activity (ideal buffer conditions for the enzymes were pH 7.2 at 37°C), the biosensors showed good and reproducible responses to different amounts of histamine. As the inset in **Figure 11** shows, the potentiometric responses of the biosensors to histamine in the sub-µM range were linear ($R^2=0.99$). The LOD was calculated for the lowest tested concentration (100 nM histamine) and found to be 363 nM.

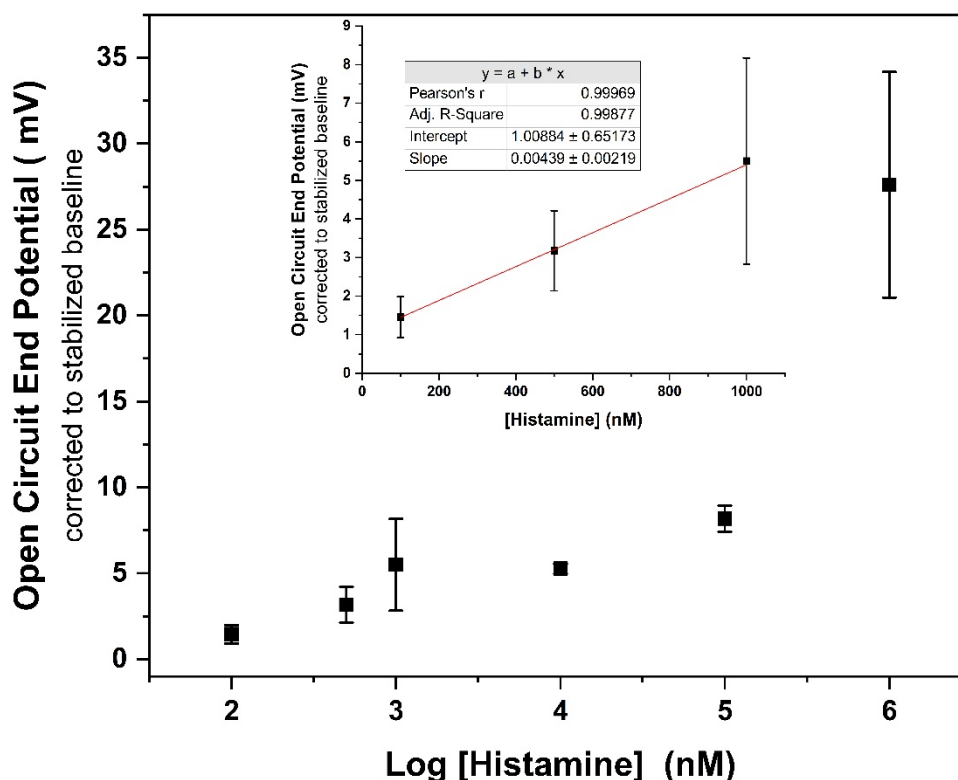


Figure 11 Potentiometric response of PB/enzyme-modified pyrolytic carbon to increasing concentrations of histamine in phosphate buffer at pH 5.5 at room temperature; calibration curve constructed by averaging the shift of open circuit end potential (value at 120 s) of five sensors from their stabilized baseline per each tested histamine concentration.

3.4. Histamine detection in cell supernatant

A proof-of-concept experiment with the supernatant of LAD2 human mast cells, containing histamine released from the activated cells, was performed on two individual biosensors. Each biosensor was prepared for quick single use to minimize any loss of PB electrocatalytic activity during the experiment and the reaction time with the histamine at open circuit was extended to 300s. To mimic the *in vivo* histamine measurement circumstances, histamine detection in the cell supernatant was performed in static conditions, unlike the previously performed experiments. Two histamine concentrations were selected to evaluate the biosensor performance; one in the sub- μM range (809 nM) above the obtained LOD and one at μM level (15.24 μM) where the probability of detecting histamine was high. Before introducing the histamine-containing samples to the biosensors, baselines were recorded in the blank (cell/histamine-free) HR buffer containing the same amount of compound 48/80 that was used for stimulation of cells, to identify any possible interference in histamine detection from other substances (including compound 48/80) present in the complex matrix of the cell supernatants. As the two OCP transients in **Figure 12 A** and **C** demonstrate, despite having different background potentials both biosensors showed stable baselines (plot (a) in both graphs shows overlapping of repeated baselines) in a blank HR buffer containing compound 48/80. In the next step, the blank HR buffers were removed, and histamine-

containing cell supernatants were introduced to the biosensors. The presence of 809 nM histamine resulted in a 3-mV potential increase (open circuit end potential corrected to baseline end potential) for the biosensor in **Figure 12A**. While the potentiometry in static condition showed a clear response to this low concentration (below 1 μM) of histamine, the current response of the same biosensor (**Figure 12B**) displayed the same challenge as it was encountered with the H_2O_2 detection in the similar concentration range. As it can be seen, the current signal from 809 nM histamine is barely distinguishable from the baseline, and therefore cannot be used for a quantitative analysis. Nevertheless, the open circuit potentiometry provides the sensitivity required for the specific detection of histamine available in low concentrations in the mast cell medium. Histamine concentration of 15.24 μM in the cell supernatant resulted in a 10-mV potential increase for the second biosensor in **Figure 12C**. The current response of the same biosensor to histamine, which is presented in **Figure 12D**, showed about 62.5 μA increase compared to the baseline confirming the results obtained from the H_2O_2 detection in the similar range (above 1 μM).

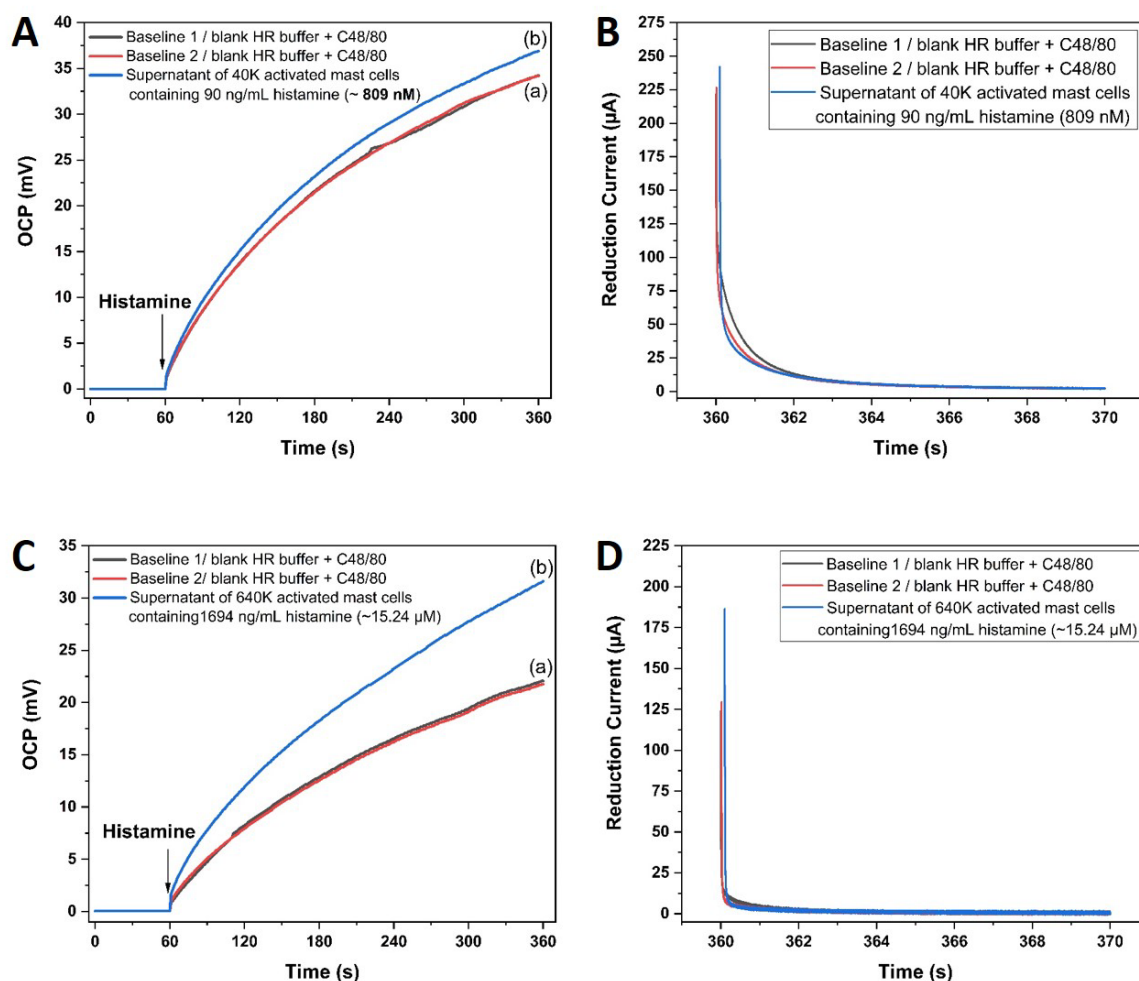


Figure 12 Potential and current responses of PB/enzyme-modified pyrolytic carbon to released histamine from activated mast cells; **A**) overlapped OCP transients (300 s) in (a) blank HR buffer containing cell stimulating compound 48/80, (b) supernatant of 40,000 activated mast cells containing 809 nM histamine; **B**) overlapped current transients of stabilized baseline in blank HR buffer+ compound 48/80 and cell supernatant containing 809 nM histamine; **C**) overlapped OCP transients (300 s) in (a) blank HR buffer containing cell stimulating compound 48/80, (b) supernatant of 640,000 activated mast cells containing 15.24 μM histamine; **D**) overlapped current transients of stabilized baseline in blank HR buffer+compound 48/80 and cell supernatant containing 15.24 nM histamine.

4. Conclusion and future perspective

Combining potentiometry and chronoamperometry techniques provides the possibility of exploiting the advantages of each technique for a versatile analysis, and dual data generation allows analyte quantification in different concentration ranges. Nevertheless, the open circuit potentiometry alone is more sensitive for H₂O₂ detection than stirred batch amperometry with PB-modified pyrolytic carbon electrode. In the combined potentiometry and chronoamperometry method, or what we here call the 'capacitive method' due to its analogy to a capacitor, not only the potential and current responses of the sensor is concentration dependent, but they are also directly proportional to the time length that the sensor spends at open circuit mode in contact with the analyte. The longer the period of the open circuit, the higher is the chance of analyte diffusion to the sensor's surface. Allowing more molecules to diffuse and react, means that the loss of electrons from the PW film to the H₂O₂ molecules is larger. Thus, the sensor's potential shift and recharging current were enhanced by increasing the OCP runtime. However, it was observed that when the sensors were given longer times than 300 s or were used repeatedly, the instability of the PB film over time, especially when in contact with oxygen and H₂O₂, had an adverse effect on the amplitude of the potential and the current responses. Although the reaction of dissolved oxygen with PB film causes a non-zero baseline, the open circuit potentiometry as a method of measurement showed remarkable sensitivity to concentrations of H₂O₂ at sub- μ M level (down to 100 nM) in the presence of oxygen, such that the endpoint value of OCP of the sensors after 120 s of exposure to analyte was distinguishable from the stabilized baseline in the blank buffer. The current response to H₂O₂ with concentrations below 1 μ M in the presence of dissolved oxygen did not show the same sensitivity as the potential response, as the current and the corresponding charge values were not distinguishable from the background and more than often it was observed that the amount of the measured charge from sub- μ M concentrations of H₂O₂ was less than the stabilized background charge. One hypothesis is that the amount of lost charge due to PB electroactivity decay was larger than the charge produced due to regeneration of PW. One way which we investigated to solve this problem, was to remove the dissolved oxygen from the buffer by purging it with nitrogen gas. In the absence of oxygen, the baseline was lower and the stability of the PB film was enhanced, so was current and the corresponding charge response of the sensor greatly improved. However, the oxidase enzymes require oxygen as the electron acceptor to catalyze the oxidation or reduction of substrates. Therefore, removing oxygen is not always favorable. In future, one could tackle this challenge by enhancing the stability of PB film. Another hypothesis which was not fully investigated in this study because of the potentiostat limitations, is that the current measurement in low concentration ranges could be enhanced by reducing the current sampling time interval to less than 1 ms. Nevertheless, the current and the corresponding charge response to larger concentrations (above 1 μ M) of analyte behaved as the main hypothesis of the capacitive electrochemical transduction concept predicted. Further, plant-derived DAO was immobilized on PB-modified pyrolytic carbon electrodes as a receptor to capture histamine and catalyze its oxidation. LOD of 363 μ M from histamine measurement in buffer was obtained based on the potentiometric data. Selective detection of histamine (809

nM and 15.24 μM) released from activated LAD2 human mast cells was demonstrated by using the capacitive method. Having a better sensitivity than the stirred batch amperometry though in static conditions makes the capacitive method ideal transduction for on-chip cell-based electrochemical measurements, *in vivo* H_2O_2 sensors and oxidase-based biosensors integrated in dermal microneedle patches or in wearable devices.

References

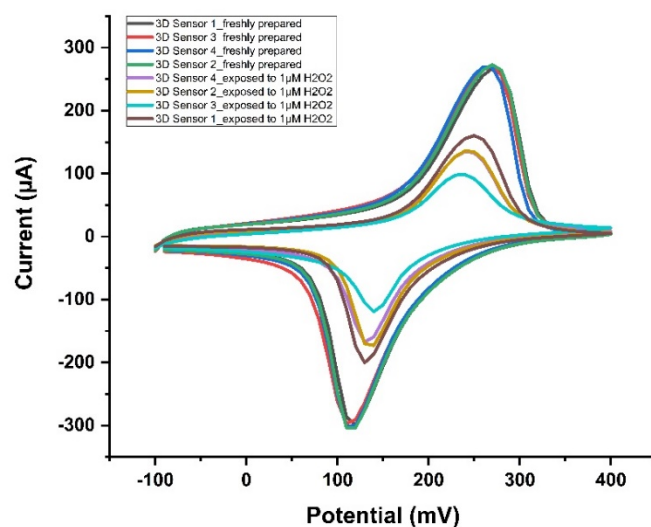
- [1] V.D. Neff, Electrochemical Oxidation and Reduction of Thin Films of Prussian Blue, *J. Electrochem. Soc.* 125 (1978) 886–887. <https://doi.org/10.1149/1.2131575>.
- [2] H. Yi, R. Qin, S. Ding, Y. Wang, S. Li, Q. Zhao, F. Pan, Structure and Properties of Prussian Blue Analogues in Energy Storage and Conversion Applications, *Adv. Funct. Mater.* 31 (2021) 1–25. <https://doi.org/10.1002/adfm.202006970>.
- [3] L. Wang, Y. Han, X. Feng, J. Zhou, P. Qi, B. Wang, Metal-organic frameworks for energy storage: Batteries and supercapacitors, *Coord. Chem. Rev.* 307 (2016) 361–381. <https://doi.org/10.1016/j.ccr.2015.09.002>.
- [4] R. Koncki, Chemical sensors and biosensors based on Prussian blues, *Crit. Rev. Anal. Chem.* 32 (2002) 79–96. <https://doi.org/10.1080/10408340290765452>.
- [5] P. Salazar, M. Martín, R.D. O’Neill, P. Lorenzo-Luis, R. Roche, J.L. González-Mora, Prussian Blue and Analogues: Biosensing Applications in Health Care, *Adv. Biomater. Biodevices.* 9781118773 (2014) 423–450. <https://doi.org/10.1002/9781118774052.ch12>.
- [6] Y. Matos-Peralta, M. Antuch, Review—Prussian Blue and Its Analogs as Appealing Materials for Electrochemical Sensing and Biosensing, *J. Electrochem. Soc.* 167 (2020) 037510. <https://doi.org/10.1149/2.0102003jes>.
- [7] A.A. Karyakin, E.E. Karyakina, L. Gorton, Prussian-Blue-based amperometric biosensors in flow-injection analysis, *Talanta.* 43 (1996) 1597–1606. [https://doi.org/10.1016/0039-9140\(96\)01909-1](https://doi.org/10.1016/0039-9140(96)01909-1).
- [8] A.A. Karyakin, E.E. Karyakina, L. Gorton, The electrocatalytic activity of Prussian blue in hydrogen peroxide reduction studied using a wall-jet electrode with continuous flow, *J. Electroanal. Chem.* 456 (1998) 97–104. [https://doi.org/10.1016/S0022-0728\(98\)00202-2](https://doi.org/10.1016/S0022-0728(98)00202-2).
- [9] A.A. Karyakin, E.E. Karyakina, L. Gorton, On the mechanism of H₂O₂ reduction at Prussian Blue modified electrodes, *Electrochem. Commun.* 1 (1999) 78–82. [https://doi.org/10.1016/S1388-2481\(99\)00010-7](https://doi.org/10.1016/S1388-2481(99)00010-7).
- [10] A.A. Karyakin, E.E. Karyakina, Prussian blue-based “artificial peroxidase” as a transducer for hydrogen peroxide detection. Application to biosensors, *Sensors Actuators, B Chem.* 57 (1999) 268–273. [https://doi.org/10.1016/S0925-4005\(99\)00154-9](https://doi.org/10.1016/S0925-4005(99)00154-9).
- [11] A.A. Karyakin, Advances of Prussian blue and its analogues in (bio)sensors, *Curr. Opin. Electrochem.* 5 (2017) 92–98. <https://doi.org/10.1016/j.coelec.2017.07.006>.
- [12] F. Ricci, G. Palleschi, Sensor and biosensor preparation, optimisation and applications of Prussian Blue modified electrodes, *Biosens. Bioelectron.* 21 (2005) 389–407. <https://doi.org/10.1016/j.bios.2004.12.001>.
- [13] L. Chao, W. Wang, M. Dai, Y. Ma, L. Sun, X. Qin, Q. Xie, Step-by-step electrodeposition of a high-performance Prussian blue-gold nanocomposite for H₂O₂ sensing and glucose biosensing, *J. Electroanal. Chem.* 778 (2016) 66–73. <https://doi.org/10.1016/j.jelechem.2016.08.017>.
- [14] J.Z. Tao, G.R. Xu, H.L. Hao, F.X. Yang, K.S. Ahn, W.Y. Lee, Poly(m-phenylenediamine)-Prussian blue hybrid film formed by one-step electrochemical deposition for glucose biosensor, *J. Electroanal. Chem.* 689 (2013) 96–102. <https://doi.org/10.1016/j.jelechem.2012.09.043>.
- [15] Y. Lin, L. Hu, L. Yin, L. Guo, Electrochemical glucose biosensor with improved performance based on the use of glucose oxidase and Prussian Blue incorporated into

- a thin film of self-polymerized dopamine, *Sensors Actuators, B Chem.* 210 (2015) 513–518. <https://doi.org/10.1016/j.snb.2014.12.107>.
- [16] H. Lee, C. Song, Y.S. Hong, M.S. Kim, H.R. Cho, T. Kang, K. Shin, S.H. Choi, T. Hyeon, D.H. Kim, Wearable/disposable sweat-based glucose monitoring device with multistage transdermal drug delivery module, *Sci. Adv.* 3 (2017) 1–9. <https://doi.org/10.1126/sciadv.1601314>.
- [17] E. V. Daboss, D. V. Tikhonov, E. V. Shcherbacheva, A.A. Karyakin, Ultrastable Lactate Biosensor Linearly Responding in Whole Sweat for Noninvasive Monitoring of Hypoxia, *Anal. Chem.* (2022) 9201–9207. <https://doi.org/10.1021/acs.analchem.2c02208>.
- [18] S. Varma, Y. Yigzaw, L. Gorton, Prussian blue-glutamate oxidase modified glassy carbon electrode: A sensitive L-glutamate and β -N-oxalyl- α,β -diaminopropionic acid (β -ODAP) sensor, *Anal. Chim. Acta.* 556 (2006) 319–325. <https://doi.org/10.1016/j.aca.2005.09.047>.
- [19] S. Cinti, F. Arduini, D. Moscone, G. Palleschi, L. Gonzalez-Macia, A.J. Killard, Cholesterol biosensor based on inkjet-printed Prussian blue nanoparticle-modified screen-printed electrodes, *Sensors Actuators, B Chem.* 221 (2015) 187–190. <https://doi.org/10.1016/j.snb.2015.06.054>.
- [20] S. Piermarini, D. Migliorelli, G. Volpe, R. Massoud, A. Pierantozzi, C. Cortese, G. Palleschi, Uricase biosensor based on a screen-printed electrode modified with Prussian blue for detection of uric acid in human blood serum, *Sensors Actuators, B Chem.* 179 (2013) 170–174. <https://doi.org/10.1016/j.snb.2012.10.090>.
- [21] H. Shi, Y. Yang, J. Huang, Z. Zhao, X. Xu, J. ichi Anzai, T. Osa, Q. Chen, Amperometric choline biosensors prepared by layer-by-layer deposition of choline oxidase on the Prussian blue-modified platinum electrode, *Talanta.* 70 (2006) 852–858. <https://doi.org/10.1016/j.talanta.2006.02.012>.
- [22] X.X. Dong, J.Y. Yang, L. Luo, Y.F. Zhang, C. Mao, Y.M. Sun, H.T. Lei, Y.D. Shen, R.C. Beier, Z.L. Xu, Portable amperometric immunosensor for histamine detection using Prussian blue-chitosan-gold nanoparticle nanocomposite films, *Biosens. Bioelectron.* 98 (2017) 305–309. <https://doi.org/10.1016/j.bios.2017.07.014>.
- [23] C. Kaçar, P.E. Erden, B. Dalkiran, E.K. İnal, E. Kiliç, Amperometric biogenic amine biosensors based on Prussian blue, indium tin oxide nanoparticles and diamine oxidase– or monoamine oxidase–modified electrodes, *Anal. Bioanal. Chem.* 412 (2020) 1933–1946. <https://doi.org/10.1007/s00216-020-02448-4>.
- [24] S. Leonardo, M. Campàs, Electrochemical enzyme sensor arrays for the detection of the biogenic amines histamine, putrescine and cadaverine using magnetic beads as immobilisation supports, *Microchim. Acta.* 183 (2016) 1881–1890. <https://doi.org/10.1007/s00604-016-1821-8>.
- [25] S. Piermarini, G. Volpe, R. Federico, D. Moscone, G. Palleschi, Detection of biogenic amines in human saliva using a screen-printed biosensor, *Anal. Lett.* 43 (2010) 1310–1316. <https://doi.org/10.1080/00032710903518724>.
- [26] A.P. Fontenot, R.S. Peebles, Allergy and hypersensitivity, *Curr. Opin. Immunol.* 25 (2013) 736–737. <https://doi.org/10.1016/j.coi.2013.10.007>.
- [27] S.C. Bischoff, Role of mast cells in allergic and non-allergic immune responses: Comparison of human and murine data, *Nat. Rev. Immunol.* 7 (2007) 93–104. <https://doi.org/10.1038/nri2018>.
- [28] S. Wernersson, G. Pejler, Mast cell secretory granules: Armed for battle, *Nat. Rev.*

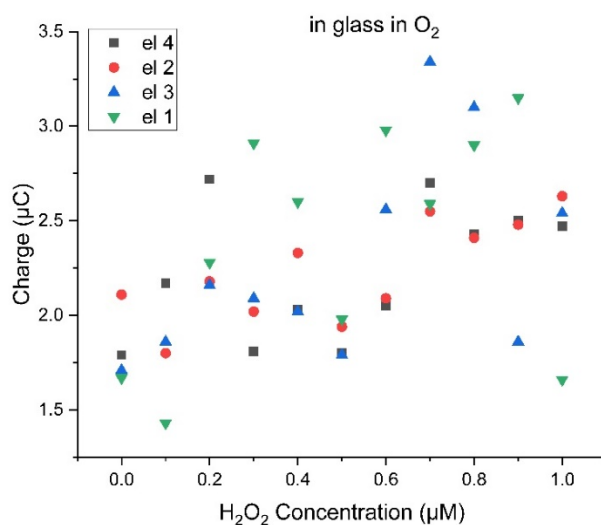
- Immunol. 14 (2014) 478–494. <https://doi.org/10.1038/nri3690>.
- [29] J. -C Schwartz, H. Pollard, T.T. Quach, Histamine as a Neurotransmitter in Mammalian Brain: Neurochemical Evidence, *J. Neurochem.* 35 (1980) 26–33. <https://doi.org/10.1111/j.1471-4159.1980.tb12485.x>.
- [30] H.L. Haas, O. Selbach, O.A. Sergeeva, Sleep and sleep states: Histamine role, Elsevier, 2016. <https://doi.org/10.1016/B978-0-12-809324-5.02851-0>.
- [31] L. Fernández-Novoa, R. Cacabelos, Histamine function in brain disorders, *Behav. Brain Res.* 124 (2001) 213–233. [https://doi.org/10.1016/S0166-4328\(01\)00215-7](https://doi.org/10.1016/S0166-4328(01)00215-7).
- [32] B. Rose, Rôle of histamine in anaphylaxis and allergy, *Am. J. Med.* 3 (1947) 545–559. [https://doi.org/10.1016/0002-9343\(47\)90200-3](https://doi.org/10.1016/0002-9343(47)90200-3).
- [33] R.W. Schayer, The Origin and Fate of Histamine in the Body, in: *Ciba Found. Symp. - Histamine* (Eds G.E.W. Wolstenholme C.M. O'Connor), WILEY, n.d. <https://doi.org/https://doi.org/10.1002/9780470718957.ch24>.
- [34] J.M. Hungerford, Histamine and Scombrottoxins, *Toxicon.* 201 (2021) 115–126. <https://doi.org/10.1016/j.toxicon.2021.08.013>.
- [35] P. Visciano, M. Schirone, R. Tofalo, G. Suzzi, Histamine poisoning and control measures in fish and fishery products, *Front. Microbiol.* 5 (2014) 1–3. <https://doi.org/10.3389/fmicb.2014.00500>.
- [36] S. Esmail Tehrani, L. Quang Nguyen, G. Garelli, B.M. Jensen, T. Ruzgas, J. Emnéus, S. Sylvest Keller, Hydrogen Peroxide Detection Using Prussian Blue-modified 3D Pyrolytic Carbon Microelectrodes, *Electroanalysis.* 33 (2021) 2516–2528. <https://doi.org/10.1002/elan.202100387>.
- [37] K. Sasaki, H. Furusawa, K. Nagamine, S. Tokito, Charge-accumulative Potentiometric Measurements for Ammonia Detection Using an Enzymatic Cascade Reaction on a Prussian Blue Electrode, *Chem. Lett.* 47 (2018) 1412–1415. <https://doi.org/10.1246/cl.180692>.

Supporting Information for Capacitive Method as an Alternative Transduction Technique for Developing Prussian Blue-Based Electrochemical Sensors and Biosensors: A Case Study of Enzyme Catalyzed Histamine Oxidation

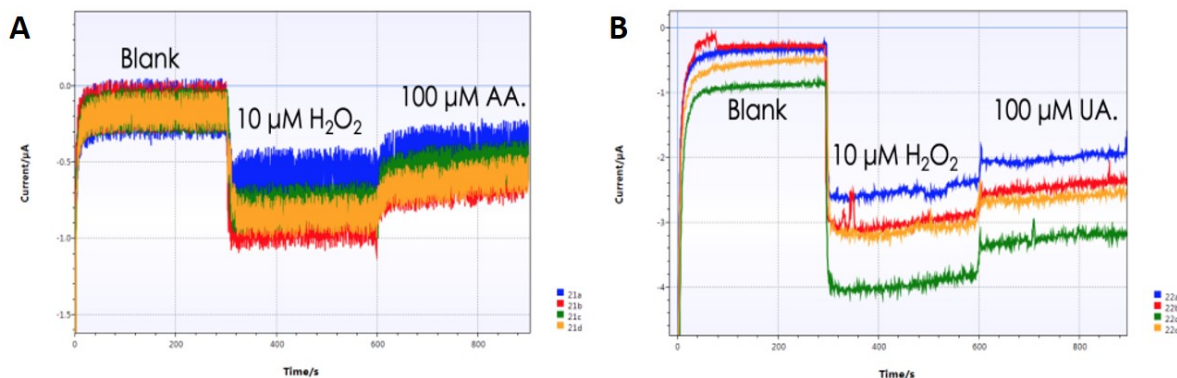
Sheida Esmail Tehrani, Long Quang Nguyen, Jesper Yue Pan, Bettina M. Jensen, Jenny Emnéus, Tautgirdas Ruzgas, Stephan Sylvest Keller



S 1 Cyclic voltammograms of four PB-modified pyrolytic carbon electrodes were obtained in phosphate buffer pH 5.5 before and after exposure to 1 μM H_2O_2 in a time course of 600 s. Scan rate 50 mVs^{-1} . As it can be seen, the oxidation and reduction peak currents of PB drop to half the initial value after just about 10 minutes of continuous exposure to H_2O_2 indicating the loss of electrocatalytic activity in the electrodeposited PB film.



S 2 Charge was produced by four PB-modified pyrolytic carbon sensors as they were exposed to increasing concentrations of H₂O₂ in buffer (pH 5.5 at RT) at the sub-µM level in the presence of dissolved oxygen. At the sub-µM concentration level, the current responses to each concentration and the corresponding charges do not follow the same linear trend as the potentiometric responses in figure 5B.



S 3 Selectivity assessment of H₂O₂ sensor by testing the interference of A) ascorbic acid (AA) and B) uric acid (UA). The responses of four PB-modified pyrolytic carbon sensors to 100 µM AA and UA (four sensors per compound) were assessed individually by stirred batch amperometry at E=0.0 V. First, stable baselines in blank phosphate buffer (pH 5.5) were established. Then, the responses of the sensors to 10 µM H₂O₂ (final concentration) were obtained which showed an obvious increase in the current level indicating the reduction of H₂O₂. Next, 100 µM (final concentration) of each potentially interfering compound (AA and UA) was introduced to the sensors. If both or either of the compounds were reduced at the same time as the H₂O₂ was reduced, the current would have increased significantly as the concentrations of the potentially interfering compounds were ten times larger than H₂O₂. But in both cases, the reduction current level dropped (shifted towards zero by becoming more positive), which was due to the dilution of the H₂O₂ containing working solution, as adding a volume of solution containing AA or UA would cause a decrease in a final concentration of H₂O₂.